Anisotropic confinement effects in semiconductor nanostructures

Ana Ballester Caudet

THESIS

Ana Ballester Caudet

Anisotropic confinement effects in semiconductor nanostructures

September 2013

Thesis Advisors:
Josep Planelles Fuster
José Luis Movilla Rosell

Universitat Jaume·I

Ana Ballester Caudet

Universitat Jaume·I

THESIS

Anisotropic Confinement Effects in Semiconductor Nanostructures

BY
Ana Ballester Caudet

THESIS ADVISORS
Josep Planelles Fuster
José Luis Movilla Rosell

September 2013

Departament de Química Física i Analítica
Universitat Jaume I
Castelló de la Plana, Spain

A mis padres,
siempre os estaré agradecida.

Els Doctors Josep Planelles Fuster i José Luis Movilla Rosell, del Departament de Química Física i Analítica de la Universitat Jaume I,

CERTIFIQUEN:

Que la memòria presentada per la llicenciada Ana Ballester Caudet amb títol "Anisotropic confinement effects in semiconductor nanostructures" ha estat realitzada sota la nostra direcció i constitueix la Tesi Doctoral de l'esmentada llicenciada. Autoritzem la presentació d'aquesta mitjançant el present escrit.

Castelló de la Plana, Setembre del 2013.

Josep Planelles Fuster

José Luis Movilla Rosell

Agradecimientos

La elaboración de esta Tesis no habría sido posible sin la colaboración y la ayuda de todas las personas que han compartido conmigo mis años de doctorado. En primer lugar, me gustaría agradecer a mis directores de tesis, el Dr. Josep Planelles y el Dr. José Luis Movilla, la oportunidad que me han brindado al poder trabajar con ellos y conocer el mundo de la investigación. Su profesionalidad, su dilatada experiencia investigadora, su dedicación, su dirección y su labor en equipo han sido fundamentales para el buen desarrollo de esta Tesis. Todo lo que he aprendido y la experiencia profesional que he adquirido durante los cuatro años de doctorado han sido gracias a trabajar con ellos.

También ha sido muy importante la contribución de mis compañeros de grupo. A Fernando Rajadell, Nacho Climente, Miquel Royo y Carlos Segarra quisiera agradecerles su compañerismo en la convivencia diaría y su colaboración profesional en los trabajos que hemos desarrollado conjuntamente. Asimismo, esta tesis se ha enriquecido de colaboraciones con otros grupos de investigación tanto nacionales como internacionales. Cabe mencionar, por tanto, al profesor Martí Pi y al Dr. Jose María Escartín, a quienes agradezco su generosa participación en los trabajos que hemos realizado conjuntamente, así como su ayuda a la hora de tratar detalles computacionales relacionados con la Teoría del Funcional de la Densidad. También, quisiera dar las gracias al profesor Guido Goldoni y al Dr. Andrea Bertoni, por su cálido acogimiento y su colaboración profesional durante las dos estancias que realicé en Modena (Italia). En especial, al Dr. Andrea Bertoni, mi tutor de estancia, quisiera mostrar mi gratitud tanto por su dedicación profesional como su hospitalidad.

A nivel personal el doctorado ha supuesto para mí un gran esfuerzo a la vez que una experiencia inolvidable. Ya desde el principio supuso un gran reto e incluso muchas veces hasta inalcanzable. Sin embargo, el apoyo incondicional e inestimable de mis padres fue fundamental para reactivar la

ilusión en los momentos difíciles, tanto profesionales como personales. A ellos les dedico esta Tesis. Además, me gustaría mencionar a mi hermano, a Rosa Mari, a mi prima Paula y a todos mis amigos que han sido partícipes de mis momentos de flaqueza pero también de mis alegrías, entre los cuales se encuentran Carlos, cuya amistad ha traspasado las fronteras del ámbito de trabajo, Tomás, compañero de carrera y de doctorado, Pamela, Elena, Pablo y Erica. Además, quisiera mencionar a Tahereh, Attila, Mariela, Marco Cavazzuti y Farah&Omer a los que he tenido la oportunidad de conocer durante mis estancias en Italia y con los que mantengo una buena amistad.

Finalmente, agradezco a Juanjo G. Ansuátegui la ayuda incondicional en la elaboración de la portada de esta Tesis, al Ministerio de Educación y Ciencia y a la Universitat Jaume I por la ayuda económica para poder llevarla a cabo, así como a todo el personal del Departamento de Química Física y Analítica por el compañerismo y la ayuda prestada en los trámites administrativos. En particular, agradezco a Merche su predisposición siempre positiva para gestionar estos trámites durante mis años de doctorado.

Contents

Introduction

In the last decades, the modern world has paid close attention to microscopic objects in order to acquire unprecedented material properties that may offer amazing benefits for human lifestyle. In this respect, numerous investigations refer to nanoscale structures as a challenging area with novel physical phenomena. Such small objects show interesting properties that are only understood by means of the fundamental basis of Quantum Theory, in comparison to the classical properties assigned to the macroscopic world. This theory, based on the wave-particle duality of the essential constituents of matter, determines the existence of quantum confinement effects responsible for the physical phenomena observed at the nanoscale. Since the *de Broglie wavelengths* of the charge carriers are of the order of the spatial dimensions of the above-mentioned nanostructures, quantum confinement plays a key role in defining their physical properties. Advancement of miniaturization techniques provides new design of nanoelectronic-based devices, composed mainly by semiconductor materials, whose electronic functions can be controlled leading to useful applications. This is the aim of *nanotechnology*. It is a recent, multidisciplinary area that attempts to build up faster, more efficient, and more intelligent devices by means of *top-down* and *bottom-up* nanofabrication techniques [1]. Particularly, artificial crystal structures containing between 1,000 and 100,000 atoms, the so-called *Quantum dots (QDs)* [2], are being widely investigated because of their novel potential uses as versatile basic components for microelectronics engineering purposes. A wide variety of studies suggest that such QDs, whose properties depend on their composition, size and shape, have huge technological interest in, e.g., substituting classic computation silicon devices [3], offering a wide range of electronic and optical properties [4, 5], or acting as biological labels [6, 7, 8].

Colloidal semiconductor QDs are synthesized following the well-known *Wet chemistry* routes [9]. Highly monodisperse nanocrystals (NCs) with precise size and nearly spherical shape are obtained by using organic ligands in solution. The electronic structure of these QDs resembles that of real atoms, since quantum confinement leads to quantized energy levels of carriers with preserved spherical symmetry [10]. This is the reason why they are usually known as *artificial atoms*. This quantum confinement can be traced back to the different band alignment between the material composing the QD and the surrounding media, or between neighboring materials in multishell systems. Concerning the last case, several heterostructures are being synthesized which offer significant modification of their physical properties compared with single-composition QDs. Braun *et al.* reported on the first preparation of a spherical multishell system [11] and it was concluded that there is an important interplay between layers. Later, the synthesis of hetero-NCs with radially graded composition [12] or type-II or quasi-type II core/shell NCs [13, 14] has been achieved thanks to well-established and extremely precise growth techniques [15, 16]. The possibility to engineer charge carrier wave functions in these structures may enable optimization of nanoelectronic applications [17].

The term Quantum dot is derived from the most widely accepted classification of the so-called *low-dimensional structures,* which depends on the confinement degree that exert on the charge carriers (electrons and holes). QDs confine carriers in all three dimensions. Instead, *Quantum Wells* are two-dimensional heterostructures that confine carriers along one direction, whereas quasi one-dimensional structures, the so-called *Quantum Wires* [18], show long lengths and confer free carrier motion along the growth direction. The transition from the spherical shape to quasi one-dimensional structures can be achieved by increasing the *aspect ratio* of NCs. Among nearly one-dimensional structures is worth to mention an elongated variant of spherical QDs called *Nanorods* [19], i.e., which are nearly cylindrical NCs with an aspect ratio lower than nanowires. Furthermore, recent experimental methodologies have produced more complex heterostructural systems based on nanorods that are called *Nanodumbbells* [20]. They are composed by a nanorod sandwiched between two semispherical caps.

In this Thesis, the electronic structure of semiconductor nanocrystals is theoretically investigated. To be specific, the *k·p method* [21] is employed to model conduction band states by means of the effective-mass and envelope function approximations. This one-band model is a good approximation when conduction band states can be considered fairly isolated from possible valence band perturbations [22]. Regarding most III-V and II-VI wide direct-gap semiconductor nanostructures, as the ones studied through this Thesis, the one-band model is a reasonable approximation. This semi-empirical method enables the addition of nonperiodic potentials such as impurity atoms, heterojunctions or external electromagnetic fields to the *k·p Hamiltonian* [23], taking advantage of a reasonable computational cost. Such flexibility let us investigate the physical properties of semiconductor NCs in various quantum confinement conditions. Initially, a detailed description of the interplay between the spatial and dielectric confinements is carried out in a simple molecular system formed by two coupled impurities in a QD. Including polarization potentials derived from dielectric response mismatches, in addition to the intrinsic spatial confinement present in nanocrystals, it is shown how the physical properties of a H_2^+-like system hosted in a QD can be designed to fullfil the requirements needed to act as the physical building blocks for quantum computation purposes [24]. Once dielectric mismatch effects in simple QDs are carefully understood, the attention is mainly focused on the role of the most important confinement in nanostructures, i.e., the spatial confinement. More complex systems subject to anisotropic spatial confinement are rigorously addressed when electronic interactions come into play. *Configuration Interaction (CI) and Density Functional Theory (DFT)* methods are employed to assess the many-body problem in elongated systems. Although high computationally demanding theories, they offer complementary accurate depictions of the energy balance in multi-electron systems within low- and high-density cases. Transitions from high to low correlation regimes, as well as novel phases of mixed correlation, are pointed out by monitoring addition spectra and optical spectra. Furthermore, absorption spectra simulations of core/shell heterorods stand out the key role of asymmetric spatial confinement in the description of one- and two-photon-induced excitation transitions. The importance of anisotropic confinement effects in NCs is attracting widespread

interest and it will be the fundamental issue during this work.

The research activity developed is exposed according to a coherent discussion of the results obtained, which have been published (or to be published inminently) in international scientific journals. This PhD Thesis memory is set out as follows:

The first chapter outlines the theoretical models employed to investigate the electronic properties of semiconductor nanostructures. The EMA model within the *Envelope function approximation (EFA)* will be introduced to provide the lowest-energy conduction band states in finite heterostructured crystals. Afterwards, Coulomb interaction will be incorporated in nanocrystal simulations by means of Configuration Interaction (FCI) approach and Density Functional Theory (DFT). Firstly, a brief theoretical description about FCI basics will be exposed, including a novel computing code that has been applied to improve the time-consuming of the CI simulations. Ground states and occasionally several excited states will be calculated in few-electron regimes. Absorption energies and their corresponding rates will be also obtained within the dipole approximation in the FCI scheme. Secondly, large-electron densities will be addressed via DFT within the so-called *Local Spin Density Approximation (LSDA)*. The fundamental basics will be briefly explained in order to eventually understand the perturbation scheme chosen for computing absorption responses.

The second chapter describes the molecular properties of two shallow donor impurities. Quantum confinement effects will be evaluated when the system is hosted inside a free standing spherical QD. Additionally, dielectric confinement effects will be included in a second step to take into account the different dielectric response of the QD and its environment. Highly non-additive effects will be shown, leading to specific physical properties of potential interest for quantum computing.

In the third chapter the electronic structure of quasi one-dimensional systems will be investigated. Highly anisotropic confinement effects will be monitored by means of addition energy spectra and electron-density profiles.

Furthermore, elongated nanostructures under inhomogeneous confining potentials, such as those provided by an applied electric field or the presence of heterostructural effects, will be characterized by constructing their absorption spectrum. Finally, the key role of asymmetries in the confining potential of core/shell heterorods will be evidenced, providing in turn theoretical explanation to unexpected experimental results.

The fourth chapter deals with a description of the electronic correlation effects in the few-electron regime of wurtzite multishell nanowires. Multielectron states will be considered in an effective 2D potential formed along the radial direction of a multishell nanowire. Addition energy spectra for ground states, electron density profiles and also conditional densities either for the ground state or excited states will be analyzed.

Finally, a summary of the main conclusions obtained will be stated.

The following list contains the publications derived to date from the Thesis project:

1. J. L. Movilla, A. Ballester and J. Planelles. "Coupled donors in quantum dots: Quantum size and dielectric mismatch effects" Phys. Rev. B, **79** (2009) 195319.1-6[1]

2. J. Planelles, M. Royo, A. Ballester and M. Pi. "From quantum dots to quantum wires: Electronic structure of semiconductor nanorods" Phys. Rev. B, **80** (2009) 045324.1-5[2]

3. A. Ballester, J. M. Escartin, J. L. Movilla, M. Pi and J. Planelles. "Mixed correlation phases in elongated quantum dots" Phys. Rev. B, **82** (2010) 115405.1-8[3]

[1] Selected for the June 1, 2009 issue of Virtual Journal of Nanoscale Science & Technology (Volume 19, Issue 22).
Selected for the June, 2009 issue of Virtual Journal of Quantum Information (Volume 9, Issue 6).

[2] Selected for the August 10, 2009 issue of Virtual Journal of Nanoscale Science & Technology (Volume 20, Issue 6).

[3] Selected for the September 13, 2010 issue of Virtual Journal of Nanoscale Science & Technology (Volume 22, Issue 12).

4. A. Ballester, J. L. Movilla, J. M. Escartin, M. Pi and J. Planelles "Configuration interaction approach to Fermi liquid-Wigner crystal mixed phases in semiconductor nanodumbbells" J. Appl. Phys., **112** (2012) 024311.1-5

5. A. Ballester, J. Planelles and A. Bertoni "Multiple-particle states of semiconductor hexagonal rings: Artificial benzene" J. Appl. Phys. **112** (2012) 104317.1-9

6. M. Allione, A. Ballester, H. Li, A. Comin, J. L. Movilla, J. I. Climente, L. Manna, and I. Moreels "Two-Photon-Induced Blue Shift of Core and Shell Optical Transitions in Colloidal CdSe/CdS Quasi-Type II Quantum Rods" ACS Nano **7** (2013) 2443.1-10

7. A. Ballester, C. Segarra, J. Planelles and A. Bertoni "Suppression of the Aharonov-Bohm effect in six-electron hexagonal quantum rings" (submitted)

Chapter 1

Theoretical framework

Through this chapter we briefly describe the theoretical models employed to give a proper description of the studied semiconductor systems, in which atoms arrange themselves in regular crystalline arrays as X-ray diffraction experiments reveal. These models are well-known and their applicability on such systems is well-established [25, 26, 27]. Firstly, the k·p model in the *Effective mass approximation* for conduction band electrons is introduced. Secondly, *Envelope function approximation* is presented to study heterostructured nanoscopic materials. Last section of the present chapter concerns the many-body approaches used to deal with electronic interactions. DFT and CI methodologies arisen from different basic concepts are summarily exposed.

1.1 k·p method. Effective mass approximation (EMA)

In an infinite three dimensional crystal free electron motion can be modelled by exploiting the *Born-Oppenheimer approximation*[1]. As a result, the

[1] Within the framework of nonrelativistic theory, atoms nuclei and core electrons, i.e., inner shell electrons composing the electron configuration, are interpreted as fixed nuclear point charges in the crystal with spherical symmetry.

electrons weakly bounded to atom nuclei (valence electrons) feel an effective electrostatic potential V_{cr} which is periodic throughout the crystal[2]. In this context, one-electron time-independent Schrödinger equation reads as:

$$\left(-\frac{\hbar^2}{2m_0}\nabla^2 + V_{cr}(\mathbf{r})\right)\psi_{nk}(\mathbf{r}) = E_{nk}\psi_{nk}(\mathbf{r}) \tag{1.1}$$

where the Hamiltonian operator contains the kinetic energy term, given by the free electron mass (m_0), and an averaged electrostatic potential (V_{cr}) that computes all possible interactions that valence electrons experience.

As indicated in Eq. (1.1), single-particle wave functions are labeled with the main quantum number n for each k value. The last quantum number ensures that Hamiltonian eigenfunctions are basis of irreducible representations from the translation group T_n. The corresponding character $e^{i\mathbf{kt}}$, where $\mathbf{t}$ is the Bravais lattice vector of the crystal, is obtained by means of k, which in turn transfers the translational symmetry to the Wigner-Seitz cell of the reciprocal lattice. In addition, electron wave-functions obey the so-called Bloch's theorem. It states that eigenvectors under translational symmetric conditions can be interpreted as a periodic part (unit cell) $u_{nk}(\mathbf{r})$, the well-known Bloch function, times a slowly varying envelope function $e^{i\mathbf{kr}}$ along the crystal:

$$\psi_{nk}(\mathbf{r}) = e^{i\mathbf{kr}}u_{nk}(\mathbf{r}). \tag{1.2}$$

Hence, taking into account Bloch's theorem and after some algebra, Schrödinger equation can be rewritten as:

$$\left(-\frac{\hbar^2}{2m_0}\nabla^2 + V_{cr}(\mathbf{r}) + \frac{\hbar^2k^2}{2m_0} + \frac{\hbar}{m_0}\mathbf{k}\cdot\mathbf{p}\right)u_{nk}(\mathbf{r}) = E_{nk}u_{nk}(\mathbf{r}), \tag{1.3}$$

[2]The electrostatic potential of a crystal is modelled as a periodic function that satisfies the Born-von Karman boundary condition. It states that $V_{cr}(\mathbf{r}) = V_{cr}\left(\mathbf{r} + \sum n_i\mathbf{a}_i\right)$, where $\mathbf{a}_i$ are the primitive vectors of the Bravais lattice and n_i are integers, running both over the dimensions (i) of the lattice.

where $\mathbf{p} = -i\hbar\nabla$ and the whole term in brackets corresponds to the so-called *k·p Hamiltonian* $\left(\widehat{H_{kp}}\right)$. Eigenvalues from Eq. (1.3) represent the discrete energy levels composing the band structure of semiconductor materials. A complete basis set of functions $\{u_{n0}, n = 1, 2, ..., \infty\}$ is obtained for $k = 0$ (Γ point). This basis lets us calculate the wave function $u_{nk}(\mathbf{r})$ for any $k \neq 0$ as a linear combination of $u_{n'0}(\mathbf{r})$:

$$u_{nk}(\mathbf{r}) = \sum_{n'}^{\infty} c_{nn'} u_{n'0}(\mathbf{r}). \tag{1.4}$$

The Hamiltonian in Eq. (1.3) can be expressed as follows:

$$\widehat{H_{kp}} = \widehat{H} + \frac{\hbar^2 k^2}{2m_0} + \frac{\hbar}{m_0}\mathbf{k}\cdot\mathbf{p} \tag{1.5}$$

In Eq. (1.5) $\widehat{H}$ represents the Hamiltonian (1.1) of the system for $k = 0$, the so-called Γ point. On the other hand, the projection of the k·p Hamiltonian onto the u_{n0} basis set leads to a matrix with infinite dimensions, whose elements are:

$$< u_{n0} \mid \widehat{H_{kp}} \mid u_{n'0} > = \left(E_{n'0} + \frac{\hbar^2 k^2}{2m_0}\right)\delta_{n,n'} + \frac{\hbar}{m_0}\mathbf{k}\mathbf{P}_{n,n'} \tag{1.6}$$

where $\mathbf{P}_{n,n'} = < u_{n0} \mid \mathbf{p} \mid u_{n'0} >$ is the Kane parameter [28, 29], which is determined empirically for each material.

In the following, only wide gap semiconductor materials will be considered. It means that energy difference between the maximum of the valence band (VB) and the minimum of the conduction band (CB) is high enough

to neglect coupling interactions between them. Electrons (holes) populating the lowest conduction (valence) band states at the Γ point are the ones considered through this Thesis. Under the above conditions, the electronic structure of materials can be safely described by means of the one band model formalism. It implies that the k·p Hamiltonian in the basis $\{u_{n0}\}$ is reduced to a 1x1 matrix:

$$< u_{n0} \mid \widehat{H_{kp}} \mid u_{n0} >= E_{n0} + \frac{\hbar^2 k^2}{2m_0}. \tag{1.7}$$

Consequently, energy band dispersion shows a parabolic dependence as a function of k. This one band model can be improved following a perturbative treatment up to second order, leading to the perturbative Hamiltonian $\widehat{H'} = \frac{\hbar^2 k^2}{2m_0} + \frac{\hbar}{m_0}\mathbf{k}\cdot\mathbf{p}$. A generalization of the perturbative treatment to any $k \neq 0$ point can be achieved considering the eigenfunctions for the unperturbed Hamiltonian $\widehat{H_0} = -\frac{\hbar^2}{2m_0}\nabla^2 + V_{cr}(\mathbf{r})$. Thus, the second order of perturbation energy writes as:

$$\begin{aligned} E_{nk}^{(2)} = -\sum_{n'} \frac{|< u_{n0} \mid \frac{\hbar}{m_0}\mathbf{k}\cdot\mathbf{p} \mid u_{n'0} >^2}{E_{n'0} - E_{n0}} = \\ = \sum_{n'} \frac{\mid \hbar\,\mathbf{k}\cdot\mathbf{P}_{n,n'} \mid^2}{m_0^2\,(E_{n0} - E_{n'0})} = \sum_{\alpha=x,y,z} \sum_{n'} \frac{\hbar^2 k_\alpha^2 \mid \mathbf{P}_{n,n'}^{\alpha} \mid^2}{m_0^2\,(E_{n0} - E_{n'0})} \end{aligned} \tag{1.8}$$

Owing to the s-type orbital associated to conduction band states only k_α^2 terms take part, i.e., only integrals such as $< S \mid p_x \mid X >$ and $< S \mid p_y \mid Y >$ are set different from zero. Taking Eq. (1.8) into account, the energy up to second order of perturbation reads as:

$$E_{nk} = E_{n0} + \sum_{\alpha=x,y,z} \hbar^2 k_\alpha^2 \left\{ \frac{1}{2m_0} + \frac{1}{m_0^2} \sum_{n'} \frac{\mid \mathbf{P}_{n,n'}^{\alpha} \mid^2}{E_{n0} - E_{n'0}} \right\} = E_{n0} + \sum_{\alpha=x,y,z} \frac{\hbar^2 k_\alpha^2}{2m_\alpha^*}, \tag{1.9}$$

where a new empirical parameter appears in order to reproduce the effect of the periodic potential in the electron motion near the Γ point. A k–dependent electron mass, the so-called *Effective electron mass* (m^*_α), is obtained through experimental measurements. It depends on the material composition and can be either isotropic or anisotropic.

To sum up, the one band model within the Effective mass approximation (EMA) gives reasonable results for energy dispersion in infinite periodic crystals (*bulk region*) by using empirical masses for electrons. Specifically, conduction band shows quasi parabolic energy dispersion near the Γ point as illustrated in Fig. 1.1. Through this memory, a theoretical description of the energetically lowest-lying conduction and valence band states is discussed in direct band gap semiconductor-based structures.

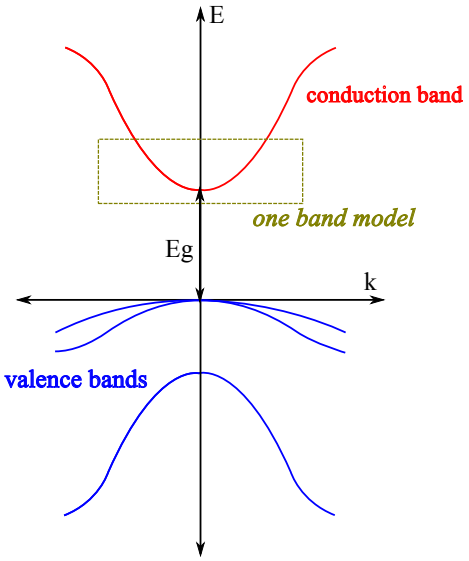

Figure 1.1: Schematic representation of direct band gap semiconductors in the k-space. Excited electrons promoting from the valence band to the conduction band are well-described by means of the one band model in the proximities of the Γ point.

1.2 Heterostructured crystals: Envelope function approximation (EFA)

Finite nanoscale-sized structures show atomically-sharp heterojunctions responsible for broken translational symmetry of the crystal. Therefore, the abovementioned effective-mass equation is inadequate to account for structural mismatches. In an attempt to fulfil the lack of periodicity in the systems, heterostructured nanocrystals are studied within the *Envelope function approximation (EFA)*. The theoretical description of the conduction-band electrons assumes a slowly-varying envelope function between the layers of adjacent materials. This is a reasonable approximation for materials with similar structural parameters (same crystalline structure and lattice constants), similar chemical composition (e.g., a common ion) and without interface defects. Hence, the wave function can be expanded in terms of the Bloch function (periodic part), assumed equivalent for the whole nanostructure, and an (initially unknown) envelope function that is treated independently [23]. In this context, the different band alignment on both sides of the heterointerface (*band-offset*), with respect to the bottom of the conduction band of the materials involved, delimits the finite spatial confining potential in the nanostructure. A steplike function (see Fig. 1.2) is assumed to correctly represent the band-edge variation in the heterostructures studied.

To compute the discrete energy states in QDs the *Effective mass - Envelope function approximation (EMA-EFA)* is employed. Now, the Schrödinger equation results:

$$\left(-\frac{\hbar^2}{2}\nabla\frac{1}{m^*(\mathbf{r})}\nabla + V(\mathbf{r})\right)\chi(\mathbf{r}) = E\chi(\mathbf{r}) \tag{1.10}$$

where the material properties are explicitly position dependent. In Eq. (1.10) $V(\mathbf{r})$ stands for the step-like confining potential aforementioned. On the other hand, the kinetic-energy operator is expressed in terms of the

BenDaniel-Duke model [30, 31] due to the fact that material properties do not commute with the spatial differential operator. Thus, the form of the kinetic-energy operator in Eq. (1.10) ensures the hermiticity of the operator. The eigenvalues in Eq. (1.10) are the allowed energies for conduction band electrons, but the eigenfunctions are now the envelope functions $\chi(\mathbf{r})$, which vary smoothly all over the nanostructure and are set to zero at large distances away from the heterostructure.

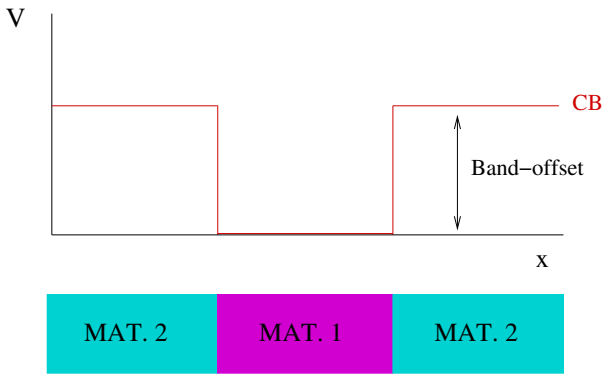

Figure 1.2: One-dimensional schematics of a heterostructure. The band-offset represents the energy difference between the bottoms of the conduction bands of the media involved. It is displayed as a steplike potential at the heterointerface.

In this Thesis, envelope wave functions and electron energies are obtained in several low-dimensional structures with axial symmetry. Analytical integration of the electron angular coordinate let us compute truly-3D systems numerically in cylindrical coordinates (ρ, z). Then, exact integration is carried out by means of a discretization scheme based on the finite differences method [32]. Discretizing the differential Schrödinger equation for each discretization grid point generally leads to asymmetric sparse matrices of considerable dimensions. Solutions are obtained by diagonalizing the resulting matrices with the implicitly restarted Arnoldi iterative method [33, 34] employing Arpack Fortran code [35]. Finally, electronic properties of

nanostructures are analyzed when different confinement regimes come into play and characterized by simulating addition energy spectra and absorption spectra. To this end, the many-body problem is addressed by two different approaches in which electron-electron interactions are properly assessed depending on the electron density.

1.3 Many-body systems

Within *Full Configuration Interaction approach (FCI)*, multi-electron wave functions are obtained by projecting the interacting Hamiltonian onto antisymmetric spin-orbitals , while, on the other hand, Kohn-Sham orbitals are employed in the framework of *Density Functional Theory (DFT)*. Both methodologies successfully account for N-electron ground states following the Variation Principle. In addition, few excited states are also considered in order to perform absorption spectra simulations. In the case of DFT calculations, a time-dependent scheme has been employed, which determines excited energies by means of perturbing the system with an external dipole field [36]. To simulate the low-energy part of the absorption spectrum, density dipole modes (preserving spin) and spin dipole modes (implying spin changes) are calculated within the *dipole approximation*. The calculations involve electronic absorptions associated with the excitation of outer shell electrons.

Depending on the number of electrons populating the conduction band of the nanostructure, FCI or DFT calculations have been performed. We provide next a brief description of the fundamentals of both approaches.

1.3.1 Full Configuration Interaction (FCI) approach

Correlation effects in few-electron regimes are studied by means of the *Full Configuration Interaction (FCI)* approach [37]. This is the most rigorous

method that gives an approximate many-particle wave function of the Hamiltonian:

$$\hat{\mathcal{H}} = \sum_{i=1}^{N} \left(-\frac{\hbar^2}{2} \nabla \frac{1}{m^*(\mathbf{r}_\mathrm{i})} \nabla + V(\mathbf{r}_i) \right) + \sum_{i<j}^{N} \frac{1}{\epsilon} \frac{1}{\mid \mathbf{r}_i - \mathbf{r}_j \mid}. \tag{1.11}$$

In Eq. (1.11) the first term in brackets corresponds to the single-particle operator within the EMA-EFA model for N electrons confined inside a nanostructure. The second one stands for the two-electron operator which involves coordinates of electrons i and j. The many-electron Hamiltonian in Eq. (1.11) is solved by means of FCI calculations. They make use of a finite N-electron basis set rigorously selected depending on the system considered. Building *all* possible N-body Slater determinants[3] $\{\phi_i\}$ out of the basis set chosen, the FCI approach gives solutions that are *exact* within the one-electron subspace spanned by the Slater determinants. This procedure lets us achieve a good approximation to the real many-electron problem, being impossible to be implemented in practice for the complete solution, i.e., an infinite basis set. The electronic configuration of the multi-particle system obeys the Pauli's Principle and the resulting many-electron wave function is expressed as a linear combination of Slater determinants:

$$\mid \Psi_m > = \sum_i c_i^m \mid \phi_i > . \tag{1.12}$$

In Eq. (1.12) the multi-particle state $\mid \Psi_m >$ is a good approximation to the exact ground state wave function and even excited states as MacDonald theorem states [38].

[3] A Slater determinant is an antisymmetrized product of spin-orbitals that describes the multi-particle wavefunction of the non-interacting system. Slater determinants formed from orthonormal spin orbitals are normalized and meet the requirement of the Pauli exclusion principle.

The interaction between the radiation and the polielectronic system is quantified by charge and spin transition probabilities from the ground state Ψ_0 to the excited state Ψ_f as [39]:

$$| \mathbf{k}\cdot < \Psi_0 \mid \sum_{i=1}^{N} \mathbf{r}_i \mid \Psi_f > |^2 \tag{1.13}$$

$$| \mathbf{k}\cdot < \Psi_0 \mid \sum_{i=1}^{N} \eta_{\sigma i}\mathbf{r}_i \mid \Psi_f > |^2 \tag{1.14}$$

where $\mathbf{k}$ defines the polarization vector of the incident electromagnetic radiation which, in our axially-symmetric systems, has been assumed to be polarized either in the longitudinal direction (z-polarization transitions) or the in-plane one. Whereas Eq. (1.13) provides charge modes, Eq. (1.14) stands for spin modes, with $\eta_\sigma = +1(-1)$ for electrons with spin up (down). Selection rules imply that the z-component of the total angular momentum must change according to $\triangle M_z = \pm 1$ in the in-plane polarized radiation, while it must remain constant in z-polarized transitions ($\triangle M_z = 0$).

Although FCI conceptually constitutes the simplest approach for studying polielectronic systems, it is very high-demanding computationally. One way to avoid this drawback consists in selecting a subset of spin- and symmetry-adapted configurations that constitute a block of the whole Hamiltonian matrix. In this regard, a novel CI code[4] has been employed to obtain smaller matrices to diagonalize. Specific multi-particle states with a given total S_z and M_z quantum numbers are thus obtained.

[4]See http://code.google.com/p/citool/ for more information about the Full-Configuration-Interaction solver.

1.3.2 Density Functional Theory. LSDA approximation

We describe systems populated up to 20 electrons by means of the *Density Functional Theory (DFT)* [40, 41, 42]. DFT has its foundations in the *Hohenberg-Kohn Theorems* [43] proving that a universal functional of the density exists for a non degenerate ground state. These theorems require electron density to be N-representable and v-representable[5]. The energy functional can be expressed as:

$$E\left[\rho\right] = T\left[\rho\right] + V_{ext}\left[\rho\right] + V_{ee}\left[\rho\right] \ , \tag{1.15}$$

where the first term corresponds to the kinetic energy functional, the remaining functionals correspond to the applied external potential V_{ext} and the Coulomb interaction V_{ee}. A generalization of the Hohenberg and Kohn theorems is achieved following the Levy's formalism [44], which only assumes the N-representability of the density.

To calculate the ground-state energy of a polielectronic system as a functional of its electron density in a practical way, a fictitious noninteracting system is considered. It is the so-called *Kohn-Sham method (KS method)* [45]. The fictitious system moves under the influence of an external potential, and must have a wave function yielding the very same density as the real system. The KS Hamiltonian for the non-interacting system is defined as:

$$\hat{\mathcal{H}}_s = \sum_{i=1}^{N} \widehat{h_i} = \sum_{i=1}^{N} \left(-\frac{1}{2}\nabla_i^2 + \hat{v_s}(\mathbf{r}_i) \right) \ , \tag{1.16}$$

[5]The N-representability means that the density must be a continuous, positive defined function in all the entire space considered. Its integration must give the number of electrons on the whole system. On the other hand, a v-representable density implies that there is an external potential that generates a function which has the corresponding density when applied to the system.

where N runs over the number of electrons. Eq. (1.16) allows us to work with an artificial ground-state wave function as an antisymmetrized product of the lowest-energy KS spin orbitals (Φ_i) subject to a uniquely determined external potential υ_s. The orbitals are obtained by solving the eigenvalue Eq. (1.17). Such orbitals enable to calculate the polielectronic ground-state density (ρ) as a sum of single-particle densities (Eq. 1.18):

$$\left[-\frac{1}{2}\nabla^2 + \upsilon_s(\mathbf{r})\right]\Phi_i = \varepsilon_i\Phi_i \tag{1.17}$$

$$\rho = \rho_0 = \sum_{i=1}^{N} \mid \Phi_i \mid^2 \ . \tag{1.18}$$

The N-noninteracting system is given by

$$E_\upsilon[\rho] = T_s[\rho] + \int \rho(\mathbf{r})\upsilon_s(\mathbf{r})d\mathbf{r} = \sum_{i=1}^{N}\varepsilon_i \tag{1.19}$$

where,

$$T_s[\rho] = \sum_{i=1}^{N} < \Phi_i| - \frac{1}{2}\nabla^2|\Phi_i > \ . \tag{1.20}$$

The real polielectronic system expression reads as follows:

$$E_\upsilon[\rho] = T_s[\rho] + \int \rho(\mathbf{r})\upsilon(\mathbf{r})d\mathbf{r} + \frac{1}{2}\int\int \frac{\rho(\mathbf{r}_1)\rho(\mathbf{r}_2)}{r_{12}}d\mathbf{r}_1 d\mathbf{r}_2 + E_{xc}[\rho] \ . \tag{1.21}$$

The last term E_{xc} in the above equation is referred to exchange-correlation functional and includes all (unknown) contributions making $E_{\upsilon}[\rho]$ exact. Eq. (1.16) can be rewritten by including all the potential terms in an *effective potential* uniquely determined by the electron density:

$$\widehat{\mathcal{H}_{\mathcal{KS}}} = \sum_{i=1}^{N} \left(-\frac{1}{2}\nabla_i^2 + \widehat{\upsilon}_{eff}(\mathbf{r}_i) \right). \tag{1.22}$$

Actually, both the effective potential and the exchange-correlation functional are unknown. Nevertheless, by using approximate expressions for E_{xc}, the electron density and the effective potential can be optimized following a variational self-consistent procedure.

Although DFT emerges as a very powerful and computationally low-demanding technique, getting a good approximation to E_{xc} is not an easy task. *Local-Density Approximation (LDA)* gives accurate results for the exchange-correlation energy in systems with a rather homogeneous density. The fact that density varies slowly allows the exchange-correlation functional to be accurately given by:

$$E_{xc}^{LDA}[\rho] = \int \rho(\mathbf{r}) \varepsilon_{xc}(\rho) d\mathbf{r}\,, \tag{1.23}$$

where $\varepsilon_{xc}(\rho)$ is the exchange-correlation functional of an homogeneous electron gas.

Local-Spin-Density Approximation (LSDA) is used throughout this Thesis. This approximation allows electrons with different spin to have different spatial KS orbitals. As a consequence, LSDA deals with two different spin densities $\rho^{\alpha}(\mathbf{r})$ and $\rho^{\beta}(\mathbf{r})$ which are connected, since Coulomb and correlation functionals depend on both of them. The Coulomb functional now reads as:

$$J\left(\rho^{\alpha},\rho^{\beta}\right)=\frac{1}{2}\int\int\frac{\rho^{\alpha}(\mathbf{r}_1)\rho^{\alpha}(\mathbf{r}_2)}{r_{12}}d\mathbf{r}_1d\mathbf{r}_2+\frac{1}{2}\int\int\frac{\rho^{\alpha}(\mathbf{r}_1)\rho^{\beta}(\mathbf{r}_2)}{r_{12}}d\mathbf{r}_1d\mathbf{r}_2\ . \tag{1.24}$$

On the other hand, exchange-correlation functionals become functionals of spin densities $E_{xc}=E_{xc}\left[\rho^{\alpha},\rho^{\beta}\right]$.

LSDA has been proved to yield satisfactory results in the study of nanostructures [46, 47, 48, 49], taking, in particular, the exchange-correlation functional as a sum of the Dirac exchange functional of a homogeneous electron gas and the correlation functional parametrized by Perdew and Zunger [50].

In this thesis, ground-state energies in elongated nanostructures are carried out by numerical integration of the KS equations. Absorption spectra simulations are computed within the framework of time-dependent LSDA [36]. In order to obtain the dipole strength in the spin and density channels, we study the time evolution, following an initial perturbation, of the dipole signal $D(t)=\mathbf{n}\cdot<\mathbf{D}>$, where $\mathbf{D}=\sum_{\mathrm{j}}\mathbf{r}_{\mathrm{j}}$ for density-dipole modes and $\mathbf{D}=\sum_{\mathrm{j}}\mathbf{r}_{\mathrm{j}}\sigma_j^z$ for spin-dipole modes, $<\cdot>$ means expected value in the time-dependent state, and $\mathbf{n}$ is the unit vector pointing toward the direction given by the polarization of the incident electromagnetic wave. To calculate $D(t)$, we first solve the static LSDA KS equations, and the appropriate static solutions of the KS equations are then used as initial conditions for solving the time-dependent KS equations:

$$i\hbar\frac{\partial}{\partial t}\Psi_{\sigma}\left(\mathbf{r},t\right)=\mathcal{H}_{\mathcal{KS}}\left[\rho^{\alpha}\left(\mathbf{r},t\right),\rho^{\beta}\left(\mathbf{r},t\right)\right]\Psi_{\sigma}\left(\mathbf{r},t\right)\ . \tag{1.25}$$

In order to describe the interaction of the system with an external dipole field, the ground-state single-particle wave functions are slightly excited initially according to $\Psi_{\sigma}^{'}(\mathbf{r},0)=U\Psi_{\sigma}(\mathbf{r},0)$, with $U=e^{ik\mathbf{n}\cdot\mathbf{r}}$ for the density-dipole modes and $U=e^{ik\eta_{\sigma}\mathbf{n}\cdot\mathbf{r}}$, where $\eta_{\sigma}=+1(-1)$ for $\sigma=\alpha(\beta)$,

for the spin-dipole modes. The wave number k is taken small enough to keep the response of the system within the linear regime, in which the Fourier transform of the dipole signal, $D(\omega) = \int e^{i\omega t} D(t) dt$, is directly related to the dipole strength, $S_{\mathbf{n}}(\omega) = \frac{1}{k} Im[D(\omega)]$. Hence, a frequency analysis of $D(t)$ provides the absorption energies and their respective intensities.

As a summary, this section gives a general overview of the multi-particle approaches employed for characterizing the systems studied: LSDA and FCI. In spite of their different background, the obtained FCI density profiles are in qualitative agreement with LSDA calculations. The obtained results are concisely exposed in chapter 3.

Chapter 2

Dielectric modulation of size confinement effects in QDs

In this chapter, we deal with anisotropic confinement effects in the presence of a new confinement source: the dielectric confinement. Its effects have become an important factor to take into account in order to understand the nanostructures properties, specially those of colloidal QDs. Since they are typically synthesized surrounded by organic solutions, the different dielectric response between the semiconductor nanosystem and the environment yields to polarization charges in the interface between both materials [51]. Determining the role of these polarization charges has led to both experimental [52, 53] and theoretical [54, 55, 56] efforts in order to integrate the dielectric effects as control variables for new nanoscopic devices. Indeed, dielectric confinement is an additional confinement source that eventually can compete with the confinement originated by the band-offset between adjacent materials.

In the following, we analyze the interplay between both spatial and dielectric confinements in anisotropic conditions. In order to do that, we explore the molecular properties of a D_2^+ system (a system of potential interest for quantum computation purposes which consists of a singly-ionized double donor system hosted in a semiconductor) when it is embedded in a quantum dot of variable size and surrounding medium. The EMA-EFA model successfully describes quantum size and asymmetric confinement

effects, as well as dielectric mismatch effects on the single-particle energy and wave function localization by means of polarization charge potentials. A computational scheme which incorporates all confining potentials in a balanced way is employed, which incorporates the dielectric effects by using a macroscopic treatment of the Coulomb interactions, the validity of which has been well established for semiconductor QDs [57].

2.1 The D_2^+ system

While electron energies in single QDs are totally quantized resembling atomlike states, an array of QDs coupled electrostatically or by tunneling junctions displays features characteristic of *artificial molecules*. Their electron states can couple to each other and form covalent bonding states which are characterized by the so-called *binding energy* of the molecule. These artificial molecules are of interest in new materials engineering in order to add more capability and performance to electronic devices. For instance, QD solar cells [58], optoelectronics [59] and spintronics [60] devices have been involved in a deeper understanding of powerful novel applications. Lateral-type coupled QDs [61, 62, 63] or vertically coupled QDs [64, 65] can be used to create two-level systems with precise and rapid control of the coupling between quantum states by adjusting interdot tunnel coupling [66]. In particular, a highly coherent coupled QD leading to a two-level quantum system or *quantum bit* (*qubit*)[1] has been proposed as promising candidate in processing quantum computer information [67, 68]. This system can encode the logical information on the charge degrees of freedom, as Barenco *et al.* described for the first time in a semiconductor QD charge-based qubit [69].

Alternatively, impurity doping in low dimensional structures has become an additional useful and reproducible technology that provides new perspectives to control electronic and optical properties of semiconductor

[1] Coherent interactions and high entanglement between pairs of qubits form the basis of non-classical building blocks for quantum computation.

devices [70, 71]. The presence of new confinement sources apart from spatial confinement gives rise to more complexity in the understanding of the properties of quantum dots, but also to more opportunities to mould their electronic spectrum. Indeed, the work of Kang *et al.* [72] revealed that the system composed by a singly-ionized shallow donor impurity pair (namely a D_2^+ system) hosted in a quantum dot could be a plausible candidate for charge qubit realizations. Modulation on the physical behaviour of the two lowest-lying impurity states is of theoretical interest, being the decoherence of the excited state a key drawback for qubit realizations.

With the aim of determining the optimum conditions to tune the energy spectrum, charge distributions and coherence times of orbital states, the theoretical work summarized in this chapter is based on analyzing the effects of quantum confinement and impurity-related potentials. Particularly, polarization and self-polarization potentials coming from different dielectric response in different media may become a crucial issue to take into account. The interplay between different dielectric environments, quantum size effects, and asymmetric spatial locations of the coupled impurities inside a spherical QD is addressed, revealing the conditions which might be of interest to improve the performance of donor-based charge qubit schemes.

2.2 Size and dielectric confinement interplay in colloidal QDs

The electronic properties of the D_2^+ shallow donor impurities hosted in a semiconductor colloidal QD are analyzed depending on QD size, donors position inside the nanostructure and dielectric mismatch effects. The interplay between both, spatial and dielectric confinements, and the derived D_2^+ properties are of interest prompted by future perspectives for designing solid structures with controlled physical properties. Quite a larger amount of work has been devoted to the study of single shallow donor impurities [73, 74, 75] and it has been determined that, although the quantum dot

shape has a minor influence in shallow donor impurities [76, 77], the impurity position confined in a QD and the size of the nanostructure strongly influence donor levels [78, 79, 80, 81]. In the following, we probe how several anisotropic confinement conditions (such as the impurity position, for instance) influence the lowest-lying molecularlike states in coupled shallow impurities.

Modeling a shallow donor impurity as a hydrogen atom which provides an extra electron to the electronic structure of the semiconductor nanostructure, electron energies and wave functions can be obtained within the effective mass and envelope function approximations. The corresponding Hamiltonian reads, in atomic units:

$$\mathcal{H} = -\frac{1}{2}\nabla\left(\frac{1}{m^*(\mathbf{r})}\nabla\right) + V(\mathbf{r}) - \sum_{i=1,2}\frac{1}{\epsilon_{QD} \mid \mathbf{r}-\mathbf{r}_i \mid}\,, \tag{2.1}$$

where the kinetic-energy operator involves position-dependent effective electron masses and the finite confining potential $V(\mathbf{r})$ corresponds to the conduction band-offset between the materials involved. The last term represents the *direct Coulomb potential* between the impurities and the electron, including impurities position inside the QD ($\mathbf{r}_i$) and the dielectric constant of the bulk material ϵ_{QD}.

Fig. 2.1 assumes, however, a similar response of the QD material and that of surrounding medium. Nevertheless, in colloidal QDs a major contribution to the binding energy comes from *polarization charges* caused by dielectric mismatch at the edge of the QD [71]. Its effects are of theoretical interest due to the fact that they can introduce novel physical phenomena when a finite nanostructure and the surrounding media have different dielectric constants. The induced charges have the same sign as the impurity if the dielectric constant of the quantum dot (ϵ_{QD}) is larger than the external medium (ϵ_{out}). This fact yields an attractive interaction with the electron of the donor impurity and, consequently, an appreciable increase in the binding energy occurs. In the opposite case, that is an external dielectric constant

larger than the quantum dot one, induced charges show opposing sign in comparison with the impurity and, therefore, a reasonable decrease in the binding energy. Furthermore, dielectric confinement produces an additional polarization potential, the so-called *self-polarization potential*, which characterizes the interaction between the electron bound to the impurity and its own induced charges at the nanostructure boundaries.

The electronic structure of the two coupled impurities D_2^+ hosted in a spherical QD has been examined. The impurities are located on the z axis of a spherical CdS QD (see Fig. 2.1), with an effective mass $m^* = 0.15$ and dielectric constant $\epsilon_{QD} = 5.5$. The dot is isolated from the external medium by a confining well with a height equal to the typical electron affinity of semiconductor materials (4 eV). The effective mass of vacuum ($m^* = 1$) is assigned to the surrounding media. Fixing these parameters, we evaluate both, together ($\epsilon_{out} \neq \epsilon_{QD}$) and separately ($\epsilon_{out} = \epsilon_{QD}$), the influence of the spatial and dielectric asymmetric confinements on the molecular properties of the D_2^+ system.

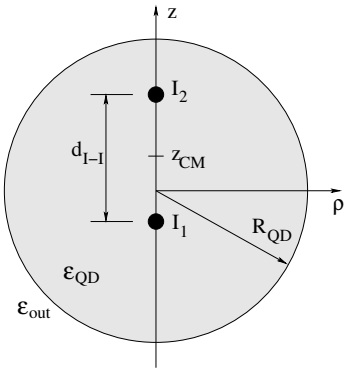

Figure 2.1: Schematic representation of the two shallow donor impurities under study. The center of mass of the two donors z_{CM} and the distance between them d_{I-I} are defined along the z axis of a two dimensional grid expressed in cylindrical coordinates. Dielectric mismatch effects are taken into account by using ϵ_{QD} as the dielectric constant of the QD material, while the surrounding media shows a different response.

The Hamiltonian that accounts for quantum size effects but also impurity polarization charges and electron self-energy (a.u.) reads:

$$\mathcal{H} = -\frac{1}{2}\nabla\left(\frac{1}{m^*(\mathbf{r})}\nabla\right) + V(\mathbf{r}) + \phi_s(\mathbf{r}) + \sum_{i=1,2}\phi_c^{I_i}\left(\mathbf{r},\mathbf{r}_i\right), \qquad (2.2)$$

where the first term is the kinetic energy operator for a position-dependent mass. $V(r)$ is a realistic (3D), finite confining potential represented by a steplike function that accounts for the spatial confinement coming from the band offset of the materials involved. Regarding dielectric mismatch, a steplike dielectric function is assumed for a position-dependent dielectric constant. In such a case, the corresponding *Poisson equation* for spherical dielectric interfaces can be solved analytically, yielding explicit expressions for the polarization terms [82]. In Eq. 2.2 the ϕ_c^I is the Coulomb potential generated by the impurities located at the fixed position r_i, including the effect of polarization charges. On the other hand, ϕ_S is the electron self-polarization energy, which can be obtained from ϕ_c^I. Their explicit expressions together with a detailed description of the integration method can be found in [81, 83]. The axial symmetry of the system allows us to integrate analitically the angular coordinate of the electron in Eq. (2.2). Then, numerical integration of (ρ, z) coordinates has been performed to finally obtain electron energies and wave functions.

2.3 Results

To characterize the effects of the confinement on the D_2^+ system, several molecular properties, such as charge-density distributions of the ground and first excited states, their energy splittings and the first excited decay rate have been analyzed.

First, we calculate the dipolar moment of electron charge distributions with respect to the center of mass (z_{CM}) of the artificial molecule for two

different sets of calculations. On the one hand, pure spatial confinement effects ($\varepsilon_{out} = \varepsilon_{QD} = 5.5$) are investigated for different size regimes. Next, dielectric mismatch effects are also included in addition to spatial confinement. In both situations the dipolar moment let us quantify the symmetry breakdown of the electron density. Finally, first excited state lifetimes have been calculated taking into account decoherence only coming from vacuum electromagnetic fluctuations as a first approximation [84, 85]. The results reveal that:

- In the absence of dielectric mismatch, impurities off-centering (asymmetric spatial confinement) brings the molecular system to behave as heteropolar, diminishing the interdonor tunnel coupling and localizing the ground and first excited states in different donors. This fact can be observed in the top panels of Fig. 2.2, where the dipolar moment relative to d_{I-I} (distance between the donors) is displayed as a function of the QD radius (R_{QD}) and the center of mass of the donors[2] (z_{CM}). As illustrated in the figure, the ground state is localized in the inner donor while the first excited state mainly concentrates on the outer one, this trend being more pronounced as the QD size decreases and large z_{CM} values are considered. Interestingly, the polarity of the states is generally the opposite in the presence of dielectric mismatch with $\varepsilon_{out} \ll \varepsilon_{QD}$ (see the bottom panels of Fig. 2.2). This is a direct consequence of the contribution of polarization charges induced by the impurities at the QD surface. Coulomb potential preferably stabilizes the ground state electron density closer to the outer donor (positive values of μ/d_{I-I} or red color), whereas the inner donor is occupied by the excited state (negative values μ/d_{I-I} or blue color).

[2]Through all the study, the dipole moment (μ) is defined with respect to the center of mass of the two donors. Thus, a positive value of μ is obtained for states preferably localized in the outer donor, whereas a negative value is obtained when the preference is for the inner one.

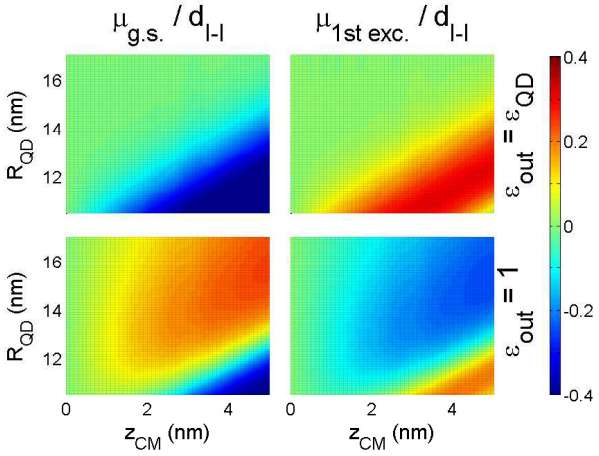

Figure 2.2: Dipolar moment of the electron charge distribution in the ground state (left) and first excited state (right) for a confined donor system with $d_{I-I} = 10$ nm. Fixing the origin at the QD center, several asymmetric confinement configurations are considered as a function of the QD size. In top panels the environment has the very same dielectric constant as the QD (pure spatial confinement), whereas the bottom panels concern an external medium with $\varepsilon_{out} = 1$. In the figure, positive values of μ/d_{I-I} indicate that the electron is distributed to a greater extent around the donor closer to the QD border, whereas negative values manifest its preference for the innermost impurity.

- Spatial and dielectric confinement sources operate in different length scales, which makes possible to modulate the tunnel coupling strength and charge-density distribution of the two lowest-lying electron states at will, by choosing the appropriate dot size and external environment. This effect is a consequence of the long range of the (image charge) Coulomb interactions as compared with the spatial confinement scale. As shown in Fig. 2.3 pure spatial confinement yields homopolarity for large QD sizes, whereas the system still behaves as heteropolar in the presence of dielectric mismatch. Also, it is worth to mention that, despite of the presence of polarization charges, spatial confinement dominates for low QD radius (see Fig. 2.3). However, for intermediate values of QD size ($R_{QD} \approx 14$ nm), both spatial and dielectric con-

finement effects are significant. In fact, it is observed that dielectric confinement compensates, and even inverts, the trend imposed by the spatial confinement.

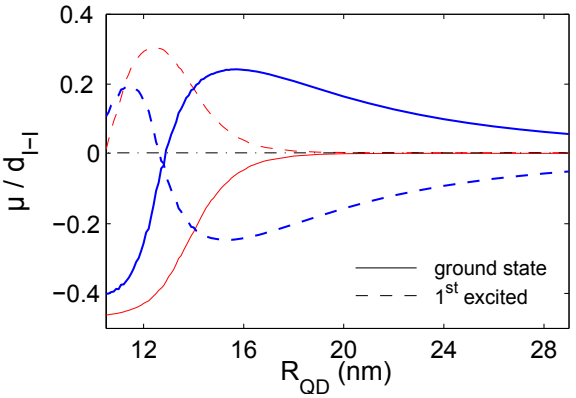

Figure 2.3: Dipolar moment of the electron charge distribution of the confined coupled donor system corresponding to pure spatial confinement (red lines) and in the presence of dielectric confinement (blue lines, $\varepsilon_{out} = 1$). In this figure the particular case of $z_{CM} = 5$ nm with one of the impurities located at the QD center and $d_{I-I} = 10$ nm is represented.

- The spatial separation of the two lowest-lying electron states induced by the asymmetric confinement is more pronounced as the interdonor distance increases. This is observed by comparing Fig. 2.3 ($d_{I-I} = 10$ nm) and Fig. 2.4 ($d_{I-I} = 15$ nm). This last figure also exemplifies the effect of the dielectric environment. As can be observed from the $R_{QD} = 20$ nm case, when $\epsilon_{out} > \varepsilon_{QD}$ the dielectric confinement magnifies the spatial separation of states imposed by the spatial confinement, that is, $\varepsilon_{out} = 5.5$. Nevertheless, this trend is inverted as ε_{out} diminishes. At low enough values of the external dielectric constant, dielectric mismatch effects dominate and yield a spatial separation of the lowest-lying molecular states but opposite polarity.

This fact implies that the bulklike homopolar character is recovered for an external media with an intermediate dielectric constant, where the effect of the spatial confinement is compensated (in the particular case of the system under study we found this to occur at $\varepsilon_{out} = 3.9$).

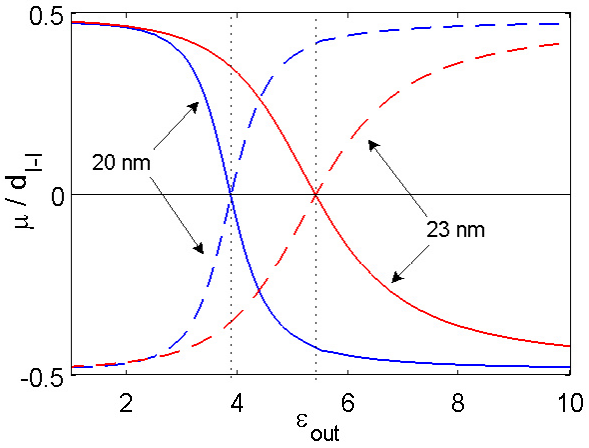

Figure 2.4: Ground state (solid lines) and first excited state (dashed lines) dipolar moments for the impurities separated by $d_{I-I} = 15$ nm, hosted inside a QD of 20 nm and 23 nm, with one of the impurities at the QD center.

- The spatial separation of states strongly influence the *energy splitting* ($\triangle E$) between the ground state and the first excited state, a key quantity for qubit operations. The larger spatial separation, the higher the energy splitting. Also, it reaches a minimum, close to the bulk value, when homopolar character is achieved.

- Radiative lifetimes may increase orders of magnitude when the QDs are embedded in low-dielectric constant media in comparison with the bulk value. Concerning pure spatial confinement, we observe that coherence drops strongly for small dot sizes (see Fig. 2.5), whereas it

reaches the bulk value when homopolar electron charge distributions are recovered. When the external media where the QD is embedded has a low-dielectric constant an important enhancement of the radiative lifetime is obtained. As can be observed in Fig. 2.5, more than 1 order of magnitude larger than in bulk is observed despite spatial separation of the two lowest-lying states in the whole range of the dot sizes studied. It is worth to notice that the wide range tuning capability of the radiative lifetime could be of interest to increase the relatively low bulk coherence times of orbital states in charge qubit realizations.

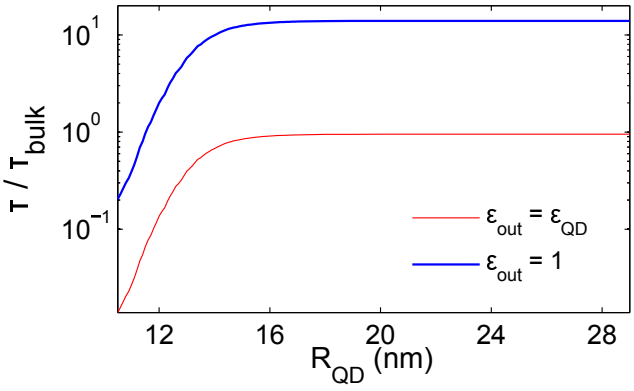

Figure 2.5: First excited-state radiative lifetimes relative to bulk values when pure spatial cofinement effects are considered (red line) and in the presence of an external media that surrounds the QD with $\varepsilon_{out} = 1$ (blue line).

Chapter 3

Electronic properties of elongated quantum dots

Highly monodisperse colloidal nanocrystals are obtained with precise size and shape for a wide range of II-VI and III-V semiconductor materials. Typically, spherical morphology in QDs has been synthesized and such nanostructures have a three-dimensional confining potential that leads to atomiclike electronic structure [86, 87]. These *artificial atoms* show a shell structure in which orbital shell filling and relative ground state stability can be quantified by computing addition energy. This energy, analogous to electron affinity in atomic physics, is a key quantity that characterizes transport into a QD. Building up addition spectrum, electronic structure of nanocrystals can be envisaged to eventually interpret kinetic and Coulomb energy contributions.

However, additional control of the growth kinetics of II-VI semiconductors has lead to elongated structures that exhibit electronic and optical properties very different from the spherical counterparts [88, 89]. One-dimensional structures have become the focus of intensive research since their anisotropic shape posed many benefits for optical and transport applications [90, 91]. Such peculiar physical behaviour originates from the rod shape. Indeed, by increasing the aspect ratio of nanostructures, the transition from zero- to one-dimensional systems occurs and rod-shaped nanocrystals form. They manifest a highly anisotropic confinement which is

distinguished by a strong quantum confinement of carriers for the radial direction, whereas weak confinement holds along the growth direction of the nanostructure [92, 93]. Then, elongated but finite structures have attracted much attention, specially the so-called *nanorods (NRs)* and *quantum wires (QWs)*. Experimental measurements provided by scanning-tunneling, optical spectroscopies and addition energy spectra offer a powerful approach to envisage the electronic structure of such elongated systems.

Recent experimental techniques produce high-controlled rod-shaped CdS, CdSe and CdTe nanocrystals, in which topological control over composition is achieved [94]. The preferable growth direction of quasi-one dimensional systems eventually give rise to a transition from strong to weak confining regime where the role of electron-electron interactions is not well-established yet. The lack of discussion concerning perturbing potentials effects in quasi-one dimensional quantum dots is the main motivation for discussing in this chapter. Therefore, a comprehensive study of anisotropic confining potentials effects in nanocrystals is exposed. To this end, truly three-dimensional models are used in order to accurately characterize the electronic structure of rod-shaped systems. As it will be shown, electron density profiles let us determine the presence of strongly correlated regimes and the physical parameters leading to quasi-classical Wigner distribution of the charge maxima in diluted NR. We also evidence the formation of new correlation phases in 3-D elongated structures under highly inhomogeneous confining potentials. Such phases show an uneven electronic-density distribution that evidence different correlation regimes in different regions of the structure (*mixed phases*)[1]. We will show that one can get a *mixed phase* by applying an electric field along the longitudinal axis of diluted nanorods. On the other hand, the nanorod confining potential will be modified by structural effects yielding the chemical synthesis of *nanodumbbells (NDs)* in which mixed phases are also present. Additionally, the presence of such new phases is probed by means of optical spectra simulations.

[1] Initial attempts focused on identifying the presence of new phases were made by Mueller *et al* [95] in strictly one-dimensional Hartree-Fock calculations.

Furthermore, well-established synthesis routes are producing more complex structures like core/shell colloidal semiconductor NCs. In particular, cadmium chalcogenide heterostructures have received most of the attention due to their peculiar opto-electronic properties under quantum confinement effects [96]. In this regard, while one-photon transitions have been widely addressed [97, 98, 99, 100], only few studies exist on multiphoton absorption in heterostructured NCs [101, 102, 103]. Up to date, reports have focused on understanding two-photon-induced photoluminiscence excitation (2PPLE) spectra in the limit of strong confinement [104], where evidence of a breakdown of the optical selection rules is suggested. We theoretically compute and describe one-photon (1PA) and two-photon (2PA) optical spectra of CdSe/CdSe core/shell heterorods and compare them with core-only CdSe quantum dots (QDs). The numerical simulations of the dipole-allowed transitions show a good agreement with new experimental data, which in turn stand in contradiction with previous studies concerning lead chalcogenide nanocrystals [105].

3.1 Correlation phase transitions in nanorods

The many-electron problem in nanorods (NRs), an elongated variant of colloidal QDs, has been addressed within the framework of the Local Spin-Density Approximation (LSDA). NRs are modelled as a cylinder ended in two semispheres of the same radius (see inset in Fig. 3.1). This model fits nicely to our purpose of studying anisotropic effects derived from the existence of a preferable growth direction of the nanostructure. Actually, a smooth transition from spherical NCs to NRs several tens of nanometers long can be reported by varying the cylinder length L.

To obtain the ground state energy of NRs axially symmetric, Kohn-Sham equations [46] are numerically solved using the well-known Dirac exchange functional of a homogeneous electron gas and the correlation functional parametrized by Perdew and Zunger [50]. By fixing a typical 4 eV confining

barrier[2] and using CdSe bulk material parameters[3], anisotropic confinement effects due to a preferable growth direction have been investigated. The anisotropy of the confining potential is monitored by increasing the NR length to eventually form quasi 1-D structures, in which electronic interactions are analyzed within LSDA calculations. In this study, dielectric mismatch effects will be not considered in the following since it does not alter in any case the electron correlation phase found in related N-diluted nanorods [106].

At the single electron level, nanorod states can be labeled as (n, m_z), where $n = 1, 2, 3, ...$ is the main quantum number and $m_z = 0, \pm 1, \pm 2, ...$ is the envelope angular momentum projection. According to Fig. 3.1, spherical quantum dots ($L = 0$) show the expected typical 1-3-5 atomic-like degeneracy. Conversely, this degeneracy pattern disappears as the nanostructure elongates. Fixing the nanorod radius, orbitals with $m_z = 0$ preferably stabilize and converge toward the lowest conduction band resembling the electronic structure of an infinite wire[4].

The previous qualitative trend persists when including exchange and correlation contributions for a given N-electron ground state. LSDA results point out that only the lowest orbitals with $m_z = 0$ are occupied and energy differences between orbitals get closer as nanorod length increases. This fact can be monitored by studying the addition energy spectra for different nanorod lengths. The addition energy (E_{add}) is estimated by the formula:

$$E_{add}(N) = E(N+1) - 2E(N) + E(N-1) \tag{3.1}$$

[2]Generally, 4 eV is the average value of the electron affinity in most semiconductor materials.

[3]One of the most satisfactory growth materials is CdSe. Its large band gap (1.84 eV) allows us to theoretically study large aspect ratio systems within the one-band effective mass model. We employ a CdSe effective mass of 0.13 and a dielectric constant of 9.2.

[4]Further stabilization of $m_z = \pm 1, \pm 2, ...$ orbitals can be foreseen as higher energy conduction bands of infinite wires.

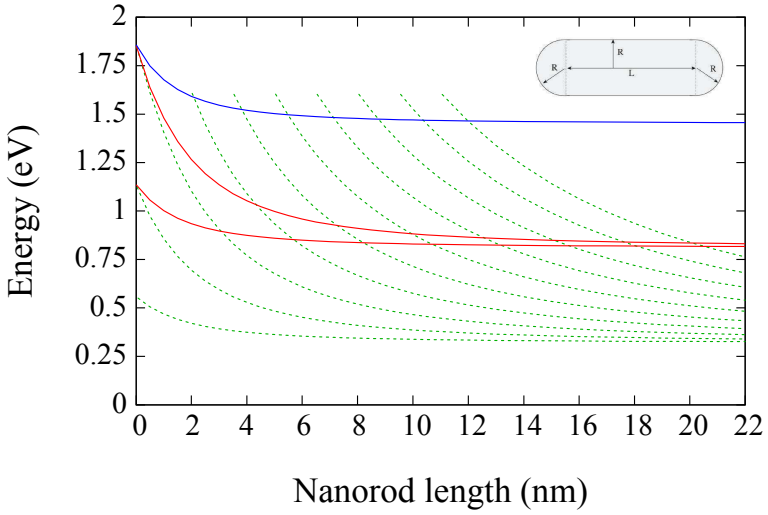

Figure 3.1: Single-particle noninteracting energy levels (eV) vs the NR length L (nm). Dotted lines correspond to the preferable stabilized orbitals with azimutal quantum number $m_z = 0$. Full and dashed lines indicate higher energy orbitals with $m_z = \pm 1$ and $m_z = \pm 2$, respectively.

where $E_{add}\,(N)$ is the energy required in order to place an extra electron into the system that has initially $N-1$ electrons. Such quantity is calculated by computing the total energy of the N-electron system ground state $E(N)$ and the total energies for the system occupied with $N+1$ and $N-1$ electrons, i.e., $E(N+1)$ and $E(N-1)$, respectively.

Spherical degeneracy patterns are observed in the addition energy spectra as can be seen at the top of Fig. 3.2. Energy maxima at 2, 8, and 18 electrons display the shell filling of orbitals with $m_z = 0, \pm 1, \pm 2$ within the so-called strong confinement regime in spherical QDs. Next, as we move to elongated structures, excited $m_z = 0$ levels fall below the low-lying $m_z = \pm 1$ states (see Fig. 3.1) and, consequently, an increment of density of states with $m_z = 0$ occurs, yielding remarkably changes in the addition spectrum. As the NR gets longer, featureless addition energy spectra are gradually obtained, leading to an almost flat region at low electron densities whereas

it wrinkles as the number of particles populating the conduction band increases. Such featureless addition spectrum constitute the fingerprint of the transition from weakly to strongly correlated regimes.

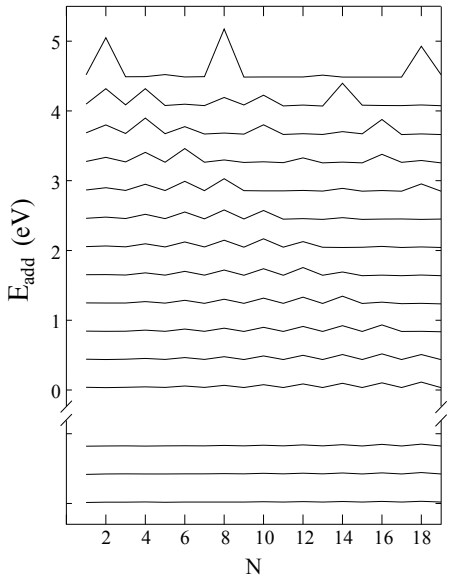

Figure 3.2: Addition energy spectra are represented for spherical QDs (top) and increasingly larger NRs (in steps $\triangle L = 2\,nm$) ranging from $L = 2$ nm up to 22 nm NR length. The three almost flat profiles at the bottom correspond to the low-density NRs of $L = 40, 45$ and 55 nm long, respectively. These profiles have been offset 400 meV.

Specific density profiles revealing the transition between different correlation regimes are found depending on the number of electrons populating the NR. As a highly anisotropic confining potential is reached, remarkable strong Coulomb interactions come out in the low-density limit. While an average of kinetic and Coulomb contributions yields to a *Charge Density Wave (CDW)* phase in the density profile (see Fig. 3.3), with half

number of maxima as electrons are in the system, a Wigner crystal electron density distribution is found when electron-electron interactions dominate over the kinetic energy. It consists of a density profile with same number of peaks as electrons are in the nanostructure, with broken spin symmetry with alternating opposite spin maxima. In the framework of LSDA this phase is referred to as *Spin Density Wave (SDW)* and it has been found for 4- and 6-electron NRs (see panels in Fig. 3.3). This Wigner phase is characterized by a noticeable decrease in the energy difference between the highest and lowest occupied quantum levels. In such a case, a strongly correlated state is found and charges spatially reorganize as quasi-classical particles with fixed positions along the growth direction of the nanocrystal (z axis). This ordered spatial distribution minimizes the energy in quasi-one dimensional structures. For extremely diluted regimes, a fully *Spin polarized* state is reached as it is illustrated in Fig. 3.3 for the 4-electron NR 55 nm length. However, the existence of this polarized state must be taken with caution. It may possibly come from an overestimation of exchange and correlation effects within LSDA framework or from intrinsic limits of its mean-field approach.

To support LSDA results, additional full configuration interaction (FCI) calculations have been performed when describing multi-carrier states of nanorods. Since FCI approach is computationally highly demanding, only 4-, 6- and 8-electron calculations are carried out by employing the novel FCI code already addressed in sec. 1.3.1. CI-density profiles indicate that the transition from weakly to strongly correlated regime occurs at smaller rod lengths in comparison to LSDA results. For instance, a 4-electron CDW phase is observed up to 20 nm rod length meanwhile this electronic distribution is found up to 10 nm within LSDA. The evolution to a strongly correlated regime occurs gradually (see Fig. 3.4) to eventually form a quasi-classical electron distribution for the longest NR length considered, i.e., 55 nm. This is a CI feature that is not observed with LSDA results.

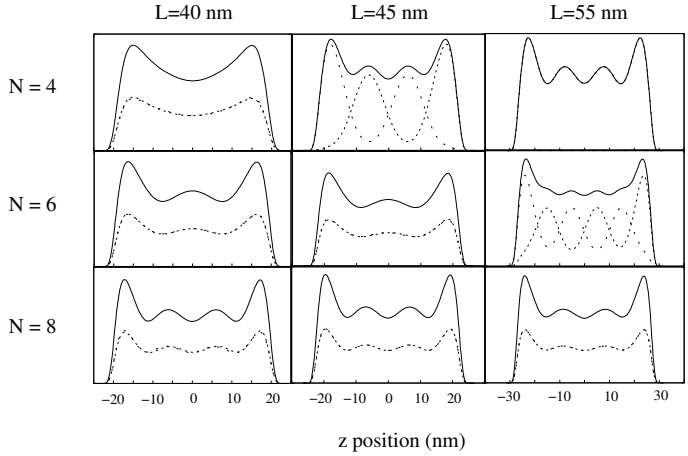

Figure 3.3: LSDA electron density profiles along the NR z axis for different NR lengths. From left to right panels, highly anisotropic confining potential is achieved and total (full thick line), spin up (dashed line), and spin down (dotted line) density profiles are shown for 4, 6 and 8 electrons. A charge density wave (CDW) phase is observed for all the populations considered for the shortest nanorod. Strongly correlated states are identified with a Wigner crystal density distribution, yielding the same number of maxima as electrons present in the nanostructure, as shown for instance in the 4-electron ground state 45 nm nanorod length. A spin polarized state is achieved for the 4-electron case in the limit of weak confinement regime.

Wigner crystal phase, characterized by strong Coulomb interactions, spatially distribute spin densities nearly overlapping to each other (see Fig. 3.5). Whereas LSDA calculations predict spin-symmetry breaking, CI method foresees overlapping of spin densities, as it has already been addressed for an exclusively one-dimensional system [107]. The lack of complete spin densities superposition is due to numerical issues when computing Coulomb integrals. The discrepancy of the Wigner phase characterization by means of electron density between both methodologies could be explained because of the different treatment of the electronic interaction. Conversely, Wigner crystallization generally disappears when promoting the system into a excited state. For example, the first excited

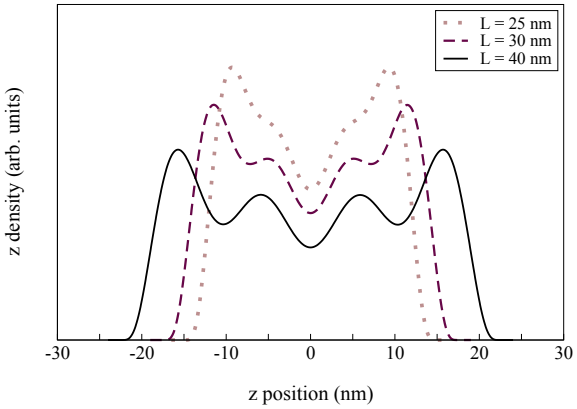

Figure 3.4: FCI ground state z-density profile for a nanorod with N=4 electrons and variable length: 25, 30 and 40 nm length. Only total density is represented.

state is also explored in the 4-electron system (see right panel in Fig. 3.5). It is a doubly degenerated polarized spin state for a nanorod 25 nm length. These excited states with $S_z = +1$ and $S_z = -1$, respectively, do not show overlapping spin densities. The density of the majority spin is maximum at the edges of the system.

It is worth to mention that Wigner phase with broken spin symmetry is also achieved in spin polarized multi-particle ground states. This situation holds for odd number of electrons in dilute regime. Concerning the case of a 3-electron nanorod, a double-degenerate ground state forms and spin density profiles reveal a broken-spin symmetry related to Coulomb interaction between electrons with different spin (see Fig. 3.6). Total density shows the same number of peaks as electrons inside the system, leading to a smaller intensity in the central peak. Whereas electrons with same spin tend to localize as far as possible in order to avoid to each other, i.e., at the extreme of the nanorod, electrons with opposite spin show a maximum around the center of the CdSe nanostructure.

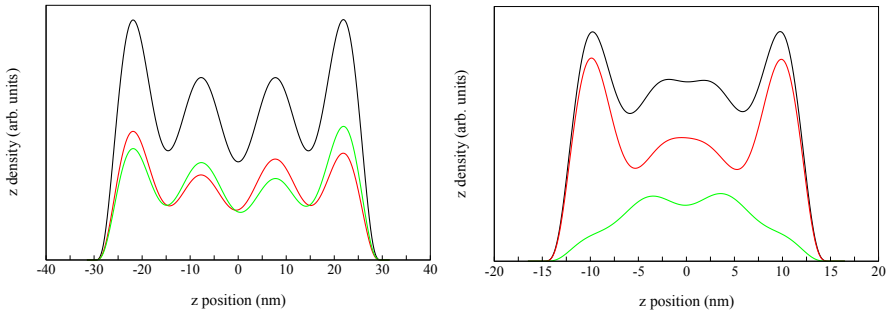

Figure 3.5: Left: FCI density profile in the weak confinement regime (55 nm rod length). Black line corresponds to total electron density while green (blue) lines indicate spin up (down) densities. Ground state with $S_z = 0$ for a 4-electron nanorod. Wigner crystallization is clear in the electron-charge distribution. Right: FCI first excited state with $S_z = 1$ for a nanorod with N=4 electrons and 25 nm length. Here, spin densities do not overlap each other: the density of the majority spin (up) is maximum at the edges.

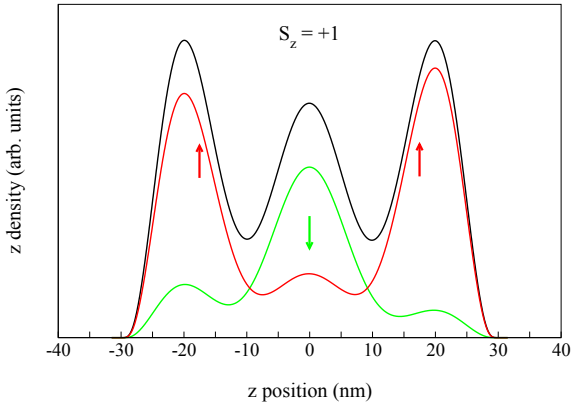

Figure 3.6: FCI ground state for a nanorod 55 nm length populated with 3 electrons. Specifically, this ground state is a spin polarized state with $S_z = +1$. The spin density profiles reveal a broken-spin symmetry related to the Coulomb interaction between electrons with different spin. This ground state is doubly degenerated, so the opposite spin density profile leads to a state $S_z = -1$ with the same energy as the state represented, but opposite spin orientation.

To sum up, noticeable agreement has been found when exploring the weak confinement regime of truly three-dimensional nanorods in the low-density limit. It has been observed that the weak confinement along the growth direction results in strongly correlated regimes. In such regimes, Coulomb energy dominates the electronic behaviour and spatial reorganization of electrons saturates the space along the z axis. From the mean field approach considered with DFT method, the Wigner crystallization signature corresponds to *Spin Density Waves (SDW),* which show the same number of peaks as electrons and broken spin symmetry. Such density profile tries to describe the classical behaviour of electrons with opposite spins when they try to avoid each other. A mean field approach can only account for this effect by symmetry breaking, as it is found within LSDA. The transition from CDW to Wigner phase occurs for smaller nanorod lengths according to FCI than DFT. FCI results also predict Wigner crystallization, though it is not associated with the SDW-phase with broken spin symmetry.

3.2 Crystallization process in highly inhomogeneous confining potentials

Wigner crystallization process in the presence of highly anisotropic potentials is now addressed in the low-density limit, in which electrons behave as waves with finite extension yielding the SDW-phase in the LSDA density profile. This situation is the result of remarkable Coulomb interactions that dominate the electronic structure of such elongated systems. As shown next, the presence of inhomogeneous confining potentials in elongated, diluted N-electron quantum dots can significantly modify the density profile. In this section we expose that inhomogeneous anisotropic potentials lead to the coexistence of different correlation regimes simultaneously. The different phases found at the very same structure will be named as a whole as *Mixed phase (MP).* Fixing the geometrical parameters of the longest nanorod considered before, i.e., 55 nm length, ground states up to 20 electrons are studied in two different situations. The

first one accounts for the formation of a MP in diluted NRs subject to an electric field along the growth direction of the nanostructure. On the other hand, the existence of MPs is due to the modification of the NR confining potential by means of the chemical synthesis of nanodumbbells (NDs).

The effect of an external electric field applied along the z-axis of the nanorod yields a complex electronic structure. Fig. 3.7 shows the density profile for the ground state of a NR with 6 electrons and a 20 KV/cm applied electric field, which is representative of the most noticeable effects in the density distribution. The density gradient generated is high enough to display a mixed phase characterizing the electron density profile. It is composed by three different regions present in the very same system. All together resemble the Wigner crystallization process, where starting from a Fermi liquid phase (Fermi liquid region in Fig. 3.7) with a single total density maxima, evolves to a typical SDW-phase (see region SDW in Fig. 3.7). Since crystallization process occurs gradually, an intermediate phase forms, the CDW phase, which displays half number of maxima inthe total electron density and broken spin symmetry.

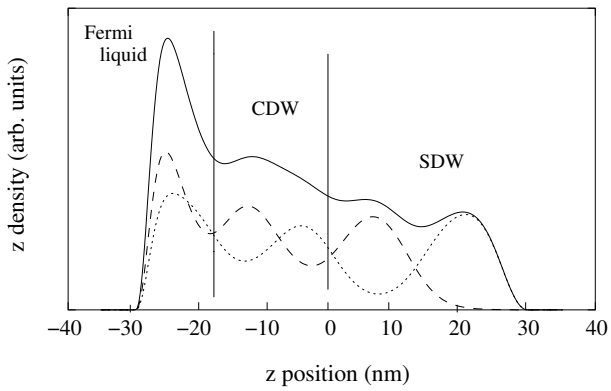

Figure 3.7: 6-electron LSDA density profile for a NR ground state subject to a 20 kV/cm electric field along the z direction. Solid line corresponds to total charge density. Dotted/dashed line illustrates spin up/down densities, respectively.

Nanodumbbells (NDs) are chemically synthesized heterostructures composed by a central nanorod of a given material sandwiched between two-end spherical caps of a different material. They are considered as promising structures for photovoltaic devices, including solar cells and photodetectors [108, 109]. From the fundamental point of view, the spherical caps add (structural) inhomogeneities to the anisotropic confinement potential of the nanorod. Here, we will show the formation of mixed phases in CdSe/CdTe/CdSe dumbbell-like structures when geometrical parameters are those indicated in Fig. 3.8. This system renders better defined MPs than those produce by an external electric field and both LSDA and FCI methodologies have been employed to confirm and reinforce the existence of mixed correlation phases in many electron ground states. An exhaustive analysis on the electronic structure of NDs has been carried on taking into account CdSe and CdTe materials, since they are used nowadays in many synthesis of elongated nanocrystals [110, 111]. These materials have a rather large band offset [112] but similar effective masses and dielectric constants, so that no relevant effects coming from effective mass and/or dielectric constant inhomogeneities will mask those coming from an inhomogeneous confining potential derived from the band offset. It allows us to employ uniform parameters for the entire system such as an effective mass $m^* = 0.13$, and dielectric constant, $\epsilon = 9.2$, similar to those of the bulk material [113] and analyze the influence of a purely inhomogeneous confining potential on the electronic structure.

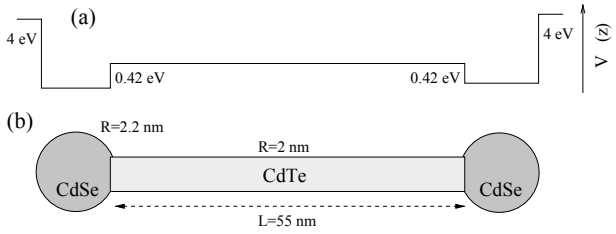

Figure 3.8: Schematics of the studied nanodumbbell. (a) z-profile of the spatial confining potential with 0.42 eV CdSe/CdTe conduction band offset. A typical 4 eV confining QD-environment barrier is assumed. (b) The ND modelled consists of a CdTe cylinder of radius R= 2 nm and length L = 55 nm sandwiched between two R = 2.2 nm radius spherical CdSe caps.

Concerning FCI calculations, ground and lowest-lying excited states of $N = 4, 6$, and 8 electrons have been computed using a $2 - 10 - 2$ basis set. This basis includes the 10 lowest-lying $m_z = 0$ orbitals[5] and the lowest-lying degenerate pair of $m_z = \pm 1$ orbitals. We can conclude that this basis set is more than enough to describe the ground state and the low-lying energy part of the many-electron ND in all cases studied[6]. Actually, we have checked that $m_z = \pm 1$ orbitals make a negligible contribution to the lowest-lying states and results indicate that the basis already saturates the required Hilbert space. Within the EMA framework, the ND lowest-lying $m_z = 0$ orbitals can be seen in Fig. 3.9. We observe from Fig. 3.9 that the two lowest-lying s orbitals are mostly localized within the two spheres of the ND, whereas the more excited orbitals $(s_3, ..., s_6)$ are spread along the central cylinder of the ND (also referred to as nanorod in the following) since orbitals must be orthogonal.

When including Coulomb repulsion, FCI and LSDA density results confirm the existence of mixed phases. Since both methodologies agree with the density profiles, we will focus on LSDA computations that let us reach higher densities. Up to 4 electrons, the multi-particle wave function is mainly localized at the CdSe caps, with a single density maximum in each one. This ground-state density profile corresponds to the so-called *Fermi liquid* phase (see top panel in Fig. 3.10), in which the physical behaviour of electrons has a strong kinetic contribution. Increasing electron population up to 8, Fermi liquid phase remains at the spheres while the rest electron density shows Wigner crystal phase along the trunk of the ND (see middle panel in Fig. 3.10). This mixed correlation phase implies that a strong kinetic energy governs the 4 electrons populating the spheres while, simultaneously, the other 4 electrons are described by strongly correlated states with a high Coulomb contribution. This mixed phase, composed by

[5] From now on the single-electron states which have a null z-component of the angular momentum are also labeled as s single-particle states. The ones that have ± 1 values are identified as p single-particle states.

[6] We computed additional FCI calculations using a $2 - 14 - 2$ basis set. The results for the 4-electron ND, both the energy and the relevant components of the low-lying eigenvectors, were almost identical as the ones obtained with the $2 - 10 - 2$ basis.

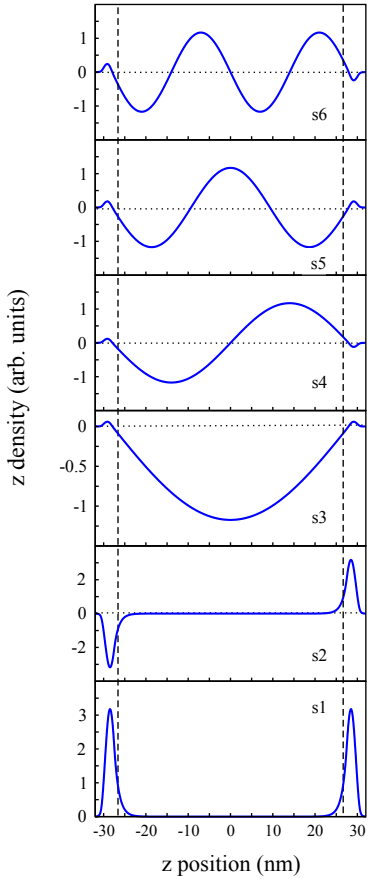

Figure 3.9: The six lowest-lying orbitals of the nanodumbbell studied are plotted along the growth direction of the ND. Vertical dashed lines indicate the boundaries between the rod and the caps of the ND. The two lowest-lying s orbitals ($m_z = 0$) are quasi-degenerate ($\varepsilon_{s1} \approx \varepsilon_{s2} = 0.489\,eV$) and are mainly concentrated inside the caps. The more excited s orbitals localize along the central cylinder and show very close energies. Although not shown in the figure, the two lowest-lying p orbitals ($m_z = \pm 1$) concentrate the electron wave function in the spherical caps too, although show a very excited energy in comparison with the s orbitals ($\varepsilon_{p1} \approx \varepsilon_{p2} = 0.963\,eV$).

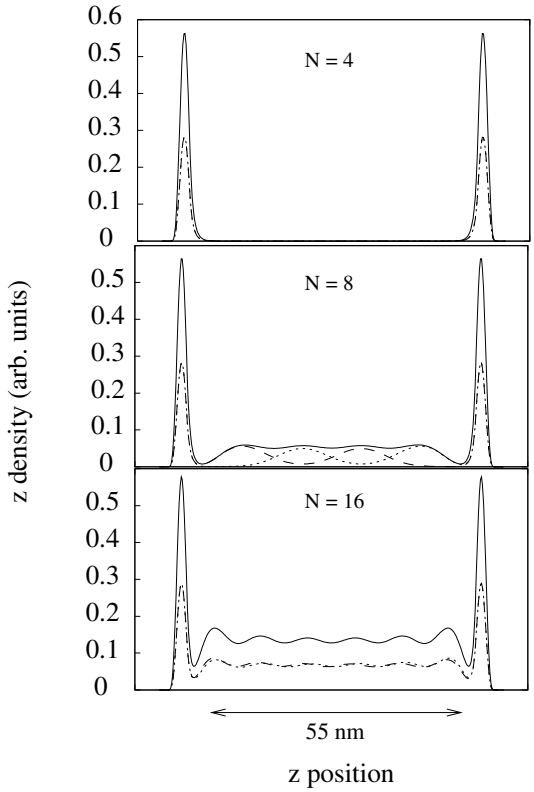

Figure 3.10: From top to bottom: 4-electron LSDA density profile gives rise to a Fermi liquid phase in the ND studied. Total density (solid line) and overlapping spin densities (dotted/dashed) are localized at the spherical CdSe caps, yielding a single density maximum in each one. 8-electron ND z-density profile obtained within LSDA calculations. The mixes phase represented corresponds to a Fermi liquid localized at the caps and a nice central Wigner crystal emerged along the cylinder of the ND. The Wigner phase is identified as a SDW phase with four maxima and broken spin symmetry. 16-electron ND characterized by a mixed phase composed by a Fermi liquid and a CDW phase. LSDA z-density profile shows complete spin densities overlapping at the caps (Fermi liquid) and half number of maxima as electrons are in the trunk (CDW-phase).

a Fermi liquid and a Wigner crystal, is modified for $N = 6$ and $N = 7$, i.e., in extremely diluted NDs. A fully polarized phase located at the cylinder is found coexisting with the Fermi liquid phase. Nevertheless, this phase should be considered as a pure signature of high diluted regimes where LSDA shows practical limitations. Finally, ranging high electron densities from 12 to 20 electrons, density profiles are characterized by a Fermi liquid in the spheres and a CDW-phase along the cylinder. This mixed phase associated with high electron densities (not computed within FCI approach because of the highly computationally demanding point of view) is represented at the bottom in Fig. 3.10 for a 16-electron ND.

The relative stability of the N-electron mixed correlation phases in NDs is represented by means of the addition energy spectrum. In the low-density limit, the Fermi liquid phase corresponding to a 4-electron ND is reflected by an intense peak (see Fig. 3.11) that shows up due to the full filling of the first s shell. The formation of the mixed correlated phase composed by a Fermi liquid and a SDW-phase can be detected by a noticeable decrease in the addition energy in contrast to the pure Fermi liquid phase for 4 electrons. When increasing electron population up to 12 electrons, the existence of such mixed phase is monitored by a flat region in the addition spectrum. As we have already shown for a very long nanorod in Fig. 3.2, addition spectrum becomes featureless in the presence of the Wigner crystal (SDW-phase within LSDA) because of the high density of states along the nanorod. It is a direct consequence of the anisotropic confining potential that electrons experience. Whereas they feel a stronger radial confinement along the cylinder than in the caps, the longitudinal direction is characterized by a weak confinement regime. This quasi one-dimensional structure enhances electron repulsion along the growth direction and particles distribute like quasi-classical charges with close energy. The transition from a SDW-phase to a CDW-phase in the cylinder can be detected by the appearance of typical shell-filling peaks (see right part in Fig. 3.11).

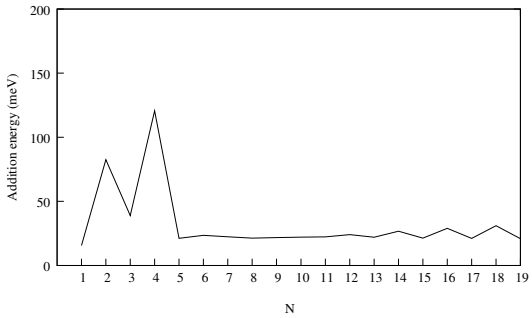

Figure 3.11: LSDA addition energy spectrum for the nanodumbbell schematized in Fig. 3.8 For low electron densities, electronic structure gives rise to an almost flat curve in the addition energy spectrum. It is a signature of Wigner crystallization. In high electron densities, a wrinkle profile forms characteristic of the Charge Density Wave (CDW) phase.

3.3 Absorption spectra analysis

Absorption spectra simulations are performed to further characterize the existence of mixed phases. To this end, spin and charge-density modes are computed within the dipole approximation according to both, a time-dependent LSDA scheme and FCI approach. Following a time-dependent LSDA scheme, the physical behavior of the abovementioned elongated systems is described when an external dipole field interacts with them. Mathematically, this external perturbation is described by a slight excitation of the Kohn-Sham orbitals in the linear regime response (see sec. 1.3.2). Concerning FCI calculations, transition probabilities follow the selection rules in axially symmetric systems by assuming a low temperature of the system (1 K). Since both methods confirm the different correlation regimes occurring simultaneously in the elongated structures studied, we will focus on LSDA results and only stress the qualitative differences obtained within FCI calculations in the few-electron densities.

The simulations provide the infrared response of NRs and NDs whose schematic geometry has been already described in Fig. 3.8, in the limit

of weak confinement regime along the growth direction of the nanostructure. Spectral signals associated with the z-axis, *longitudinal responses*, are obtained at lower energies than the ones promoted by in-plane polarizations, *transversal responses.* This fact is due to the remarkably different confinement that carriers undergo in longitudinal and in radial directions in these nanostructures.

Analyzing spin- and charge-density oscillations in the ***LSDA transverse spectra***, it is concluded that the Fermi liquid phase present at the ND caps displays a strong spin peak at 450 meV, as illustrated in Fig. 3.12. This transverse spin peak, absent in the 4-electron NR, let us identify low correlation regimes in the low-density limit where kinetic energy dominates the physical behaviour of electrons[7]. As a whole, spin-density responses in the transverse spectra let us recognize electrons localized at the caps that form a pure Fermi liquid phase.

Regarding ***LSDA longitudinal spectra***, we can differentiate between low-energy signals and peaks that appear in a higher energy range (see Fig. 3.13). The **low-enery part** of the spectra concerns electronic transitions in the weak confinement regime. We found that strong correlation regime can be identified by means of charge-density response that appears at lower energies than spin-density modes. Traces of Wigner-like electron density distributions arise for the 8-electron ND and its 4-electron NR partner. In the specific case of an 8-electron ND, the Wigner crystal phase gives rise to a fragmented spin and charge-density peaks. This fact can be explained because attraction associated with the spin falls behind the Coulomb repulsion and coming from exchange-correlation term in the KS Hamiltonian. This can be interpreted as a characteristic of N-diluted

[7]It is worth mentioning that FCI calculations foresee a complete overlapping between spin- and charge-transitions peaks. It can be understood by the fact that the double degeneracy found for the lowest s-type orbitals (s_1 and s_2) and p-type orbitals (p_1 and p_2) yields to practically the same amount for the Coulomb and exchange bielectronic integrals. Similar energies are, therefore, obtained for charge and spin density modes in singlet and triplet multi-electron configurations.

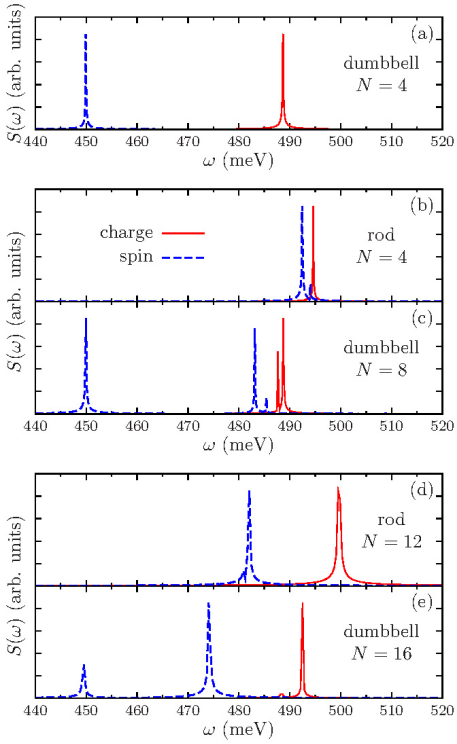

Figure 3.12: LSDA transverse responses of the NR and ND whose population is indicated at each of the panels. Spin-density (dashed lines) and charge-density (solid lines) modes are compared between NRs and NDs with the same number of electrons in the central cylinder (4 and 12, respectively).

systems within the LSDA approach[8]. Alternatively, Mayrock *et al.* associated optical and acoustic modes to electron density oscillations [114, 115]. Since the local magnetization of Wigner molecules contradicts the unusual higher energy observed for spin-density oscillations, small density oscillations can be associated to intercell interactions, which are smaller in energy than those related to optical modes. Hence, spin-density oscillations may correspond to the so-called acoustic modes effects.

[8]When referring to FCI absorption spectra simulations, spin transitions emerge at lower energy than charge transitions.

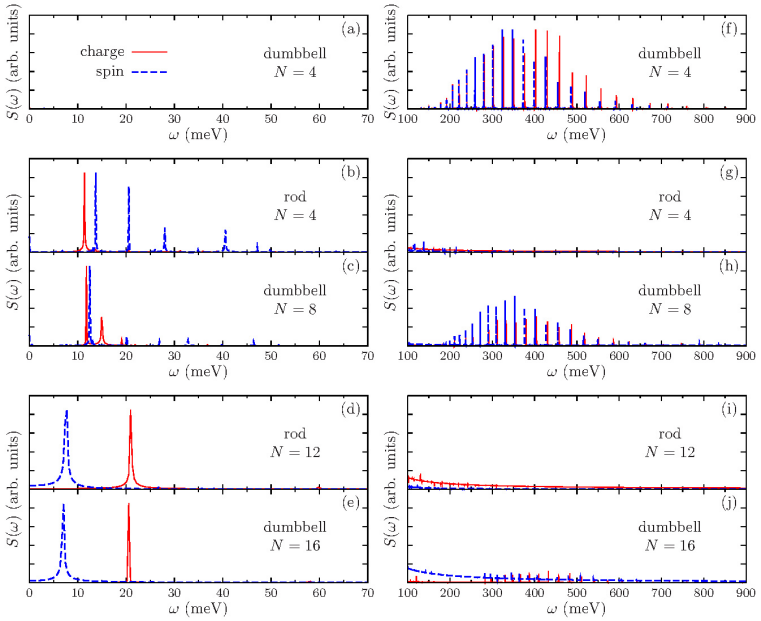

Figure 3.13: LSDA longitudinal spectra of different NRs and NDs in the low-energy (left panels) and high-enery range (right panels). The very same number of electrons is preserved at the central trunk in all the systems considered. Responses are magnified two orders of magnitude in right panels with respect to their corresponding low-energy responses.

In high electron-densities, the coexistence of the Fermi liquid and the CDW-phase is observed in the 16-electron ND and its NR partner. In this case, only LSDA simulations let us interpret the presence of such mixed phase because of the highly computationally demanding FCI approach for large-electron systems. Since larger electron density is mainly localized at the central cylinder in comparison to the 8-electron ND, absorption spectra simulations show charge-density oscillations at energies higher than spin-density responses, due to the fact that Coulomb repulsion exceeds the attraction associated with the spin.

In the **high-energy part** of the longitudinal spectra a series of regularly spaced electronic oscillations appear within 160-800 meV range for all studied ND populations. These peaks can be associated with the stronger confinement of states principally confined at the ND caps.

3.4 CdSe/CdS core/shell quasi-type II heterorods. Multiphoton absorption spectra

The so-called dot-in-rod nanocrystals are peculiar structures that involve the interaction between a highly isotropic confinement (yielded by an internal, nearly spherical dot or core) and a highly anisotropic one (an outer, approximately cylindrical rod or shell). These (core/shell) heterostructured systems, also named as *heterorods*, are usually cadmium chalcogenide-based nanocrystals whose typical core and shell configurations are shown in Fig. 3.14. These structures are promising candidates for composing photonic and optoelectronic devices because they can exhibit a large two-photon absorption cross section [101, 116]. Thus, the study and understanding of their optical properties are of utmost relevance.

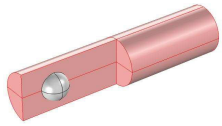

Figure 3.14: Schematics of a dot-in-rod nanostructure.

The group of I. Moreels at Istituto Italiano di Tecnologia in Genova studied the one- and two-photon absorption spectra (1PA and 2PA, respectively) of several CdSe dots and CdSe/CdS core/shell heterorods (which present a quasi type-II band alignment at the heterointerface between the two semiconductors) to probe the role of the parity symmetry breaking suposedly induced by the rod shell over the electron and hole wavefunctions. These studies were motivated by previous reports on lead chalcogenide quantum dots, which evidenced significant 2PA dipole-forbbiden resonances

coincident with the main 1PA absorptions. This fact was attributed to the breakdown of the parity symmetry of the electron and/or hole wavefunctions. Moreels and co-workers obtained instead no evidence of symmetry breaking in the spectra of their CdSe and CdSe/CdS samples, which showed a strong blueshift of the onset of 2PA with respect to that of 1PA transitions.

To provide a theoretical interpretation of Moreels results, we simulated the dipole-allowed 1PA and 2PA spectra of CdSe dots and CdSe/CdS heterorods. The heterorods under study are modelled as a CdSe sphere embedded in a cylindrical CdS shell, 2 nm away from its base (see insets in Fig. 3.15). The CdSe-CdS heterojunction is defined as a finite step-like potential that accounts for the conduction- and valence-band offsets, which are $0.44\,eV$ and $0.3\,eV$, respectively [117]. Electron and holes states are labeled with the conventional notation of axially symmetric states[9], due to the shell-induced symmetry reduction of electron and hole wave functions. On the other hand, those states mainly localized in the spherical CdSe core are also tagged using spherical notation similar to spherically symmetric states in truly CdSe QDs, that is, nL_j, where n is the main quantum number and $L = S, P, D, ...$ represents the envelope angular momentum. Position-dependent electron effective masses are considered. We use $m_e^* = 0.13m_0$ in the CdSe core and $m_e^* = 0.17m_0$ in the CdS shell [113, 118]. When referring to valence band, we use anisotropic hole masses, which are heavier along the longitudinal (growth) direction ($m_{h,\parallel}^* = 1.19m_0$, $m_{h,\perp}^* = 0.48m_0$) [113]. This mass anisotropy leads to the splitting of the P_h shell into $P_{h\parallel}$ and $P_{h\perp}$.

Different selection rules apply for 1PA and 2PA transitions, as detailed in Fig. 3.15. In the dipole approximation, interband transitions coupling initial (hole) and final (electron) states with the same angular momentum (m_z) are allowed via one-photon absorption. On the other hand, two-photon transitions are given by $\triangle m_z = 0, \pm 1$ between the initial and final states involved [119, 120]. This leads to different absorption peaks in the spectra,

[9] In cylindrical coordinates, electron and hole eigenfunctions in the k·p Hamiltonian are identified by $(n, m_z)_j$, where $n = 1, 2, 3, ...$ is the main quantum number, $m_z = 0, \pm 1, \pm 2, ...$ is the envelope angular momentum projection and $j = e, h$ stands for electron and hole.

which are simulated within the $k{\cdot}$p formalism in the single-band, single-particle approximation[10]. Numerical simulations of 1PA and 2PA transition rates have been computed from the first- and second-order Fermi golden rules, which read as:

$$W_{1PA} = \frac{2\pi}{\hbar} \sum_{c,v} |< c \mid e{\cdot}p \mid v >|^2 \, \delta \left(E_c - E_v \right) \tag{3.2}$$

and

$$W_{2PA} = \frac{2\pi}{\hbar} \sum_{c,v} | \sum_{i} \frac{< c \mid e{\cdot}p \mid i >< i \mid e{\cdot}p \mid v >}{E_i - E_v - h\nu} |^2 \, \delta \left(E_c - E_v - 2h\nu \right) \tag{3.3}$$

where $h\nu$ is the photon energy, e is the polarization vector of the light, v the initial (valence band) state and c the final (conduction band) state. In addition to ν and c, two-photon transitions also entail *intermediate states (i)*, which may belong to either the valence or the conduction band. Hence, 2PA absorptions can be formally seen as the combination of inter and intraband transitions.

Three different samples have been considered (see the top in Fig. 3.15). First, a CdSe core-only QD with a diameter of 4.4 nm. Next, two distinct CdSe/CdS heterorods: one with a core diameter of 2.5 nm, rod diameter 4.5 nm and 20 nm rod length (HR1), and the other one with a larger core, 5.0 nm diameter, 5.2 nm of the rod diameter and 28 nm rod length (HR2).

[10]The validity of this single-particle approximation has been supported with FCI calculations of the lowest excitonic states in the heterorods studied. The excitonic states, built as linear combinations of a large number of Hartree products of the single-particle electron and hole states, show negligible electron-hole correlations for the core states. Thus, the lowest energy range of the 1PA and 2PA spectra is reasonably described by non-correlated states. Concerning the high-energy range of the spectra, the role of Coulomb effects are expected not to significantly change excitonic energies and transition rates.

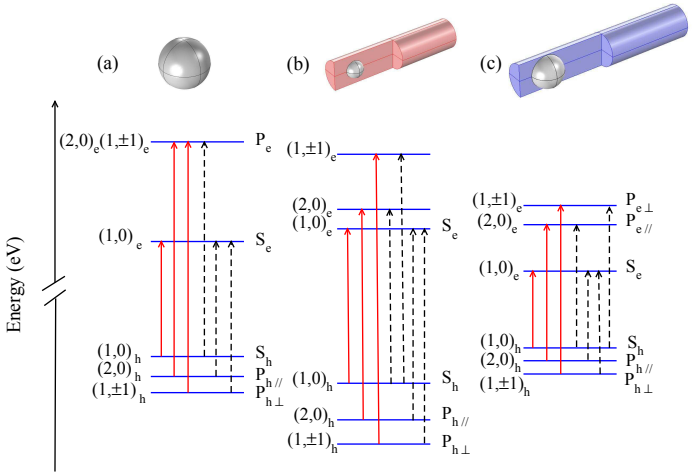

Figure 3.15: Near-gap energy levels of: (a) a CdSe core-only QD, (b) a heterorod with a 2.5 nm core diameter and (c) a heterorod with a 5.0 nm core diameter. States mainly localized at the core are labeled following both, spherical and axial symmetry notations. In the case of states preferably delocalized along the rod-shaped shell are identified by axial symmetry notation. Vertical arrows represent the dipole-allowed 1PA (red, solid lines) and 2PA (black, dashed lines) transitions.

The simulated spectra are displayed in Fig. 3.16 jointly with the experimental data (black lines in the figure). 1PA and 2PA optical transitions of CdSe/CdS core/shell heterorods are obtained over the entire visible spectrum, and compared to spherical CdSe core-only QDs. The qualitative agreement between experiments and theoretical results is achieved taking the CdSe energy gap so as to fit the fundamental $1S_h \rightarrow 1S_e$ transition with the energy of the first experimental 1PA peak.

In the case of core-only QDs (left panels in Fig. 3.16), spherically symmetric states obey the selection rules in terms of conservation of the parity with respect to the inversion symmetry. It implies that for 1PA

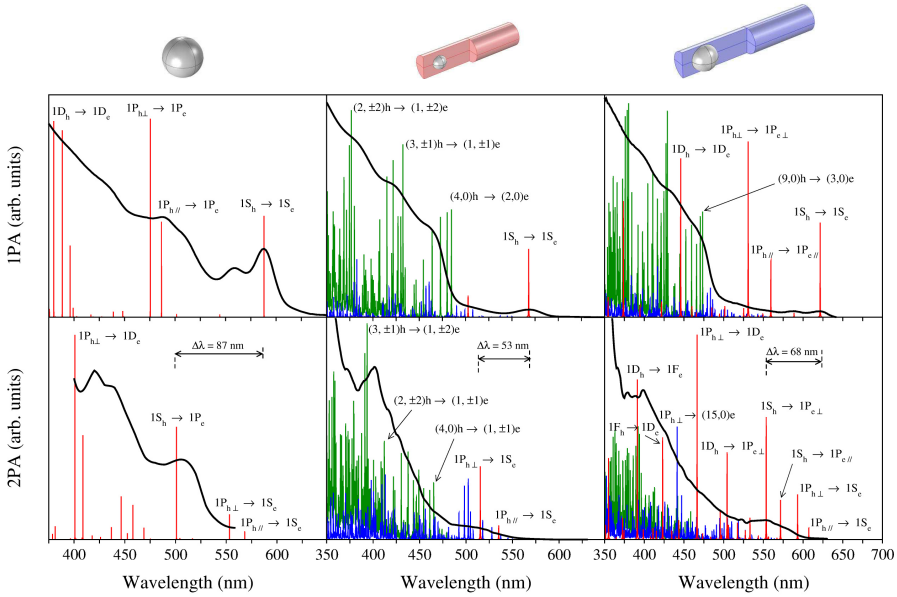

Figure 3.16: Absorption spectra simulations for the three nanostructures under study. Black lines represent the experimental data. Different types of transitions are distinguished attending to the preferential localization of the initial and final states involved: *dot-dot* (red), *dot-rod* (blue) and *rod-rod* (green) transitions. To enable the comparison between 1PA and 2PA spectra, the horizontal axis has been set equal to the photon wavelength for the 1PA transitions and to half the photon wavelength for the 2PA transitions. The blue shift ($\triangle\lambda$) of the onset of 2PA transitions with respect to that of 1PA is indicated in the 2PA spectra.

transitions the parity of the initial and final envelope states must be the same, whereas the opposite holds for 2PA transitions. A remarkable intense blue shift ($\triangle\lambda = 87\,nm$) appears between the first intense 1PA and 2PA peaks. This can be understood because the main dipole-allowed 2PA peak, corresponding to the $1S_h \rightarrow 1P_e$ transition ($\lambda \approx 500$ nm), has stronger oscillator strength than the lower energy $1P_{h\perp} \rightarrow 1S_e$ and $1P_{h\parallel} \rightarrow 1S_e$ transitions. The origin of this peculiar feature can be explained by analyzing

the influence of the intermediate states that principally contribute to the 2PA rate. Such influence can be mainly derived from the denominator in Eq. 3.3. The leading 2PA transition paths occur through the intermediate states closest to the resonant condition. Since electron states have larger energy splitting than hole states, the $1S_h \rightarrow 1P_e$ transition is favored by the intermediate state $1S_e$, yielding a smaller denominator and, consequently, a stronger oscillator strength (see Fig. 3.17).

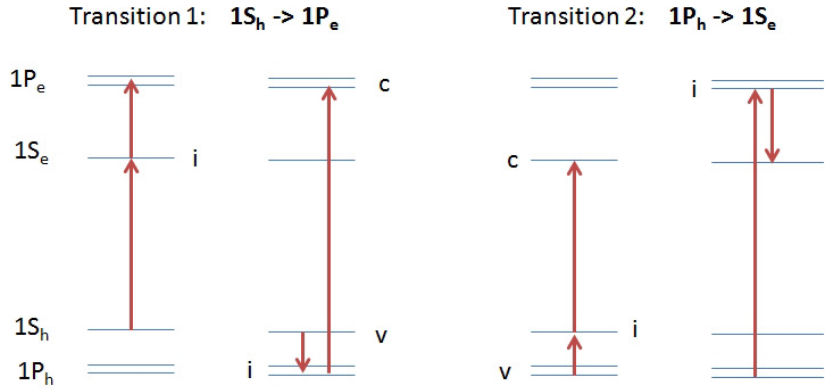

Figure 3.17: Most important paths contributing to the 2PA transition rate of $1S_h \rightarrow 1P_e$ and $1P_h \rightarrow 1S_e$ absorptions. The corresponding intermediate state (i) in each via can belong to the conduction band or to the valence band. The $1S_h \rightarrow 1P_e$ transition takes place principally through the intermediate states $1S_e$ and $1P_h$, while the $1P_h \rightarrow 1S_e$ transition occurs mostly through $1S_h$ and $1P_e$. The intermediate state $1S_e$ is closest to the resonant photon due to the larger energy splitting of electron states in comparison to hole states. Therefore, 2PA transition rate is higher for the $1S_h \rightarrow 1P_e$ absorption peak.

Concerning CdSe/CdS heterorods, more complex absorption spectra are obtained. They also reveal a strong blueshift between the band-edge absorptions of one- and two-photon transitions. The strength of the blueshift depends on the size parameters. For instance, the two heterorods considered in Fig. 3.16 display a blue shift $\triangle\lambda = 55\,nm$ for the small core and

$\triangle\lambda = 68\,nm$ for the larger one, involving 1S and 1P states in both cases. This provides an unprecedented control over the band-edge two-photon absorption. In contrast with a supposed breakdown of the optical selection rules in lead chalcogenide quantum dots, the blue shift of the 2PA spectral position in comparison to the 1PA peak is produced despite the parity symmetry breaking in the electron wavefunction via the elongated shape of the shell, and favored by the low conduction band offset barrier and the lighter electron effective mass with respect to the hole[11]. While moving to the high-energy range, the CdS shell provides a high density of states with very similar energies. Thus, there are bunched groups of states with similar energy concerning *rod-rod* transitions that coexists with the core transitions. Therefore, heterorods fingerprint is detectable by a complex electronic structure with transitions mainly associated to the core, others to the shell, but also few mixed transitions.

As for the high-energy range (beyond the CdS band gap), the rod-shaped shell provides a high density of states with very similar energies and the same M_z, which explains the brunched groups of peaks dominating the 1PA spectra. The corresponding transitions involve electron and hole states mainly delocalized over the shell region. We refer to these transitions as *rod-rod* transitions, as opposed to the *dot-dot* transitions that govern the low-energy range of the spectra. We should point out here that such a classification relies on the fact that the electron and hole wavefunctions show a preferential location (dot or rod) in the heterostructure. The dot- and rod-like states give rise to three types of transitions in the spectra, which are exemplified in Fig. 3.18: *rod-rod* (Fig. 3.18 (a)), *dot-rod* (Fig. 3.18 (b)), and *dot-dot* (Fig. 3.18 (c)) transitions. Interestingly, it has been found that some electron and hole states are *mainly* confined to the spherical core even at energies exceeding the respective band offsets, which translates into the appearance of dot-dot transitions in the high-energy range of the spectra (see red peaks in Fig. 3.16). This unexpected result can be explained

[11] Additional calculations concerning lower conduction band offset 0.1 eV have been carried out to probe the robustness of our conclusions. No appreciable consequences for the spectra profiles have been found. Thus, the qualitative interpretation of the spectra is essentially the same as using the original $0.3\,eV$ conduction band offset.

as coming from the similar diameters of core and shell. In this situation, one can describe the electron (hole) motion in the lowest-lying state of each m_z symmetry assuming the so-called *adiabatic approximation*. It implies decoupling the (strongly confined) in-plane motion from the (weakly confined) 1D longitudinal one. This allows us to consider an effective 1D confining potential in the heterorod, with an m_z-independent profile. In consequence, and as long as this approach is applicable, the lowest-lying states of each m_z symmetry will be mainly confined to the core regardless of the energy range considered.

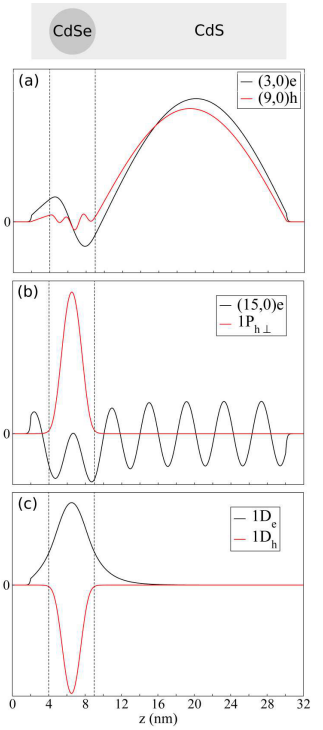

Figure 3.18: Longitudinal (z) profiles of the initial and final states involved in same ofthe absorptions arisen in the larger heterorod (sample HR2). Vertical dashed lines show the core spatial limits. Three types of transitions are found: (a) rod-rod, (b) dot-rod and (c) dot-dot, whose states involved are labeled accordingly to the preferential wave function localization in the nanostructure.

Chapter 4

Multi-electron states in hexagonal quantum rings

The aim of this chapter is to provide insight into anisotropic confinement effects in semiconductor *core-multishell nanowires (CSNWs)* [121, 122, 123, 124]. These hetero-nanowires, with an unconstrained longitudinal direction (can reach several micrometers) and different material composition along the orthogonal plane (radial direction), may become an effective 2D system when a proper material modulation along the growth axis generates a strong confinement of carriers in that direction. Most III-V nanowires with a diameter less than about 400 nm have a very neat hexagonal section even after a few overcoating processes [125, 126, 127, 128], and can eventually be cut to form an hexagonal flat quantum ring [129, 130, 131] that confine the free carriers on a square-well type potential in the radial direction. Then, we examine the physical properties of few-interacting-electron states in semiconductor hexagonal rings within the FCI approach. We shall see that charge localization patterns reflect the hexagonal symmetry and that electron correlation is a crucial aspect to be taken into account for material engineering purposes [132]. Small deviations of the ring shape (irregular hexagon) and the effect of an external magnetic field are also investigated. Thus, N-electron ground states but also excited states have been carefully analyzed to interpret the role of quantum confinement in hexagonal rings of typical synthetic sizes, and especial attention is paid to the different response to magnetic field in comparison to circular quantum rings (QRs)

[133, 134, 135, 136, 137, 138]. It is well known that by increasing the strength of an axially applied magnetic field, oscillations of the QR ground state energy occur. The period and amplitude of the oscillations depends on the electron population and it is referred to as *fractional Aharanov-Bohm (AB)* effect [139]. We may trace back to the work by Keyser [140] as the first unambiguous experimental evidence of this effect. Soon after, Emperador *et al.* [141] related this fractional response to a low kinetic energy and a phenomenon of electronic localization. The full configuration interaction (FCI) calculations by Niemelä *et al.* [142] revealed that the electron-electron interaction plays a crucial role on the decrease of the period and amplitude of the ground state energy and its fractional character. The fractional character of the AB effect was though fully explored earlier using the empirical Hubbard model [143], where it was concluded that fractional AB oscillations arise for small values of the factor $\alpha = \frac{N\,t}{(U\,L)}$, where N is the number of electrons in the QR, t is the tunneling integral, U the repulsion one and L the number of sites along the QR where the single-particle functions are located. In our work, we recover the main trends predicted by abovementioned calculations and find some peculiarities derived from the lowering of symmetry from circular to hexagonal. Additionally, we theoretically demonstrate the complete suppression of the AB effect when the hexagonal ring is in the low-density regime and it is populated with $N = 6$ electrons. This suppression translates into a smooth magnetization profile that should be experimentally observed.

4.1 Single-particle states in hexagonal rings

Single-particle states and energies of semiconductor hexagonal rings are numerically computed within the envelope function approximation. In particular, a three-layer AlAs-GaAs-AlAs core-shell nanowire (CSNW) that crystallizes in a wurtzite structure is studied. The cross section of this nanostructure is modeled as a regular hexagonal ring with edges 66.5 nm long, which in turn contains an hexagonal GaAs quantum well that is 6.8 nm wide (see Fig. 4.1). The GaAs well is covered by a 13.5 nm AlAs

capping layer and an AlAs core.

The single-particle Hamiltonian,

$$h = -\frac{1}{2}\left(\mathbf{p}+\mathbf{A}\right)\frac{1}{m^*(\mathbf{r})}\left(\mathbf{p}+\mathbf{A}\right) + V(\mathbf{r}) \tag{4.1}$$

where $\mathbf{r}$ is the 2D coordinate on the hexagonal domain, $m^*(\mathbf{r})$ is the isotropic material-dependent effective mass, $\mathbf{A}$ is the potential vector (zero in the absence of magnetic field) and $V(\mathbf{r})$ is the confining potential, is numerically integrated using finite volume and finite-elements methods. In both cases, a regular triangular grid with hexagonal elements is employed. This grid reproduces the symmetry of the system thus avoiding numerical artifacts originated by discretization asymmetries of the six domain boundaries, as would be the case, e.g., using a rectangular grid. Isotropic material-dependent electron effective masses $m^* = 0.063m_0$ ($m^* = 0.15m_0$) in GaAs (AlAs), a dielectric constant $\epsilon = 12.9\epsilon_0$ ($\epsilon = 10\epsilon_0$) in GaAs (AlAs), and a conduction-band offset between the two materials of 438 meV are employed.

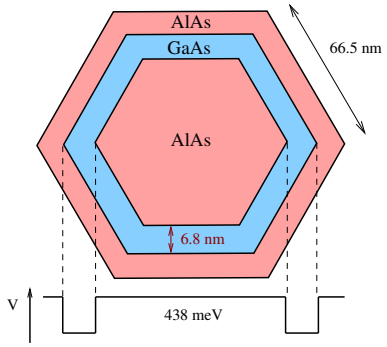

Figure 4.1: Schematics of the ring-type nanostructure considered. The regular-hexagon domain employed has edges 66.5 nm long. A GaAs quantum well 6.8 nm wide is wrapped around an hexagonal AlAs core and capped by a 13.5 nm AlAs shell.

The low-energy range of the spectrum for the N-electron hexagonal ring is properly described by using a basis set composed by the lowest 12 orbitals. We have checked that, although only the first 6 orbitals are populated with a significant probability, including 6 extra excited states becomes crucial due to the closeness of energy between the states.

The hexagonal symmetry of the GaAs quantum well gives a energy-level structure of the single-particle states with 1-2-2-1 degeneracies, as illustrated in Fig. 4.2. Such degeneracy pattern involves 6 orbitals leading to two different shells, well separated in energy, and having different preferential wave functions localization. The first shell (left in Fig. 4.2) contains orbitals that preferably accumulate electron density at the corners of the hexagonal ring. Conversely, the second one involves orbitals that tend to localize it on the hexagon edges. These wave functions localizations can be related to the widder area available around the six corners of the hexagonal ring in the case of the first shell, meanwhile the higher localization energy along the edges, found for the second shell, is due to the larger number of nodal lines that these orbitals possess.

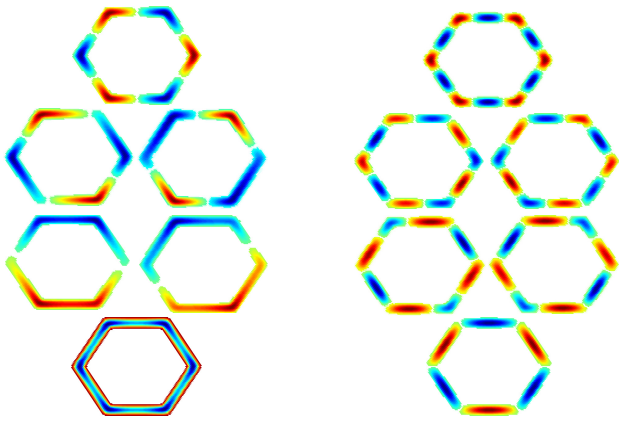

Figure 4.2: Twelve lowest-lying single-particle states of the hexagonal quantum ring. Red (blue) color indicates positive (negative) values. The system shows degeneracies 1-2-2-1, resembling an artifical benzene molecule.

The localization patterns in Fig. 4.2 are distorted when an asymmetric spatial confinement is considered (corresponding to small deviations from the perfect hexagonal symmetry during the synthetic procedure). These structural defects are modeled as an hexagonal ring with one side thicker than the others. As show in Fig. 4.3, the anisotropic confinement yields the breakdown of the degeneracies. As the thickness of one side increases, a larger number of levels depart from the energy of the symmetric case and their energy dramatically decreases. Moreover, energy levels from the upper shell join the lower shell. States with energy below that of the first shell of the symmetric system are mainly localized in the large edge. Indeed, an asymmetric hexagon with an extra top edge thickness of 0.8 nm (7.6 nm of total width) has the first three wave functions concentrated in the thicker edge, the wave functions with higher energy having a strong occupation in the rest of the hexagon.

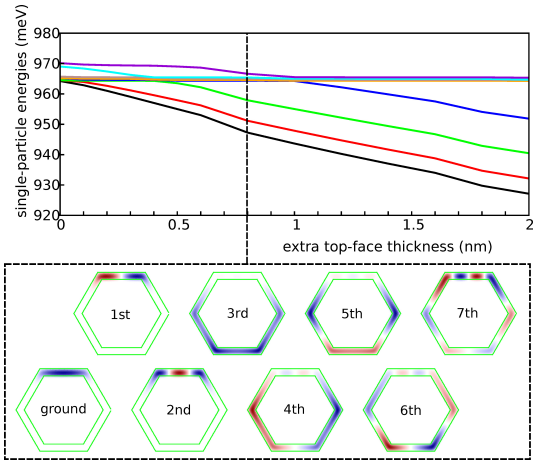

Figure 4.3: The top panel represents the energy spectrum as a function of the extra thickness of the upper edge in an asymmetric hexagon. The lower panel shows the first seventh orbitals in ascending energy order from left to right, for an extra thickness of 0.8 nm (dashed vertical line). Starting from the third excited state, the electronic density is also distributed on the edges with smaller thickness.

4.2 Few-electron states analysis

Multi-electron calculations up to 7 electrons have been performed within the framework of the FCI approach. It implies highly-computing demanding simulations[1] in which Coulomb potential energy has been computed as $U(\mathbf{r}) = \frac{e}{4\pi(\mathbf{r})(|\mathbf{r}|+\tau)}$, where τ stands for the effective mesh thickness. The cutoff parameter has been rigorously fixed at $\tau = 2$ nm [144, 145] to ensure that Coulomb repulsion smooths at short distance between two electrons[2].

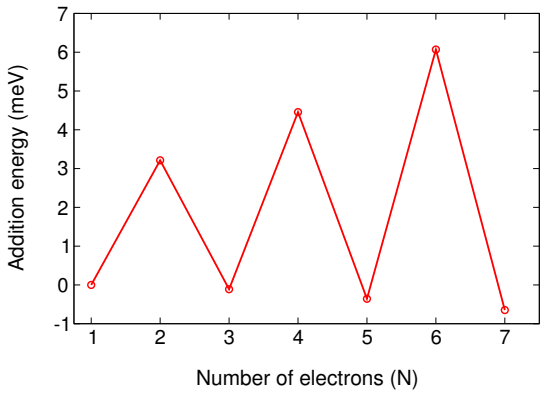

Figure 4.4: Addition energies of the hexagonal ring up to $N = 7$ electrons.

The addition-energy spectrum (Fig. 4.4) reflects the orbital shell filling for the hexagonal symmetry up to $N = 6$. The first shell is identified with the peak for 2 electrons, where system stabilizes because of the closed shell configuration. The degeneracy pattern of the symmetry of the system is observed when comparing 4- and 6-electron peaks. A half-filled shell is

[1] Our simulations take into account 3396 non-zero Coulomb integrals within the 12 orbital basis set. This quantity is remarkably larger than the one corresponding to a 6 orbital basis set, which includes only 234 non-zero integrals.

[2] We have also carried out accurated Montecarlo calculations of the exact integrals confirming the correctness of the value assigned to the τ parameter.

involved for the 4-electron configuration while a closed shell is formed for the 6-electron ground state. The extra stabilization effect for the closed shell can be detected thanks to the higher peak for six electrons. This six-electron case corresponds to that of a benzene ring. With seven electrons, the system stability decreases having a single unpaired electron in the two degenerate orbitals above two closed shells, resulting in a negative addition energy. All the studied N-electron ground states are highly correlated and larger correlation effects are detected as the number of particles increases. In fact, the weight of the leading Slater determinant for the two-particle case is 63%, whereas it is only 16% for the seven-particle case.

The strong correlation regime, present in the N-electron hexagonal system, is characterized by a preferential corner localization of the total and the spin electron densities (see Fig. 4.5). Conditional density calculations have also been performed to assess the effects of Coulomb-induced correlation. By fixing one electron with spin up in an arbitrary corner, opposite spin electron density is distributed in favoured corners due to Coulomb effect. We can see in Fig. 4.6 that while the 2-electron ground state (left hexagon) localizes spin down density at the opposite corner of the hexagon, for the 3-electron case (middle hexagon) the spin down density is mainly found on the other two corners forming with the first one an equilateral triangle. The 6-electron system distributes opposite electron spin density in alternate corners (typical Wigner phase).

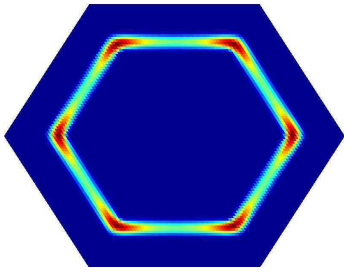

Figure 4.5: Schematics of the total electron density profile obtained for the considered N-electron ground states.

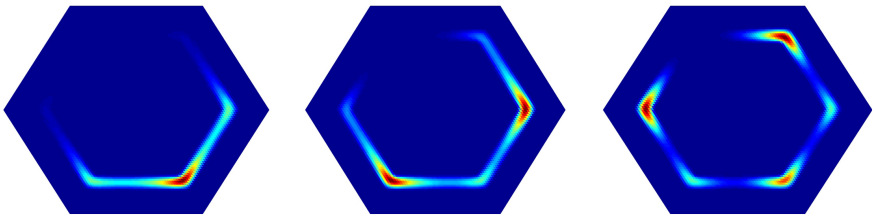

Figure 4.6: Conditional densities for 2-, 3- and 6-electron ground state when an electron with spin up is fixed in a corner and opposite spin density is taken into account.

If we consider correlation effects in the asymmetric hexagon, the ground state electron density shows a strong concentration in the large edge. In few-electron cases, the electronic density is completely localized in the large edge, as e.g. in the 3-electron system (see Fig. 4.7). In this case, it is worth to notice that by increasing the top edge thickness, a crossing between states $S = \frac{3}{2}$ (symmetric hexagon ground state) and $S = \frac{1}{2}$ (asymmetric hexagon ground state) occurs. On the other hand, as N increases, the electron density is still mainly concentrated in the large edge, but also in the other four corners, as shown in Fig. 4.7 for the 7-electron case. Additionally, conditional density distributions present a distribution typical of strong correlation (see Fig. 4.7).

4.3 Single- and multi-electron states under an applied magnetic field

Hereafter, we study the electronic structure of the hexagonal ring under magnetic field effects. The presence of axial or in-plane magnetic fields induces an extra magnetic confinement. Details on the way we include axial and in-plane magnetic fields in the Hamiltonian are given in Ref. [146].

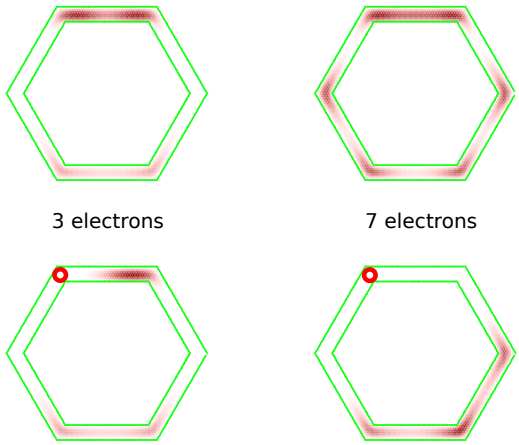

Figure 4.7: Total electron density (top) and conditional electron density (bottom) for the 3-electron (left) and 7-electron (right) ground states of the asymmetric hexagon with 7.6 nm width.

Let's first consider the $N = 1$ hexagonal ring pierced by an ***axial magnetic field*** (as illustrated in Fig. 4.8). The energy spectrum is quite different from the one of a circular quantum ring, the differences originating in the symmetry lowering from circle to hexagon. In a circular ring, the infinite number of irreducible representations label orbitals that cross as the magnetic field rises. In the case of C_6 symmetry, anticrossings between orbitals with the same symmetry yield different non-crossing shells where orbitals with different symmetry repeteadly cross as the magnetic field increases. The shell structure, shown in Fig. 4.8, allows us to employ the basis set of the twelve lowest-lying orbitals to calculate the many-body low-lying states with the same level of accuracy, independently of the strength of the magnetic field.

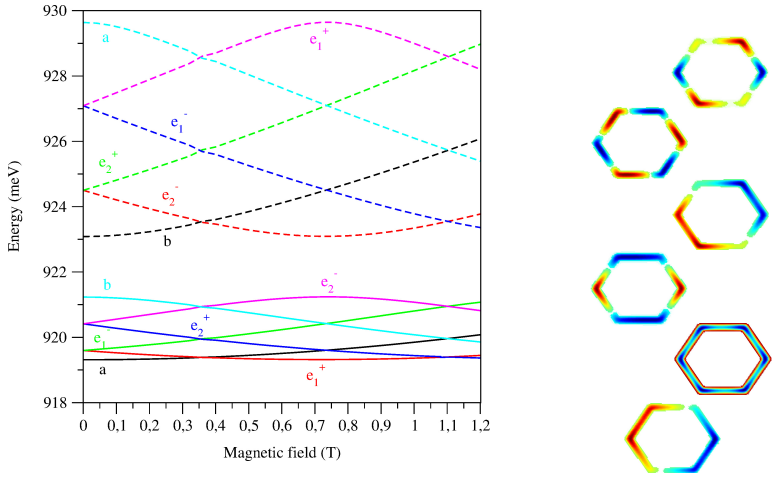

Figure 4.8: Left: Orbital energies vs magnetic field (B). They are labeled according to the C_6 symmetry group. Right: Real part of the orbital functions at $B = 0.6$ T ordered, from bottom to top, by increasing energy.

When the ***magnetic field*** is applied ***in-plane***, two different orientations have been considered: corner-to-corner (shown on the left in Fig. 4.9) and edge-to-edge (see right side in Fig. 4.9). We observe similiar qualitative trends in both cases. Since the axial symmetry of the ring is broken by these external fields, signatures of the AB effect are absent. In particular, as the magnetic field increases, consecutive single-particle energy levels arrange in pairs, these couples becoming quasi-degenerated for a large enough strength of the magnetic field. This has an outcome in the ground state wave functions localizations: the most significant wave function accumulation is localized in preferential corners, depending on the in-plane field direction, as illustrated on the rigth in Fig. 4.9.

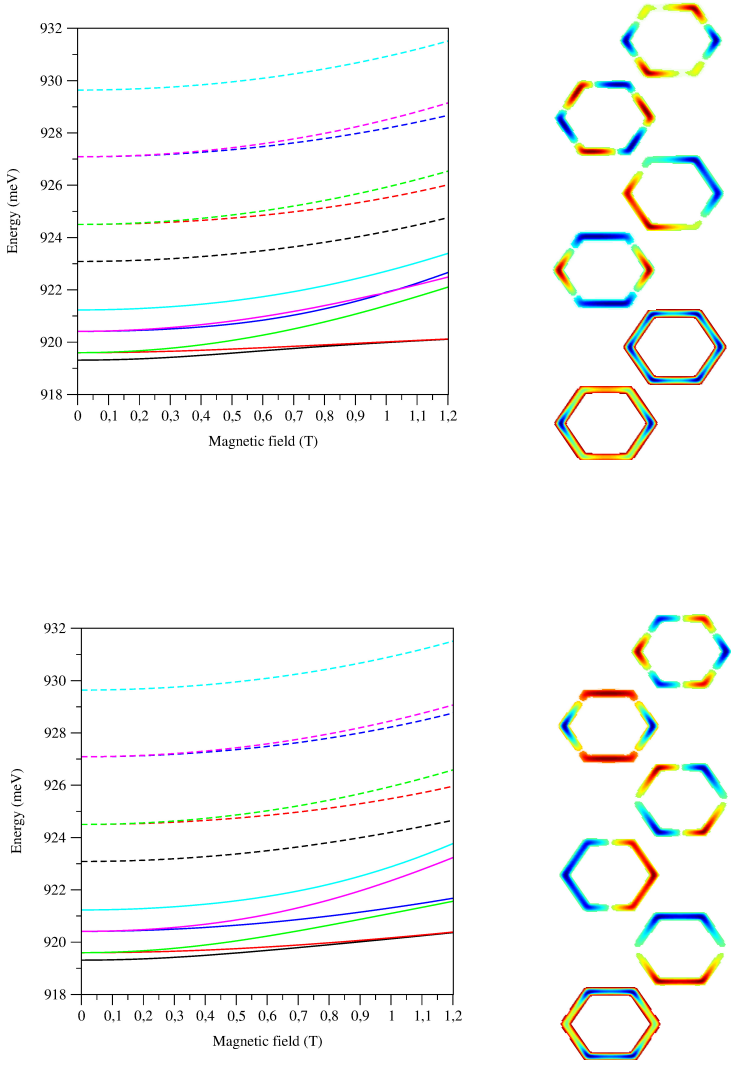

Figure 4.9: In-plane magnetic field effects on the orbital enery levels (left). Similar qualitative trends are obtained for an in-plane corner-to-corner (top) and edge-to-edge (bottom) magnetic field. On the right, real part of the six lowest orbitals when an in-plane $B = 0.6$ T magnetic field is applied corner-to-corner (top) and edge-to-edge (bottom).

When we include the electron-electron interactions via FCI, in the presence of an in-plane magnetic field, the obtained results are as expected. In the particular, for small N the electron density distribution concentrates in selected corners (see Fig. 4.10 for $N = 2$) while it spreads gradually over the remaining corners as N increases.

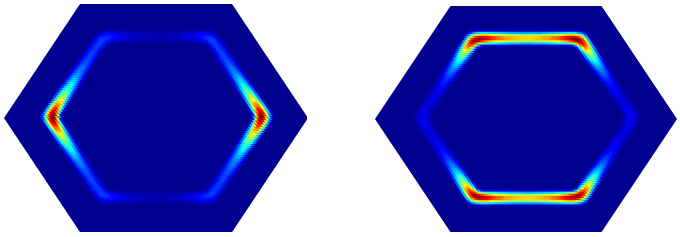

Figure 4.10: Total density profiles for a 2-electron hexagon under the effects of an in-plane magnetic field oriented corner-to-corner (left) and edge-to-edge (right).

Next, we focus our attention on the response of the many-electron system to an externally applied axial magnetic field. Calculations have been carried out for the hexagonal quantum ring populated with $N = 1$ up to $N = 7$ electrons. In the plot energy vs. magnetic field, Fig. 4.11, we can see some gaps separating shells of repeteadly crossing many-electron states. These gaps can neatly be observed for $N = 2, 3, 5$ and 6, the last case displaying a relatively large gap separating the 64 lowest-lying states, all of them having quite close energies, from the rest of the spectrum.

In Fig. 4.12 we show the lowest-lying states of the spectra, labeled according to symmetry and spin multiplicity. The comparison with the $N = 1$ system, Fig. 4.8, reveals a perfect fractional Aharanov-Bohm effect for $N = 2$ and $N = 3$, while the oscillation amplitude pattern of $N = 4$ and especially $N = 5$ is not regular. When the hexagonal ring is populated with $N = 6$ electrons a complete suppression of the AB effect occurs. Finally, $N = 7$ shows the same period of amplitude than $N = 1$.

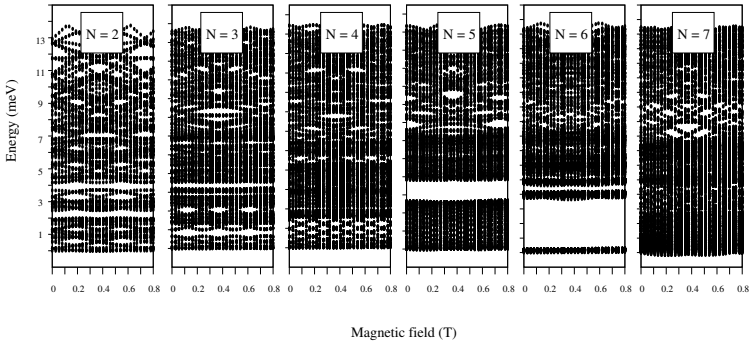

Figure 4.11: Multi-particle energy spectra simulations of the hexagonal ring populated up to 7 electrons. Well-separated shell of states can be clearly seen for $N = 2, 3, 5$ and 6 electrons.

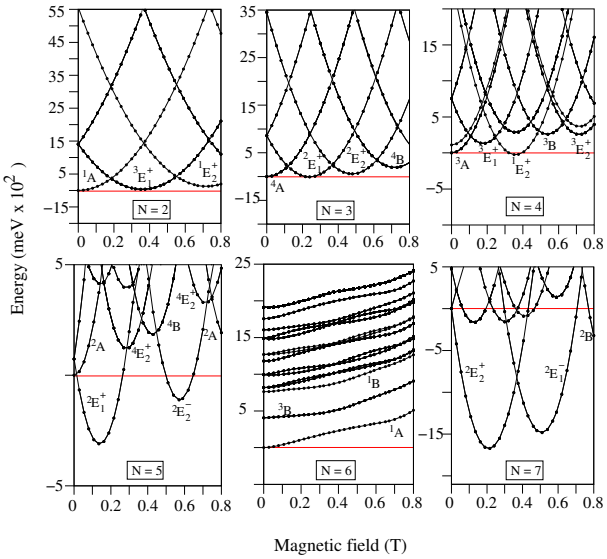

Figure 4.12: Energy of the lowest-lying many-electron states in hexagonal quantum rings as a function of the magnetic field. Energies are relative to the N-electron ground state energy in the absence of field (horizontal red line). Multi-particle states are labeled according to the C_6 symmetry group and spin multiplicity.

All our results, except for $N = 6$, are consistents with the results known for circular quantum rings [141, 142, 143]. The singular behaviour of the $N = 6$ system can be rationalized from the independent particle spectra (Fig. 4.13): only for $N = 6$ two electronic configurations with very different energies at $B = 0$ T cross when the ring is pierced by half unit of flux. In order to confirm this hypothesis, we perform a set of FCI calculations in which we modulate the Coulomb interaction by introducing an scaling factor f multiplying the electron-electron integrals. Then, ranging from a non-interacting six-electron ring, ($f = 0$, see Fig. 4.13) with a crossing at about $\frac{1}{2}$ of flux, to higher scaling factors ($f = 0.1, 0.2$ and 0.5 as shown in Fig. 4.14) we can identify the crucial role of two configurations, namely $a^2(e_1^+)^2(e_1^-)^2$ and $(e_1^+)^2a^2(e_2^+)^2$, that yield the same total symmetry and total spin, ^1A, for both configurations[3]. The states associated to these configurations anticross and the anticrossing becomes larger as the electron-electron interaction increases, up to reach an almost flat profile of the ground state in the case of no scaling ($f = 1$).

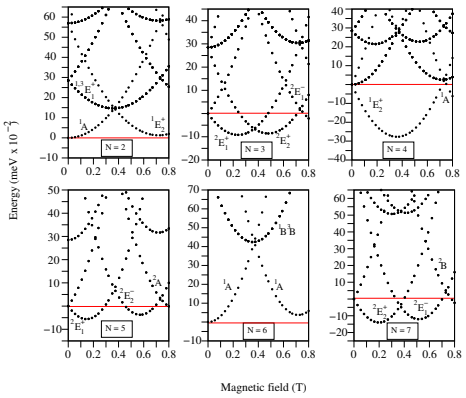

Figure 4.13: Non-interacting particle low-lying energy spectra for $N = 2$ up to $N = 7$ electrons in the hexagonal quantum ring. Red line indicates the ground state energy of non-interacting particles in the absence of magnetic field effects. It is assumed as the origin of energies. States are labeled by symmetry and spin multiplicity.

[3]When the electron-electron repulsion is included in the simulations (scaling factor different from zero) we identify these configurations as the dominant ones.

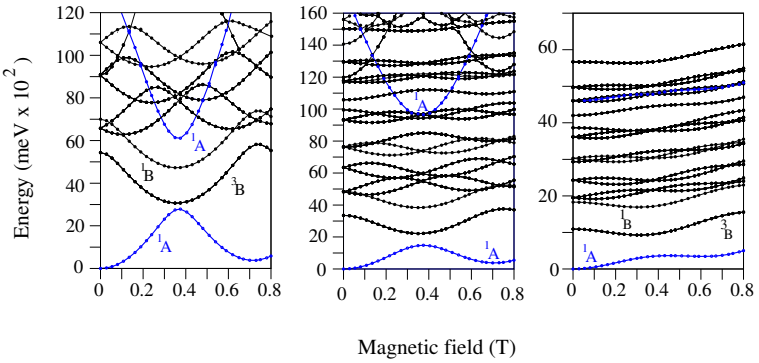

Figure 4.14: From left to right: lowest-lying states for the six-electron hexagon for increassing Coulomb interactions. Coulomb repulsion is scaled by a factor $f = 0.1$ (left panel), $f = 0.2$ (middle panel) and $f = 0.5$ (right panel). Blue lines correspond with the states with the same symmetry that anticross.

The singular behavior of the 6-electron system is reflected in the magnetization response. Magnetization profiles for all considered N-electron systems are shown in Fig. 4.15. According to Kusmartsev, the fractional Aharonov-Bohm (AB) effect should appear when the factor $\alpha = N\frac{t}{U}\frac{1}{L}$ is small [143]. In this factor, N represents the number of electrons, t stands for the tunneling, U indicates the repulsion, and L the number of sites where the orbitals are located (six in a semiempirical Hubbard model of an hexagonal ring). By fixing $L = 6$ and the tunneling t value, we have that α is proportional to N and inversely proportional to the Coulomb term U. Since α must be small, for a given U, the fractional AB effect will arise for a low value of N. In our case, the fractional AB effect occurs for $N = 2, 3, 4$ whereas it is absent for $N = 5, 6, 7$, being the 6-electron a singular case where a complete suppression of the AB effect occurs, and a flat magnetization profile vs. the magnetic field results (see Fig. 4.15).

To assess the role of the density regime, we carried out similar calculations for an hexagonal ring three times smaller (hereafter ***small hexagon***).

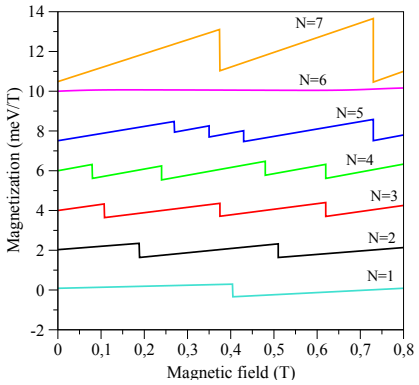

Figure 4.15: Magnetization profiles vs. magnetic field for the hexagonal quantum ring populated with $N = 1$ (bottom) up to $N = 7$ (top). For the sake of clarity, the magnetization profiles have been offset by 2 meV/T.

Fig. 4.16 contains the full energy spectra of the small system populated with $N = 2$ up to $N = 7$ electrons and Fig. 4.17 contains the zoom of the low-lying spectra. The remarkable difference between Fig. 4.11 and Fig. 4.16 is that no gaps separating shells (groups of states) can be seen in the small system. On its side, Fig. 4.17 reveals that only the $N = 2$ case displays a fractional AB effect. The rest of systems behave similar to the independent particle case (see Fig. 4.13). In the $N = 6$ case, the ^{1}A $-$ ^{1}A anticrossing is not as severe as in the large ring and a small window where ^3B becomes the ground state occurs. This behavior leaves a signature in the magnetization profile (Fig. 4.18). We can see in this figure that only $N = 2$ shows a fractional AB effect. As N increases, the magnetization profiles show kinks with irregular periods and amplitudes. In particular, $N = 5$ and $N = 7$ behave like $N = 1$, while the six-hexagonal ring magnetization profile displays two close kinks at about one half of unit of flux, as a signature of the short ^3B window shown in Fig. 4.17. The existence of this window reveals that the larger density of the small hexagon leads to an ^{1}A $-$ ^{1}A anticrossing that cannot completely overcome the relative stabilization of triplet ^3B originated from the exchange integrals.

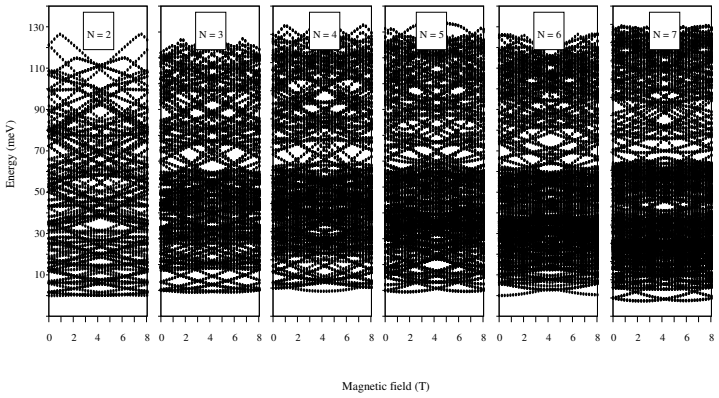

Figure 4.16: Multi-particle energy spectra simulations of the small hexagonal ring populated up to 7 electrons.

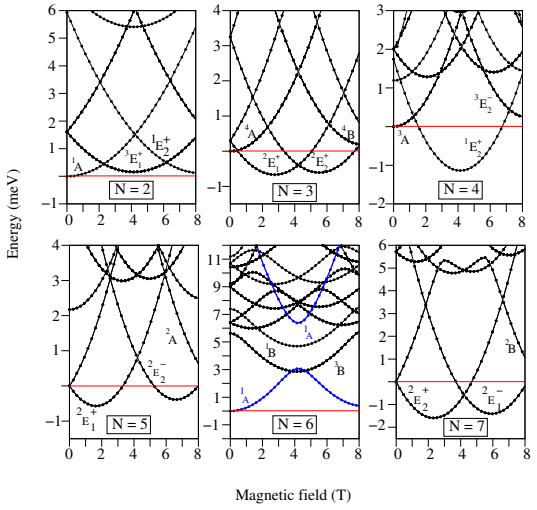

Figure 4.17: Lowest-lying electron states of the small hexagonal ring. Energies are relative to the ground state energy in the absence of magnetic field effects, represented by the red line. The ground state is labeled according to the C_6 symmetry group and spin multiplicity.

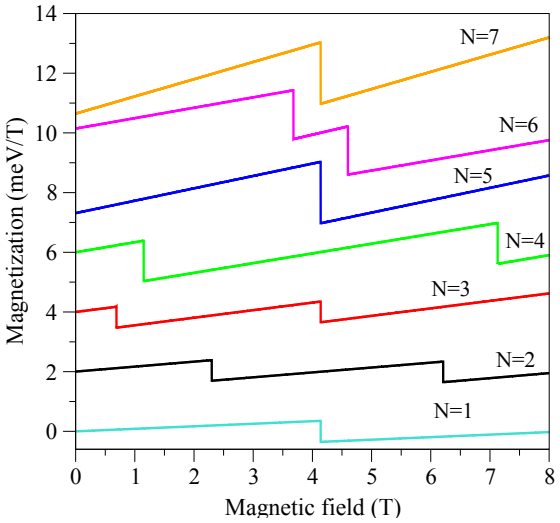

Figure 4.18: Magnetization profiles of the small hexagonal ring. The different profiles have been offset 2 meV/T.

In conclusion, the complete suppression of the AB effect and the associated flat magnetization profile calculated in the case of an hexagonal ring populated with $N = 6$ electrons is a symmetry-related response that only can emerge in the low-density regime.

Conclusions

The aim of this thesis is to provide a theoretical description of the physical properties of semiconductor nanocrystals under anisotropic confining potentials. The theoretical understanding of the role of the spatial confinement, the most important confining source in nanostructures, as well as other sources of confinement (dielectric, magnetic, Coulombic, etc) is carried out by means of the Effective mass - Envelope function approximation (EMA-EFA). The influence of several quantum confinement conditions, such as quantum size and structural effects, polarization potentials coming from the different dielectric response of adjacent materials or external field effects, is investigated by performing numerical simulations.

The interplay between spatial confinement and dielectric mismatch effects is studied when a singly-ionized double donor system is hosted in a semiconductor colloidal quantum dot. It has been found that spatial and dielectric confinements operate in different length scales. In large dot size regimes dielectric effects dominate the electronic properties of the donor system, so that spatial confining effects are modeled by the dielectric confinement and they can even be reversed. Conversely, in small dot size regimes spatial confinement overcomes dielectric effects and governs the molecular properties of the coupled impurities. This makes possible to modulate the tunnel coupling strength and charge-density distribution of the lowest-lying states of the system at will, by choosing the appropriate dot size and surrounding medium. Additionally, the decoherence of the first excited state of the single-ionized double donor system can be tuned to eventually increase the relatively low bulk coherence times of orbital states in possible charge qubit realizations.

Moreover, different spatial confining regimes have been explored in quantum dots with variable aspect ratio. The transition from zero-dimensional quantum dots to one-dimensional quantum wires has been characterized by means of addition energy spectra and electron density profiles. It is concluded that finite elongated quantum dots (nanorods) in the limit of weak confining regime show electronic structures that resemble that of infinite nanowires, with preferable stabilization of orbitals with null angular momentum. Electron-electron interactions govern the electronic structure of nanorods, and several correlation phases are obtained depending on the number of electrons populating the system. In the low-density limit, the transition from charge density waves (CDW) to spin density waves (SDW) identifies the existence of strong correlated multi-electron ground states.

In the limit of weak confining regime, we show that diluted systems subject to inhomogeneous spatial confining potentials can form a mixed correlation phase. The formation of this phase entails a ground state whose electronic-density distribution exhibits the coexistence of a Fermi liquid in some regions of the polielectronic system while, simultaneously, other more dilute regions display a typical Wigner crystal density distribution. The presence of different correlation regimes in the very same nanostructure is also characterized in the addition spectrum and the infrared response. In the latter case, the presence of a highly anisotropic confining potential allows us to differentiate between longitudinal and transversal responses that appear in different energy ranges. The fingerprint of strongly correlated states is driven by low energy transitions associated to the growth direction of the nanostructure.

An even more complex confining potential acts on the electron-hole pairs in quasi-type II core-shell dot-in-rod structures. These heterostructures involve the interaction between a highly isotropic confinement (the core) and a highly anisotropic one (the shell). This interaction becomes apparent when analyzing the simulated optical spectra. Dipole-allowed transitions show a non-negligible interplay between core and shell states. A blue shift between one-photon and two-photon absorption spectra is obtained due to the reduced oscillator strength of low-energy two-photon transitions. This

blue shift can be controlled by the strength of quantum confinement. Our theoretical model has been able to interpret the available experimental data.

Finally, the role of spatial confinement is addressed in hexagonal semiconductor quantum rings of typical synthetic sizes, populated with $N = 1$ up to $N = 7$ electrons. We find that the system is in the low-density regime with typical signatures of partial electron density localization in the corners where a larger room is available. Conditional density distributions show spin alternances, the $N = 6$ electron system displaying a typical spin density wave with alternate spin signs in consecutive corners. The interplay of an externally applied magnetic field in the axial direction has a striking outcome in comparison to typical circular quntum rings, as the complete suppression of the Aharanov-Bohm oscillations and a flat magnetization profile when the hexagonal ring is populated with $N = 6$ electrons, this being a symmetry-related response that only can emerge in the high correlation, low-density regime.

Resumen

En las últimas décadas, el mundo moderno ha prestado especial atención a los objetos microscópicos con el fin de conseguir propiedades inéditas de los materiales, las cuales puedan ofrecer importantes beneficios para la vida humana. A este respecto, numerosas investigaciones han dado a conocer nuevas estructuras cuyas dimensiones están acotadas en la nanoescala y que constituyen un área de conocimiento muy prometedora que añade novedosos fenómenos físicos. Tales nanoestructuras muestran propiedades interesantes que sólo pueden ser entendidas mediante las bases fundamentales de la Mecánica Cuántica, en comparación con las propiedades clásicas asignadas al mundo macroscópico. La teoría cuántica, basada en la naturaleza dual onda-partícula de las partículas esenciales de la materia, determina la existencia de efectos de confinamiento cuántico responsables de los fenómenos físicos observados en la nanoescala. Dado que las longitudes de onda *de Broglie* de los portadores de carga son del orden de las dimensiones espaciales de las nanoestructuras mencionadas anteriormente, el confinamiento cuántico juega un papel clave a la hora de determinar sus propiedades físicas.

El avance de las técnicas de miniaturización proporciona nuevos diseños de dispositivos nanoelectrónicos, compuestos principalmente por materiales semiconductores, cuyas funciones electrónicas asociadas pueden ser controladas para dar lugar a aplicaciones útiles. Este es el objetivo de la *nanotecnología*. Ésta es un área multidisciplinaria y reciente que trata de construir dispositivos cada vez más rápidos, eficientes e inteligentes por medio de técnicas de nanofabricación conocidas como *top-down* y *bottom-up* [1]. En concreto, están siendo ampliamente investigadas aquellas estructuras cristalinas conocidas como *puntos cuánticos* (en inglés *quantum dots*, QDs) [2], que contienen entre 1.000 y 100.000 átomos, al descubrirse sus

novedosos usos potenciales como componentes básicos versátiles de cara a los propósitos de la ingeniería microelectrónica. Una amplia variedad de estudios sugieren que dichos puntos cuánticos, cuyas propiedades dependen de su composición, tamaño y forma, tienen un enorme interés tecnológico, por ejemplo, como candidatos a sustituir los dispositivos de silicio actuales basados en esquemas clásicos de computación [3], por el hecho de ofrecer una amplia gama de propiedades electrónicas y ópticas [4, 5], o por su capacidad para actuar como marcadores biológicos [6, 7, 8].

Los puntos cuánticos semiconductores de tipo coloidal (también llamados nanocristales) se sintetizan empleando un protocolo conocido como la *Química húmeda* [9] en el que el crecimiento de las nanopartículas se desarrolla en el seno de materiales vítreos, orgánicos o biológicos, o simplemente en aire o vacío. Esta vía de síntesis posibilita la obtención de nanocristales con muy baja densidad de defectos y extremadamente monodispersos, con tamaños comprendidos entre 1 y 10 nm y, generalmente, de forma esférica (que a su vez pueden estar formados por capas concéntricas de diferentes materiales). La estructura electrónica de estos puntos cuánticos de simetría esférica se asemeja a la de los átomos reales, ya que el confinamiento cuántico de los portadores de carga conduce a niveles de energía cuantizados [10]. La distribución energética de las bandas de conducción (CB) y de valencia (VB) adquiere un carácter discreto similar al de los átomos, motivo por el cual también se conoce a estas nanoestructuras como *átomos artificiales*. El confinamiento espacial surge como consecuencia de la ausencia de alineamiento de las bandas de energía (*band offset*) entre el material que conforma el punto cuántico y el medio circundante donde se encuentra sumergido dicho sistema, o entre materiales adyacentes en sistemas multicapa. Durante el proceso de fabricación de este último tipo de sistemas tanto el espesor como la composición de las capas son controlables, de manera que es posible diseñar varios tipos de heteroestructuras cuyas propiedades físicas son significativamente diferentes a los puntos cuánticos formados por un único tipo de material. Braun *et al.* informaron sobre la primera preparación de un sistema multicapa esférico [11], concluyendo que existe una importante interacción entre las capas. Más tarde, la síntesis de heteronanocristales con una variación gradual de la composición radial [12],

o de estructuras con disposición core-shell de tipo II [13, 14] se ha logrado gracias a técnicas de crecimiento bien establecidas y extremadamente precisas [15, 16]. La posibilidad de modular las funciones de onda de los portadores de carga en estos nanocristales permitiría la optimización de aplicaciones nanoelectrónicas [17].

El término *punto cuántico (QD)* deriva de la clasificación más ampliamente aceptada de las denominadas *estructuras de baja dimensión*, que depende del grado de confinamiento que se ejerce sobre los portadores de carga (electrones y huecos). Los puntos cuánticos confinan los portadores de carga en las tres dimensiones del espacio. En su lugar, los *pozos cuánticos* son heteroestructuras bidimensionales que confinan las cargas a lo largo de una dirección, mientras que las estructuras casi unidimensionales, los llamados *hilos cuánticos* [18], son de longitudes largas y confieren libre movimiento de carga a lo largo de la dirección de crecimiento. La transición desde una nanoestructura de forma esférica a las estructuras casi unidimensionales, caracterizadas por presentar un potencial confinante altamente anisótropo, se puede lograr mediante el aumento de la *relación de aspecto* de los nanocristales. Entre las estructuras aproximadamente unidimensionales cabe mencionar una variante alargada de los puntos cuánticos conocida como *nanovarillas* o *nanorods* [19], es decir, nanocristales de forma aproximadamente cilíndrica que presentan una relación de aspecto menor que los hilos cuánticos. El interés en su estudio reside en el hecho de que suponen el nexo de unión entre los puntos cuánticos esféricos y los hilos cuánticos unidimensionales. Por otra parte, pueden sintetizarse estructuras más complejas basadas en los nanorods, entre las que cabe mencionar a los *nanodumbbells* [20]. Estas nanoestructuras están constituidas por un nanorod adherido a dos volúmenes de geometría aproximadamente esférica en sus extremos.

Objetivo y Metodología

La presente Tesis Doctoral aborda el estudio teórico de la estructura electrónica y propiedades derivadas de diversas nanoestructuras semiconductoras anisótropas mediante el modelado teórico de nanosistemas con simetría axial, puesto que dicha geometría cubre la geometría de los puntos

cuánticos de mayor interés (esferas, varillas, anillos, lentes,...). Para ello, se ha empleado el *Método k·p* [21] en su aproximación de masa efectiva y función envolvente (EMA-EFA) [22, 23]. Esta aproximación, también conocida como modelo de una banda, se ha utilizado tanto para describir electrones en exceso de la banda de conducción como para huecos de valencia, y resulta ser una aproximación ampliamente aceptada cuando los estados de la banda de conducción (valencia) se pueden considerar prácticamente aislados con respecto a posibles perturbaciones de la banda de valencia (conducción). En esta Tesis tratamos con nanoestructuras semiconductoras compuestas por la combinación de elementos químicos de los grupos III-V y II-VI (como por ejemplo CdS, CdSe, CdTe, GaAs, AlAs) que presentan un band gap directo y suficientemente ancho, de manera que el modelo de una banda constituye una aproximación razonable y ofrece buenos resultados. Este método semi-empírico permite la adición de potenciales no periódicos, tales como impurezas, heterouniones o campos electromagnéticos externos al *Hamiltoniano k·p* bajo un coste computacional razonable. Esta flexibilidad nos permite investigar las propiedades físicas de nanocristales semiconductores sometidos a diferentes condiciones de confinamiento cuántico.

La metodología de trabajo desarrollada ha consistido, por tanto, en modelizar el comportamiento de nanoestructuras mediante la implementación de códigos computacionales empleando el lenguaje FORTRAN, junto con la ayuda del programa MATLAB. La integración numérica de los Hamiltonianos de partícula independiente y, posteriormente, el cálculo multipartícula mediante la diagonalización de la matriz de *interacción de configuraciones CI* o el empleo de la *Teoría del Funcional de la Densidad (DFT)* en su aproximación local de espín (LSDA) para sistemas poblados con un gran número de electrones, constituyen las herramientas de trabajo para estudiar el efecto que producen variaciones del potencial de confinamiento sobre la estructura electrónica de nanocristales semiconductores. Adicionalmente, la simulación de espectros de adición, perfiles de densidad y energías de absorción, junto con la investigación bibliográfica oportuna han contribuido al análisis, comprensión y discusión de los resultados obtenidos.

Aportaciones originales y conclusiones

En primer lugar, se estudian los efectos de la superposición de los confinamientos espacial y dieléctrico sobre el sistema formado por dos impurezas donoras $\left(D_2^+\right)$ -de especial interés en computación cuántica- en un nanocristal. Se ha determinado que las propiedades moleculares de dicho sistema pueden ser moduladas por ambas fuentes de confinamiento, dado que éstas actúan en diferentes escalas. En efecto, en nanocristales de gran tamaño las propiedades moleculares de interés vienen determinadas por los efectos de discontinuidad dieléctrica entre el material que compone el punto cuántico y el medio exterior que lo envuelve. En cambio, en nanocristales de pequeño tamaño el confinamiento espacial prevalece sobre el confinamiento dieléctrico. Esta versatilidad en el comportamiento del sistema dopado posibilita el diseño de sus propiedades electrónicas en función del tamaño del punto cuántico y la naturaleza del medio envolvente. En particular, se ha encontrado un amplio rango de control dieléctrico en la velocidad de emisión espontánea. Este resultado es especialmente interesante, pues permitiría aumentar el relativamente escaso tiempo de coherencia que los estados excitados del sistema $\left(D_2^+\right)$ presentan en el bulk.

También hemos abordado el estudio de diferentes regímenes de confinamiento en puntos cuánticos con relación de aspecto longitud/diámetro creciente. En concreto, hemos analizado la transición entre nanocristales cero dimensionales (puntos cuánticos) y unidimensionales (hilos cuánticos), definida dicha evolución mediante un crecimiento en la anisotropía del potencial confinante espacial. La estructura electrónica de dichos sistemas se ha caracterizado mediante el espectro de energías de adición de nanorods de longitud creciente. En regímenes de baja densidad de electrones, se ha encontrado el fenómeno de fusión cuántica, esto es, la transición entre una fase ordenada y fuertemente correlacionada, donde hay un aparente comportamiento clásico de los electrones (fase Wigner) y un sistema de partículas débilmente interaccionantes, donde los términos cinéticos dominan (líquido de Fermi).

A continuación, un diseño adecuado del potencial confinante nos ha permitido encontrar y caracterizar estados en los que coexisten fases de

correlación diferentes en distintas regiones espaciales de un mismo nanocristal. La presencia de fases mixtas, compuestas por un líquido de Fermi y un cristal Wigner, se ha caracterizado mediante el espectro de energías de adición y la simulación del espectro óptico del nanocristal. La coexistencia de ambas fases supone un comportamiento dual clásico-cuántico que tiene un claro reflejo en su respuesta infrarroja. Aparte de su interés teórico, las fases mixtas pueden ser útiles en el diseño de dispositivos optoelectrónicos, tales como sensores infrarrojos.

Seguidamente, hemos investigado las propiedades ópticas de nanoheteroestructuras constituidas por un punto cuántico esférico (core) inmerso en una varilla o rod (shell), satisfactoriamente sintetizadas y caracterizadas experimentalmente. La simulación teórica de su espectro de absorción mono- y bifotónico, que reproduce los datos experimentales, confirma la existencia de un desplazamiento a energías mayores de las transiciones asociadas al espectro bifotónico con respecto al monofotónico. Este hecho se explica en base a la conservación de las reglas de selección que rigen las transiciones ópticas, en contraposición a resultados ya publicados en sistemas en que también se rompe la simetría de paridad [105]. Cabe destacar, además, la existencia de transiciones vinculadas a estados ligados principalmente al core que exceden la diferencia de energía asociada al band offset de la banda de valencia (estados de hueco) y de conducción (estados del electrón).

Finalmente, se estudian los efectos de la interacción electrónica sobre el comportamiento de los estados multipartícula en anillos cuánticos heteroestructurados con forma hexagonal. Teniendo en cuenta tamaños típicos de síntesis de dichas nanoestructuras, se ha determinado que la estructura electrónica de los estados electrónicos confinados en el anillo presenta una importante localización de densidad electrónica en los vértices del sistema. Además, se ha determinado que en régimen de alta correlación se origina una respuesta magnética anómala para el caso del sistema poblado con 6 electrones. Esta respuesta del sistema deriva de la confluencia de un régimen de baja densidad electrónica y condicionantes específicos de simetría del anillo hexagonal poblado con 6 electrones.

Los resultados que brevemente hemos mencionado han conformado los artículos publicados (o de inminente publicación) en revistas internacionales, recogidos en el siguiente listado:

1. J. L. Movilla, A. Ballester and J. Planelles. "Coupled donors in quantum dots: Quantum size and dielectric mismatch effects" Phys. Rev. B, **79** (2009) 195319.1-6[1]

2. J. Planelles, M. Royo, A. Ballester and M. Pi. "From quantum dots to quantum wires: Electronic structure of semiconductor nanorods" Phys. Rev. B, **80** (2009) 045324.1-5[2]

3. A. Ballester, J. M. Escartin, J. L. Movilla, M. Pi and J. Planelles. "Mixed correlation phases in elongated quantum dots" Phys. Rev. B, **82** (2010) 115405.1-8[3]

4. A. Ballester, J. L. Movilla, J. M. Escartin, M. Pi and J. Planelles "Configuration interaction approach to Fermi liquid-Wigner crystal mixed phases in semiconductor nanodumbbells" J. Appl. Phys., **112** (2012) 024311.1-5

5. A. Ballester, J. Planelles and A. Bertoni "Multiple-particle states of semiconductor hexagonal rings: Artificial benzene" J. Appl. Phys. **112** (2012) 104317.1-9

6. M. Allione, A. Ballester, H. Li, A. Comin, J. L. Movilla, J. I. Climente, L. Manna, and I. Moreels “Two-Photon-Induced Blue Shift of Core and Shell Optical Transitions in Colloidal CdSe/CdS Quasi-Type II Quantum Rods” ACS Nano **7** (2013) 2443.1-10

[1] Selected for the June 1, 2009 issue of Virtual Journal of Nanoscale Science & Technology (Volume 19, Issue 22).
Selected for the June, 2009 issue of Virtual Journal of Quantum Information (Volume 9, Issue 6).

[2] Selected for the August 10, 2009 issue of Virtual Journal of Nanoscale Science & Technology (Volume 20, Issue 6).

[3] Selected for the September 13, 2010 issue of Virtual Journal of Nanoscale Science & Technology (Volume 22, Issue 12).

7. A. Ballester, C. Segarra, J. Planelles and A. Bertoni “Suppression of the Aharonov-Bohm effect in six-electron hexagonal quantum rings” (enviado a publicar)

Publications

Coupled donors in quantum dots: Quantum size and dielectric mismatch effects

J. L. Movilla, A. Ballester, and J. Planelles*
Departament de Química Física i Analítica, Universitat Jaume I, Box 224, E-12080 Castelló, Spain
(Received 17 February 2009; revised manuscript received 17 April 2009; published 20 May 2009)

Spatial and dielectric confinement modulations of the spontaneous emission rates, transition energies, and charge-density distributions of a singly ionized double donor system (D_2^+) in a spherical quantum dot are calculated within the framework of the effective-mass envelope function approximation. Dipole moments, energy splittings, transition moments, electron-density distributions, and spontaneous emission rates involving bonding and antibonding lowest-lying molecular states are addressed for different dielectric environments, quantum dot radii, and relative locations of the coupled impurities inside the dot. The results indicate that the donor molecule behaves as heteropolar when the spatial confinement breaks the inversion symmetry, which is paralleled by a strong reduction in the excited-state radiative lifetime. Dielectric confinement, acting on a larger length scale than spatial confinement, may recover the bulklike homopolar character when the dot is embedded in a low dielectric constant medium. In the weak spatial confinement regime, dielectric effects can increase the corresponding bulk radiative lifetimes significantly and simultaneously modulate the charge-density distribution.

DOI: 10.1103/PhysRevB.79.195319 PACS number(s): 71.55.−i, 73.21.La, 77.22.Ej, 03.67.Lx

I. INTRODUCTION

The system built of two coupled semiconductor quantum dots (QDs) containing electrons, holes, or an exciton constitutes one of the simplest solid structures proposed as the functional part in a wide range of device applications, including spintronics,[1] optoelectronics,[2] photovoltaics,[3] and quantum information technologies.[4,5] The widespread interest in this system relies on the ability to manipulate conveniently its molecular properties, such as the energy splitting between the bonding (nodeless) and antibonding (noded) lowest-lying molecularlike states or the spatial distribution of carriers in the system.[6] In this regard, the asymmetry of the constituent dots (either intrinsic or intentional) has been viewed not as a flaw but as an essential design choice to provide additional control over the system properties.[5,7,8]

Advances in single-dopant fabrication[9–11] and charge detection[12,13] have led atomic scale electronics (particularly the field of quantum computing) to pear increasing attention to another molecular system. Namely, the D_2^+ system, i.e., the system built of two coupled donor impurities in a semiconductor host in which one of the two excess electrons has been ionized. This system encodes the logical information either on the spin or on the charge degrees of freedom of the remaining excess electron.[14–20] Initial proposals relied on spin encoding. However, direct detection of a single spin remains today a major challenge.[21] On the contrary, a fraction of a single electron charge can be easily detected with state-of-the-art single electron-tunneling devices.[12,13] This readout feasibility, together with the relative simplicity for the manipulation of charge degrees of freedom as opposed to spin, has raised interest in charge qubits, where the logical states are represented by the two lowest-lying electron orbital states positioned at the different donors. All the same, the short coherence times of orbital states severely limit the scalability of charge qubits,[16] so that mechanisms enhancing coherence would be desirable.

Studies on confined D_2^+ systems have been recently addressed in the literature.[22–24] Particularly, Kang *et al.*[24] found that the confinement of the D_2^+ system in a spherical QD can greatly enhance the energy differences between the two lowest-lying electron states and more excited states, favoring the identification of the quasi-two-level system required for quantum computation purposes.[25]

Quite a larger amount of work has been done in the study of the electronic structure and related properties of single shallow donors in nanoscale semiconductor heterostructures.[26–28] In addition to the well-known quantum size effect, the influence of the dielectric confinement (coming from the different dielectric response of the QD and the surrounding medium) on the donor levels has been revealed as a particularly noticeable effect in colloidal quantum dots as they are usually synthesized in media with a dielectric response rather different to that of the dot material.[26,29,30]

Prompted by the important role of coupled impurities in nanotechnology, we present in this paper a theoretical study on the molecular properties of a D_2^+ system confined in a spherical quantum dot. We focus on the influence of both the QD size and the dielectric mismatch on the radiative lifetime, the bonding-antibonding energy splitting, and the electron charge distributions in the lowest-lying D_2^+ molecular states, and analyze the dependence of the results on the relative position of the donors inside the quantum dot.

The paper is organized as follows. In Sec. II, we introduce the model employed in the description of the confined double donor system and outline the details of the numerical procedure used to solve the resulting Hamiltonian. The effects of spatial and dielectric confinements on the double donor system are presented and discussed in Sec. III. Conclusions, given in Sec. IV, end the paper.

II. MODEL AND THEORETICAL OUTLINE

The present study is carried out within the framework of the effective-mass and envelope function approximations. Consequently, we employ a macroscopic treatment of Coulombic interactions, and use a parameter, the dielectric con-

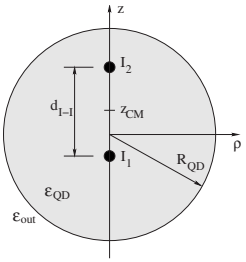

FIG. 1. Schematic representation of the system under study: an electron bound to two shallow donors separated by a distance d_{I-I} within a diameter of a confining spherical QD with radius R_{QD} and dielectric constant ε_{QD} surrounded by a dielectric medium of permittivity ε_{out}. z_{CM} stands for the center of mass of the coupled donors.

stant, to characterize the dielectric response of each material involved. The validity of such a treatment has been well established for both doped and undoped semiconductor heterostructures.[31] Our model consists of a shallow donor pair confined in a spherical quantum dot with dielectric constant ε_{QD}, which is in turn immersed in a dielectric medium with permittivity ε_{out} (see Fig. 1). The corresponding effective-mass Hamiltonian for the bound conduction-band electron reads, in atomic units,

$$H = -\frac{1}{2}\nabla\left(\frac{1}{m^*(\mathbf{r})}\nabla\right) + V(\mathbf{r}) + \phi_s(\mathbf{r}) + \sum_{i=1,2}\phi_c^{I_i}(\mathbf{r},\mathbf{r}_i). \tag{1}$$

The first term on the right-hand side of Eq. (1) is the generalized kinetic-energy operator,[32] which accounts for different electron masses in different materials. $V(\mathbf{r})$ is a steplike function representing the finite spatial confining potential due to the conduction-band offset between the media involved. $\phi_c^{I_i}(\mathbf{r},\mathbf{r}_i)$ stands for the Coulomb potential generated by the impurity located at the fixed position $\mathbf{r}_i$, including the effect of the polarization charges induced at the dot surface as a consequence of the dielectric mismatch between the QD and the surrounding medium. The electron itself also induces polarization charges at the dot boundaries, whose effects are described by the self-polarization potential $\phi_s(\mathbf{r})$. When (as is the case here) a $\varepsilon(\mathbf{r})=\varepsilon(r)$ steplike dielectric function is assumed, ϕ_c and ϕ_s admit analytical expressions.[33]

In order to reduce the number of variables in the study, we fix the QD material parameters close to those of CdS ($\varepsilon_{QD}=5.5$ and $m^*=0.15$) (Ref. 34) unless otherwise indicated. Since we are not dealing with a specific surrounding medium, we will assume a typical depth of $V_0=4$ eV for the QD confining well and an effective mass $m^*=1$ for the external medium. Likewise, we will concentrate on donors which are aligned along an axis of the QD (see Fig. 1), although the conclusions obtained make possible to envisage the trends characterizing other configurations. This facilitates the calculation since the axial symmetry of the system allows us to integrate analytically the angular coordinate of the electron in Eq. (1). Then, to obtain electron energies and wave functions, we carry out an exact (numerical) integration of (ρ,z) coordinates by means of a discretization scheme based on the finite differences method. The explicit expressions of ϕ_c and ϕ_s together with a detailed description of the integration method can be found in Ref. 28.

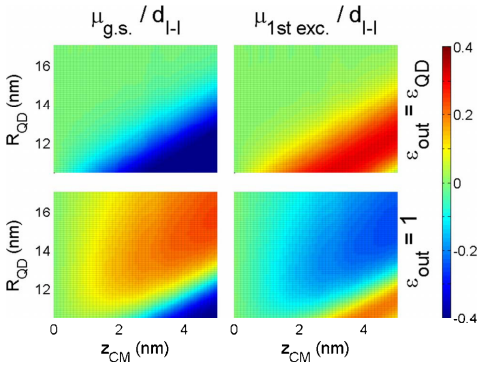

FIG. 2. (Color online) Dipolar moment [Eq. (2)] of the electron charge distribution for a confined D_2^+ system with $d_{I-I}=10$ nm as a function of R_{QD} and the system location in the dot. Left (right) panels correspond to the electron in the ground (first excited) state. In top (bottom) panels the QD is embedded in a $\varepsilon_{out}=\varepsilon_{QD}$ ($\varepsilon_{out}=1$) dielectric medium. The origin has been located at the QD center.

III. RESULTS

We start by investigating the effect of the spatial and dielectric confinements on the electron charge distribution of the double donor lowest-lying states. When the center of mass of the donor pair is not located at the dot center ($z_{CM}\neq 0$, see Fig. 1), the asymmetry of the QD confinement is expected to break the inversion symmetry of these states. To monitor (and quantify) the symmetry breakdown, we calculate the dipolar moment of the corresponding electron charge distributions with respect to z_{CM},

$$\mu = \langle i|\mathbf{r} - z_{CM}\mathbf{u}_z|i\rangle, \tag{2}$$

where $i=1,2$ labels the ground and first excited states of the system. The results are shown in Fig. 2, where μ/d_{I-I} (with $d_{I-I}=10$ nm) is represented for these states as a function of the QD radius and the donors location within the dot. Calculations have been performed for two different surrounding dielectric constants, namely, $\varepsilon_{out}=\varepsilon_{QD}$ (absence of dielectric confinement) and $\varepsilon_{out}=1$ (spatial and dielectric confinements). In the figure, positive values of μ/d_{I-I} indicate that the electron is distributed to a greater extent around the donor closer to the QD border, whereas negative values indicate its preference for the innermost impurity. From the $\varepsilon_{out}=\varepsilon_{QD}$ panels we can observe that the spatial confinement favors the localization of the ground state in the inner donor

and the excited state in the outer one. This trend, more pronounced for low QD radii and large z_{CM} values, is a consequence of the larger destabilization that the potential barrier produces in the surroundings of the outermost impurity. To minimize its energy, the electron in the ground state localizes in the inner donor and, to preserve orthogonality, the excited state concentrates in the outer one. In other words, nonsymmetric spatial confinement brings the homopolar D_2^+ system to behave as heteropolar, leading to the spatial separation of the two lowest-lying electron states.

In the case $\varepsilon_{out}=1$ (lower panels in Fig. 2), we can see that, except for very small dot radii and very large z_{CM} values, the polarity of the states is opposite to that in the absence of dielectric confinement. Now, the ground state localizes the electron density in the outer donor, whereas the inner donor is occupied by the excited state. This effect can be explained as originated by the contribution of the polarization charges induced by the impurities at the QD surface. Impurity off-centering increases the nonhomogeneity of the corresponding induced charge distribution at the dot surface, this lack of homogeneity being responsible for an additional stabilization of off-centered electron locations.[35] As a consequence, the total Coulomb potential is deeper at the position of the donor closer to the surface, so that the ground state distributes preferably around it. Therefore, spatial and dielectric confinements yield opposite spatial separation of the electron states[36] and their interplay will determine the final configuration of the corresponding electron charge distributions in each case.

For a more detailed description of this interplay, in Fig. 3(a) we have depicted μ/d_{I-I} for the same system as in Fig. 2 ($d_{I-I}=10$ nm) but for the particular case of $z_{CM}=5$ nm and a more extended R_{QD} range. For this value of z_{CM}, one of the impurities is located at the QD center, a situation *a priori* easier to be obtained experimentally than any other. In the figure, solid (dashed) curves correspond to the ground (first excited) state. Interestingly, the case of pure spatial confinement ($\varepsilon_{out}=\varepsilon_{QD}$, thin red lines) shows homopolarity for large R_{QD} values, whereas in the presence of dielectric mismatch ($\varepsilon_{out}=1$, thick blue lines) the system behaves as heteropolar. This is a signature of the different length scales in which spatial and dielectric confinements operate and is a consequence of the long range of image charge Coulomb interactions. The different length scales of these confinement sources were already reported by Goldoni *et al.*,[37] who also introduced the concept of remote dielectric tailoring to tune at will exciton-binding energies in semiconductor/insulator hybrid nanostructures.

For intermediate values of R_{QD} [see e.g., $R_{QD}\approx 14$ nm in Fig. 3(a)], where both spatial and dielectric confinement effects are significant, we can observe that the dielectric confinement compensates, and even inverts, the trend imposed by the spatial confinement. Finally, for low R_{QD} values, the spatial confinement dominates and the inner donor is preferred by the ground state in both cases.

The spatial separation of the two lowest-lying electron states is more pronounced as the interdonor distance increases. This is apparent in Fig. 4(a), which corresponds to the same system as in Fig. 3 (with one of the impurities at the dot center) but for $d_{I-I}=15$ nm. In this case, μ/d_{I-I} is

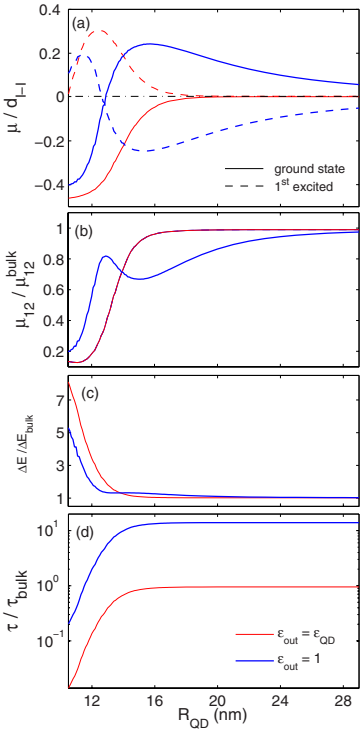

FIG. 3. (Color online) (a) Dipolar moment [Eq. (2)] of the electron charge distribution in the ground (solid lines) and first excited (dashed lines) states of the confined coupled donor system ($d_{I-I}=10$ nm) with one of the impurities located at the QD center as a function of the QD radius. Thick blue lines correspond to $\varepsilon_{out}=1$, whereas thin red lines correspond to $\varepsilon_{out}=\varepsilon_{QD}$ (absence of dielectric confinement). (b) Corresponding transition moments, (c) splitting energies, and (d) first excited-state radiative lifetimes relative to bulk values.

plotted as a function of ε_{out} for two different dot radii, namely, $R_{QD}=20$ and 23 nm. Again, solid and dashed lines are used for the ground and first excited states. As can be observed from the $R_{QD}=20$ nm curves, when $\varepsilon_{out}>\varepsilon_{QD}$ the dielectric confinement magnifies the states spatial separation imposed by the spatial confinement ($\varepsilon_{out}=5.5$). On the contrary, this trend is inverted as ε_{out} diminishes. The bulklike homopolar character is recovered for a given value of ε_{out} (3.9 in this case), compensating the effect of the spatial confinement. Finally, dielectric mismatch effects dominate for low enough values of ε_{out}, yielding again a spatial separation of the lowest-lying molecular states but with opposite polarity.

This evolution can be seen in Fig. 4(d), where the modulus of the wave function $\Psi(\mathbf{r})$ restricted to the azimuthal angle $\phi=0$ is represented for both the ground and first excited states and three different values of the surroundings

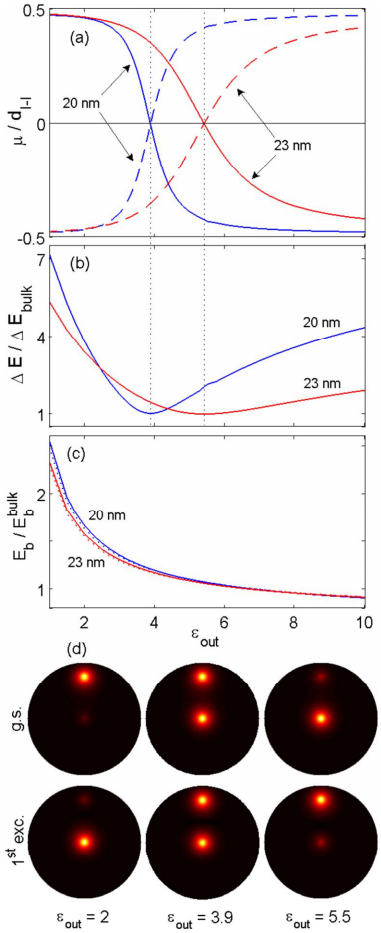

FIG. 4. (Color online) (a) Ground state (solid lines) and first excited-state (dashed lines) dipolar moments for a $d_{I-I}=15$ nm confined D_2^+ system with one donor at the QD center as a function of ε_{out}. Curves are shown for two different QD radii. (b) Splitting energy dependence on ε_{out} for the two QD radii studied. (c) Corresponding ground-state binding energies (solid lines). Curves corresponding to $z_{\text{CM}}=0$ (dotted lines) have been included for comparison. (d) Modulus of the wave function $\Psi(\mathbf{r})$ restricted to the azimuthal angle $\phi=0$ for the same system as above with $R_{\text{QD}}=20$ nm and different values of ε_{out}.

permittivity, i.e., $\varepsilon_{\text{out}}=5.5$ (absence of dielectric confinement), $\varepsilon_{\text{out}}=3.9$ (situation in which the homopolar character is recovered), and $\varepsilon_{\text{out}}=2$ (a typical value of organic capping materials[30]).

The case shown in Fig. 4 for $R_{\text{QD}}=23$ nm represents an additional example of the long range of dielectric effects. While in this case bulk charge distributions are hardly affected by the QD spatial confinement, the proper choice of the QD environment can still yield important changes in the relative electronegativity of the donors and, therefore, in the electron charge distributions.

The energy splitting (ΔE) between the ground and first excited states is also influenced by dielectric and spatial confinements [see Fig. 4(b)]. As derived from the figure, ΔE increases as the spatial separation of the states is more pronounced, presenting a minimum, close to the bulk value, when homopolar conditions are tuned. Contrary to ΔE, the corresponding binding energies[38] (E_b) are negligibly correlated with the spatial separation of the states [see Fig. 4(c)]. This can be derived from the comparison of solid and dotted curves in the figure, which correspond to $z_{\text{CM}}=7.5$ nm (one donor at the QD center) and $z_{\text{CM}}=0$ (symmetric confinement), respectively. Indeed, though both cases present similar E_b values, for $z_{\text{CM}}=0$ the system presents homopolarity regardless of ε_{out}, whereas this is not the case for $z_{\text{CM}}=7.5$ nm. Therefore, E_b is negligibly influenced by the off-centering of the D_2^+ system and then by the spatial separation of the states. Conversely, as expected, E_b is strongly affected by the dielectric environment, undergoing a large increase as ε_{out} decreases.

It is well known that the spatial separation of logic states in charge-based qubit realizations can efficiently reduce the decoherence of the charge degrees of freedom coding the qubit, which makes possible to perform the coherent quantum logic operations at a fairly high ratio.[8] Therefore, confinement is expected to affect coherence in our system. In donor-based charge qubits, decoherence caused by interaction with phonons occurs in time scales that can be made much longer than all other time scales in the problem by choosing an appropriate donor separation.[20] Then, to study how confinement affects decoherence in our system, we will neglect in a first approximation acoustic and optical phonon scattering and will only take into account decoherence coming from vacuum electromagnetic fluctuations (radiative decay).

The radiative decay rate in a spherical quantum dot can be estimated within the dipole approximation by[39]

$$\tau^{-1} = \frac{9\varepsilon_{\text{out}}^{5/2}}{(2\varepsilon_{\text{out}}+\varepsilon_{\text{QD}})^2}\frac{\Delta E^3}{3\pi\varepsilon_0\hbar^4c^3}\mu_{12}, \tag{3}$$

where c is the speed of light in vacuum, ε_0 is the vacuum dielectric constant, τ is the radiative lifetime, and $\mu_{12}=|\langle 1|\mathbf{r}|2\rangle|^2$ is the square of the dipole transition moment between the states $|1\rangle$ and $|2\rangle$, which are in our case the ground and first excited states of the system.

μ_{12}, relative to its value in the absence of spatial and dielectric confinements, is depicted in Fig. 3(b) for the studied system. Again, results for $\varepsilon_{\text{out}}=\varepsilon_{\text{QD}}$ and $\varepsilon_{\text{out}}=1$ are shown. As can be seen in the figure, μ_{12} decreases as the system moves away from homopolar conditions. By inspection of Eq. (3), one could expect that a decrease in μ_{12} would help in increasing the lifetime. However, the dependence of τ^{-1} on ΔE^3 cannot be neglected in this case since, as we showed before, spatial separation of the two lowest-lying states is paralleled by an increase in the transition energy [see Fig. 3(c)]. On balance, the influence of ΔE on the radia-

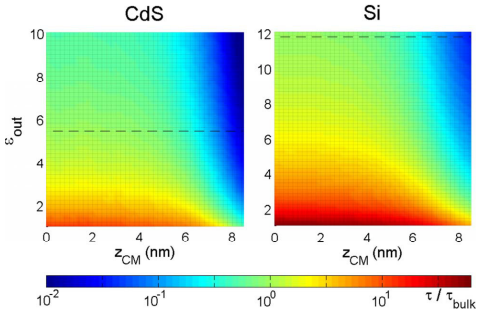

FIG. 5. (Color online) First excited-state radiative lifetime (relative to bulk) for a $d_{I-I}=10$ nm D_2^+ system confined in a $R=14$ nm QD as a function of ε_{out} and the system location within the QD. Host material parameters are similar to those of CdS (left) and Si (right). Dashed lines indicate the absence of dielectric confinement in each case.

tive lifetime is larger than that of μ_{12}. This can be seen in Fig. 3(d), where τ has been represented relative to τ_{bulk}. Referring to the results for $\varepsilon_{out}=\varepsilon_{QD}$ (where only the spatial confinement is influencing the system), we observe that τ drops strongly for small values of R_{QD}, whereas it reaches the bulk value when the spatial separation of the two lowest-lying states disappears and homopolar conditions are recovered.

The results for $\varepsilon_{out}=1$ are more interesting. τ shows a profile similar to that of $\varepsilon_{out}=\varepsilon_{QD}$ calculations but despite spatial separation still persists in the whole range of R_{QD} under study, τ reaches values more than 1 order of magnitude larger than in bulk. The enhancement of τ when the QD is surrounded by a low-dielectric constant medium is a consequence of the influence of local-field effects,[39] which have been observed experimentally through measurements of exciton recombination rates in QDs embedded in apolar solvents with low refractive indices.[30]

The drop of τ for small values of R_{QD} in Fig. 3(d) is induced, in both represented cases, by the spatial confinement through the large increase that it yields on ΔE. This can be confirmed in Fig. 5 (left panel) where the radiative lifetime of our system as a function of ε_{out} and the system location within a $R=14$ nm QD is shown. When the off centering of the donor pair is not much pronounced (low and medium z_{CM} values), the influence of the spatial confinement is negligible and, in the absence of dielectric mismatch, τ keeps close to the bulk value. In these conditions, τ increases noticeably with respect to the bulk as ε_{out} decreases. However, as the donor pair gets closer to the dot surface (large z_{CM} values), the radiative lifetime becomes dominated by the effects of spatial confinement. τ experiences a strong reduction, which is only partially compensated by decreasing ε_{out}.

Finally, to probe the effect of increasing the QD dielectric constant, we have repeated the calculations for QD parameters similar to those of Si ($\varepsilon_{QD}=11.7$ and $m^*=0.26$). The results, shown in the right panel of Fig. 5, evidence that in this case τ may increase up to almost 2 orders of magnitude with respect to the corresponding bulk value.

IV. CONCLUDING REMARKS

We have probed the influence of spatial and dielectric confinements on spontaneous emission rates, energy splittings, and charge-density distributions in the lowest-lying states of a D_2^+ double donor system confined in a spherical quantum dot. We found that asymmetric confinement (produced when the donors are not symmetrically distributed around the QD center) leads the otherwise homopolar donor pair to behave as heteropolar, diminishing the interdonor tunnel coupling and localizing the ground and first excited states in different donors. In this regard, when (as usual) $\varepsilon_{out}<\varepsilon_{QD}$, spatial confinement tends to localize the ground/first excited state in the inner/outer donor, whereas dielectric effects tend to distribute them oppositely. However, these confinement sources operate in different length scales. While in the large dot size regime only dielectric effects influence the D_2^+ system, in the small dot size regime spatial confinement effects dominate. This makes possible to tune the tunnel coupling strength and charge-density distribution in the D_2^+ system at will, by choosing the appropriate dot size and surrounding medium.

We also found that bulk radiative lifetimes are strongly reduced by spatial confinement due to the enhanced splitting energies. On the other hand, when spatial confinement effects are no longer involved (large dot sizes), radiative lifetimes may increase orders of magnitude when the QDs are embedded in low-dielectric constant media.

Summing up, the confinement of the D_2^+ system in a quantum dot provides additional mechanisms to mold its properties; it is worth to notice the spatial distribution of the lowest-lying states, the corresponding energy splittings, and the radiative lifetimes. The (wide range) tuning capability of this last property could be of interest to increase the relatively low bulk coherence times of orbital states in charge qubit realizations.

We close by stressing that confinement might also be useful to improve the performance of optically driven donor-based charge qubit schemes.[17,18] In such schemes, the decoherence caused by the ionization and spontaneous emission of the excited states acting as connecting channels between the logical states could be minimized through the proper choice of QD size and dielectric environment. On one hand, quantum confinement would lift the quasidegeneracy among near-continuum states, increasing the corresponding ionization threshold and excitation selectivity. On the other hand, the employment of low dielectric constant surrounding materials would help in reducing their (otherwise limiting) spontaneous emission rates.

ACKNOWLEDGMENTS

Support from MICINN under Project No. CTQ2008-03344 and Bancaixa under Project No. P1-1B2006-03 is acknowledged.

*josep.planelles@qfa.uji.es

[1] S. A. Wolf, D. D. Awschalom, R. A. Buhrman, J. M. Daughton, S. von Molnár, M. L. Roukes, A. Y. Chtchelkanova, and D. M. Treger, Science **294**, 1488 (2001).
[2] *Nano-optoelectronics: Concepts, Physics and Devices*, edited by M. Grundmann (Springer-Verlag, Berlin, 2002).
[3] A. J. Nozik, Physica E (Amsterdam) **14**, 115 (2002).
[4] B. Bayer, P. Hawrylak, K. Hinzer, S. Fafard, M. Korkusinski, Z. R. Wasilewski, O. Stern, and A. Forchel, Science **291**, 451 (2001).
[5] E. A. Stinaff, M. Scheibner, A. S. Bracker, I. V. Ponomarev, V. L. Korenev, M. E. Ware, M. F. Doty, T. L. Reinecke, and D. Gammon, Science **311**, 636 (2006).
[6] J. R. Petta, A. C. Johnson, C. M. Marcus, M. P. Hanson, and A. C. Gossard, Phys. Rev. Lett. **93**, 186802 (2004).
[7] A. S. Bracker, M. Scheibner, M. F. Doty, E. A. Stinaff, I. V. Ponomarev, J. C. Kim, L. J. Whitman, T. L. Reinecke, and D. Gammon, Appl. Phys. Lett. **89**, 233110 (2006).
[8] X. Q. Li and Y. Arakawa, Phys. Rev. A **63**, 012302 (2000).
[9] J. L. O'Brien, S. R. Schofield, M. Y. Simmons, R. G. Clark, A. S. Dzurak, N. J. Curson, B. E. Kane, N. S. McAlpine, M. E. Hawley, and G. W. Brown, Phys. Rev. B **64**, 161401(R) (2001).
[10] S. R. Schofield, N. J. Curson, M. Y. Simmons, F. J. Ruess, T. Hallam, L. Oberbeck, and R. G. Clark, Phys. Rev. Lett. **91**, 136104 (2003).
[11] T. Shinada, S. Okamoto, T. Kobayashi, and L. Ohdomari, Nature (London) **437**, 1128 (2005).
[12] R. J. Schoelkopf, P. Wahlgren, A. A. Hozhevnikov, P. Delsing, and D. E. Prober, Science **280**, 1238 (1998).
[13] A. Aassime, G. Johansson, G. Wendin, R. J. Schoelkopf, and P. Delsing, Phys. Rev. Lett. **86**, 3376 (2001).
[14] M. J. Calderón, B. Koiller, and S. Das Sarma, Phys. Rev. B **75**, 125311 (2007).
[15] M. J. Calderón, B. Koiller, X. Hu, and S. Das Sarma, Phys. Rev. Lett. **96**, 096802 (2006).
[16] L. C. L. Hollenberg, A. S. Dzurak, C. Wellard, A. R. Hamilton, D. J. Reilly, G. J. Milburn, and R. G. Clark, Phys. Rev. B **69**, 113301 (2004).
[17] A. V. Tsukanov, Phys. Rev. B **76**, 035328 (2007).
[18] L. A. Openov, Phys. Rev. B **70**, 233313 (2004).
[19] B. Koiller, X. Hu, and S. Das Sarma, Phys. Rev. B **73**, 045319 (2006).
[20] S. D. Barrett and G. J. Milburn, Phys. Rev. B **68**, 155307 (2003).
[21] F. H. L. Koppens, C. Buizert, K. J. Tielrooij, I. T. Vink, K. C. Nowack, T. Meunier, L. P. Kouwenhoven, and L. M. K. Vandersypen, Nature (London) **442**, 766 (2006).
[22] B. Li, B. Partoens, F. M. Peeters, and W. Magnus, Phys. Rev. B **79**, 085306 (2009); Microelectron. J. **40**, 446 (2009).
[23] S. Kang, Y. M. Liu, and T. Y. Shi, Eur. Phys. J. B **63**, 37 (2008).
[24] S. Kang, Y. M. Liu, and T. Y. Shi, Commun. Theor. Phys. **50**, 767 (2008).
[25] X. Hu and S. Das Sarma, Phys. Rev. A **61**, 062301 (2000).
[26] R. Tsu and D. Babić, Appl. Phys. Lett. **64**, 1806 (1994).
[27] M. Lannoo, C. Delerue, and G. Allan, Phys. Rev. Lett. **74**, 3415 (1995); G. Allan, C. Delerue, M. Lannoo, and E. Martin, Phys. Rev. B **52**, 11982 (1995); J. M. Ferreyra, P. Bosshard, and C. R. Proetto, *ibid.* **55**, 13682 (1997); B. Li, A. F. Slachmuylders, B. Partoens, W. Magnus, and F. M. Peeters, *ibid.* **77**, 115335 (2008).
[28] J. L. Movilla and J. Planelles, Phys. Rev. B **71**, 075319 (2005); Comput. Phys. Commun. **170**, 144 (2005).
[29] M. Bruchez, Jr., M. Moronne, P. Gin, S. Weiss, and A. P. Alivisatos, Science **281**, 2013 (1998); R. Tsu, Microelectron. J. **34**, 329 (2003).
[30] S. F. Wuister, C. M. Donegá, and A. Meijerink, J. Chem. Phys. **121**, 4310 (2004).
[31] C. Delerue, M. Lannoo, and G. Allan, Phys. Rev. B **68**, 115411 (2003); X. Cartoixà and L. W. Wang, Phys. Rev. Lett. **94**, 236804 (2005); D. Ninno, F. Trani, G. Cantele, K. J. Hameeuw, G. Iadonisi, E. Degoli, and S. Ossicini, Europhys. Lett. **74**, 519 (2006).
[32] D. BenDaniel and C. B. Duke, Phys. Rev. **152**, 683 (1966); P. Harrison, *Quantum Wells, Wires and Dots* (Wiley, Chichester, 2001).
[33] P. G. Bolcatto and C. R. Proetto, J. Phys.: Condens. Matter **13**, 319 (2001).
[34] A. D. Yoffe, Adv. Phys. **50**, 1 (2001).
[35] A thorough analysis of the dependence of the polarization potentials on the impurities off-centering can be found in Ref. 28.
[36] This is true as long as $\varepsilon_{out} < \varepsilon_{QD}$ (the usual situation). When $\varepsilon_{out} > \varepsilon_{QD}$, both sources of confinement favor the localization of the ground state in the inner donor.
[37] G. Goldoni, F. Rossi, and E. Molinari, Phys. Rev. Lett. **80**, 4995 (1998).
[38] The binding energy has been calculated as the difference between the electron ground-state energies in the absence and in the presence of the impurities.
[39] A. Thränhardt, C. Ell, G. Khitrova, and H. M. Gibbs, Phys. Rev. B **65**, 035327 (2002); R. J. Glauber and M. Lewenstein, Phys. Rev. A **43**, 467 (1991).

From quantum dots to quantum wires: Electronic structure of semiconductor nanorods

J. Planelles,[1,*] M. Royo,[1] A. Ballester,[1] and M. Pi[2]
[1]*Departament de Química Física i Analítica, Universitat Jaume I, P.O. Box 224, E-12080 Castelló, Spain*
[2]*Departament ECM, Facultat de Física and IN2UB, Universitat de Barcelona, E-08028 Barcelona, Spain*
(Received 28 May 2009; revised manuscript received 24 June 2009; published 28 July 2009)

The transition bridge between zero-dimensional quantum dots and one-dimensional quantum wires is explored theoretically by means of the construction of the addition energy spectra of nanorods with different lengths. Spin density-functional theory supplemented with full configuration interaction calculations are carried out. The addition energy spectra are qualitatively related to the single particle correlation diagram. The transition from charge-density waves to spin-density waves, characterizing the Wigner crystallization in the low density limit is shown.

DOI: 10.1103/PhysRevB.80.045324 PACS number(s): 73.21.−b, 71.15.Mb, 73.22.Gk, 85.35.Be

I. INTRODUCTION

Nanorods (NRs) constitute the bridge between zero-dimensional quantum dots (QDs) and one-dimensional quantum wires (QWs). Investigations of the transition regime from QDs to QWs are of particular interest in the case of colloidal semiconductor nanocrystrals because size and shape control enables the synthesis of NRs with precise length and diameter,[1] so that by tuning the aspect ratio one can follow the transition from zero- to one-dimensional systems.

By changing the gate voltage attached to a nanocrystal, tunnel conductance and capacitance measures yield a peak every time the number of electrons in the QD increases by one. The spacing of peaks or addition spectrum, reflects differences between the ground states with different number of electrons. This shell filling is a neat manifestation of quantum-mechanical degeneracy. While for large dots containing many electrons, oscillations in the spectrum are periodic because the single-electron charging energy is determined classically by the total dot capacitance, for a dot containing few electrons both, quantum effects reflecting the symmetry of the confining potential and electron-electron interactions, lead to modifications of the oscillations so they are no longer periodic,[2] thus revealing the shell structure of the dot.

Tunneling spectra of single CdSe NRs of radii and lengths ranging between 1.8–3.2 and 11–60 nm, respectively, have been reported.[3] The spectra were measured with the tip at a distance avoiding charging effects. On the basis of a theoretical formalism for QWs, the observed peaks were assigned to low-lying conduction bands with azimultal angular momentum $m_z=0,1,2$, but no discretization of these bands originated from confinement was resolved. Similar InAs NR spectra with not well resolved conduction band states has also been published.[4] Not many experimental addition spectra of short NRs can be found in the literature. Long and wide Si NWs display a uniform peak height and width and equidistant spacing in the current vs gate voltage spectrum[5] while shorter thinner Si NRs show a more irregular spectra,[6] thus revealing a shell structure.

Theoretical understanding of QD addition spectra usually rely on isotropic and anisotropic harmonic confining potentials.[2,6,7] Thus, two-dimensional (2D) harmonic QDs has a 2, 4, 6, 8… degeneracy pattern yielding high peaks in the addition energy spectrum at $N=2,6,12,20\ldots$ electrons,[8] this structure being partially destroyed by elliptical deformation of the QD.[9] On the other hand, the confining potential of a spherical colloidal nanocrystal, typically synthesized by wet chemistry methods, is better represented by a steplike hard wall potential,[10] which corresponds to the band gap difference between neighboring materials. This confining potential yields a 2, 6, 10… degeneracy pattern which shows up at $N=2,8,18\ldots$ electrons. NRs are an elongated variant of colloidal QDs,[1] i.e., may be considered as a QD with a highly anisotropic confining potential, which is resposible for some remarkably strong Coulomb interactions.[11,12] Then, the transition from QD to NR is not only characterized by a symmetry change of the confining potential, but additionally by a transition from strong to weak confinent regime. Monitoring this change of symmetry and confining regime in the addition spectra is the aim of this work. We carry out local spin-density-functional theory calculations supplemented with full configuration interaction (FCI) computations. An interesting 2D model calculation, correlating the addition spectra of squared and rectangular boxes with the same area, shows the abovementioned double transition.[13] Our calculations, which correspond to a truly three-dimensional (3D) NR system of constant section and variable length, display a different addition energy pattern, as it corresponds to different confining potentials, but converges toward qualitative similar profiles in the limit of weak confining regime. In the low-density limit we also find a transition from charge-density waves (CDW) with $N/2$ peaks in the density profile vs the NR axis and preserved spin symmetry to spin-density waves (SDW) with N peaks (Wigner crystallization) and broken spin symmetry.[14] Further, the fully spin polarized state is reached.[15]

II. THEORY

Local spin density functional theory (LSDFT), which has given satisfactory results in the study of related structures,[8,13,18,19] is employed in the present work. Numerical integration of the Kohn-Sham equations is carried out. Details of the method followed are described in Ref. 8. The

exchange-correlation functional is taken as a sum of the Dirac exchange functional of a homogeneous electron gas and the correlation functional parametrized by Perdew and Zunger.[20] The electron effective mass and the dielectric constant, screening the electron-electron interaction, are assumed to be equal to that of the NR bulk material.[21] The confining potential is the same we used in a previous study of NRs,[22] namely, zero within the NR composed by a cylinder of radius R and variable length L, attached to two hemispherical caps of the same radius R, and V^{out} elsewhere. Some FCI calculations are carried out for $N=4,6,8$ electrons and $L=10$ nm, in order to confirm the density profiles obtained with LSDFT. As we will see, in these cases only $m_z=0$ orbitals come into play. Then, we select a basis set of orthogonalized floating spherical Gaussian functions. The original nonorthogonal spherical Gaussian functions $g(\mathbf{r})=e^{-\alpha(\mathbf{r}-\mathbf{R}_i)^2}$ are defined by the exponent α and the position $\mathbf{R}_i$ where they are centered. The exponent α is fitted variationally in a $L=0$ NR (sphere) calculation in which a single Gaussian function is employed. The floating Gaussian functions are centered along the NR axis, equally spaced, so that they saturate the space. The number of Gaussians is increased up to convergence in energy. The same density of Gaussian functions along the NR axis is employed in all calculations. Once the primitive Gaussian functions are established, orthonormalization yielding a new basis set which most closely resemble the original basis functions, i.e., a symmetric orthogonalization employing $S^{-1/2}$, the inverse of the original basis set metrics square root, is carried out.[23] With this orthonormal basis set, the many-body Hamiltonian reads in second quantization language,

$$H=\sum_{pq}^{M} h_{pq}a_p^+a_q+\sum_{pqrs}^{M} g_{pqrs}a_p^+a_q^+a_ra_s, \qquad (1)$$

where a_p^+, a_q are fermion creator and annihilator operators, and h_{pq} and g_{pqrs} the one- and two-electron integrals. Except for the contribution of the potential energy coming from the confining potential to the single-electron integrals, which is calculated numerically, all integrals are computed analytically.[23]

In order to carry out FCI calculations, once the one-electron basis set $\{\phi_p\}_{p=1}^{M}$ is selected, we build all possible N-body Slater determinants $\Phi_\alpha=\det\{\phi_1\phi_2\ldots\phi_N\}$ out of them. In a second step, we project Hamiltonian (1) onto the basis set of Slater determinants yielding matrix elements $\langle\Phi_\alpha|H|\Phi_\beta\rangle$. Finally, we proceed with the diagonalization.

III. RESULTS AND DISCUSSION

We study the electronic structure of CdSe NRs. The geometry, described in the previous section, is defined by the NR radius, fixed to $R=2$ nm, and the length, which we range from $L=0$ up to $L=55$ nm. The material parameters employed are those of the bulk material,[24] namely, effective mass $m^*=0.13$ and dielectric constant $\varepsilon=9.2$. The height of the confining potential is set to $V^{out}=4$ eV.

In Fig. 1 we show the low-lying single particle noninteracting energy (sp) levels obtained within the effective mass approach formalism. We represent sp energy vs NR length L. Dotted lines correspond to orbitals with $m_z=0$, full lines to $m_z=\pm1$ and dashed lines to $m_z=\pm2$. At $L=0$ we can see the typical spherical 1–3–5… degeneracy (2–6–10… including spin). As $L\neq0$, the symmetry reduces from spherical to axial, with just one- and two-dimensional irreducible representations, i.e., with just nondegenerate and twofold degenerate orbitals (degeneration 2 and 4 including spin). In the figure one can also see how very excited $m_z=0$ orbitals at $L=0$ stabilize as L increases, converging toward the lowest conduction band of the infinite wire. This accumulation of $m_z=0$ states looks similar to the formation of Landau bands in the Fock-Darwin energy spectra vs magnetic field. Additionally, despite only two $m_z=\pm1$ and one $m_z=\pm2$ levels are included in Fig. 1, one can envisage the formation of the second conduction band and the bottom of the third one. These bands correspond to the ones observed in Ref. 3. Also, the figure allows us to determine degeneracy/quasidegeneracy vs L, which shows up as peak patterns in the addition energy spectra. Thus, one can foresee that for $L=0$ (sphere) the consecutive electron charging up to $N=20$ yields three strong peaks at 2, 8, and 18 electrons, while in the case of $L=20$ nm a featureless addition energy spectrum will be obtained. As can be seen in Fig. 2, these qualitative trends are fully confirmed by the LSDFT calculations, where exchange and correlation are included. In this figure we represent addition energies $\Delta_2(N)=E(N+1)-2E(N)+E(N-1)$, with $E(N)$ being the ground state total energy of the N-electron NR system, vs the number N of electrons for NRs of different length. From top to bottom, we represent $L=0$ up to $L=22$ nm in steps of $\Delta L=2$ nm. Addition energies are given in eV. However, in order to group all the results within a single figure, the different profiles have been offset 400 meV. For example, addition energies for $L=0$ should be subtracted by an amount of 4.4 eV.

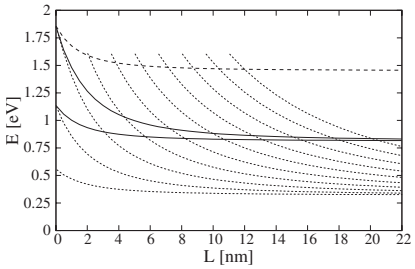

FIG. 1. Energy of the lowest NR sp noninteracting energy levels (eV) vs the NR length L (nm). Dotted, full and dashed lines correspond to orbitals with azimutal quantum number $m_z=0$, $m_z=\pm1$, and $m_z=\pm2$, respectively.

As pointed out above, Fig. 2 qualitatively reproduces the degeneracy pattern observed in Fig. 1. Thus, for $L=0$, in addition to three main peaks at $N=2$, 8, and 18 electrons, which correspond to the filling of the three lowest shells, one can see secondary, less intense, peaks at $N=5$ and $N=13$ electrons, corresponding to half fillings. As shown in Fig. 1, as the NR gets longer, excited $m_z=0$ levels fall below the

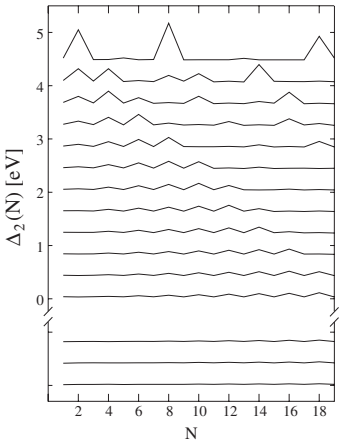

FIG. 2. Addition energy spectra (eV) for NR of increasing length L vs the number N of electrons. Increasingly larger NRs are represented from top to bottom, starting with $L=0$ (spherical QDs) up to $L=22$ nm NR, in steps $\Delta L=2$ nm. The different profiles have been offset 400 meV. The three almost flat profiles at the bottom correspond to the low-density NRs of length $L=40$, 45 and 55 nm.

low-lying $m_z=\pm 1$ one, and occupied orbitals become closer in energy, i.e., the density of states increases. This leads to a change in peak pattern and a general lowering of the addition energies (see Fig. 2). For long NR, e.g., $L=20$ nm, we also see in this figure that the spectrum starts almost flat at low N and wrinkles as this number increases. It is related to a growth in the energy gap between neighboring levels of the $m_z=0$ lowest band as we move toward higher energies, i.e., as we fill the NR with a larger number of electrons (see Fig. 1). For very large L we reach the Wigner crystallization limit and, as expected, an almost flat curve for all N (see bottom of Fig. 2). We will turn our attention to this limit later on in the paper.

Details of the addition spectra vs L can be understood with the help of Fig. 1. For example, as can be seen in this figure, if we fill with $N=18$ electrons an $L=2$ nm NR, we have the following electronic configuration: $0^2\ 0^2\ 1^4\ 0^2\ 1^4\ 2^4$, where the exponents represent the number of electrons filling the orbital whose m_z-modulus is being powered. This configuration will show main peaks at $N=2,4,8,10,14,18$ electrons (filled shells) and secondary peaks at $N=6,12,16$ (half fillings). This result is confirmed in Fig. 2, although this figure also reveals that the peak at $N=18$ does not exist. Coming back to Fig. 1, one can see that at $L=2$ nm there is a quasidegeneration of the first $m_z=\pm 2$ and the fourth $m_z=0$ levels, so that instead of an electronic configuration 2^4 one may think of $(2,0)^4$, which does not yield a main peak in the addition energy spectrum at $N=18$.

As a main result of this set of calculations one may conclude that for CdSe NRs, with a shape ratio larger than 6, the addition energy spectra will become featureless. Since CdSe, with an effective mass of 0.13 and a dielectric constant of 9.2, has an effective Bohr radius of about 3.8 nm, one can foresee that semiconductor materials such as InAs, with effective Bohr radius about ten times larger, will display features revealing a given degeneracy pattern until much larger shape ratios.

We further explore the low-density limit. A comprehensive study on phase diagrams for interacting fermions in one-dimensional periodic potentials[25] brings a description of the electron system in terms of fields representing fluctuations in the spin and charge densities. The existence of localization and magnetic transitions in the low-density limit, have also been reported for infinite[26] and finite[27] wires defined by harmonic confinement potentials. In order to explore here the low-density limit of free standing NRs we calculate the LSDFT ground state of long but finite NRs. The obtained results are summarized in Fig. 3, where total (full thick line), spin up (dashed line), and spin down (dotted line) density profiles vs the NR axis, for NR lengths $L=40$, 45, and 55 nm, and populations $N=4,6,8$ electrons, are represented. For the sake of comparison, results for a short $L=10$ nm NR are also enclosed. In this case, also the total density profile coming from FCI calculations (+) is shown. The reason of these FCI calculations is to confirm the observed concentration of total density distribution toward the ends of the NR. A similar behavior was already noticed in the model calculation of Ref. 13, in which LSDFT calculations were carried out, and contrast with the results in Ref. 27, where the total density is more pronounced at the center, due to the harmonic confinement employed in this last study. The same concentration of total density distribution toward the ends of the NR can also be seen in 16, where CI calculations of an effective one-dimensional (1D) model is performed. In this last calculation, the CI expansion employs the numerical *sp* eigenfunctions of the single-electron Hamiltonian. Provided the recently reported difficulties concerning CI calculations based on *sp* orbitals owing to a lack of saturation of the space along the axis of quasi-1D systems,[12] we have checked the obtained results with FCI calculations, as outlined in the previous section, which employ a basis set ensuring saturation along the NR axis. Comparison in Fig. 3 confirms the observed trend in the density profile of NR given by LSDFT calculations, which is probably related to the minimization of the electron-electron repulsion.

Figure 3 shows that for $L=40$ nm and $N=4$, 6, and 8, the so-called charge-density waves, with $N/2$ maxima in the density profile and same spin up and down density profiles (i.e., with preserved spin symmetry) appear. At $L=45$ nm, the more diluted $N=4$ electron system shows up another phase while less diluted, $N=6$ and 8 electron systems remain in the CDW phase. This phase, referred to as spin-density wave, shows N maxima in the density profile and broken spin symmetry.[14] This corresponds to a Wigner-like crystallization, in which the electrons behave like classical density charge arranged within the NR to avoid each other as much as possible. This phase transition, referred to as spin-Peierls transition, is paralleled by a pronounced increasing of the Fermi gap.[27] We also observe this opening. For example, for $N=6$, the ratio between the occupied bandwidth (energy difference between the lowest and highest occupied levels) and the Fermi gap (energy difference between the highest occu-

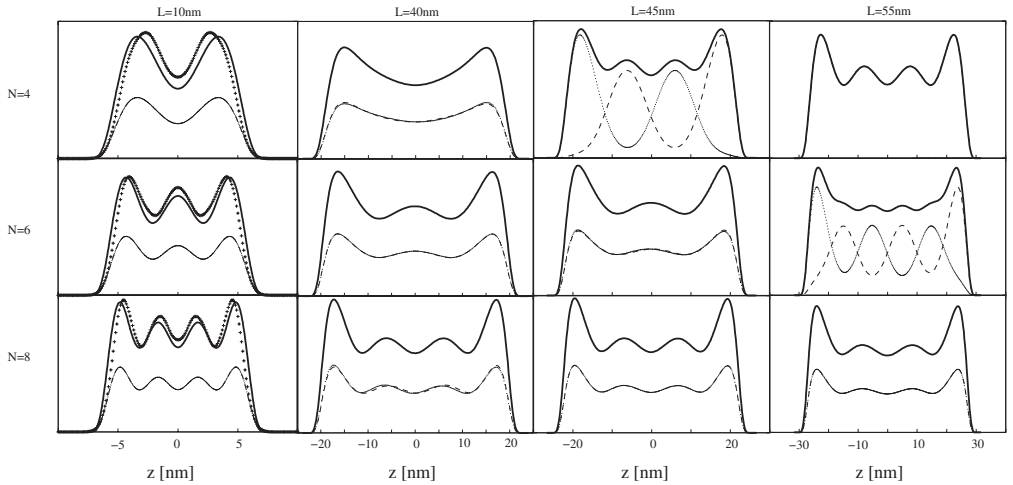

FIG. 3. Electron density profiles along the NR z axis, corresponding to NRs of different lengths L, populated with different number N of electrons. Columns from left to right cover the different lengths: $L=10$, 40, 45, and 55 nm, respectively. From top to bottom rows, increasing number N of electrons, $N=4$, 6, and 8. Total (full thick line), spin up (dashed line), and spin down (dotted line) density profiles are shown. For $L=10$ nm, FCI total density (+) is also enclosed. In those cases in which spin up and down density are equal, dashed and a dotted lines overlap and almost a full thin line profile results.

pied and lowest unoccupied levels) is 1.17 at $L=45$ nm (CDW phase) and 0.51 at $L=55$ nm (SDW phase). At $L=55$ nm the $N=8$ system still remains in the CDW one while the most diluted $N=4$ system undergoes a transition to a fully spin polarized state.[15]

IV. CONCLUDING REMARKS

We have investigated the electronic structure of semiconductor NRs. Most calculations employ LSDFT. A few FCI calculations supporting LSDFT results have been also performed. We study the transition from zero-dimensional QDs, with well defined energy levels, to one-dimensional QWs, with energy bands in one dimension. We monitor this transition with the addition energy spectrum which reveals changes in degeneracy and the increasing role of the electron-electron interactions as L increases. The obtained addition spectra are qualitatively related to the *sp* correlation diagram vs the NR length L. The limit of low-density is explored and the transition from CDW to SDW and, further, to the fully spin polarized phase is shown and discussed.

ACKNOWLEDGMENTS

We wish to thank J. I. Climente for helpful comments. Continuous support from MCINN Projects No. CTQ2008-03344 and No. FIS2008-00421/FIS and UJI-Bancaixa Project No. P1-1B2006-03 is gratefully acknowledged.

*josep.planelles@qfa.uji.es

[1] X. Peng, L. Manna, W. Yang, J. Wickham, E. Scher, A. Kadavanich, and A. P. Alivisatos, Nature (London) **404**, 59 (2000); S. Kan, T. Mokari, E. Rothenberg, and U. Banin, Nature Mater. **2**, 155 (2003).

[2] S. Tarucha, D. G. Austing, T. Honda, R. J. van der Hage, and L. P. Kouwenhoven, Phys. Rev. Lett. **77**, 3613 (1996).

[3] D. Katz, T. Wizansky, O. Millo, E. Rothenberg, T. Mokari, and Uri Banin, Phys. Rev. Lett. **89**, 086801 (2002).

[4] D. Steiner, D. Katz, O. Millo, A. Aharoni, S. Kan, T. Mokari, and U. Banin, Nano Lett. **4**, 1073 (2004).

[5] S. Huang, N. Fukata, M. Shimizu, T. Yamaguchi, T. Sekiguchi, and K. Ishibashi, Appl. Phys. Lett. **92**, 213110 (2008).

[6] K. H. Cho, Y. C. Jung, B. H. Hong, S. W. Hwang, J. H. Oh, D. Ahn, S. D. Suk, K. H. Yeo, D.-W. Kim, D. Park, and W.-S. Lee, Appl. Phys. Lett. **90**, 182102 (2007).

[7] S. M. Reimann and M. Manninen, Rev. Mod. Phys. **74**, 1283 (2002).

[8] M. Pi, A. Emperador, M. Barranco, and F. Garcias, Phys. Rev. B **63**, 115316 (2001).

[9] D. G. Austing, S. Sasaki, S. Tarucha, S. M. Reimann, M. Koskinen, and M. Manninen, Phys. Rev. B **60**, 11514 (1999).

[10] M. Pi, M. Royo, and J. Planelles, J. Appl. Phys. **100**, 073712 (2006); M. Royo, J. Planelles, and M. Pi, Phys. Rev. B **75**, 033302 (2007); J. Planelles, M. Royo, and M. Pi, J. Appl. Phys. **102**, 094304 (2007).

[11] A. Shabaev and Al. L. Efros, Nano Lett. **4**, 1821 (2004); J. I. Climente, M. Royo, J. L. Movilla, and J. Planelles, Phys. Rev. B **79**, 161301(R) (2009).
[12] J. Planelles, J. I. Climente, M. Royo, and J. L. Movilla, J. Phys.: Condens. Matter **21**, 215801 (2009).
[13] E. Räsänen, H. Saarikoski, V. N. Stavrou, A. Harju, M. J. Puska, and R. M. Nieminen, Phys. Rev. B **67**, 235307 (2003).
[14] The spin-symmetry breaking observed in LSDFT is not observed in CI calculations (Ref. 16). An internal-space spin order shows up instead, so that this phase can be identified as the tendency of mean field to mimic such an internal ordering.
[15] The real existence of the fully polarized phase should be taken with caution, in the sense that LSDA generally overestimates exchange and correlation in extremely diluted systems (see, e.g., Ref. 17). In the particular $N=4$, $L=55$ nm case, represented in Fig. 3, one may converge both the fully polarized and the SDW phase. The total energy of the fully polarized ground state is found to be 1.26 eV, just 0.3 meV below the SDW state. Then, owing the abovementioned exchange and correlation overestimation of LSDA in diluted system, the obtained result may be just considered as a signature of attainment of the extremely diluted regime.
[16] B. Szafran, F. M. Peeters, S. Bednarek, T. Chwiej, and J. Adamowski, Phys. Rev. B **70**, 035401 (2004).
[17] F. Pederiva, A. Emperador, and E. Lipparini, Phys. Rev. B **66**, 165314 (2002).
[18] M. Pi, A. Emperador, M. Barranco, F. Garcias, K. Muraki, S. Tarucha, and D. G. Austing, Phys. Rev. Lett. **87**, 066801 (2001).
[19] A. Wensauer, O. Steffens, M. Suhrke, and U. Rössler, Phys. Rev. B **62**, 2605 (2000).
[20] J. P. Perdew and A. Zunger, Phys. Rev. B **23**, 5048 (1981).
[21] Since no specific NR environment is determined, possible polarization effects coming from the dielectric mismatch between the NR and the surrounding medium are disregarded.
[22] F. Rajadell, J. I. Climente, J. Planelles, and A. Bertoni, J. Phys. Chem. C **113**, 11268 (2009).
[23] A. Szabo and N. S. Ostlund, *Modern Quantum Chemistry* (McGraw-Hill, New York, 1989).
[24] U. E. H. Laheld and G. T. Einevoll, Phys. Rev. B **55**, 5184 (1997).
[25] E. B. Kolomeisky and J. P. Straley, Rev. Mod. Phys. **68**, 175 (1996).
[26] K. Kärkkäinen, M. Koskinen, S. M. Reimann, and M. Manninen, Phys. Rev. B **72**, 165324 (2005).
[27] S. M. Reimann, M. Koskinen, and M. Manninen, Phys. Rev. B **59**, 1613 (1999).

Mixed correlation phases in elongated quantum dots

A. Ballester,[1] J. M. Escartín,[2] J. L. Movilla,[1] M. Pi,[2] and J. Planelles[1,*]
[1]*Departament de Química Física i Analítica, Universitat Jaume I, P.O. Box 224, E-12080 Castelló, Spain*
[2]*Departament ECM, Facultat de Física, IN2UB, Universitat de Barcelona, E-08028 Barcelona, Spain*
(Received 13 May 2010; published 7 September 2010)

It is theoretically shown, within the local spin-density-functional theory framework, that inhomogeneous confining potentials in elongated, diluted *N*-electron quantum dots may lead to the formation of mixed phases in which some regions of the *N*-electron system behave like a Fermi liquid while, simultaneously, other, more dilute regions display quasiclassical Wigner crystallization. The characterization of the mixed phases in the addition energy spectrum and the infrared response is reported. An infrared sensor of electron filling is suggested.

DOI: 10.1103/PhysRevB.82.115405 PACS number(s): 73.21.−b, 71.15.Mb, 73.22.Gk, 85.35.Be

I. INTRODUCTION

In 1934 Wigner[1] predicted that, below a critical electron density, the electron gas crystallizes and forms a lattice of electrons arranged in precise classical configurations. This is due to the fact that the kinetic energy becomes negligible relative to the Coulomb energy so that correlations dominate the electronic structure. Many classical electron configurations in quantum dots (QDs) have been reported up to date (see, e.g., Refs. 2 and 3), and classical rotational and vibrational models have shown quantitative agreement with quantum-mechanical treatments.[4,5] All the same, Wigner crystals in QDs do not actually consist of classical pointlike electrons but of quantum electrons having finite extension, which is of relevance for the properties of these crystals. It should be mentioned that, in addition to their intrinsic theoretical interest, these strongly correlated states are of technological significance, e.g., because of their potential use in nanoscale systems for the implementation of qubits and quantum logic gates in quantum computers.[6]

Many studies show that the quantum melting proceeds through intermediate, partially melted Wigner molecular states. Quantum melting is the transition from an ordered strongly correlated Wigner crystal to a Fermi liquid, i.e., to a system of weakly interacting particles where the kinetic energy dominates the Coulomb repulsion. This melting is induced by an increase in the confining potential strength. Thus, in the case of *N* electrons confined in a 2D parabolic trap, we first face an angular melting, yielding a radially ordered crystal, and a further radial melting finally yields the Fermi liquid.[7–9] Similar behavior is observed in a three-particle Wigner molecule confined in a 2D torus, the melting of which proceeds through an intermediate state that can be described as a delocalized electron plus a rigid two-particle Wigner molecule.[10] In the case of *N*-electron quasi-one-dimensional systems, the Wigner phase is characterized by a density profile with *N* peaks regularly spaced along the axial direction. The transition to the Fermi liquid goes through an intermediate phase, called charge-density wave (CDW),with $N/2$ peaks in the density profile.[2,11–13] This phase may also be considered as a partially melted Wigner molecule.

In contrast, crystallization processes in the presence of highly inhomogeneous potentials seem to have attracted much less attention. On the one hand, Wigner crystallization in the presence of an attractive defect was considered, albeit briefly, by Szafran *et al.*[14] They studied a quasi-one-dimensional QD populated with $N=2$ and $N=3$ electrons and perturbed by a steplike defect potential localized at the center of the system. In the absence of the defect, their configuration-interaction (CI) study reveals that the number of maxima equals the number *N* of electrons, as corresponds to Wigner molecules. After switching on the defect, three charge maxima in the electron-density profile arise in both cases. They conclude then that the influence of the central attractive potential showed to be qualitatively different for $N=2$ and $N=3$ electrons. While for the even case the defect potential destroys the Wigner crystallization, yielding an extra maximum, for $N=3$ it simply enhances the localization of the central electron. Also, incidentally, in Fig. 10 of Appendix B in Ref. 15, a representation of the electron densities corresponding to a Hartree-Fock calculation of a strictly one-dimensional box with a double-well-like potential profile is displayed. An interesting feature emerges in this picture, which is only briefly referred to in the figure caption. Namely, the represented state show a low-density crystal-like central region surrounded by a high-density liquidlike one.

In general, Wigner molecules are associated with weak-confinement regimes. However, it has been reported[16] that the presence of the narrow, deep self-polarization potential coming from the dielectric mismatch at the QD border in free standing small spherical two-electron nanocrystals may induce the formation of surface states. These states concentrate the electronic density within the narrow, deep well at the QD surface, i.e., are in the strong-confinement regime and, nevertheless, show an angular Wigner type of localization.[16]

Finally, the effect of the effective electron-mass anisotropy on the Wigner phase formation has also been explored.[17] The study is motivated by the fact that effective electron-mass anisotropy may occur in semiconductor materials. The authors theoretically explore a 2D system and conclude that anisotropic electrons require larger spacing to form Wigner lattices.

In a recent paper,[13] we theoretically studied, within the local spin-density-functional theory (LSDFT), the electronic structure of nanorods (NRs), elongated QDs which constitute the bridge between zero-dimensional QDs and one-

dimensional quantum wires (QWs), and monitorized the Wigner crystallization in the addition energy spectra. Note that, by changing the gate voltage attached to a nanocrystal, tunnel conductance and capacitance measures yield a peak every time the number of electrons in the QD increases by one. The spacing of peaks, or addition spectrum, reflects differences between the ground states with different numbers of electrons and can be used to monitorize localization-delocalization transitions in QDs.[18] Additionally, calculated electron-density profiles nicely displayed the phase transition found in the low-density limit, from CDW, with $N/2$ peaks in the density profile and preserved spin symmetry, to spin-density waves (SDW), with N peaks (Wigner crystallization) and broken spin symmetry.[19] The LSDFT calculation was supported with a few CI calculations. We would like to stress that investigations on the transition regime from QDs to QWs are of particular interest in the case of these colloidal, elongated semiconductor nanocrystrals because size and shape control enables the synthesis of NRs with precise length and diameter[20] so that one can follow the transition from zero- to one-dimensional systems by tuning their aspect ratio.

To the best of our knowledge, except in the above mentioned, strictly one-dimensional Hartree-Fock calculation by Mueller,[15] no new phases produced by perturbing potentials or anisotropic effective masses have been reported to date. In the present paper we will show that inhomogeneous confining potentials may lead to the formation of new phases in truly three-dimensional systems, driven by an uneven electronic-density distribution, in which some regions of the N-electron system behave like a Fermi liquid while, simultaneously, other more dilute regions display the typical quasiclassical Wigner distribution of the charge maxima in the electron-density profile. Hereafter we will refer to these phases as mixed phases (MPs). We will show that one can get a MP by applying an electric field along the longitudinal axis of a dilute NR. Nowadays, though, there is another way to modify the NR confining potential which we will show renders better defined MPs than those produced by an external electric field. It is the chemical synthesis of nanodumbbells (NDs).[21–23] Nanodumbbells are NRs of a given material sandwiched between two-end spherical caps of a different material. Then we first will look for MPs in nanodumbbells, i.e., MPs produced by structural effects. Afterwards, we will study MPs in diluted NRs subject to an electric field along the NR axis. Also, we will pay attention to the way of probing MPs, in particular, the addition spectrum and the infrared response.

II. THEORY AND MODELS

LSDFT, also referred to as local spin-density-approximation (LSDA), which has given satisfactory results in the study of related structures,[12,24–26] is employed in the present work. Numerical integration of the Kohn-Sham (KS) equations is carried out. Details of the method followed are described in Ref. 24. The exchange-correlation functional is taken as a sum of the Dirac exchange functional of a homogeneous electron gas and the correlation-functional parametrized by Perdew and Zunger.[27]

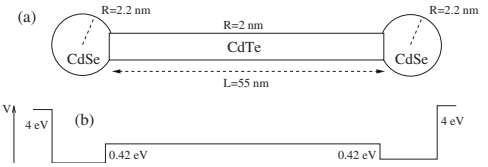

FIG. 1. (a) Schematic geometry of the nanostructures under study. (b) Schematic profile of the spatial confining potential along the z axis.

In addition to the ground-state calculations, we also compute the spin- and charge-density responses within the framework of time-dependent LSDFT.[28] In order to obtain the dipole strength in the spin and density channels, we study the time evolution, following an initial perturbation, of the dipole signal $\mathcal{D}(t)=\mathbf{n}\cdot\langle\mathbf{D}\rangle$, where $\mathbf{D}=\Sigma_j\mathbf{r}_j$ for density-dipole modes and $\mathbf{D}=\Sigma_j\mathbf{r}_j\sigma_j^z$ for spin-dipole modes, $\langle\cdot\rangle$ means expected value in the time-dependent state, and $\mathbf{n}$ is the unit vector pointing toward the direction given by the polarization of the incident electromagnetic wave. To calculate $\mathcal{D}(t)$, we first solve the static LSDA KS equations, and the appropriate static solutions of the KS equations are then used as initial conditions for solving the time-dependent KS equations,

$$i\hbar\frac{\partial}{\partial t}\Psi_\sigma(\mathbf{r},t)=\mathcal{H}_{\mathrm{KS}}[\rho_\uparrow(\mathbf{r},t),\rho_\downarrow(\mathbf{r},t)]\Psi_\sigma(\mathbf{r},t). \quad (1)$$

In order to describe the interaction of the system with an external dipole field, the ground-state single-particle (sp) wave functions are slightly excited initially according to $\Psi'_\sigma(\mathbf{r},0)=U\Psi_\sigma(\mathbf{r},0)$, with $U=\exp(ik\mathbf{n}\cdot\mathbf{r})$ for the density-dipole modes and $U=\exp(ik\eta_\sigma\mathbf{n}\cdot\mathbf{r})$, where $\eta_\sigma=+1(-1)$ for $\sigma=\uparrow(\downarrow)$, for the spin-dipole modes. The wave number k is taken small enough to keep the response of the system within the linear regime, in which the Fourier transform of the dipole signal, $\mathcal{D}(\omega)=\int e^{i\omega t}\mathcal{D}(t)dt$, is directly related to the dipole strength, $S_{\mathbf{n}}(\omega)=\frac{1}{k}\mathrm{Im}[\mathcal{D}(\omega)]$. Hence, a frequency analysis of $\mathcal{D}(t)$ provides the absorption energies and their respective intensities (see details in Refs. 28 and 29).

Unless otherwise stated, we study Wigner crystallization and MPs in CdTe NRs and CdSe/CdTe/CdSe NDs. The NR is modeled by a cylinder of radius $R=2$ nm and length $L=55$ nm, and the ND is built by attaching two $R=2.2$ nm radius spherical caps to this NR, as depicted in Fig. 1. A twofold reason leads us to choose these materials. On the one hand, they are materials employed nowadays in many syntheses of elongated nanocrystals,[21–23] and, on the other hand, they have very similar effective masses and dielectric constants, but they have a rather large band offset so that no relevant effects coming from effective mass and/or dielectric constant inhomogeneities will mask those coming from an inhomogeneous confining potential derived from the band offset. The uniform electron effective mass, $m^*=0.13$, and dielectric constant, $\epsilon=9.2$, employed in our models are those of bulk material.[30] We assume the 0.42 eV CdSe/CdTe conduction-band offset[31] as confining barrier height between

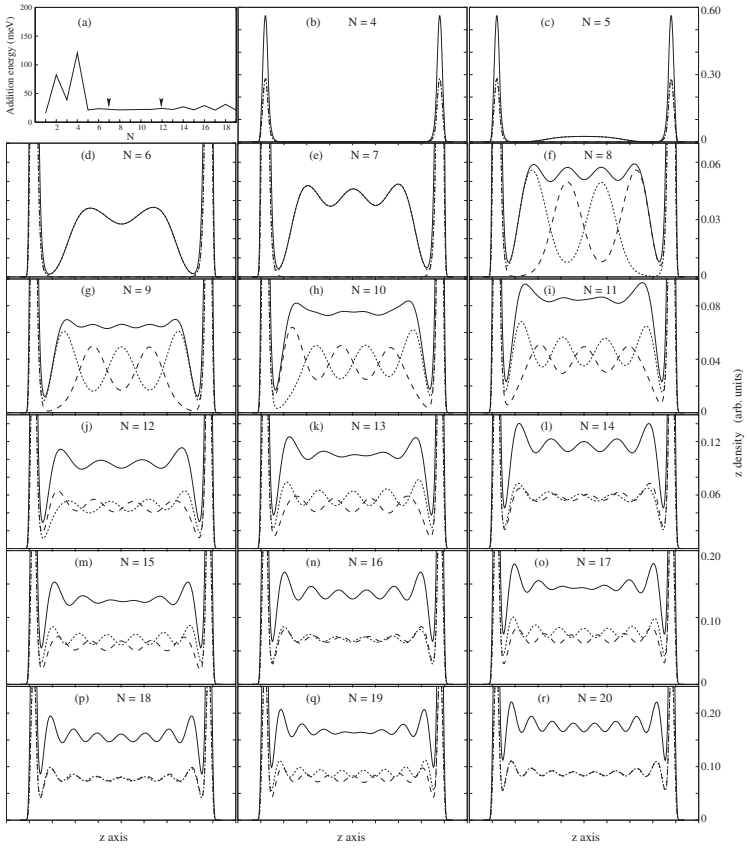

FIG. 2. (a) Addition energy spectrum of the studied nanodumbbell (cylinder of $R=2$ nm radius and length $L=55$ nm, ended with two $R=2.2$ nm radius spherical caps). [(b)–(r)] Ground state z-density profiles of this nanodumbbell populated with 4 up to 20 electrons, respectively. Solid line: total charge density. Dotted/dashed line: spin up/down density. Panels (d)–(r): density profiles have been cut to better display it in the ND trunk region.

these materials. Since no specific QD environment is determined, we assume a typical 4 eV confining QD-environment barrier (see Fig. 1).

III. RESULTS AND DISCUSSION

We first study the electronic structure of CdSe/CdTe/CdSe NDs. The geometry, material parameters, and confining potential are those described in the previous section. The geometry has been selected to show the gradual appearance of the different phases.

In Fig. 2(a) we show the addition energy spectrum of this ND, i.e., the energy $E_{\mathrm{add}}(N)=U(N+1)-2U(N)+U(N-1)$, where $U(N)$ is the total energy of the N-electron system ground state. As stated in Sec. I, this magnitude, analogous to the electron affinity in atomic physics, quantifies the relative stability of the N-particle system and can be measured experimentally as a function of N. It constitutes a key quantity that characterizes transport into the nanostructures.

In order to theoretically obtain this spectrum, the more rigorous, but computationally very demanding, exact diagonalization could be attempted. In practice, unfortunately, this heavy method can only be applied to few-electron systems. Larger systems require less-demanding methods, such as the DFT here employed. The practical limitations of this method come from the not exactly known exchange-correlation potential but general experience is that DFT results are quite reliable,[32] and they have substantially contributed to an understanding of QD addition spectra.[2,33]

The addition energy profile, see Fig. 2(a), shows a peak at $N=2$ electrons corresponding to a half filling of the first $\ell_z=0$ shell, and a second, larger peak at $N=4$ electrons, corresponding to the complete filling of this shell. Up to $N=4$

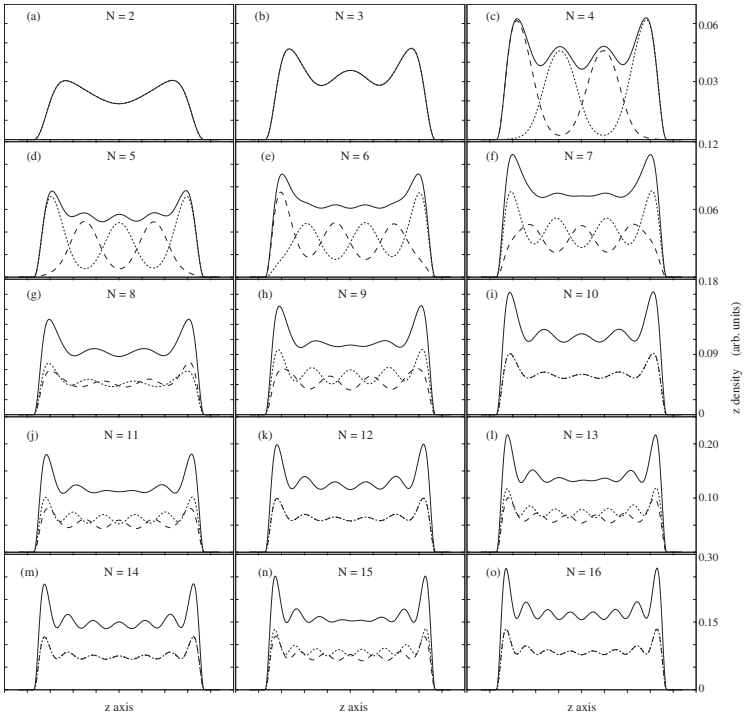

FIG. 3. Ground state z-density profiles of the studied nanorod (cylinder of $R=2$ nm radius and length $L=55$ nm) populated with 2 up to 16 electrons, respectively. Solid line: total charge density. Dotted/dashed line: spin up/down density.

electrons the density is completely localized within the ND spherical caps, as can be seen in Fig. 2(b), where the ground-state z-density profile, i.e., $\rho(z)=\int\rho(r,z,\phi)dS$, of the ND populated with $N=4$ electrons is represented. As can be seen, for $N=4$, the electronic spin-up density (dotted line) equals the electronic spin-down density (dashed line), adding up to the total density [solid line in Fig. 2(b)].

After filling the ND with $N=4$ electrons, the addition energy profile shows a flat region. It corresponds to the filling of sp wave functions localized in the ND cylinder. Thus, Fig. 2(c) shows how the fifth electron with spin up (dotted line) fills a sp localized at the central region of the cylinder. Figures 2(d) and 2(e) show the z-density profile of the ND populated with $N=6$ and $N=7$ electrons. We see that in both cases four electrons are filling the spherical caps at the ND ends (we have checked that the integration of the charge density within the caps regions yield four electrons). Figures 2(d) and 2(e) also reveal that, within the cap regions, the electronic spin-up density (dotted line) equals the electronic spin-down density (dashed line), i.e., the total spin density is zero. On the other hand, the central cylinder shows full spin polarization with the spin-up density showing two (three) peaks and the spin-down profile showing a zero height. The real existence of the fully polarized phase should be taken with caution, in the sense that LSDA generally overestimates exchange and correlation in extremely diluted systems (see, e.g., Ref. 34). The same behavior takes place when removing the two ND caps, thus yielding a cylindrical NR and filling it with $N=2$ and $N=3$ electrons, [see Figs. 3(a) and 3(b)]. Furthermore, in the particular $N=6$ and $N=7$ ND cases, the total energy of the fully polarized ground state is found to be very close to the SDW state. Then, due to the above-mentioned exchange and correlation overestimation of LSDA in diluted system, the obtained result may be just considered as a signature of attainment of the extremely diluted regime. Also, it reveals the achievement of a MP in which four electrons are filling the caps forming a Fermi liquid[35] and the rest jump into the central cylinder forming a dilute phase. Another interesting feature of these two pictures, Figs. 2(d) and 2(e), is that the electrons at the cylinder are quite wavy, i.e., they behave like quantum electrons having finite extension and partially overlapping.

When an extra electron is added into the ND, in addition to the Fermi liquid in the caps at the ND ends, a nice central SDW emerges, i.e., a typical Wigner crystallization with N peaks and broken spin symmetry[19] [see Fig. 2(f)]. However, the addition energy spectrum remains flat, as corresponds to the filling of extremely diluted systems [see region after the left vertical arrow in Fig. 2(a)]. In this case, the overlap between neighbor electrons with the same spin is nearly

zero, as can be seen in Fig. 2(f), where the density profile of a given spin goes down to zero as the opposite spin-density profile reaches a maximum.

As we keep filling the ND with electrons, from $N=8$ up to $N=11$, the scenario does not change. The addition energy spectrum remains flat and the previously described MP, with Fermi liquid within the caps at the ND ends and SDW at the central cylinder, remains. However, as the number of electrons increases, they become wavier, in the sense that the overlap between neighbor electrons with the same spin starts to increase (the density profile of a given spin starts being no longer negligible at the places where the opposite spin-density profile reaches its maxima).

When the ND is filled with $N=12$ electrons, i.e., the central cylinder is populated with $N=8$ electrons, the number of maxima in the central cylinder is reduced to four, i.e., one half of the number of electrons in the trunk, as corresponds to a CDW phase. As pointed out in Sec. I, this phase arises when the density of electrons starts rising up, but it is still too low as to form a Fermi liquid. In a typical CDW, the electronic spin-up density equals the electronic spin-down one so that the corresponding profiles are superposed. However, this is not exactly the case in Fig. 2(j), which better seems a phase in between CDW and SDW. As far as the addition energy spectrum is concerned, the transition from SDW to CDW is monitorized by the end of a completely flat profile and the appearance of typical shell-filling features in the spectrum.

A typical CDW phase in the central cylinder is obtained when filling the ND with $N=14$, 16, 18, and 20 electrons [see Figs. 2(l), 2(n), 2(p), and 2(r)]. However, the odd fillings, i.e., $N=13$, 15, 17, and 19 electrons, lead to density profiles similar to that of the above-mentioned ND filled with $N=12$ electrons, where the maxima of the electronic spin-up density do not completely occur at the positions of the maxima of the electronic spin-down one so that the corresponding profiles do not completely match [see Figs. 2(k), 2(m), 2(o), and 2(q)].

This intriguing feature characteristic of the low diluted, odd-populated ND is also reproduced in the low diluted odd-populated NRs. It can be seen in Fig. 3, where the ground state z-density profiles of a NR built of a cylinder of $R=2$ nm radius, $L=55$ nm length, and populated with 3 up to 16 electrons, respectively, are displayed. This asymmetry between the spin-up and -down density profiles may come from the different self-consistent potentials appearing in the spin-up and spin-down KS equations.

Since the MPs seem to come from inhomogeneous confining potentials, we explore next the possibility of producing MPs by means of the application of an external electric field. To this end, we apply an external electric field along the z axis of the above mentioned $R=2$ nm radius and $L=55$ nm length NR. Several electric field intensities and NR populations are considered. As expected, the neat separations of the two phases found when inhomogeneity comes in the confining potential so that steplike potentials act upon the system cannot be seen when applying an electric field. As an example, we show in Fig. 4 the ground-state z-density profiles of a NR populated with $N=6$ electrons and subject to a 20 kV/cm electric field along the z axis. Three different

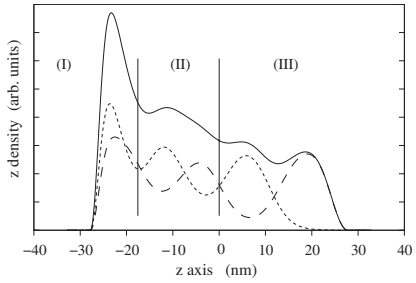

FIG. 4. NR ground state z-density profiles (the NR is modeled by a cylinder of $R=2$ nm radius and $L=55$ nm length) populated with $N=6$ electrons, subject to a 20 kV/cm electric field along the z direction. Solid line: total charge density. Dotted/dashed line: spin up/down density.

regions, labeled (I), (II), and (III) in the figure, can be distinguished in this profile. While region (III) looks like a typical SDW (Wigner crystallization) with as many peaks as electrons and broken spin symmetry, region (I) looks like a CDW with a number of peaks half the number of electrons. Finally, region (II) displays an intermediate feature. On the one hand, we can see broken spin symmetry with the maximum of the spin-up(-down) density arising at the position of the minimum of the spin-down(-up) density. On the other hand, the number of peaks is half the number of electrons.

We conclude that the presence of inhomogeneity may lead to the formation of MPs, and that structural inhomogeneities, i.e., steplike potentials coming from spatial confinement, yield the more neat MPs.

Next we explore the infrared response. Our system feels a strong radial confinement and thus the responses in the directions perpendicular to the symmetry axis of the nanostructure (transverse response), both to spin- and charge-density oscillations, arise in the high-energy region so that no peaks are found in the low-energy region of the spectrum. We enclose in Fig. 5 the transverse spin- and charge-density responses of the studied ND populated with $N=4$ [no electrons in the central cylinder, see Fig. 2(b)], $N=8$ [four electrons yielding a SDW in the central cylinder, see Fig. 2(f)], and $N=16$ [12 electrons yielding a CDW in the central cylinder, see Fig. 2(n)]. Also, the transverse spin- and charge-density responses of the NR populated with $N=4$ [yielding a SDW, see Fig. 3(c)] and $N=12$ [yielding a CDW, see Fig. 3(k)] are also enclosed in the figure for the sake of comparison.

Figure 5 reveals that the spin responses of all studied NDs have a strong peak at 450 meV which is absent in the NRs. We may associate this peak to transverse oscillations of the electrons in the ND caps. The NDs with more than four electrons show a second strong spin peak at higher energies (474 meV for $N=16$ and 483 meV for $N=8$, the latter displaying a second weaker transition at an energy a bit higher than 485 meV, see Fig. 5). Also the partner NRs (those populated with $N=4$ and $N=12$) show this strong spin peak, and it also happens that the more diluted system shows the response at a higher energy and has a second weaker transition at a bit higher energy (482 meV for $N=12$ and 492 and 494

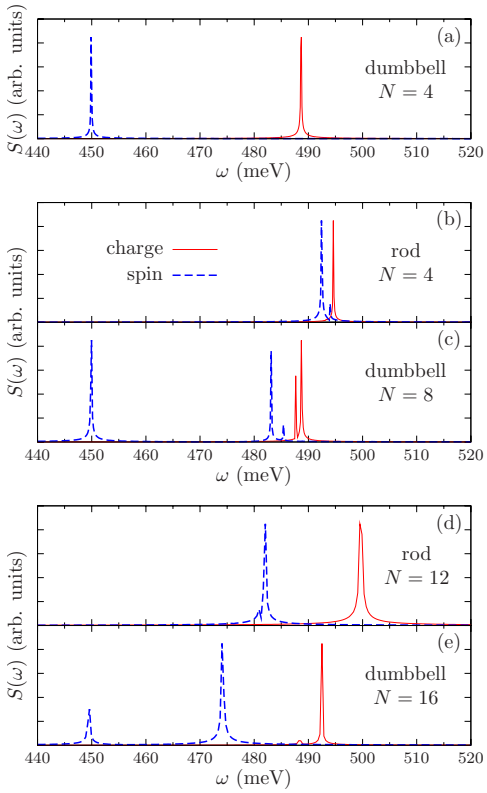

FIG. 5. (Color online) Spin-density (dashed lines) and charge-density (solid lines) transverse responses (arb. units) of different NRs and NDs. Geometry and electron population are indicated at each of the panels. Panels (b) and (c), on the one hand, and (d) and (e), on the other hand, correspond to the same number of electrons in the central cylinder (4 and 12, respectively).

meV for $N=4$). We may associate this peak to transverse-spin oscillations of the electrons in the ND cylinder and in the NR, respectively. The charge-density response arises between 487 and 500 meV, being distributed among one or two peaks for all five cases studied. Therefore, we conclude that, as expected, the transverse-spin and -charge responses do not show any fingerprint of dilute (Wigner) electronic distributions. In fact, the transitions associated to the cylinder appear at energies higher than those related to the cap, as the cylinder radius is smaller than that of the caps, thus just revealing a higher (radial) confinement.

Let us consider next the longitudinal or axial response. Figure 6 collects the low [Figs. 6(a)–6(e)] and high [Figs. 6(f)–6(j)] energy parts of the spin- and charge-density responses for the different NDs and NRs studied. As far as the high-energy part of the response concerns, we can see that for all studied ND populations the spectra have a series of regularly spaced peaks within the 160–800 meV range with a smooth envelope, the spacing between consecutive peaks slightly increasing with energy [see Figs. 6(f), 6(h), and 6(j)]. For the $N=4$ ND these peaks take all the strength for both spin- and charge-density responses [see Fig. 6(f)]. For the other two studied NDs, with $N=8,16$, the strengths of these high-energy peaks are one or more orders of magnitude smaller than those of the peaks arising at low energies—that we are going to describe next [see Figs. 6(h) and 6(j), respectively]. These peaks, absent in NRs [see Figs. 6(g) and 6(i)], can therefore be associated with the confinement in the ND caps.

Finally, we turn our attention toward the low-energy range of the longitudinal response. On the one hand, we can see in Figs. 6(e) and 6(d) that both the $N=16$ electron ND and the $N=12$ electron NR concentrate almost all the strength of their charge-density response in respective single peaks at approximately 21 meV. The same happens to their spin-density response, appearing respective single peaks between 7 and 8 meV. On the other hand, the spin response of the $N=8$ electron ND and its corresponding $N=4$ electron NR partner [see Figs. 6(c) and 6(b), respectively] arise quite fragmented in this low-energy part of the spectra. Furthermore, and in contrast with the other cases, the spin peaks appear at energies higher than those of the charge-density peaks. It is remarkable the close similarity in the response (fingerprint) of the $N=16$ ND and its $N=12$ NR partner, on the one hand, and that of the $N=8$ ND and its $N=4$ NR partner, on the other hand. Finally, the $N=4$ ND has not a single peak in this low-energy region of the spin- and charge-density responses [see Fig. 6(a)].

In general, the charge-density response emerges at energies higher than those of the spin-density response, due to the fact that the Coulomb repulsion exceeds the attraction associated with the spin and coming from the exchange-correlation term in the KS Hamiltonian. The observed feature in the systems with Wigner localization ($N=8$ ND and $N=4$ NR) seems to come from the fact that the maxima of the densities of both spins lie apart from each other forming the Wigner molecules. All the same, these spin peaks arising at energies higher than those of the charge-density might not correspond to a genuine spin response, due to the relevant local magnetization of the system, and may correspond to the so-called acoustic modes.[36]

In summary, we do have some elements allowing (i) to distinguish NDs from NRs in the transverse-spin response, (ii) to discriminate whether ND electrons are exclusively located in the caps or also in the central trunk (longitudinal high-energy response and presence or absence of peaks in its low-energy range), and finally (iii) to detect the Wigner phase in the ND trunk or in the NR: spectra fragmentation and absence of spin response at energies lower than those of the charge-density one (acoustic modes).

IV. CONCLUDING REMARKS

In the present paper we have shown that inhomogeneous confining potentials may lead to the formation of mixed phases, driven by an uneven electronic-density distribution,

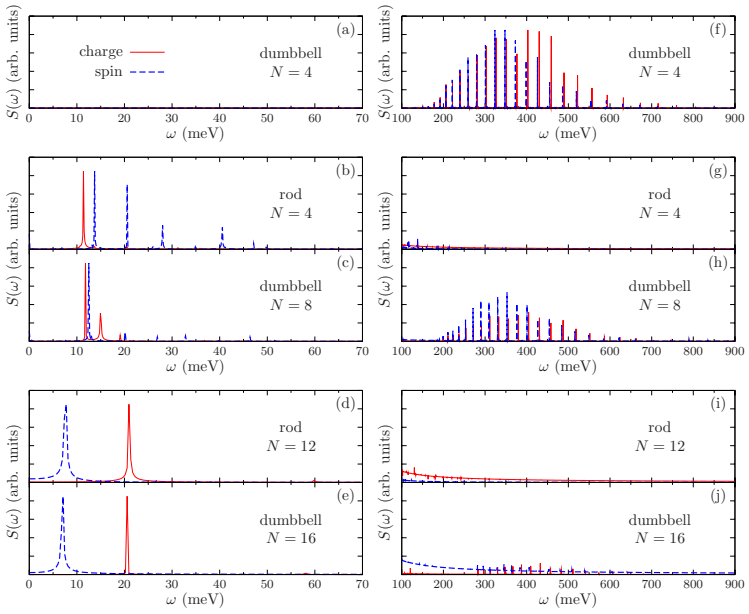

FIG. 6. (Color online) Low-energy (left column) and high-energy (right column) spin-density (dashed lines) and charge-density (solid lines) axial responses (arb. units) of different NRs and NDs. Geometry and electron population are indicated at each of the panels and both are the same for every row of panels. Grouped panels correspond to the same number of electrons in the central cylinder. Responses are magnified two orders of magnitude in panels (g)–(j) with respect to their corresponding low-energy responses in panels (b)–(e).

in which some regions of the *N*-electron system behave like a Fermi liquid while, simultaneously, other more dilute regions display the typical quasiclassical Wigner distribution of the charge maxima in the electron-density profile, either CDW or proper SDW. Furthermore, we have shown the characterization of MPs in the addition spectrum and the infrared response. Finally, we would like to stress that beyond its intrinsic theoretical interest, MPs may be useful in the design of optoelectronic devices. For example, the low-energy axial infrared response of a ND attached to a gate, the voltage of which is changing to fill the ND with electrons, may be used as an infrared sensor of electron filling, since once the caps are full of electrons and the next one jumps into the trunk, an abrupt low-energy infrared sign is emitted.

ACKNOWLEDGMENTS

Continuous support from MCINN under Projects No. CTQ2008-03344 and No. FIS2008-00421, UJI-Bancaixa under Project No. P1-1A2009-03, and Generalitat de Catalunya under Project No. 2009SGR1289 are gratefully acknowledged. A.B. and J.M.E. acknowledge the support from the Spanish FPI (MCINN), FPU (ME) programs, respectively.

*josep.planelles@qfa.uji.es

[1] E. P. Wigner, Phys. Rev. **46**, 1002 (1934).
[2] S. M. Reimann and M. Manninen, Rev. Mod. Phys. **74**, 1283 (2002).
[3] C. Yannouleas and U. Landman, Rep. Prog. Phys. **70**, 2067 (2007).
[4] J. P. Nikkarila and M. Manninen, Solid State Commun. **141**, 209 (2007).
[5] P. A. Maksym, Phys. Rev. B **53**, 10871 (1996).
[6] S. Weiss, M. Thorwart, and R. Egger, Europhys. Lett. **76**, 905 (2006).
[7] A. V. Filinov, M. Bonitz, and Yu. E. Lozovik, Phys. Rev. Lett. **86**, 3851 (2001).
[8] M. Bonitz, P. Ludwig, H. Baumgartner, C. Henning, A. Filinov, D. Block, O. Arp, A. Piel, S. Kading, Y. Ivanov, A. Melzer, H. Fehske, and V. Filinov, Phys. Plasmas **15**, 055704 (2008).
[9] S. M. Reimann, M. Koskinen, M. Manninen, and B. R. Mottelson, Phys. Rev. Lett. **83**, 3270 (1999).
[10] Z. A. Németh and J.-L. Pichard, Europhys. Lett. **58**, 744 (2002).
[11] M. Koskinen, M. Manninen, and S. M. Reimann, Phys. Rev.

Lett. **79**, 1389 (1997).
[12] E. Räsänen, H. Saarikoski, V. N. Stavrou, A. Harju, M. J. Puska, and R. M. Nieminen, Phys. Rev. B **67**, 235307 (2003).
[13] J. Planelles, M. Royo, A. Ballester, and M. Pi, Phys. Rev. B **80**, 045324 (2009).
[14] B. Szafran, F. M. Peeters, S. Bednarek, T. Chwiej, and J. Adamowski, Phys. Rev. B **70**, 035401 (2004).
[15] E. J. Mueller, Phys. Rev. B **72**, 075322 (2005).
[16] J. L. Movilla, J. Planelles, and W. Jaskolski, Phys. Rev. B **73**, 035305 (2006).
[17] X. Wan and R. N. Bhatt, Phys. Rev. B **65**, 233209 (2002).
[18] N. B. Zhitenev, M. Brodsky, R. C. Ashoori, L. N. Pfeiffer, and K. W. West, Science **285**, 715 (1999).
[19] The spin-symmetry breaking observed in LSDFT is not found in CI calculations (Ref. 14). An internal-space spin order appears instead so that this phase can be identified as the tendency of mean field to mimic such an internal ordering.
[20] X. Peng, L. Manna, W. Yang, J. Wickham, E. Scher, A. Kadavanich, and A. P. Alivisatos, Nature (London) **404**, 59 (2000); S. Kan, T. Mokari, E. Rothenberg, and U. Banin, Nature Mater. **2**, 155 (2003).
[21] L. Carbone, S. Kudera, C. Giannini, G. Ciccarella, R. Cingolani, P. D. Cozzoli, and L. Manna, J. Mater. Chem. **16**, 3952 (2006).
[22] F. Shieh, A. E. Saunders, and B. A. Korgel, J. Phys. Chem. B **109**, 8538 (2005).
[23] J. E. Halpert, V. J. Porter, J. P. Zimmer, and M. G. Bawendi, J. Am. Chem. Soc. **128**, 12590 (2006).
[24] M. Pi, A. Emperador, M. Barranco, and F. Garcias, Phys. Rev. B **63**, 115316 (2001).
[25] M. Pi, A. Emperador, M. Barranco, F. Garcias, K. Muraki, S. Tarucha, and D. G. Austing, Phys. Rev. Lett. **87**, 066801 (2001).
[26] A. Wensauer, O. Steffens, M. Suhrke, and U. Rössler, Phys. Rev. B **62**, 2605 (2000).
[27] J. P. Perdew and A. Zunger, Phys. Rev. B **23**, 5048 (1981).
[28] M. Pi, F. Ancilotto, E. Lipparini, and R. Mayol, Physica E **24**, 297 (2004).
[29] A. Puente and Ll. Serra, Phys. Rev. Lett. **83**, 3266 (1999).
[30] Since no specific NR (ND) environment is determined, possible polarization effects coming from the dielectric mismatch between the NR (ND) and the surrounding medium are disregarded.
[31] Ch. H. Wang, T. T. Chen, Y. F. Chen, M. L. Ho, Ch. W. Lai, and P. T. Chou, Nanotechnology **19**, 115702 (2008).
[32] J. Kainz, S. A. Mikhailov, A. Wensauer, and U. Rössler, Phys. Rev. B **65**, 115305 (2002).
[33] M. Pi, D. G. Austing, R. Mayol, K. Muraki, S. Sasaki, H. Tamura, and S. Tarucha, in *Trends in Quantum Dots Research*, edited by P. A. Ling (Nova Science, New York, 2005); D. G. Austing, S. Sasaki, K. Muraki, Y. Tokura, K. Ono, S. Tarucha, M. Barranco, A. Emperador, M. Pi, and F. Garcias, in *Nano-Physics & Bio-Electronics: A New Odyssey*, edited by T. Chakraborty, F. Peeters, and U. Sivan (Elsevier, New York, 2002).
[34] F. Pederiva, A. Emperador, and E. Lipparini, Phys. Rev. B **66**, 165314 (2002).
[35] Since only two electrons fill a cap, one cannot actually distinguish a Fermi liquid from a CDW. In both cases only a peak arises in the density profile. However, we have checked that when the same electronic density is obtained by filling with four electrons a (larger) spherical QD a Fermi liquid results.
[36] O. Mayrock, S. A. Mikhailov, T. Darnhofer, and U. Rössler, Phys. Rev. B **56**, 15760 (1997); O. Mayrock, S. A. Mikhailov, O. Steffens, and U. Rössler, Physica E **1**, 232 (1998).

Configuration interaction approach to Fermi liquid–Wigner crystal mixed phases in semiconductor nanodumbbells

A. Ballester,[1] J. L. Movilla,[1] J. M. Escartín,[2,3] M. Pi,[4] and J. Planelles[1,a)]
[1]*Departament de Química Física i Analítica, Universitat Jaume I, Box 224, E-12080 Castelló, Spain*
[2]*CNRS, UMR 5152, 31062 Toulouse Cedex 4, France*
[3]*Laboratoire de Physique Théorique, IRSAMC, Université de Toulouse, UPS, 31062 Toulouse Cedex 4, France*
[4]*Departament ECM, Facultat de Física, and IN2UB, Universitat de Barcelona, E-08028 Barcelona, Spain*

(Received 8 May 2012; accepted 20 June 2012; published online 20 July 2012)

Full configuration interaction calculations demonstrate the existence of mixed correlation phases in truly three-dimensional elongated nanocrystals subject to inhomogeneous spatial confining potentials. In such phases, the electron density behaves like a Fermi liquid in some regions, while, simultaneously, other more dilute regions display the typical quasi-classical Wigner distribution. The present results confirm and strengthen previous local spin-density functional theory predictions [Ballester *et al.*, Phys. Rev. B **82**, 115405 (2010)]. Additionally, simulation of the in-plane and *z*-polarized modes of the absorption spectra reveals the different correlation regimes occurring in these systems. © *2012 American Institute of Physics*. [http://dx.doi.org/10.1063/1.4737774]

I. INTRODUCTION

Semiconductor quantum dots (QD) have been an active field of research in chemistry, materials science, and solid state physics over the last decades.[1] The interest of these structures arises from their atomic-like behavior, i.e., discrete energy spectrum and finite number of confined carriers, along with the possibility of tuning their behavior artificially by changing the dimensions and the composition of the dots. This flexibility has made it possible to investigate systems with atomic-like response in physical regimes, which are unattainable for natural atoms. The gain in basic science this has brought about has allowed researchers to envisage new technological devices, which were inconceivable a few years ago. The practical development of these devices, in turn, has opened new theoretical and experimental challenges.

Dependence of nanocrystal properties on size and shape has been investigated, thanks to successful control of growth during experimental synthesis.[2] In particular, colloidal elongated quantum dots are of theoretical interest due to their anisotropic spatial confinement. These nanosystems represent the transition from spherical to rod-like shape with a preferential growth direction. The relaxation of the spatial confinement along the longitudinal direction leads to a weak confinement regime, in which the electronic correlations may play an important role. As a consequence, anisotropic shape confers different properties to nanorods as compared to their spherical counterpart. Thus, depending on the dimensions of nanorods, the band gap[3] and the optical properties[4] are modified.

In addition to size and shape, heterogeneous composition introduces new structural effects. Nowadays, mixed-semiconductor heterostructures are synthesized[5] with precise shapes. In particular, CdSe/CdTe heterojunctions yield structures composed of a nanorod sandwiched between two spherical caps. This structure is referred to as nanobarbell or nanodumbbell (ND)[6] and presents an inhomogeneous confining potential and promising technological applications.[7]

Among the exotic physical regimes difficult to attain in natural atoms but straightforwardly reachable in artificial heterostructures, we may mention the Wigner crystal. In 1934 Wigner predicted that, below a critical electron density, the electron gas crystallizes and forms a lattice of electrons arranged in precise classical configurations.[8] This is due to the fact that the kinetic energy becomes negligible relative to the Coulomb energy so that correlations dominate the electronic structure. Many classical electron configurations in artificial structures have been reported up to date (see, e.g., Refs. 9 and 10). In contrast, crystallization processes in the presence of highly inhomogeneous potentials seem to have attracted much less attention.[11–13]

In a recent paper,[14] local spin-density functional theory (LSDFT) calculations demonstrated the existence of mixed phases (MPs) in CdSe/CdTe/CdSe NDs, driven by the inhomogeneous spatial confining potentials. In a MP the electron density behaves like a standard Fermi liquid in some regions while, simultaneously, other more dilute regions display the profile of a typical Wigner crystal.

In this article, we carry out full configuration interaction (FCI) calculations of the ground and lowest-lying excited states of many electrons confined in a CdSe/CdTe/CdSe ND. We identify the formation of MPs in the ground states, thus confirming and reinforcing the previous results obtained at the LSDFT level. Additionally, we carry out the simulations of absorption spectra to find out fingerprints and thus probe the different correlation regimes occurring in the MPs of these systems.

II. THEORY AND MODELS

We study MPs in CdSe/CdTe/CdSe NDs. The ND model is built by attaching two $R = 2.2$ nm radius spherical

a)Author to whom correspondence should be addressed. Electronic mail: josep.planelles@qfa.uji.es.

CdSe caps to the tips of a CdTe cylinder of radius $R=2$ nm and length $L=55$ nm, as depicted in Fig. 1. We have previously studied this system at the LSDFT level and found the existence of MPs in the system.[14] A twofold reason leads us to choose the employed materials. On the one hand, they are materials used nowadays in many syntheses of elongated nanocrystals,[5,6,15] and, on the other hand, they have a rather large band offset but very similar effective masses and dielectric constants, so that no relevant effects coming from effective mass and/or dielectric constant inhomogeneities will mask those coming from an inhomogeneous confining potential derived from the band offset. The isotropic and uniform electron effective mass, $m^*=0.13$, and dielectric constant, $\epsilon=9.2$, employed in our models are those of bulk material.[16] We assume the 0.42 eV CdSe/CdTe conduction band offset[17] as the confining barrier height between these materials, and set the origin of energies at the bottom of the CdTe conduction band. Since no specific QD environment is determined, we assume a typical 4 eV confining QD-environment barrier (see Fig. 1).

The Hamiltonian (in a.u.) of an electron confined in this ND reads as follows:

$$\hat{h}_i=-\frac{1}{2m^*}\nabla_i^2+V_i^c \tag{1}$$

with V_i^c standing for the spatial confining potential (see Fig. 1(b)). Therefore, the many-electron Hamiltonian for the system results

$$\hat{H}=\sum_{i=1}^{N}\hat{h}_i+\sum_{i<j}^{N}\frac{1}{\epsilon}\frac{1}{|\mathbf{r}_i-\mathbf{r}_j|}, \tag{2}$$

where N is the number of electrons.

The many-electron Hamiltonian equation (2) is solved variationally by means of a FCI approach. To this end, we employ the CI code available at the address given in Ref. 18. In order to carry out the FCI calculation, one first has to select a given finite M-dimensional one-electron basis set $\{\phi_p\}_{p=1}^{M}$ and then build all possible N-body Slater determinants $\Phi_i=\det\{\phi_1\phi_2\ldots\phi_N\}$ out of them. In a second step, the projection of Hamiltonian (2) onto the basis set of Slater determinants is carried out, yielding matrix elements $\langle\Phi_i|\hat{H}|\Phi_j\rangle$ (one may eventually select a subset of spin- and symmetry-adapted configurations, thus yielding smaller matrices to diagonalize). The last step is the diagonalization. For practical purposes, the one-electron basis set is generally taken orthogonal. Our orbital choice is the set of single-particle (SP) states, i.e., the eigenfunctions of the one-electron Hamiltonian (1), which we compute by first integrating $\hat{h}_i$ using a finite differences scheme, and then diagonalizing the resulting matrices with the implicitly restarted Arnoldi iterative method.[19] Since we must select a finite basis set, the natural choice is the M lowest-energy eigenvectors. Actually, in our system the lowest-energy part of the single-electron spectrum has a null ($l_z=0$) z-component of the angular momentum, i.e., many s ($l_z=0$) SP states lie energetically below the first p ($l_z=\pm1$), and higher angular momentum states are much more excited. Then, we employ a $2-n-2$ basis set in the FCI calculations, i.e., a basis set including the n lowest-lying s and the lowest-lying degenerate pair of p orbitals (both p_{+1} and p_{-1} orbital pairs), these orbitals making, in all studied cases, a negligible contribution to the ground and lowest-lying excited states. In practice, we have checked that, in order to describe the low-lying energy part of the many-electron system, setting $n=10$ is more than enough (e.g., the results for the 4-electron system—both the energy and the relevant components of the low-lying eigenvectors—are almost identical employing either $n=10$ or $n=14$ s orbitals). With the eigenvectors obtained, we also simulate the low-lying part of the absorption spectrum. To this end, we calculate, within the dipole approximation, the $0\rightarrow K$ charge transition probability from the ground state Ψ_0 to the state Ψ_K (both of them expressed as linear combinations of the many-electron basis set of Slater determinants $\{\Phi_i\}$). These transitions, related to the density dipole modes, preserve the spin of the system, and the corresponding transition probability is given by

$$\left|\mathbf{k}\cdot\left\langle\Psi_0\left|\sum_{i=1}^{N}\mathbf{r}_i\right|\Psi_K\right\rangle\right|^2, \tag{3}$$

where $\mathbf{k}$ is the polarization vector of the incident electromagnetic radiation.

We also simulate the spin transition probability (spin dipole modes, implying spin changes). The corresponding transition probability reads

$$\left|\mathbf{k}\cdot\left\langle\Psi_0\left|\sum_{i=1}^{N}\eta_{\sigma_i}\mathbf{r}_i\right|\Psi_K\right\rangle\right|^2, \tag{4}$$

where $\eta_\sigma=+1(-1)$ for $\sigma=\uparrow(\downarrow)$ and, as above, $\mathbf{k}$ defines polarization. For both, density and spin dipole modes, we

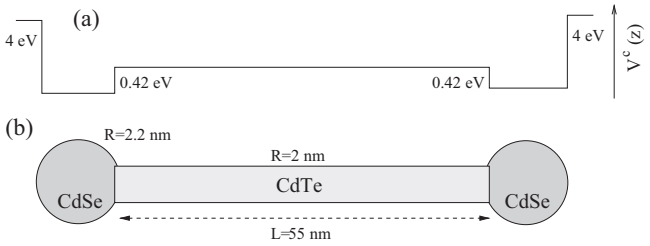

FIG. 1. (a) Schematic profile of the spatial confining potential along the z axis for the nanostructures under study sketched in (b).

consider in-plane ($\mathbf{k} \perp \hat{\mathbf{z}}$) and z ($\mathbf{k} \parallel \hat{\mathbf{z}}$) polarizations. The in-plane polarization transition changes the z-component of the total angular momentum ($\Delta L_z = \pm 1$), while z-polarization preserves it ($\Delta L_z = 0$). Our simulations assume a low temperature of the system ($T = 1$ K, i.e., 0.1 meV approximately). We assume the Boltzmann thermal distribution $p_i(T) = \frac{g_i}{g_0} e^{-\Delta E_i / k_B T}$ for the initial-state occupation at temperature T, with $g_i(g_0)$ as the degeneracy factor of the state Ψ_i (ground state), ΔE_i the energy difference between Ψ_i and the ground state, and k_B the Boltzmann constant. We then use an intermediate normalization, i.e., the ground-state occupation is always set to one.

III. RESULTS AND DISCUSSION

We first study the electronic structure of the ground state of CdSe/CdTe/CdSe NDs whose geometry, material parameters, and confining potential are described in Sec. II. The z profiles of the lowest-lying orbitals are represented in Fig. 2. Such profiles are obtained by integrating the in-plane coordinates of the corresponding orbital. From this figure one can see that the two lowest-lying orbitals, that are quasi-degenerate, are mostly localized within the two spheres of the ND, while the more excited orbitals expand their density in the central cylinder, with a negligible density in the spheres. The preferential localization of the density along the ND can be rationalized from the orbital energies. Thus, while the energy $\varepsilon(s_1) \approx \varepsilon(s_2)$ is 0.489 eV, close to the barrier height (0.42 eV), the energy $\varepsilon(s_3) = 0.737$ eV is already much higher and, since orbitals must be orthogonal, the localization of s_1 and s_2 in the spheres pushes the rest of orbitals towards the long central cylinder, their orbital energies being close ($\varepsilon(s_4) = 0.740$ eV, $\varepsilon(s_5) = 0.744$ eV,…, $\varepsilon(s_{10}) = 0.794$ eV). As for the p orbitals of possible interest, the two lowest-lying orbitals with $l_z = \pm 1$ have also their density concentrated within the spheres and have a very excited energy: $\varepsilon(p_1) \approx \varepsilon(p_2) = 0.963$ eV.[20] And, in a similar way to s orbitals, also p_i, $i > 2$ expand their density in the central cylinder, with a negligible density in the spheres and have an orbital energy much higher than those of the two lowest-lying p orbitals: $\varepsilon(p_3) = 1.218$ eV, $\varepsilon(p_4) = 1.220$ eV, $\varepsilon(p_5) = 1.225$ eV, etc. Then, the contribution of the Slater determinants that include these p orbitals to the ground and low-lying many-electron states is foreseeably negligible, as the calculations confirm.

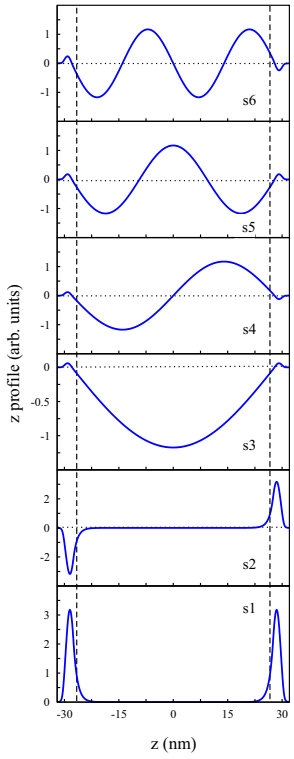

FIG. 2. z profiles of the six lowest-lying $l_z = 0$ orbitals corresponding to the ND whose geometry is depicted in Fig. 1. Vertical dashed lines indicate the boundaries between the rod and the caps of the ND.

Next, we calculate the ground state of the ND populated with $N = 4$, 6, and 8 electrons by means of the FCI methodology. Several $2 - n - 2$ basis sets are employed, and the results indicate that a 2-10-2 basis set already saturates the required Hilbert space.

In the $N = 4$ case, the dominant configuration is $s_1^2 s_2^2$ with a weight larger than 99% (99.6% with the 2-10-2 basis and 99.5% with the 2-14-2 basis). This means that electronic correlation is small and that our system is in the so-called strong confinement regime, as corresponds to the electrons within the spheres. The z-profile of the total density and spin-up density (same as spin-down one) is represented in Fig. 3(a). It shows two strong maxima, one in each spherical cap, and a negligible density in the central cylinder, just a small penetration tail into the cylinder barrier. The integration of the density in each cap amounts to nearly 2, as corresponds to two electrons in each cap. The lack of fine details modulating the profile of the two density peaks denotes the low level of correlation between the electrons populating each cap.[14] We may refer to this configuration as a Fermi liquid phase, i.e., a system of weakly interacting particles where the kinetic energy dominates over the Coulomb repulsion.

We next increase the number of electrons in the ND up to $N = 6$. In this case, the ground state dominant configuration is $s_1^2 s_2^2 s_3^2$ with a weight of only 64%. As pointed out above, orbitals s_1 and s_2 are energetically separated from the rest of orbitals, and their electronic densities are concentrated within the spherical caps. On the other hand, s_3 has an orbital energy close to many other orbitals s_i, $i > 3$, all of them with densities concentrated within the central cylinder (see Fig. 2). The closeness of orbital energies of many orbitals s_i, $i > 2$, explains the relevant contributions to the ground state of many excited configurations $s_1^2 s_2^2 s_i^2$, $i > 3$ and $s_1^2 s_2^2 s_i s_j$, where either $i > 3$ or i and $j > 3$, and therefore the fact of a high electronic correlation. The z-profile of the total density and spin-up density is represented in Fig. 3(b). It shows two strong maxima, one in each spherical cap, and additionally a pair of maxima in the central cylinder. The

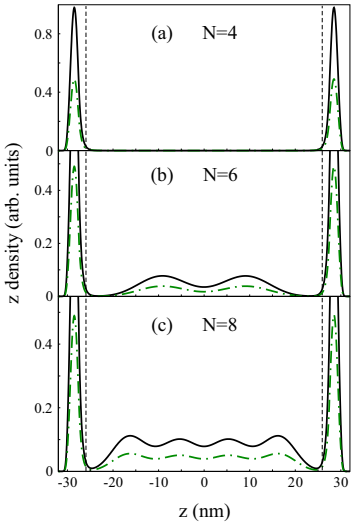

FIG. 3. (a) 4-electron ND z-density profiles: total density (full line) and spin-up density (dot-dashed line). The spin-down density has the same profile as the spin-up one. (b) 6-electron ND z-density profiles. (c) 8-electron ND z-density profiles. In the case of $N = 6$ and $N = 8$, the density profiles have been cut to better display spin-density-waves in the ND central region. Vertical dashed lines indicate the boundaries between the rod and the caps of the ND.

integration of the density in each cap is nearly 2, as corresponds to two electrons in each cap and two electrons in the central cylinder. Thus, while the *pair* of electrons in each cap displays a density profile with a single maximum (Fermi liquid), the *pair* in the cylinder displays a twofold maximum, as correspond to a strongly correlated Wigner crystal, i.e., a phase where the Coulomb repulsion dominates. We are thus in front of a phase with a mixed situation, i.e., a MP. In these truly three-dimensional systems, the inhomogeneous confining potential along the z axis leads to the formation of a phase characterized by an uneven electronic-density distribution, in which some regions of the many-electron system behave like a Fermi liquid while, simultaneously, other more dilute regions display the typical quasi-classical Wigner distribution of the charge maxima in the electron-density profile. Due to the relatively long cylinder length, the quantum effects coming from the longitudinal confinement are negligible. Then, electron-electron interactions dominate over the kinetic energy, and a high correlation regime is achieved. In order to minimize the energy of the system, electrons localize in an ordered way, resembling quasi-classical particles along the central cylinder.

Finally, we consider the case with $N=8$ electrons. The ground state dominant configuration is now $s_1^2 s_2^2 s_3^2 s_4^2$ with a weight of only 58%, which means high correlation regime. However, as in the case of $N=6$, we are actually dealing with a MP, as is revealed by the z-density profiles shown in Fig. 3(c). In this case, the density profile integrates around 4 within the central cylinder and shows four maxima, while integrates around 2 in each cap, where a single maximum is displayed. The overall obtained results confirm and strengthen the previous ones obtained at the LSDFT level.[14]

We complete our study with the simulation of some absorption spectra. As stated in Sec. II, our computations assume a temperature $T=1$ K, consider in-plane and longitudinal polarizations, and include density and spin dipole modes. For axially symmetric systems, the transition probability equations (3) and (4) lead to the following selection rules: $\Delta L_z = \pm 1$ for in-plane polarization and $\Delta L_z = 0$ for longitudinal or z polarization.

The in-plane polarization transitions are well defined and highly energetic. They are displayed in Fig. 4 for the case of $N=4$ and $N=6$ electrons. As we can see, the spectra of $N=4$ and $N=6$ are very similar. In the $N=4$ case, it includes a single peak at 538 meV that can be fairly described as a superposition of nearly degenerate $s_1 \rightarrow p_1$ and $s_2 \rightarrow p_2$ SP absorptions. In the $N=6$ case, the electron correlation is quite more relevant, and the orbital description is at most qualitative. However, we may say that the strong peak arising at 535 meV [see Fig. 4(b)] mainly corresponds to $s_1 \rightarrow p_1$ and $s_2 \rightarrow p_2$ SP transitions too (transitions $s_{i>2} \rightarrow p_1$ or p_2 are almost forbidden due to the negligible orbital overlaps associated). The second peak at 544 meV is weak and can be qualitatively ascribed to a mixture of SP transitions, involving $s_1 \rightarrow p_1$, $s_2 \rightarrow p_2$, $s_1 s_3 \rightarrow s_4 p_1$, etc. The reason for the similarity of the in-plane spectra despite the different correlation regimes of the $N=4$ and $N=6$ systems traces back to the fact that s_1, s_2, p_1, and p_2 orbitals are concentrated in the caps, while s_i, $i > 3$, orbitals are basically confined within the cylinder. Interestingly, the spin and charge modes are almost degenerate (see Fig. 4). It comes from the fact that configurations $s_2 p_2$ and $s_1 p_1$ are almost degenerate and that, due to the confinement of the orbitals s_1, s_2, p_1, and p_2 within the caps (see Fig. 1), the bielectronic integrals[21] $J_1 = (s_1 s_1 | p_1 p_1) \approx J_2 = (s_2 s_2 | p_2 p_2)$ and $K_1 = (s_1 p_1 | p_1 s_1) \approx K_2 = (s_2 p_2 | p_2 s_2)$, amount almost to the same than $(s_1 s_2 | p_1 p_2)$ and $(s_1 p_1 | s_2 p_2)$, respectively. Then, the configurations interaction yields a quasidegeneracy of the singlet and triplet final states.[22]

The z-polarized spectra of $N=6$ and 8 electrons in the ND are collected in Fig. 5. These are the most interesting

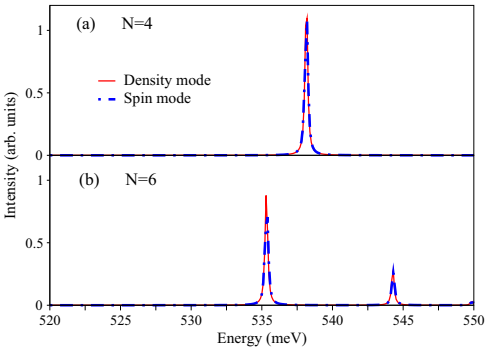

FIG. 4. Simulation of the in-plane polarized spectra for (a) $N = 4$ and (b) $N = 6$ electrons in the ND. Full (dot-dashed) lines represent density (spin) modes.

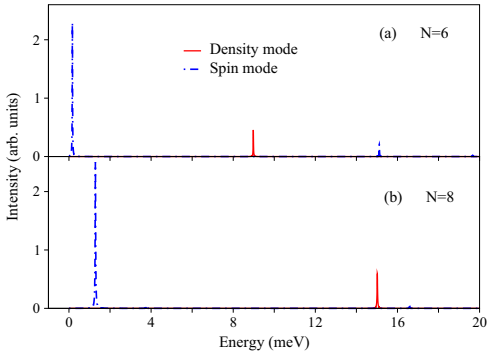

FIG. 5. Simulation of the z-polarized spectra corresponding to (a) $N = 6$ and (b) $N = 8$ electrons in the ND. Full (dot-dashed) lines represent density (spin) modes. An offset in the origin of the energy axis is used in order to display low-energy peaks more clearly.

modes, as far as the identification of correlation regimes is concerned. A first main difference arises between the $N=4$ system and those with $N=6$ and $N=8$. The former does not contain any visible density (nor spin) mode in the lower part of the spectrum, i.e., in the region 0-20 meV (not shown). Conversely, the other systems present a strong density mode at 9 meV ($N=6$) and 15 meV ($N=8$), and the spin counterpart mode at lower energy. In the $N=6$ system this peak corresponds to the transitions $s_3 \rightarrow s_4$, $s_3 \rightarrow s_5$, and in the $N=8$ case to the transitions like $s_4 \rightarrow s_5$, $s_3 \rightarrow s_5$, $s_3 \rightarrow s_7$. These transitions between s orbitals confined in the cylinder cannot be observed in the case of the $N=4$ system because in this case $s_i, i > 2$, are empty, and the transition from s_1 and s_2 to $s_i, i > 2$, presents an almost negligible oscillator strength due to the negligible overlap of the regions where s_1 and s_2 on the one hand and $s_i, i > 2$, on the other hand present relevant electron density. As a result, the z-polarized absorptions observed at low energies for $N=6$ and $N=8$ can be ascribed to the presence of high correlation phases in the cylinder, the lower the transition energy the closer the involved SP states, and thus the larger the electron-electron correlation.

As a whole, the absorption spectrum reveals the signatures of both, Fermi liquid and Wigner crystal phases, turning therefore into a suitable tool to confirm the existence of mixed correlation phases in these systems.

IV. CONCLUSIONS

In the present paper, we carry out FCI calculations of the ground and low-lying states of many electrons confined in a ND. In these many-electron diluted systems subject to inhomogeneous spatial confining potentials, we find out the existence of MPs, i.e., phases in which some regions of the many-electron system behave like a Fermi liquid while, simultaneously, other more dilute regions display the typical quasi-classical Wigner distribution of the electron density. The present results confirm and reinforce previous results obtained at the local spin-density functional theory level. Additionally, we enclose the simulations of absorption spectra, which exhibit in-plane and z-polarized modes that reveal the different correlation regimes occurring in these systems.

ACKNOWLEDGMENTS

Support from MICINN projects CTQ2011-27324 and FIS2011-28617-C02-01, UJI-Bancaixa projects P1-1A2009-03 and P1-1B2011-01, and Generalitat de Catalunya Grant 2009SGR1289 is acknowledged. A.B. acknowledges the support from the Spanish FPI (MCINN) program.

[1]L. Jacak, P. Hawrylak, and A. Wójs, *Quantum Dots* (Springer, Berlin, 1998); *Semiconductor Quantum Dots*, edited by Y. Masumoto and T. Takagahara (Springer, Berlin, 2002); *Nano-Optoelectronics*, edited by M. Grundmann (Springer, Berlin, 2002); *Semiconductor Macroatoms*, edited by F. Rossi (Imperial College Press, London, 2005).
[2]S. Kan, T. Mokari, E. Rothenberg, and U. Banin, Nature Mater. **2**, 155 (2003); S. H. Kan, A. Aharoni, T. Mokari, and U. Banin, Faraday Discuss. **125**, 23 (2004).
[3]L. Li, J. Hu, W. Yang, and A. P. Alivisatos, Nano Lett. **1**, 349 (2001).
[4]X. Peng, L. Manna, W. Yang, J. Wickham, E. Scher, A. Kadavanich, and A. P. Alivisatos, Nature (London) **404**, 59 (2000).
[5]F. Shieh, A. E. Saunders, and B. A. Korgel, J. Phys. Chem. B **109**, 8538 (2005).
[6]J. E. Halpert, V. J. Porter, J. P. Zimmer, and M. G. Bawendi, J. Am. Chem. Soc. **128**, 12590 (2006).
[7]S. Geyer, V. J. Porter, J. E. Halpert, T. S. Mentzel, M. A. Kastner, and M. G. Bawendi, Phys. Rev. B **82**, 155201 (2010).
[8]E. P. Wigner, Phys. Rev. **46**, 1002 (1934).
[9]S. M. Reimann and M. Manninen, Rev. Mod. Phys. **74**, 1283 (2002).
[10]C. Yannouleas and U. Landman, Rep. Prog. Phys. **70**, 2067 (2007).
[11]B. Szafran, F. M. Peeters, S. Bednarek, T. Chwiej, and J. Adamowski, Phys. Rev. B **70**, 035401 (2004).
[12]E. J. Mueller, Phys. Rev. B **72**, 075322 (2005).
[13]J. L. Movilla, J. Planelles, and W. Jaskolski, Phys. Rev. B **73**, 035305 (2006).
[14]A. Ballester, J. M. Escartín, J. L. Movilla, M. Pi, and J. Planelles, Phys. Rev. B **82**, 115405 (2010).
[15]L. Carbone, S. Kudera, C. Giannini, G. Ciccarella, R. Cingolani, P. D. Cozzoli, and L. Manna, J. Mater. Chem. **16**, 3952 (2006).
[16]Since no specific NR (ND) environment is determined, possible polarization effects coming from the dielectric mismatch between the NR (ND) and the surrounding medium are disregarded as in Ref. 14.
[17]Ch. H. Wang, T. T. Chen, Y. F. Chen, M. L. Ho, Ch. W. Lai, and P. T. Chou, Nanotechnology **19**, 115702 (2008).
[18]See http://code.google.com/p/citool/ for more information about CITOOL computer code.
[19]R. B. Lehoucq, K. Maschhoff, D. C. Sorensen, and C. Yang, See http://www.caam.rice.edu/software/ARPACK/ for more information about arpack computer code.
[20]This energy is located in between $\epsilon(s_{18}) = 0.957$ eV and $\epsilon(s_{19}) = 0.984$ eV.
[21]We employ here the so-called chemical notation for integrals, i.e., $(ij|kl) = \int \phi_i(1)^* \phi_j(1)(1/r_{12})\phi_k(2)^* \phi_l(2)dv$.
[22]In short, we may reason as follows: If we approximate $J_1 = J_2 = (s_1 s_2|p_1 p_2) = J$ and $K_1 = K_2 = (s_1 p_1|s_2 p_2) = K$, the diagonal element of the CI matrix corresponding to the spin-adapted singlet/triplet $s_2 p_2$ configuration is $\varepsilon_s + \varepsilon_p + J \pm K$. The same can be said for the spin-adapted singlet/triplet $s_1 p_1$ configuration. The admixing off-diagonal $(s_1 p_1, s_2 p_2)$ for singlet/triplet results to be $J \pm K$. Diagonalizations yield a lowest double degeneracy involving a singlet and a triplet and additionally an excited triplet and a more excited singlet. This basic idea applies to the pair of configurations of $N=4$ $(s_1^2 s_2 p_2, s_2^2 s_1 p_1)$, $N=6$ $(s_1^2 s_3^2 s_1 p_1, s_2^2 s_3^2 s_2 p_2)$, etc.

Multi-particle states of semiconductor hexagonal rings: Artificial benzene

Ana Ballester,[1] Josep Planelles,[1] and Andrea Bertoni[2,a)]
[1]*Departament de Química Física i Analítica, Universitat Jaume I, P.O. Box 224, E-12080 Castelló, Spain*
[2]*Centro S3, CNR—Istituto Nanoscienze, Via Campi 213/A, 41125 Modena, Italy*

(Received 8 September 2012; accepted 20 October 2012; published online 20 November 2012)

We present a theoretical and numerical investigation of correlated multi-electron states of hexagonal semiconductor rings. Both single-particle and correlated states show localization patterns in the six corners and energy spectra degeneracies corresponding to a hexagonal benzene ring. Thus, our results can aid the interpretation of energy-loss or near-field experiments that, in turn, shed light on the nature of molecular few-particle orbitals of artificial benzene. Surprisingly, we find that charges get more localized in the corners as the number of electrons increases, up to six, this indicating the deficiency of a picture based on orbitals delocalized on the whole ring. We also expose the presence of several spin-correlated states and the effect of an asymmetry of the system. © *2012 American Institute of Physics*. [http://dx.doi.org/10.1063/1.4766444]

I. INTRODUCTION

Hexagonal shape is rather common in semiconductor nanowires (NWs) due to the crystal structure of the composing material.[1–4] Furthermore, a modulation in the NWs composition along the axis can lead to a further confinement of the free carriers and form a disk-shaped quantum dot whose effective two-dimensional (2D) potential results to be harmonic.[5] This essentially hides the real shape of the semiconductor pillar, i.e., the NW, from which the zero-dimensional confinement is obtained. Deep insight has been achieved on this type of nanostructures, including the nature of correlated few-particle states,[6,7] their relaxation rates,[8,9] and optical properties.[10,11]

Recently, a new kind of quasi-1D nanostructure, namely semiconductor core-multishell nanowires (CSNWs), has been realized,[12] where the carrier confinement is not limited to the center of the NW. This leads to additional degrees of freedom and interesting properties for applications in opto- and nano-electronic devices.[13]

In analogy with the fabrication of vertical or disk-shaped quantum dots from a NW, a proper material modulation along a CSNW axis should be able to generate a strong confinement of the carriers in that direction, leading to an effective 2D system. However, now the confinement in the orthogonal plane is not harmonic, and the shape of the CSNW section cannot be considered circular anymore. Rather, the carriers will be confined in a polygonal flat quantum ring. Our study addresses few-interacting-carrier states of semiconductor hexagonal rings. Due to the qualitative similarity of the system shape and symmetry with a benzene hexagonal ring, we term it *artificial benzene*. As we shall see, the few-electron density localization and the states degeneracies reflect the hexagonal symmetry as in benzene.

We focus on structures where electrons are localized on a square-well type potential in the radial direction, rather than being confined at the heterointerface by the triangular well generated by the band bending.[14,15] In fact, in the latter case, a large carrier density is needed in order to create a stable electron gas, thus concealing the correlation effects proper of the few-electron regime. We adopt an envelope function approximation for the single-particle wave functions and a full configuration interaction (FCI) approach to compute the correlated states. The FCI method provides both ground and excited states with comparable accuracy, this being essential in the calculation of electron-phonon interactions, response functions, and optical properties.[16,17]

This paper is organized as follows. In Sec. II, we describe the model of our physical system and in Sec. III, we outline the numerical approach adopted. In Sec. IV, the single-electron states are reported and in Sec. V, the correlated few-electron states are described with particular emphasis to their spin configuration and charge-density distribution. In Sec. VI, we address a system where the hexagonal symmetry is lifted by a thicker layer in one of the facets. Finally, in Sec. VII, we draw our conclusion.

II. THE PHYSICAL SYSTEM

The system we consider is constituted by a three-layer AlAs-GaAs-AlAs CSNWs with hexagonal cross section, where an additional strong confinement has been introduced in the growth direction. This gives an effective 2D system, where an hexagonal GaAs quantum well is wrapped around the AlAs core, as depicted in Figure 1. Since an excitation in the axial direction has an energy much larger than the energy scales involved in our simulations, we can neglect the motion in the (confined) axial direction and adopt an effective 2D model. To be specific, we consider a regular-hexagon domain with edges 66.5 nm long. The GaAs well is 6.8 nm wide. Its thickness is uniform all around the 37.3 nm AlAs core. This symmetry will be lifted in Sec. VI, where different thicknesses of one of the edges will be considered. The GaAs well is covered by a 13.5 nm AlAs capping layer. The conduction-band offset between the two materials is 438 meV. We consider an effective mass m^* isotropic on the ring plane, with $m^* = 0.063\, m_e$ ($m^* = 0.15\, m_e$) in GaAs (AlAs), and a dielectric constant $\varepsilon = 12.9\, \varepsilon_0$ ($\varepsilon = 10\, \varepsilon_0$) in

a)Electronic mail: andrea.bertoni@nano.cnr.it.

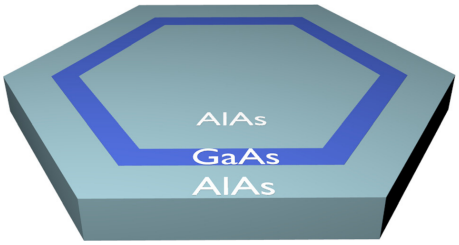

FIG. 1. Schematics of the system. A GaAs ring is wrapped around an hexagonal AlAs core and capped by an additional AlAs shell. The free electrons are confined in the GaAs region. A strong confinement in the axial direction leads to a ring-type structure.

GaAs (AlAs). An effective thickness $\tau = 2\,\text{nm}$ of the hexagonal ring in the axis direction is introduced in our model by means of an additional parameter that smooths Coulomb repulsion at short distance.[18,19]

III. NUMERICAL APPROACH

In order to find the correlated multi-electron states and assess the role of Coulomb interaction and correlation, we perform an exact diagonalization of the multi-particle Schrödinger equation via a FCI procedure. As a first step, the single-particle orbitals ψ_i and energies ϵ_i of a conduction-band electron are computed, for the confining structure described in Sec. II, through a numerical solution of the effective-mass Schrödinger equation

$$\left[-\frac{\hbar^2}{2}\nabla_{\mathbf{r}}\left(\frac{1}{m^*(\mathbf{r})}\nabla_{\mathbf{r}}\right)+E_c(\mathbf{r})\right]\psi_i(\mathbf{r})=\epsilon_i\psi_i(\mathbf{r}), \quad (1)$$

where $\mathbf{r}$ is the 2D coordinate on the hexagonal domain, $m^*(\mathbf{r})$ is the isotropic material-dependent effective mass of electrons, E_c is the conduction band profile, and i labels the single-particle state. The above equation is numerically integrated by means of a box integration method[20] on a triangular grid with hexagonal elements. The grid reproduces the symmetry of the system thus avoiding numerical artifacts originated by discretization asymmetries of the six domain boundaries, as would be the case, e.g., using a rectangular grid. Formally, the partial differential Eq. (1) is integrated on each hexagonal element. By applying the divergence theorem, the area integral is converted in a linear integral of the flux along the hexagon boundary. A balance between incoming and outgoing fluxes (obtained through a first-order finite-differences scheme) of adjacent hexagons connects the unknowns on different elements. This results in a symmetric sparse matrix whose dimension corresponds to the number of grid hexagons, and with seven non-zero elements on each row. This matrix is diagonalized through an efficient Lanczos library algorithm.[21] Our simulations typically use about 8600 hexagonal elements. Single-particle calculations are essentially irrelevant from the computational effort perspective. However, the discretization grid of the single-particle wave functions strongly affects the computational time of Coulomb integrals, as we detail in the following, and we had to choose a mesh thickness allowing for the practicable calculation of them, yet leading to a small numerical error (of the order of 1%) on the single-particle energies.

The next step is the calculation of the so-called Coulomb integrals

$$U_{ijkl}=\int d\mathbf{r}\int d\mathbf{r}'\,\psi_i^*(\mathbf{r})\psi_j^*(\mathbf{r}')\,\mathcal{U}(\mathbf{r}-\mathbf{r}')\,\psi_k(\mathbf{r}')\psi_l(\mathbf{r}), \quad (2)$$

which we perform by exploiting the hexagonal tessellation of the domain described above. In the equation above, $\mathcal{U}(\mathbf{r})=\frac{e}{4\pi\epsilon(\mathbf{r})(|\mathbf{r}|+\tau)}$ is the Coulomb potential energy between two electrons at distance $|\mathbf{r}|$. The cutoff parameter τ avoids divergences of the integrand: It mimics the effect of a finite thickness of the nanostructure in the axial direction as mentioned in Sec. II.

The multi-particle Hamiltonian matrix is then built up. First, we fix a number N of interacting electrons. Then, we build the Hilbert space by generating all possible Slater determinants $|\Phi_n\rangle$, that is, the multi-particle basis of the Hilbert space. For all the calculations presented in the following sections, we use 24 spin-orbital single-particle states, giving $\binom{24}{N}$ Slater determinants. In fact, we found that only the lowest 12 states, corresponding to the first 6 orbitals, are populated with a significant probability. We present calculations up to $N=7$, which need a basis of about 350×10^3 Slater determinants.

Finally, we compute the Hamiltonian matrix elements

$$H=\sum_{i\sigma}\varepsilon_i e_{i\sigma}^\dagger e_{i\sigma}+\frac{1}{2}\sum_{ijkl}\sum_{\sigma\sigma'}U_{ijkl}e_{i\sigma}^\dagger e_{j\sigma'}^\dagger e_{k\sigma'}e_{l\sigma}, \quad (3)$$

where $e_{i\sigma}$ ($e_{i\sigma}^\dagger$) is the annihilation (creation) operator for an electron in the orbital state i and with spin σ. The Hamiltonian matrix is finally diagonalized, leading to the complex coefficients C_n^m of the mth multi-particle state

$$|\Psi_m\rangle=\sum_n C_n^m|\Phi_n\rangle. \quad (4)$$

In order to obtain the real-space electron density of $|\Psi_m\rangle$, we compute

$$n(\mathbf{r})=\sum_{n_1,n_2}\left[(C_{n_1}^m)^*C_{n_2}^m\sum_\sigma\sum_{ij}\psi_i^*(\mathbf{r})\psi_j(\mathbf{r})\times\langle\Phi_{n_1}|e_{i\sigma}^\dagger e_{j\sigma}|\Phi_{n_2}\rangle\right], \quad (5)$$

while, for the conditional density, if an electron is found in $\bar{\mathbf{r}}$ with spin $\bar{\sigma}$, the density distribution of the remaining electrons with spin σ is

$$n(\mathbf{r},\sigma)|_{\bar{\mathbf{r}}\bar{\sigma}}=\sum_{n_1,n_2}\left[(C_{n_1}^m)^*C_{n_2}^m\sum_{ij}\sum_{kl}\psi_i^*(\mathbf{r})\psi_j^*(\bar{\mathbf{r}})\psi_k(\bar{\mathbf{r}})\psi_l(\mathbf{r})\times\langle\Phi_{n_1}|e_{i\sigma}^\dagger e_{j\bar{\sigma}}^\dagger e_{k\bar{\sigma}}e_{l\sigma}|\Phi_{n_2}\rangle\right]. \quad (6)$$

IV. SINGLE-ELECTRON STATES

The hexagonal symmetry of the GaAs quantum well gives a energy-level structure of the single-particle states with degeneracies 1-2-2-1, also typical of benzene molecule, as it is shown in Figure 2. In particular, we report in the figure, the colormaps of the lowest 12 wave functions with the corresponding energy reported on the right axis. The origin of the energy scale is set in the GaAs band gap, 60% of the gap below the bottom of the conduction band, where the Fermi level of the undoped structure should lie. As mentioned above, these single-particle states are obtained within the envelope function approximation.

In the FCI calculations reported in the following, we find that only the lowest 6 orbitals (spin-independent real-space wave functions) have significant population. Taking into account all 12 orbitals, we can identify two different types of shells, namely two groups of orbitals well separated in energy, having the same degeneracy pattern. They show different preferential localization of the wave functions. The first shell, ranging from 942.294 meV to 943.933 meV, contains the first 6 orbitals that accumulate the wave functions to the wider area around the hexagonal ring, i.e., at the corners. On the other hand, the second shell from 946.407 meV to 952.342 meV tends to localize the maxima of the wave functions along the edges of the hexagonal system, and consequently, has higher localization energy. Also, as expected, the number of nodes around the ring increases with increasing energy. In particular, we note that the double-degenerate first and second excited orbitals have one and two nodal lines, respectively. The following two orbitals have three nodal lines. However, they are not degenerate, being the last orbital of the first shell and the first one of the second shell. In fact, the electron density is modulated, so that six peaks are formed: in the first case, they are centered on the six corners, while in the second case, they are on the hexagon sides.

V. FEW-ELECTRON STATES

Multi-electron states are computed starting from the single-particle orbitals of Figure 2 by means of the FCI approach already described. Electron-density profiles up to $N = 7$ electrons reveal that Coulomb repulsion tends to localize electrons far from each other in order to minimize the electrostatic energy of the system, and the electron density for the lower-energy states accumulates on the corners of the hexagonal ring. This effect adds to the corner localization of single-particle states due to the wider area available and lower kinetic energy. In order to pick out the effect of the Coulomb interaction, in Figure 3, we report the electron density versus the position along an edge of the hexagon, for the multi-particle states up to seven electrons. The distribution is always higher at the corners, but the steepness decreases as the number of particles increases up to six, with the single-particle density higher in the middle of the edge than the six-particle one. In the latter case, the six electrons are highly localized on the six corners. This trend changes with the introduction of a seventh electron: since the lower kinetic-energy spots are all occupied the additional electron is

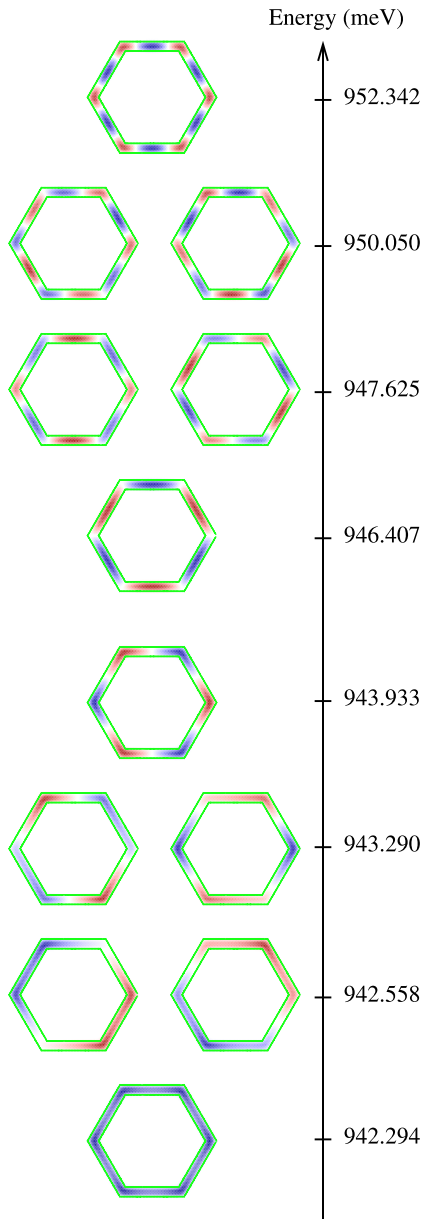

FIG. 2. Single-electron states $\Psi_i(\mathbf{r})$ for the hexagonal GaAs quantum well are represented, with red (blue) color indicating positive (negative) values. Due to the hexagonal symmetry, the electronic structure reproduces the benzene degeneracies distribution 1-2-2-1. We find two different wave function localization patterns depending on the energy: the first 6 states (first shell) stabilize their energy by accumulating the wave functions in peaks close to the corners of the hexagon, while the second 6 states (second shell) tend to localize the wave functions maxima along the edges.

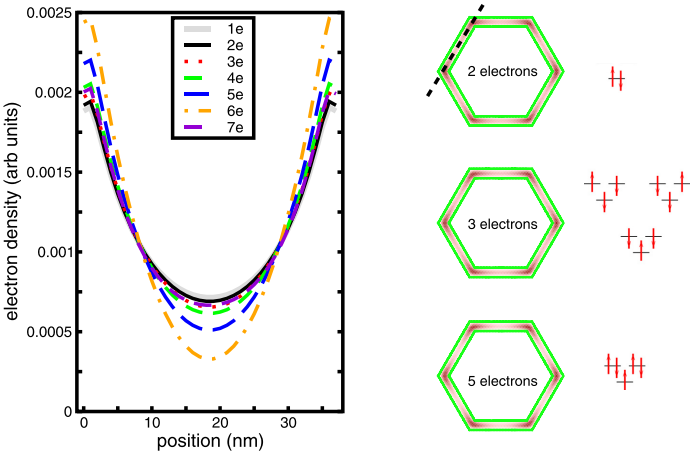

FIG. 3. Electron density along an edge (dashed line on the top right hexagon) for correlated ground states up to $N=7$. To ease the comparison, all the curves are normalized to unity. Most of the electron density is localized at the corners due to the Coulomb repulsion and lower kinetic energy. On the right, the colormap 2D plots for three cases are reported, together with their leading Slater determinants. Note that in the 3-electron case, the ground state is the spin-degenerate quadruplet $S=\frac{3}{2}$ and we plot here the state with $S_z=-\frac{1}{2}$, which has three leading Slater determinants entering the linear combination of Eq. (4) with the same coefficient.

delocalized on the whole ring. On the right part of Figure 3 we show, as an example, the electron density profiles of the ground multi-particle states with two, three, and five electrons, together with the schematic representation of the leading Slater determinant(s) $|\Phi_n\rangle$ in their configuration Eq. (4), i.e., the ones with largest $|C_n^m|^2$. To be specific, the short horizontal lines represent the three lower orbitals of Figure 2, and the arrows represent electrons with up or down spin.

Despite the similar density profiles, with high charge density on the six corners for all three cases, peculiar electronic configurations come into play in the correlated ground states. The 2-electron system attains a closed first shell as expected, while the 3-electron case shows an important contribution of electronic configurations, which do not follow the building-up and multiplicity principles, i.e., Aufbau's and Hund's rules, respectively.[22] An unusual leading configuration is also found for the 5-electron ground state, where electrons distribute in pairs in the two degenerate first-excited single-particle states forming a closed shell, while an unpaired electron lies in the first shell. However, we must stress that the above states are highly correlated, and in general, the higher the number of particles, the higher the effect of correlation. In fact, the weight of the leading Slater determinant for the two-particle state is 63%, while it is only 19% for the five-particle case.

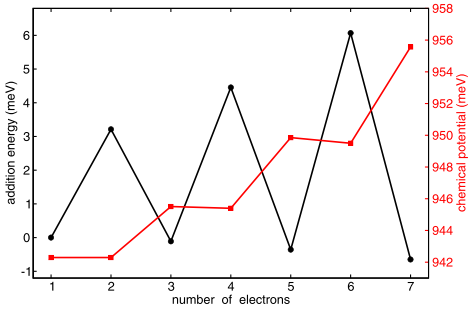

FIG. 4. Addition energies and chemical potential for different number of electrons. Two closed shells are formed at $N=2$ and $N=6$. A very stable configuration is also found for $N=4$, with the second shell half filled.

We also quantify the relative stability of the N-electron ground state by computing the addition energy, which is obtained using the formula

$$E_{add}(N) = E(N+1) - 2E(N) + E(N-1), \qquad (7)$$

where $E_{add}(N)$ is the energy required in order to place an extra electron into the system that has initially $N-1$ electrons. Such quantity, similar to electron affinity in atomic physics, is calculated by computing the total energy of the N-electron system ground state $E(N)$ and the total energies for the hexagon occupied with $N+1$ and $N-1$ electrons, i.e., $E(N+1)$ and $E(N-1)$, respectively.

The addition-energy spectrum is reported in Figure 4, together with the chemical potential, for different numbers of electrons. It reflects the orbital shell filling for the hexagonal symmetry up to $N=6$. The first shell is identified with the peak for 2 electrons, where system stabilizes because of the closed shell configuration. The degeneracy pattern of the symmetry of the system is observed when comparing 4- and 6-electron peaks. A half-filled shell is involved for the 4-electron configuration while a closed shell is formed for the 6-electron ground state. The extra stabilization effect for the closed shell can be detected thanks to the higher peak for six electrons. This six-electron case corresponds to that of a benzene ring. With seven electrons, the system stability decreases having a single unpaired electron in the two degenerate orbitals above two closed shells, resulting in a negative addition energy. The chemical potential versus the number of electrons is also reported on Figure 4.

In order to assess the effects of Coulomb-induced correlation on both ground state and excited states, we perform

conditional density calculations for several N-electron states and report the spatial distribution of the remaining $(N-1)$ electrons when one electron is found in a corner. In the 2-electron case, if an electron with spin up is fixed at one corner of the hexagon, spin down density is localized at the opposite corner as shown in Figure 5(a) for the 2-electron ground state. This Coulomb repulsion effect is also observed for excited states. For example, the double-degenerate second excited state is shown in Figure 5(b). Note that in order to preserve the symmetry of the system, a proper linear combination of the degenerate eigenstates resulting from the FCI procedure has to be considered. In fact, if a single correlated state is taken, its real-space density does not maintain the proper symmetry, as shown in Figure 5(c) and described in its caption. This is because we take Slater determinants as a basis and do not employ configuration state functions with the full system symmetry. In other words, we do not exploit quantum numbers originating from the hexagonal symmetry. This choice, although computationally expensive, gives us the freedom to alter the system geometry arbitrarily, as we will do in Sec. VI.

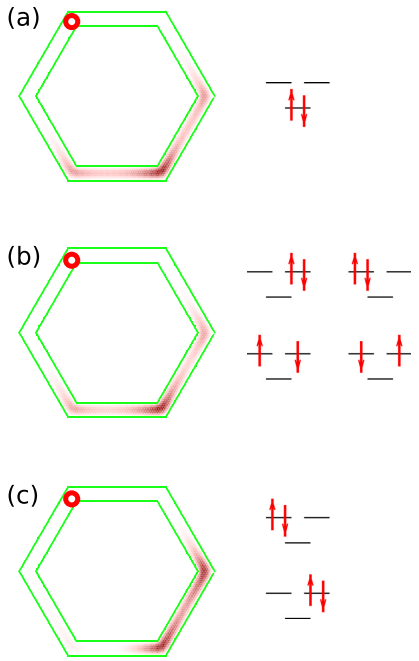

FIG. 5. Two electrons. Conditional densities, when one electron is fixed in one corner (small circle) for the ground state (a) and the double-degenerate second-excited state (b)-(c). While (b) shows the density of a proper linear combination of the two degenerate states yielding a correct symmetry, (c) shows the charge density of one of the states, as computed by our FCI approach. For each density plot, the leading Slater determinants composing the correlated state are reported on the right.

Next, we check the effect of electron-electron interaction on the correlation at higher electron densities. If we populate the hexagon with three electrons and we fix one of them in a corner, the other two are mainly found on the other two corners forming with the first one an equilateral triangle. This configuration is shown on the right of Figure 6, and it is the same for the four degenerate ground states forming the quadruplet with $S = \frac{3}{2}$. As already reported in Figure 3, this is a remarkable difference with respect to the non-correlated state, for which the ground state consists of two electrons in the lower orbital and one in the first-excited orbital, being this a $S = \frac{1}{2}$ state. The latter state will be also the ground one for the asymmetric system as we will show in Sec. VI. On the left part of Figure 6, we report the electron density along an edge, like in Figure 3. However, here, we fix the number of particles to three and report three different states. The more energetic the state, the more localized the electrons in the corners. Although the difference is small, we find that this effect is general, being present for any number of electrons, at least for the few lower states.

For the 4-electron case, we also address the spin density distribution. If one electron is fixed in a corner, the remaining particles are distributed along the rest of the system, with preferential localization in the opposite corner, as shown in Figure 7(a) for the 4-electron ground state. However, a remarkable difference is found between electrons with the same or opposite spin with respect to the fixed one. Let us fix an electron with spin down in a corner. While the other spin-down electron localizes as far as possible at the opposite corner of the hexagon, spin-up density is distributed at the next sides of the fixed electron, leaving the opposite corner empty. This is shown in Figure 7(b), on the right and left plots, respectively. This effect is much less effective in the excited states. In fact, the first excited state has a density distribution for same-spin electron (not shown) that resembles the one for ground state, i.e., in the opposite corner, while

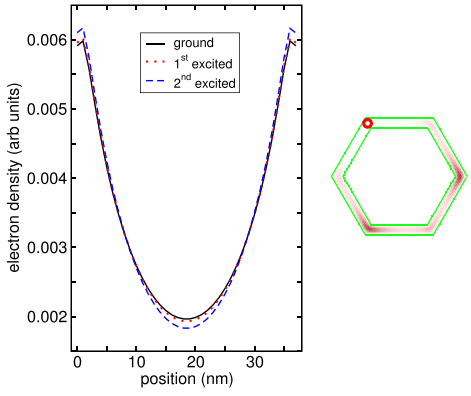

FIG. 6. Three electrons. Left: Density distribution along a hexagon edge for three different states. The higher the energy, the more localized the density in the corners. Right: Conditional density for the ground state when an electron is fixed in a corner. The other two electrons localize in two corners to form an equilateral triangle configuration.

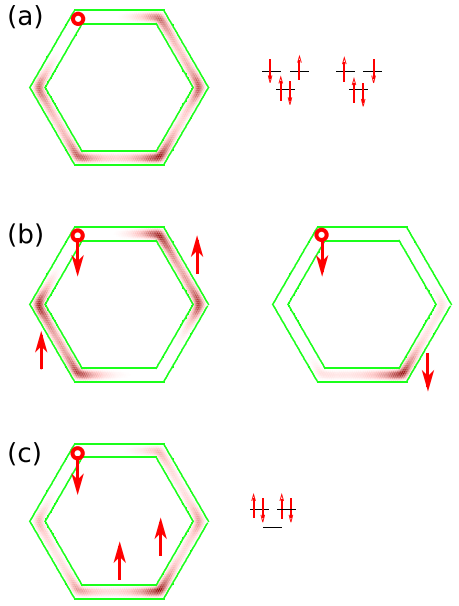

FIG. 7. Four electrons. (a) Conditional density for the ground state and its leading Slater determinants. (b) Ground-state conditional spin density for electrons with different (left) or same (right) spin as the fixed one. (c) Conditional spin density of the first-excited state (and its leading Slater determinant) for electrons with opposite spin with respect to the fixed one.

opposite-spin electrons tend to localize at the opposite corner too, as shown in Figure 7(c).

Finally, the energy balance for a 5-electron system has a strong kinetic contribution. Electron density is high enough to distribute electrons all over the corners of the hexagon in the ground state, as shown in Figure 8(a) for the opposite-spin case (the same-spin case is similar). This is not true for the first excited state, where the density for the spin with the same orientation as the fixed particle is mainly localized at the opposite corner (Figure 8(b) on the right), while the opposite-spin density is distributed close to the fixed particle (Figure 8(b) on the left). It should be noted that here we find a ground state that does not follow Aufbau principle since in the leading Slater determinant, only one electron occupies the ground single-particle state. The correlated state corresponding to the non-interacting ground state is the first-excited one, shown in Figure 8(b). To assess the effect of larger electron number, the conditional spin distribution of Figure 8(b) should be compared with the ground 4-particle state in Figure 7(b). The behavior is qualitative similar, however in the 5-electron case, spin distributions are more spread, and for the opposite-spin case, the two spin-up peaks are in the two nearest-neighbor corners. This a Coulomb effect. In fact, the two remaining spin-down electrons are localized not only on the opposite corners but also spread

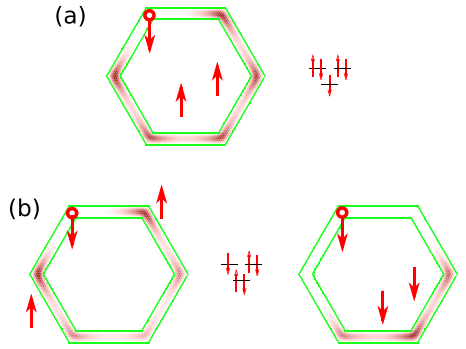

FIG. 8. Five electrons. (a) Conditional spin density for the ground state (and its leading Slater determinant) with spin opposite to that of the fixed particle. (b) Conditional spin density for the first excited state for both opposite-spin (left) and same-spin (right) cases. The leading Slater determinant of the first-excited state has lower energy than that of the ground state, this being an effect of Coulomb correlation. Spin distributions for the ground (first-excited) 5-electron case should be compared with the first-excited (ground) ones of the 4-electron case of Figure 7, where the shell-filling order is preserved.

across the other two corners as shown on the right of Figure 8(b).

VI. ASYMMETRIC HEXAGON

In this section, we analyze the case with one segment of the hexagonal ring thicker than the others. In fact, the experimental synthesis of semiconductor CSNWs achieved a very high control on the width of the overcoating semiconductor shells, as already described in the Introduction, with a nanometric precision. However, even a small deviation from the perfect symmetry of the six edges is expected to have a deep influence on the energy spectra and charge distributions of our hexagonal system. Therefore, we consider convenient to show the system's behavior when an asymmetry is introduced. Specifically, we take one edge of the hexagon up to 2 nm thicker than the others, while maintaining its inner border in the same position. We will refer to this kind of irregular system as an asymmetric hexagon.

At the single-particle level, the asymmetric spatial confinement is responsible for the breakdown of the degeneracies found in the symmetric case of Figure 2. The electron density of the lower states is now concentrated in the large edge and the energy of those states decreases dramatically. We report the energy spectrum of the first eight states as a function of the additional thickness of the hexagon top edge in Figure 9. As the thickness increases, more and more levels leave the energy of the symmetric case and decrease linearly. Moreover, levels from the upper shell (only two of them are shown in the graph) decrease as well, and join the lower shell. States with energy below that of the first shell of the symmetric system are mainly localized in the large edge. In fact, we focus on a specific case, with an extra top edge

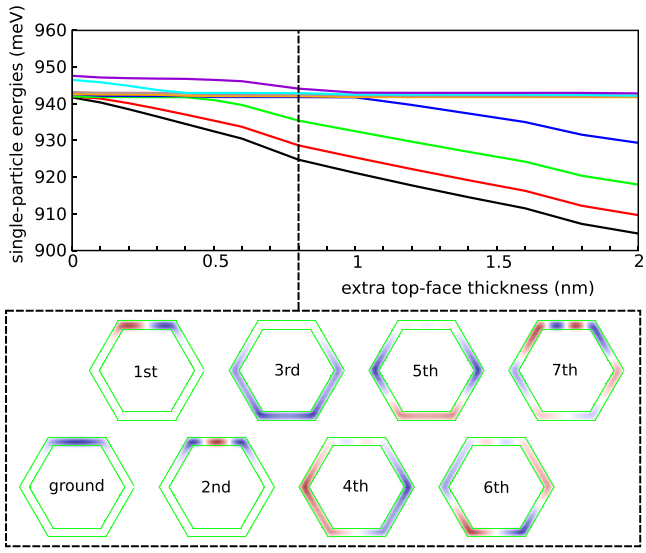

FIG. 9. Single-particle energies as a function of the additional thickness of the upper edge with respect to the symmetric hexagon. The lower panel shows several single-particle wave functions, in ascending energy order from left to right, for an extra thickness of 0.8 nm (dashed vertical line), i.e., with the larger edge 7.6 nm thick. Note that contrary to the multi-particle case, the part of the hexagon with a smaller thickness is occupied already from the third excited state.

thickness of 0.8 nm, i.e., 7.6 nm of total width, indicated by the dashed vertical line in Figure 9. The bottom panel shows the wave functions of such case, with increasing energy from left to right. Correspondingly, in the upper graph, we have three states with low (and linearly decreasing) energy. Indeed, the first three wave functions are localized in the top edge. The wave functions with higher energy have strong occupation in the rest of the hexagon and show an increasing number of nodal lines as in the symmetric case.

When including electron-electron interaction, the density profiles of the multi-electron states reflect the preferential localization in the top edge of the single-particle ones. However, Coulomb interaction tends to increase as much as possible the inter-particle distance. As a consequence, the density distribution is a balance between those effects, tailored by the number of electrons in the system. As an example, we show in the upper part of Figure 10, the charge density for three electrons (left) and seven electrons (right). In the first case, the particles are almost completely localized in the top edge, while in the second case, the larger electron density gives a high density also on the other four corners. In fact, with seven electrons, three of them are located in the top edge, and the remaining four are in the other corners, approximately. The effect of Coulomb correlation can be exposed by observing the conditional density for the 3-electron and 7-electron ground states (bottom graphs in Figure 10). While the conditional distribution for three electrons is what one would expect from a mean-field perspective, with the bottom part unchanged and a large density in the top edge around the opposite corner with respect to the fixed particle, the conditional density for seven electrons is fully located on the three opposite corners, in spite of the lower confining energy of the top ones.

Although the 3-electron conditional density resembles a mean-field solution, it results to be strongly spin-polarized, as shown in the top part of Figure 11. In fact, if we fix in a corner of the large edge a spin-down particle, we find that the charge localized on the other side of that edge has opposite spin, while the other spin-down electron is spread in the bottom edge and corners. We stress that the ground state is double spin-degenerate and that we are considering the state with $S_z = -\frac{1}{2}$. It means that a crossing between $S = \frac{3}{2}$ and

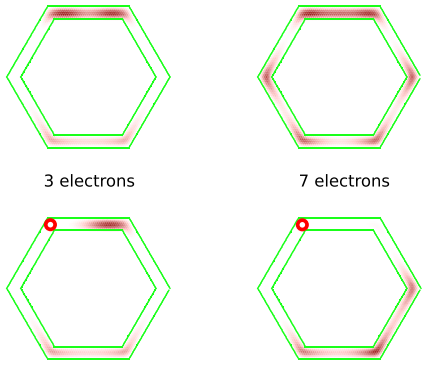

FIG. 10. Charge density (top) and conditional charge density (bottom) for the ground 3-electron (left) and 7-electron (right) state of the asymmetric hexagon described in Figure 9. In the lower-density case, the particles are completely localized in the large edge, while in the higher-density case, particles are also found in the other four corners. The conditional density distribution of the latter state shows nonlocal effects typical of strong correlation.

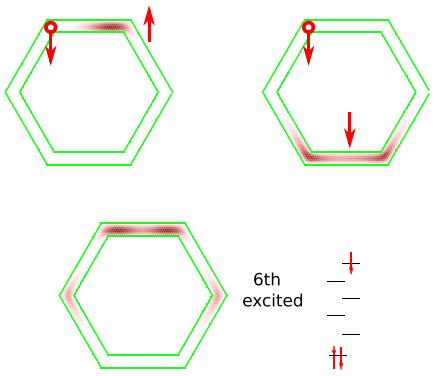

FIG. 11. Top: Conditional spin density for the ground 3-electron state of the asymmetric hexagon described in Figure 9. Two electrons with opposite spin form a two-particle state in the large edge while the other electron is completely localized in the two corners at the opposite edge. Bottom: The sixth excited state is the first one showing nonzero occupancy of the two lateral corners. The lower kinetic energy needed to occupy the larger edge also induces a preferential localization on the opposite edge and high energy is needed to occupy the remaining sites.

$S = \frac{1}{2}$ states occurs with the increase of the top edge thickness. In order to find some charge density in the two middle corners for the 3-electron case, we have to consider a high-energy state, namely the sixth excited, shown in Figure 11 together with its leading Slater determinant. This means that, while a system with higher electron density has all the corners occupied already in the ground state, a low-density asymmetric state not only localizes the charge mainly in the large edge, but completely removes electrons from the two middle corners.

VII. CONCLUSIONS

We have presented a numerical study of multi-electron states in hexagonal rings. We showed that the six corners are sites of preferential localization for electrons at both single-particle and correlated-particle levels. This makes our hexagonal system qualitatively similar to a benzene ring, where, according to its standard picture, six carbon atoms act as Coulomb centers, and six electrons are delocalized on a continuous π bond across the ring.[23] We find that in the artificial benzene system considered here, electron states are in general strongly correlated, and a picture of a single orbital delocalized on the whole ring is not appropriate.

We specifically considered an hexagonal quantum ring made by GaAs on an AlAs matrix, in analogy to CSNWs, but with an additional confinement along the axial direction. A number of ground and excited states have been addressed by analyzing their charge and spin density profiles. As the number of electrons populating the conduction band increases, stronger charge localization forms at the corners of the hexagon. However, the 7-electron ground state reveals that one electron is completely delocalized in the structure, above a closed, very stable, shell with one electron on each corner. As a consequence, the localization trend with electrons in the corners gets stronger up to six particles, then for seven particles, the density profile spreads substantially also along the edges. Although we do not find a general rule, we expose several specific ground and excited states with spin localization by considering opposite/same spin densities in conditional density calculations. We observe that opposite-spin densities tend to distribute as far as possible in order to minimize the energy of the system.

When the hexagonal symmetry is broken by the increase of an edge width, two effects are evident on the single-particle states: first, the 1-2-2-1 degeneracy pattern is broken, second, in low-energy states, the electron is mainly found in the large edge. On one hand, the above effects are not surprising, on the other hand, their consequences on the multi-particle states are of interest. For example, in the 3-electron case, we find a ground-state crossing between the symmetric ($S = \frac{3}{2}$) and the asymmetric ($S = \frac{1}{2}$) systems, while we find a highly correlated state for the 7-electron system, with consistent charge density on the corners opposite to the thick edge of the asymmetric system.

The understanding of correlation effects and the tailoring of charge localization patterns with the electron density, with asymmetries of the semiconductor structure or with external fields, are the first step towards an engineering of electronic and optical properties of semiconductor hexagonal rings. In fact, the study of artificial benzene, beside being of basic interest due to its analogy to a benzene ring, can expose the potentiality of such system for novel applications. Our methodology is the basis for both the calculation of intraband electronic and interband excitonic spectra. In fact, the calculation of multi-electron states alone can be useful to describe the far infra-red intraband spectra, but it cannot give hints on the optical properties of a nanosytem (related to interband near-UV and visible transitions). Exicton and multi-exciton spectra can be obtained once holes are also included in the calculations. However, in our paper, we focus on the multi-particle correlation in hexagonal geometry, and both the calculation of the far infra-red spectrum and the inclusion of holes are beyond the scope of our work and will possibly be a subject of future investigation.

Concerning the possible experimental fabrication of artificial benzene, we already mentioned in the Introduction how it could be obtained from a "slice" of a CSNW. In fact, while the length of CSNWs is only limited by their capability of sustaining themselves vertically while growing on a substrate and can reach several micrometers, their orthogonal shape depends on the crystallographic arrangements of their materials. In particular, most III-V NWs with a diameter less than about 400 nm grow as hexagonal crystals exposing the six 110 vertical facets normal to the (111) plane. For example, InAs/InAsP CSNWs grown on Si(111),[24] GaAs/AlAs CSNWs grown on GaAs(111)B,[2] and GaP/GaAs CSNWs grown on Si(111)[25] show a very neat hexagonal section in electron microscopy scans, even after a few overcoating processes. The overgrowth of different materials on the exposed facets leads to a prismatic heterostructure that confines eventually the free carriers either at the heterointerface or in the lower-gap semiconductor layer.[26] The two

confinement mechanisms are equivalent to that at the basis of planar two-dimensional electron gas (2DEG) formation in high-electron-mobility-transistors[27] and in rectangular quantum wells,[28] respectively. As a result, a 2DEG wrapped on the surface of an hexagonal prism can be formed.[29,33–36] The introduction of a strong confinement along the CSNW axis (e.g., via material modulation) would lead to a hexagonal ring.

Finally, we mention that the real-space electron distribution could be exposed though a near field spectroscopy. However, our hexagonal rings should lie on a substrate rather than being embedded in a CSNW in order to use such probing technique. In fact, experiments and simulations on Cu hexagonal vacancy islands clearly showed standing-wave patterns reflecting the hexagonal geometry.[30–32] Although the latter works could not reveal correlation effects due to the metallic nature of the nanometric system addressed, they demonstrated that spin polarization can be experimentally manipulated. A similar approach could be able to tailor few-particle spin-polarized states in hexagonal quantum rings.

ACKNOWLEDGMENTS

The authors thank Guido Goldoni, José Movilla, and Miquel Royo for valuable help. This work was partially supported by UJI-Bancaixa Project No. P1-1B2011-01, MCINN Project No. CTQ2011-27324, and FPI Grant (A.B.). EU Project INDEX (PITN-GA-2011-289968) is also acknowledged. Computing resources have been provided through CINECA ISCRA Project HP10CLLJ6S.

[1]F. Glas, J. C. Harmand, and G. Patriarche, Phys. Rev. Lett. **99**, 146101 (2007).
[2]A. Fontcuberta i Morral, D. Spirkoska, J. Arbiol, M. Heigoldt, J. R. Morante, and G. Abstreiter, Small **4**, 899 (2008).
[3]R. E. Algra, M. Hocevar, M. A. Verheijen, I. Zardo, G. G. W. Immink, W. J. P. van Enckevort, G. Abstreiter, L. P. Kouwenhoven, E. Vlieg, and E. P. A. M. Bakkers, Nano Lett. **11**, 1690 (2011).
[4]S. Hertenberger, S. Funk, K. Vizbaras, A. Yadav, D. Rudolph, J. Becker, S. Bolte, M. Doblinger, M. Bichler, G. Scarpa, P. Lugli, I. Zardo, J. J. Finley, M.-C. Amann, G. Abstreiter, and G. Koblmuller, Appl. Phys. Lett. **101**, 043116 (2012).
[5]L. Jacak, P. Hawrylak, and A. Wójs, *Quantum Dots* (Springer, 1998).
[6]C. P. García, V. Pellegrini, A. Pinczuk, M. Rontani, G. Goldoni, E. Molinari, B. S. Dennis, L. N. Pfeiffer, and K. W. West, Phys. Rev. Lett. **95**, 266806 (2005).
[7]J. Planelles, M. Royo, A. Ballester, and M. Pi, Phys. Rev. B **80**, 045324 (2009).
[8]J. I. Climente, A. Bertoni, G. Goldoni, and E. Molinari, Phys. Rev. B **74**, 035313 (2006).
[9]S. Amasha, K. MacLean, I. P. Radu, D. M. Zumbühl, M. A. Kastner, M. P. Hanson, and A. C. Gossard, Phys. Rev. Lett. **100**, 046803 (2008).
[10]S. Kalliakos, C. P. García, V. Pellegrini, M. Zamfirescu, L. Cavigli, M. Gurioli, A. Vinattieri, A. Pinczuk, B. S. Dennis, L. N. Pfeiffer, and K. W. West, Appl. Phys. Lett. **90**, 181902 (2007).
[11]J. I. Climente, A. Bertoni, and G. Goldoni, Phys. Rev. B **78**, 155316 (2008).
[12]G. Shen and D. Chen, Sci. Adv. Mater. **1**, 213 (2009).
[13]C. Colombo, M. Hei, M. Grätzel, and A. Fontcuberta i Morral, Appl. Phys. Lett. **94**, 173108 (2009).
[14]A. Bertoni, M. Royo, F. Mahawish, and G. Goldoni, Phys. Rev. B **84**, 205323 (2011).
[15]B. M. Wong, F. Lonard, Q. Li, and G. T. Wang, Nano Lett. **11**, 3074 (2011).
[16]A. Bertoni, M. Rontani, G. Goldoni, and E. Molinari, Phys. Rev. Lett. **95**, 066806 (2005).
[17]M. Rontani, C. Cavazzoni, D. Bellucci, and G. Goldoni, J. Chem. Phys. **124**, 124102 (2006).
[18]M. M. Fogler, Phys. Rev. Lett. **94**, 056405 (2005).
[19]W. Häusler and B. Kramer, Phys. Rev. B **47**, 16353 (1993).
[20]S. Selberherr, *Analysis and Simulation of Semiconductor Devices* (Springer, New York, 1984).
[21]R. B. Lehoucq, C. Sorensen, and D. C. Yang, *ARPACK Users Guide: Solution of Large-Scale Eigenvalue Problems with Implicitly Restarted Arnoldi Methods* (SIAM, Philadelphia, 1998).
[22]A. Franceschetti and A. Zunger, EPL **50**, 243 (2000).
[23]D. L. Cooper, J. Gerratt, and M. Raimondi, Nature **323**, 699 (1986).
[24]M. Keplinger, T. Martensson, J. Stangl, E. Wintersberger, B. Mandl, D. Kriegner, V. Holý, G. Bauer, K. Deppert, and L. Samuelson, Nano Lett. **9**, 1877 (2009).
[25]G. Zhang, K. Tateno, T. Sogawa, and H. Nakano, Appl. Phys. Express **1**, 064003 (2008).
[26]A. Nduwimana and X. Wang, Nano Lett. **9**, 283 (2009).
[27]S. M. Sze, *Modern Semiconductor Device Physics* (Wiley Interscience, 1998).
[28]T. Ando, A. B. Fowler, and F. Stern, Rev. Mod. Phys. **54**, 437 (1982).
[29]The analysis of a wrapped 2DEG with a cylindrical model simplifies the approach, in particular, if the effect of external magnetic fields is considered (Refs. 33 and 34), but in general, it is not adequate for prismatic CSNWs. In fact, it has been calculated that charge carriers tend to accumulate at the edges due to the wider area available for the carrier wave functions (Refs. 15 and 35) and, consequently, lower localization energy. This effect has been clearly demonstrated experimentally in the formation of so-called V-groove NWs (Ref. 36).
[30]L. Niebergall, G. Rodary, H. F. Ding, D. Sander, V. S. Stepanyuk, P. Bruno, and J. Kirschner, Phys. Rev. B **74**, 195436 (2006).
[31]O. O. Brovko, W. Hergert, and V. S. Stepanyuk, Phys. Rev. B **79**, 205426 (2009).
[32]A. S. Smirnov, N. N. Negulyaev, L. Niebergall, W. Hergert, A. M. Saletsky, and V. S. Stepanyuk, Phys. Rev. B **78**, 041405 (2008).
[33]G. Ferrari, A. Bertoni, G. Goldoni, and E. Molinari, Phys. Rev B **78**, 115326 (2008).
[34]V. Harutyunyan, G. Demirjian, and N. Gasparyan, Physica E **43**, 614 (2010).
[35]G. Ferrari, G. Goldoni, A. Bertoni, G. Cuoghi, and E. Molinari, Nano Lett. **9**, 1631 (2009).
[36]D. Kaufman, Y. Berk, B. Dwir, A. Rudra, A. Palevski, and E. Kapon, Phys. Rev. B **59**, R10433 (1999).

Two-Photon-Induced Blue Shift of Core and Shell Optical Transitions in Colloidal CdSe/CdS Quasi-Type II Quantum Rods

Marco Allione,[†] Ana Ballester,[‡] Hongbo Li,[†] Alberto Comin,[†] José L. Movilla,[‡,*] Juan I. Climente,[‡] Liberato Manna,[†] and Iwan Moreels[†,*]

[†]Istituto Italiano di Tecnologia, Via Morego 30, IT-16163 Genova, Italy and [‡]Departament de Quimica Fisica i Analitica, Universitat Jaume I, E-12080 Castellón, Spain

ABSTRACT The spectral dependence of the two-photon absorption in CdSe/CdS core/shell nanocrystal heterorods has been studied *via* two-photon-induced luminescence excitation spectroscopy. We verified that the two-photon absorption in these samples is a purely nonlinear phenomenon, excluding the contribution from multistep linear absorption mediated by defect states. A large absorption cross section was observed for CdSe/CdS core/shell quantum rods, in the range of 10^5 GM (1 GM = 10^{-50} cm^4 s phot^{-1}), scaling with the total nanocrystal volume and thus independent of the core emission wavelength. In the two-photon luminescence excitation spectra, peaks are strongly blue-shifted with respect to the one-photon absorption peaks, for both core and shell transitions. The experimental results are confirmed by $k \cdot p$ calculations, which attribute the shift to both different parity selection rules that apply to one-photon and two-photon transitions and a low oscillator strength for two-photon transitions close to the ground-state one-photon absorption. In contrast with lead chalcogenide quantum dots, we found no evidence of a breakdown of the optical selection rules, despite the presence of band anisotropy, *via* the anisotropic hole masses, and the explicitly induced reduction of the electron wave function symmetry *via* the rod shape of the shell. The anisotropy does lead to an unexpected splitting of the electron P-states in the case of a large CdSe core encapsulated in a thin CdS shell. Hence, tuning of the core and shell dimensions and the concurrent transition from type I to quasi-type II carrier localization enables unprecedented control over the band-edge two-photon absorption.

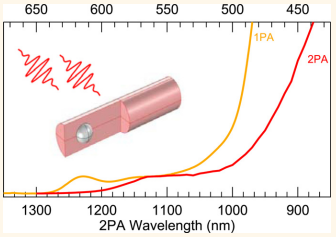

KEYWORDS: II–VI nanocrystals · quantum dots · two-photon absorption · optical selection rules · $k \cdot p$ calculations · effective mass approximation

Colloidal semiconductor nanocrystals, currently synthesized in various forms such as quantum dots (Qdots), quantum rods (Qrods), and more recently even nanosheets, have been intensively investigated for their peculiar opto-electronic properties related to the quantum confinement effect.[1−9] Among them, cadmium-based II–VI colloidal nanocrystals have received most of the attention, due to the well-established synthesis routes, a photoluminescence (PL) peak that is tunable over the entire visible spectrum, and a high photoluminescence quantum efficiency, exceeding 50% in core/shell systems.[10,11] Next to the linear optical properties, quantum confinement also allows controlling the nonlinear absorption coefficient. More specifically, Qrods can exhibit a large two-photon absorption (2PA) cross section,[12,13] and the concomitant efficient sub-band-gap excitation of the photoluminescence is of great interest for applications in photonic and opto-electronic devices. Consequently, several studies have proposed them as suitable candidates for two-photon-pumped biolabels[14] or as active materials in lasing[15−17] and optical data storage.[18,19]

Experimental and theoretical studies that focused on an improved fundamental understanding of 2PA in colloidal nanocrystals have revealed that in the limit of strong confinement, for instance experienced by small PbS and PbSe nanocrystals, quantum confinement may also weaken the optical selection rules, giving rise to one-photon-allowed transitions in 2PA spectra and *vice versa*.[20,21] Surprisingly, two-photon-induced

* Address correspondence to movilla@qfa.uji.es; iwan.moreels@iit.it.

Received for review December 13, 2012 and accepted February 26, 2013.

Published online February 26, 2013
10.1021/nn3057559

photoluminescence excitation (2PPLE) spectra for cadmium chalcogenides have been less investigated. Blanton *et al.*[22] already showed more than 15 years ago that for spherical CdSe Qdots data are in fact well reproduced by $k \cdot p$ calculations, which was confirmed on CdTe Qdots in more recent years.[23,24] Additionally, despite well-established synthesis routes for various cadmium-based core/shell nanocrystals, only a few reports exist on multiphoton absorption in heterostructured nanocrystals.[13,25,26] It is however well known that moving from a single-composition CdSe Qdot to a heterostructured system can present several advantages. In our case for instance, CdSe/CdS quasi-type II heterorods are efficient emitters, with an emission wavelength that can be controlled almost independently from the growth of the CdS shell, which constitutes the major contribution to the absorption process. Moreover, the large shell volume can reduce the luminescence reabsorption, a common issue in optically thick samples, and the rod shape itself is known to provide linearly polarized absorption and emission.[27,28]

In this work we have explored the 2PA properties of core/shell Qrods and compared them to spherical CdSe core-only Qdots. From a practical perspective, the Qrod PL is more resistant to photobleaching than CdSe Qdots, and the growth of a long CdS Qrod shell over the CdSe core conveniently allows decoupling the PL emission spectrum from the enhanced 2PA at higher energies. More importantly however, the spectral dependence of the 2PPLE yields a significant blue shift for optical transitions in both the CdSe core and CdS shell spectral region. Experimental data are confirmed by $k \cdot p$ calculations, taking into account both the effect of band anisotropy (anisotropic hole masses) and the reduced symmetry of the confining potential, due to the rod shape of the CdS shell.

RESULTS AND DISCUSSION

Two-Photon Absorption Cross Section. In Figure 1a, we compare the luminescence spectrum of typical CdSe/CdS Qrods, excited under one- and two-photon conditions, respectively. There are no remarkable differences in the luminescence induced by the two different types of excitation. The 2PA-induced spectrum shows a red shift of the intensity maximum of 1.7 ± 0.1 nm, which can be explained by a slight difference in temperature of the sample, probably induced by the more intense irradiation during the nonlinear PL measurements. More importantly, a single-exponential PL decay is observed under both types of excitations (Figure 1b, sample HB2), with no remarkable difference in decay time. We obtained 12.1 ± 0.2 and 12.0 ± 0.1 ns for the one-photon and two-photon decay times, respectively (Figure 1b), with 2PA-induced decay times in the range 8–15 ns found for the other core/shell Qrods. These are all comparable

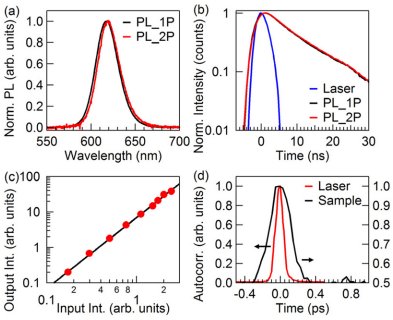

Figure 1. (a) Normalized fluorescence spectra of a typical CdSe/CdS Qrod sample, excited under one-photon (black curve, at 400 nm) and two-photon conditions (red curve, at 800 nm). The slight difference in the peak position can be ascribed to a small temperature increase of the sample under 2PA pumping. (b) Normalized fluorescence decay traces of CdSe/CdS Qrods (sample HB2), excited with nanosecond pulses. The one-photon-induced decay (red curve, excitation at 425 nm) compares well with the two-photon-induced decay (blue curve, excitation at 850 nm). The black curve gives the time response of the detector (equal to 1.8 ns). (c) Typical dependence of the 2PPLE on the input power (sample HB2). The line is a quadratic fit to the data points. (d) Femtosecond autocorrelation measurements at 800 nm for the laser pulses (red curve) and fluorescence of a CdSe/CdS Qrod sample (black curve). A Gaussian fit yields a peak width of 276 fs (full-width at half-maximum) for the latter, comparable to the laser pulse autocorrelation of 104 fs.

with the typical decay times reported for CdSe/CdS Qrods;[17,29] hence our findings are in agreement with the hypothesis that the 2PA creates a single electron–hole pair that relaxes *via* nonradiative intraband transitions to the band-edge, where it recombines predominantly radiatively.

The amplitude of the PL signal was well fitted with a quadratic dependence on the input power (Figure 1c). Such behavior was observed for all Qdot and Qrod samples, under both nanosecond and femtosecond excitation, with a power-law fit giving a value varying between 1.8 and 2.1. In order to further confirm that the 2PA of the sample is due to a pure nonlinear process rather than mediated by linear absorption *via* intermediate long-living trap states, an autocorrelation experiment was performed under femtosecond pulsed excitation (Figure 1d). In the experiment, two portions of the 800 nm laser beam are superposed in the sample cell, but their relative delay is varied. Since long-lived trap states in CdSe nanocrystals have a decay time of more than 100 ns (see Supporting Information, Figure S1), *i.e.*, far longer than the 100 fs pulse duration, the autocorrelation peak width supports a purely nonlinear effect not mediated by real states. The slightly larger full-width at half-maximum the measurement in the sample can be explained by a dispersion-induced temporal broadening of the pulse crossing the 1 mm sample thickness and by an increase of the region in

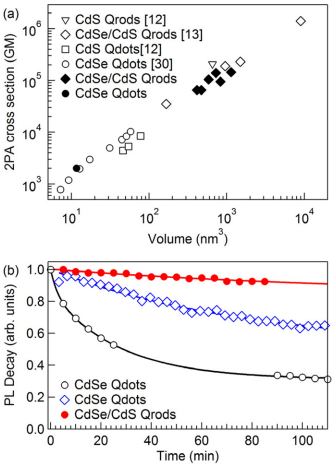

Figure 2. (a) 2PA cross section per particle for different samples (open symbols: literature results, full symbols: present data). The 2PA cross section increases linearly with particle volume in all cases. (b) Decay of two-photon-induced PL. Two typical examples of CdSe Qdots (open symbols) are compared to CdSe/CdS Qrods (full symbols), which show only a 10% drop in PL after 90 min of continuous illumination. Lines added as guide to the eye.

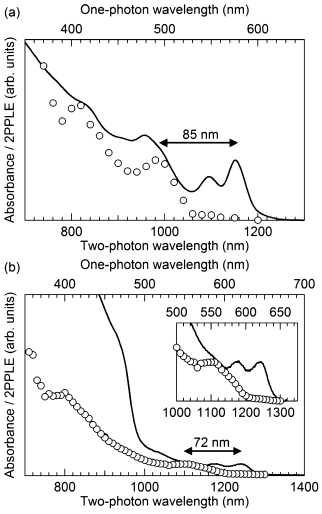

Figure 3. (a) Comparison of the absorbance (full line) and 2PPLE (symbols) spectra for a sample of 2.9 nm CdSe Qdots. A blue shift of 85 nm is observed for the first transition. (b) Absorbance (full line) and 2PPLE (symbols) spectrum for CdSe/CdS Qrods HB5. A blue shift of 72 nm is measured. Inset: Detail of the band-edge absorption. All samples, consisting of different core diameters and rod diameters and lengths, showed similar results (see Supporting Information, Figure S4).

which the two pulses are superposed inside the cuvette. Importantly, the results also allow us to safely extend the pulse duration to the ns-domain (as done for the measurement of the 2PA spectrum and cross section); as for 2PA, the pulse duration of the excitation laser merely influences the absolute amplitude of the two-photon-induced PL and does change the 2PA cross section.

At 800 nm, the 2PA cross section of our CdSe/CdS Qrods lies in the range of 10^5 GM (Figure 2a, see Table S1 in the Supporting Information for structural parameters of the Qrods). From a single-Qdot point of view, the results found here are consistent with those of Li *et al.*[12] and Xing *et al.*;[13] they reported a value of 2×10^5 GM (CdS Qrods) and $(0.3-14) \times 10^5$ GM (CdSe/CdS Qrods), respectively. We observed an enhancement of about 2 orders of magnitude for the 2PA cross section compared to a spherical CdSe Qdot sample, where we find a value of 2×10^3 GM. Except for CdTe Qdots,[30] data on spherical CdS,[12] CdSe,[30] and CdSe/CdS Qrods,[13] including the ones presented here, all show a linear dependence of the cross section on the nanocrystal volume (Figure 2a). The strong enhancement of 2PA cross sections for CdS and CdSe/CdS Qrods is therefore mainly due to the increased volume. Indeed, once normalized over the volume, results for the different CdSe/CdS Qrods measured lead to an average value of 150 ± 50 GM/nm^3, and data agree well with previous results obtained at 800 nm on CdS,[12] CdSe,[30] and CdSe/CdS heteronanocrystals.[13] They observed an average 2PA cross section of 100 ± 7, 150 ± 25, and 180 ± 30 GM/nm^3, respectively.

A comparison of the data for CdS Qdots, CdS Qrods, and CdSe/CdS Qrods suggests that the volume-normalized 2PA cross section is slightly larger for anisotropic Qrods than for spherical Qdots, which might be due to a reduced average screening of the electric field in rod-shaped nanocrystals. More importantly however, it should be stressed that the CdSe/CdS heteronanocrystals present the advantage of decoupling the emission wavelength from the nonlinear absorption provided by the CdS shell. Hence we can enhance the 2PA cross section for any predefined wavelength, while in single-composition Qdots and Qrods a large 2PA cross section can be obtained only in nanocrystals of higher volume, with concomitantly reduced quantum confinement and red-shifted emission. Furthermore, due to the growth of a CdS shell, the CdSe/CdS Qrods are much more resistant to photobleaching when exposed to continuous illumination, as their 2PA-induced PL typically does not vary by more than 10%, even after 90 min of excitation (Figure 2b). CdSe core Qdots on the other hand lost in some cases up to 70% of their initial PL after the same amount of time.

Two-Photon-Induced Excitation Spectrum. The large 2PA cross section at 800 nm combined with the control over the emission wavelength already highlights the

advantage of using heterostructured nanocrystals. Nevertheless, as we excite close to the CdS band edge, only the spectral dependence of the 2PA can reveal which wavelengths are most suitable for two-photon excitation. Moreover, the spectrum can yield a better understanding of the underlying opto-electronic band structure.[22−24,31] Figure 3 shows a typical 2PA spectrum (all measurements performed in tetrachloro ethylene, TCE, using ns-pulses) obtained on a sample of core/shell Qrods (b), compared to a spectrum for a typical CdSe Qdot suspension (a). In both cases, the one-photon absorption spectrum is shown in the same graph as well. The 2PA spectra obtained on CdSe Qdots with diameters varying from 2.5 to 4 nm (see Supporting Information, Figure S3) are comparable with previous literature reports. They show a first 2PA peak at an energy that is higher with respect to the energy for the first one-photon absorption peak. The blue shift of 85 nm agrees perfectly with values reported in similar measurements at 5 K.[22,32] Remarkably, similar results are obtained on the Qrod samples: the nonlinear absorption of the core is strongly blue-shifted compared to the linear spectrum, and also in the region of the CdS shell transitions, the onset of 2PA starts at an energy that is noticeably higher than the corresponding absorption edge observed under one-photon excitation.

It is well known that the differences in the one- and two-photon absorption spectra arise from the different selection rules that these transitions have to obey. In the dipole approximation, only transitions coupling electron and hole states characterized by the same angular momentum are allowed *via* one-photon absorption (1PA), while different selection rules apply for 2PA, which leads to different absorption peaks in the spectra.[22,32] For spherical Qdots, the first peak is generally blue-shifted in the case of 2PA. In fact, additional transitions observed for PbSe and PbS Qdots, resonant with dipole-allowed 1PA peaks, triggered a long-standing debate in the literature whether they were due to a reduced symmetry of the confining potential in these crystals or if the results could be explained by band structure anisotropy, with a substantial amount of experimental evidence and theoretical calculations supporting both hypotheses.[20,33−35] The data suggest that, although band anisotropy cannot be neglected, as it gives rise to additional transitions due to a splitting of the electron and hole P-states, only the inclusion of symmetry breaking leads to an enhancement of 2PA at the spectral position where the first one-photon transition is observed.[21]

***k*·*p* Calculations.** To obtain a better understanding of the selection rules that govern the blue shift of the 2PA spectrum in anisotropic CdSe/CdS Qrods, and the nature of the transitions at wavelengths below the CdS 1PA onset, we used one-band $k\cdot p$ calculations. We modeled three different structures and compared their theoretical 1PA and 2PA with the experimental values: (i) a core-only Qdot with diameter 4.4 nm; (ii) a heterorod with a small core (sample HB1, see Table 1); and (iii) a heterorod with a large core (sample HB5). The corresponding low-lying energy levels are plotted in Figure 4a, 4b, and 4c, respectively.

TABLE 1. Structural Parameters of the CdSe/CdS Qrods Used for the 2PPLE Spectra, As Determined by TEM

sample	core diameter, nm	rod diameter, nm	rod length, nm
HB1	2.5	4.5	20
HB2	3.8	5.8	35
HB3	3.8	5.8	23
HB4	3.4	4.2	22
HB5	5.0	5.2	28

Because all three structures have axial symmetry, the electron and hole states can be labeled as $(n,m)_j$, where $n = 1, 2, 3, \ldots$ is the main quantum number, $m = 0, \pm1, \pm2, \ldots$ is the envelope angular momentum projection, and j = e, h stands for electron or hole. For states confined to the core, we also give the conventional notation of spherically symmetric states, nL_j, where L = S, P, D, ... represents the envelope angular momentum. Owing to the anisotropic hole masses, the P_h shell is split into $P_{h|}$ and $P_{h\perp}$. Instead, the conduction band is nearly isotropic, so the P_e shell does not split. This is in contrast with PbSe and PbS Qdots, where both the conduction and valence band are anisotropic.[21] We note that strictly speaking there are no states truly confined to the core or the shell, as there is always some part of the wave function leaking into the entire heterostructure. However, we find that some electron and hole states are *mainly* confined to the spherical core, even at energies exceeding the respective band offsets. In Figure 4, we label these states using both axial and spherical notation. One can see that the Qrod HB1—where the core is only 2.5 nm—behaves as a quasi-type II heterostructure, with only the ground state of electrons ($1S_e$) and a few of the lowest lying states of holes ($1S_h$ and $1P_h$) confined to the core and the other states delocalized over the rod. By contrast, in HB5 the core is 5 nm, and it can host also $1P_e$ and higher excited electron and hole states.

The vertical arrows in Figure 4 show the dipole-allowed 1PA (red, solid lines) and 2PA (black, dashed lines) transitions. For spherical Qdots the selection rules are usually understood in terms of conservation of the even/odd parity with respect to the inversion symmetry.[21] When the symmetry is lowered to $C_{\infty v}$, as in our Qrod heterostructures, the only selection rule remaining is related to the conservation of the azimuthal angular momentum m. For 1PA processes the selection rule is given by $\Delta m = m_e - m_h = 0$, and for 2PA processes it is given by $\Delta m = 0, \pm1$.

When analyzing the absorption spectra, one finds that many allowed transitions turn out to have very weak intensity. This can be understood by considering

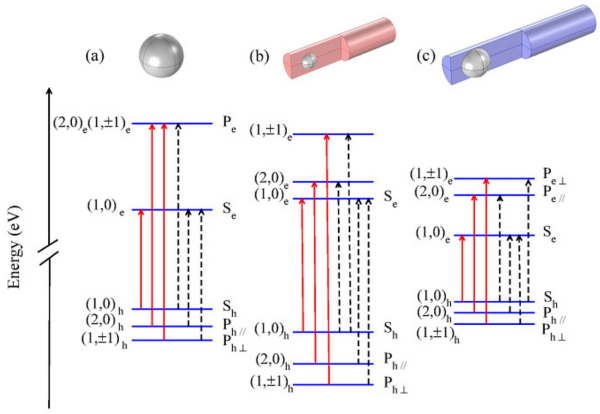

Figure 4. Near-gap energy levels and 1PA (red, solid arrows) and 2PA (black, dashed arrows) dipole-allowed transitions for (a) a core-only quantum dot with a diameter of 4.4 nm, (b) a heterorod with a small core (sample HB1 in Table 1), and (c) a heterorod with a large core (sample HB5). The states localized near the core are labeled with both axial and spherical symmetry notations.

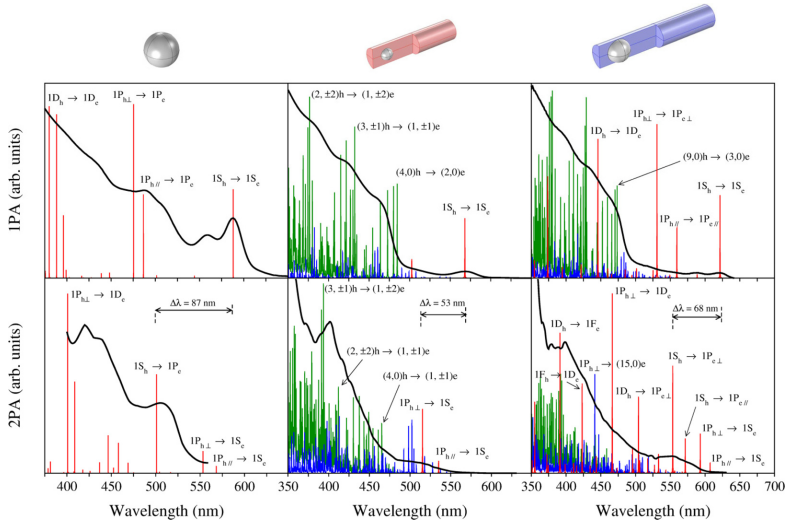

Figure 5. 1PA (top) and 2PA (bottom) experimental and calculated spectra for the CdSe Qdots (left), CdSe/CdS Qrods HB1 (middle), and CdSe/CdS Qrods HB5 (right). To facilitate the comparison between linear and nonlinear resonances, the wavelength in the horizontal axis has been set equal to the photon wavelength for the 1PA spectra and to half the photon wavelength for the 2PA spectra. The calculated absorptions are colored according to the location of the initial and final states involved in the transition: dot−dot (red), dot−rod (blue), and rod−rod (green). Black lines represent the experimental data.

that the potential felt by low-energy states confined to the core is essentially that of a sphere with inversion symmetry. Parity is then an approximate quantum number. The same occurs with high-energy states of the rod that barely feel the core potential. This adds new restrictions to the selection rules above. Namely, for 1PA (2PA) transitions the parity of the initial and final states must be the same (different). Figure 5 shows the calculated 1PA and 2PA for the three structures under study compared to the experimental measurements. Some of the main transitions are labeled by the quantum numbers of the initial (hole) and final (electron) state, using spherical notation for states localized in the core.

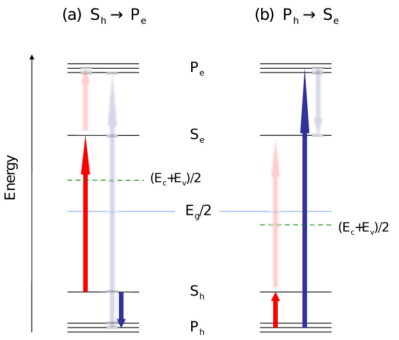

Figure 6. Most important excitation paths contributing to the 2PA transition rate of (a) $1S_h \rightarrow 1P_e$ and (b) $1P_h \rightarrow 1S_e$ absorptions. Red and blue arrows are used for different paths. The bright arrow shows the transition to the intermediate state in each case.

We start by analyzing the absorption spectrum of the spherical Qdots (left panels). The 1PA spectrum shows that the low-energy experimental resonances can be explained fairly well by the $1S_h \rightarrow 1S_e$, $1P_h \rightarrow 1P_e$, and $1D_h \rightarrow 1D_e$ transitions. Only the second absorption peak (near $\lambda \sim 560$ nm) misses a clear assignment. Previous studies have predicted the $2S_h \rightarrow 1S_e$ transition next to the fundamental one.[22,36] This transition is suppressed in our model by the spherical symmetry and strong confinement, which leads to nearly orthogonal $2S_h$ and $1S_e$ states. However, recent experimental data suggest that this transition is influenced by both the Qdot crystal structure and organic ligands;[37] hence surface functionalization and related atomic rearrangements of the nanocrystal surface, which are not captured by our theoretical model, may change the $2S_h \rightarrow 1S_e$ oscillator strength. In the 2PA spectrum, the low-energy peaks can be well described by the transitions between 1P and 1S states of electrons and holes. The most important result here is that the experimental blue shift between the first intense 1PA and 2PA peaks is in good agreement with the theoretical shift between $1S_h \rightarrow 1S_e$ and $1S_h \rightarrow 1P_e$ transitions ($\Delta\lambda \sim 87$ nm, see figure). Interestingly, there are dipole-allowed 2PA transitions at lower energy (namely $1P_{h\perp} \rightarrow 1S_e$ and $1P_{h\parallel} \rightarrow 1S_e$), which would translate into smaller blue shifts. However, these turn out to be much weaker than the $1S_h \rightarrow 1P_e$ transition. This can be understood from the denominator in the perturbational estimate of the transition rate, W_{2PA} (see eq 2). The strongest 2PA transitions are those where the intermediate state energy is close to that of the resonant photon, $E_i \approx (E_v + E_c)/2$. As illustrated in Figure 6a, the $1S_h \rightarrow 1P_e$ transition takes place mainly through the intermediate states $1S_e$ and $1P_h$, while the $1P_h \rightarrow 1S_e$ transition (Figure 6b) takes place mainly through $1S_h$ and $1P_e$. Because electron states have a larger energy splitting, one can easily see that the intermediate state $1S_e$ is closest to the resonance condition (dashed line).

Next, we analyze the absorption of heterorods. Central panels in Figure 5 show the spectra of sample HB1. The 1PA peaks are well reproduced by the theoretical transitions. Because the core of this structure is 2.5 nm, only the lowest energy transition involves states localized in the core ($1S_h \rightarrow 1S_e$). Most of the higher energy peaks arise from states essentially localized in the rod. Since the longitudinal confinement of the rod is weak, there are bunched groups of states with similar energy, which share the same angular momentum m but have different n (*i.e.*, number of nodes in the growth direction). This gives rise to branches of transitions for each m, *e.g.*, those dominated by $(4,0)_h \rightarrow (2,0)_e$, starting at $\lambda \approx 490$ nm, or those dominated by $(3,1)_h \rightarrow (1,1)_e$, starting at $\lambda \approx 430$ nm. The 2PA spectrum of HB1 is more complicated than that of the simple Qdot because the CdS shell provides a high density of intermediate states. The fundamental transition is now $1P_{h\perp} \rightarrow 1S_e$, because the $1P_e$ state is no longer localized in the core. The blue shift of this transition with respect to the fundamental 1PA one is ~53 nm, slightly reduced compared to the shift observed in core-only CdSe Qdots, and again close to the experimental value. A significant shift is also observed in the CdS shell absorption region between the sharp onset of the high-energy 1PA absorption and the most intense 2PA transitions, consistent with the experimental data. In this region, the intensity of 1PA transitions increases swiftly whenever the resonant photon reaches a new m shell, which translates into a steep increase of the 1PA spectrum. Conversely, the increase of the 2PA intensities is more gradual, explaining the gentler slope of this spectrum.

The fact that the $(3,1)_h \rightarrow (1,2)_e$ transition dominates the 2PA—giving rise to the shell blue shift with respect to the 1PA spectrum—may be surprising because there are other symmetry-allowed two-photon transitions at lower energy. Yet, the oscillator strength of these transitions is much weaker. The reason is similar to that argued in Figure 6 for the CdSe Qdot transitions. Namely, transitions between states near the band edge necessarily imply intermediate states with large values of $E_i - (E_v + E_c)/2$. These imply large denominators in W_{2PA} and are generally inefficient. However, if the initial or final states are excited, intermediate states close to $(E_v + E_c)/2$ become available and W_{2PA} is greatly enhanced.

Right panels in Figure 5 show the absorption spectra of the system HB5. Even though there are a few discrepancies when comparing to the experimental measurements (for example, for 1PA the strong $1P_{h\perp} \rightarrow 1P_{e\perp}$ transition is not observed at the predicted energy), the general features are again consistent. In particular, due to the reduced confinement in HB5 (core diameter 5.0 nm) compared to HB1 (core diameter of 2.5 nm), the

$1P_{h\perp} \rightarrow 1S_e$ and $1P_{h\parallel} \rightarrow 1S_e$ 2PA transitions are clearly closer to the fundamental $1S_e \rightarrow 1S_h$ 1PA transition (31 nm blue shift). However, the larger CdSe core diameter also gives rise to electron P-states confined to the core, yielding additional strong $1S_h \rightarrow 1P_e$ 2PA transitions in the CdSe band-edge spectral region. Moreover, in HB5 the core diameter is similar to that of the rod. Unlike for HB1, the energy scales of the core and rod states are comparable, leading to mutual interactions and a spectrum that is not just the direct sum of the two parts of the heterostructure. As a result, the $1P_e$ state splits into $1P_{e\perp}$ and $1P_{e\parallel}$, not because of the mass anisotropy (as was the case for holes) but because of the asymmetric shell. Consequently, the fundamental 2PA transition is not simply $1S_h \rightarrow 1P_e$, as expected for core-only structures (left panels). Instead, we calculate a low-energy $1S_h \rightarrow 1P_{e\parallel}$ transition and a high-energy $1S_h \rightarrow 1P_{e\perp}$ transition at $\lambda \sim 575$ nm and $\lambda \sim 555$ nm, respectively. As the oscillator strength of the $1S_h \rightarrow 1P_{e\parallel}$ transition is 3 times weaker than the $1S_h \rightarrow 1P_{e\perp}$, the resulting 68 nm blue shift between the fundamental $1S_h \rightarrow 1S_e$ 1PA transition and the $1S_h \rightarrow 1P_e$ 2PA manifold is again in good agreement with experimental data. Clearly, compared to single-composition Qdots, quasi-type II heterostructures, with a varying number of states localized near the core region depending on the extent of quantum confinement, provide an interesting additional mechanism to control the 2PA absorption spectrum (*in casu* the large blue shift between the fundamental 1PA and 2PA transitions).

Also in the spectral region of the shell absorption, the similar core and shell diameter gives rise to synergistic effects. Here, the spectrum comprises not only rod-to-rod transitions (colored green in Figure 5) but now also dot-to-rod (blue) and even dot-to-dot (red) ones. In fact, transitions between high-energy states of the core have a non-negligible contribution to the high-energy absorption. Altogether, dot-to-rod and dot-to-dot absorptions amount up to 21% of the total 1PA in the CdS shell absorption region (resonant energies above the CdS band gap). This percentage increases up to 42% in the case of 2PA, of which 22% corresponds to high-energy dot-to-dot transitions. Figure 7 illustrates the states involved in the three types of high-energy absorptions. The most intense rod-to-rod transitions take place between states localized mainly in the shell (Figure 7a). These exhibit negligible tails in the core, which gather most nodes to warrant orthogonality with the lower lying core state(s) with the same azimuthal symmetry. By contrast, the relevant dot-to-rod transitions (Figure 7b) may involve a delocalized state that spreads uniformly throughout the entire heterostructure. These transitions gain significance in the nonlinear spectrum owing to the participation of intermediate states, thus overcoming the small overlap between the initial and final states that limits their contribution to the linear absorption. But perhaps the most striking finding is the presence of intense dot-to-dot transitions at energies exceeding the CdS band gap. The reason is that one (typically the electron) or even both states involved in the transition can lie above the corresponding band offset and yet remain mainly localized in the core region. This counterintuitive result can be understood by considering that, owing to (i) the similar diameter of the core and the shell and (ii) the large anisotropy of the confining potential, the lowest lying states of each symmetry *m* can be described in the adiabatic approximation. Thus, the weak longitudinal confinement can be reasonably assumed to be decoupled from the strong in-plane one. The electron (or hole) in a given in-plane state of motion moves then in an effective 1D heterorod potential, but that is offset from the corresponding band edge by an amount given by the energy of the in-plane motion. As a consequence, at

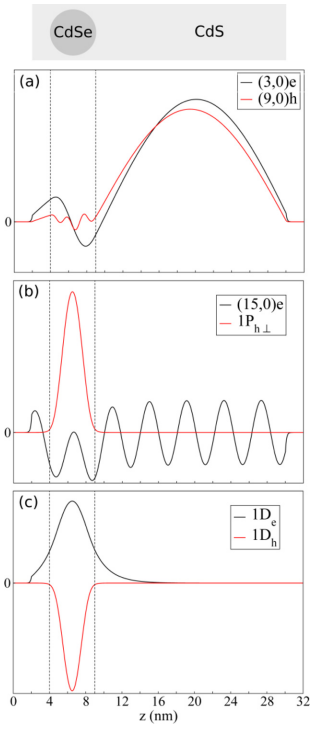

Figure 7. Typical examples of the longitudinal profiles of the initial and final states involved in the three types of absorptions arisen in CdSe/CdS Qrod HB5 beyond the CdS gap: (a) rod-to-rod, (b) dot-to-rod, and (c) dot-to-dot transitions. Vertical dashed lines indicate the Qdot spatial limits. The Qdot and Qrod nomenclature refers only to the region where the corresponding states of the system are mainly localized.

least the ground state of each symmetry *m* turns out to be mainly localized in the core region regardless of the associated in-plane energy, which can easily overcome the band offset.

Figure 7c shows the states involved in a typical dot-to-dot transition showing up above the CdS band gap. It is worth noticing that the electron wave function shows an asymmetric leakage into the rod region, a feature also shared by the ground and lowest lying electron states below the band offset. Despite such asymmetry, neither the experimental nor the simulated data reveal signatures of parity symmetry breaking in these states.[38] The reason is connected with the strong localization of the hole in the dot. Only the region where the electron and hole wave functions overlap contributes to the transition rates (see matrix elements in eqs 1 and 2), and inside the Qdot core the electron wave function is almost symmetric (see Figure 7c). Hence, despite the explicit presence of an anisotropic electron wave function induced by the electron delocalization in the shell, our experimental and theoretical data on the different CdSe/CdS core/shell Qrods do not reveal any spectral evidence for symmetry breaking. Experiments thus suggest that it has a material-dependent origin, being stronger in PbS and PbSe Qdots, compared to cadmium-based materials such as the CdSe Qdots and CdSe/CdS Qrods. Since in CdSe the exciton Bohr radius is around 5.5 nm, while for PbS and PbSe it is 4 and 8 times higher, respectively, the lower extent of quantum confinement in CdSe/CdS Qrods may lie at the origin of the differences observed.

CONCLUSIONS

We have measured 2PPLE spectra on CdSe Qdots and CdSe/CdS core/shell Qrods having different lengths and rod and core diameters. We observed that 2PA in nanocrystals is an intrinsically nonlinear phenomenon; that is, it does not involve transitions through long-living interband trap states. The absolute values of the cross section are in the range of 10^5 GM in the heterostructured Qrod samples, consistent with results on similar Qrod samples in the literature[12,13] and with the clear advantage of independent control over the emission wavelength and the 2PA absorption cross section. It suggests a large potential for such structures in multiphoton excitation applications such as bioimaging or as nonlinear gain media. 2PA spectra from our CdSe/CdS heterorod samples show transitions that are blue-shifted in energy. We did not find evidence of selection rule violations, despite the explicit inclusion of a reduced symmetry of the confining potential *via* the anisotropic shape of the quasi-type II Qrod. This reinforces the hypothesis that the breaking of the optical selection rules is observed only under conditions of exceptionally strong quantum confinement, as is the case in lead chalcogenide Qdots, rather than merely an asymmetrical shape of the crystal.

The numerical simulations of the dipole-allowed transitions based on effective mass models show a good agreement with the experimental data and corroborate that the observed blue shifts are a consequence of (i) the different selection rules that apply to 1PA and 2PA transitions despite the valence band and confinement anisotropies and (ii) the reduced oscillator strength of low-energy two-photon transitions. Furthermore, the blue shift can be controlled by the degree of quantum confinement in quasi-type II Qrods, more specifically by localizing also the electron P-states near the CdSe core region, which gives rise to a strong $1S_h \rightarrow 1P_e$ transition.

The calculations finally reveal a rich interplay between the core and shell transitions of the heterorods. This becomes apparent in the high-energy absorption, which comprises not only rod-to-rod but also dot-to-rod and even dot-to-dot transitions with a non-negligible contribution. The latter ones involve electron and hole states which are mainly localized in the spherical core despite energetically exceeding the band offset, a result that can be understood only by considering the heterorod as a unique system, more complex than the mere sum of its constituents.

METHODS

CdSe core Qdots and CdSe/CdS core/shell Qrods were synthesized according to established literature methods. The Qrod diameter and length were determined by transmission electron microscopy (TEM), giving lengths ranging from 20 to 60 nm and diameters spanning 4 to 7 nm (average values, obtained by measuring the dimensions of at least 100 particles). Properties of the Qrod samples used for the 2PPLE measurements are summarized in Table 1. After synthesis, they were dispersed in toluene or TCE, depending on the 2PA wavelengths examined (toluene shows distinct absorption peaks beyond 1100 nm, requiring the use of optically transparent TCE). Typical Qdot/Qrod concentrations in the optical experiments varied between 5 and 20 nM for the rods and between 20 and 200 nM for the dots. The concentration was determined using the absorption of the Qdot/Qrod solution at 295 nm, according to methods described in ref 39. Briefly, it is calculated taking into account the different local field factors associated with their respective size and shape and using the optical constants of bulk CdSe[40] and CdS.[41]

For the 2PPLE spectroscopy, we used a laser beam coming from an optical parametric oscillator operating in the nanosecond regime (Vibrant IIE, OPOTEK, 410−2000 nm wavelength range, 10 Hz repetition rate, maximum energy per pulse of 6 mJ). The beam was focused to a diameter of approximately 1 mm in the center of a 10 mm thick quartz cell. Two-photon-induced PL from the sample was collected at a 90° angle with respect to the excitation. Alternatively, an amplified Ti:Sapphire laser (Coherent, 800 nm wavelength, 1 kHz repetition rate, maximum energy per pulse of 30 μJ) was used in the same geometry. Again, the excitation beam was focused in the optical cell, here to a spot size of approximately 0.5 mm.

The PL was collected by a photomultiplier tube (PMT) coupled to an oscilloscope. The PMT was continuously calibrated against a reference photodiode that collected part of the incoming beam using a 5% beamsplitter. The photodiode response itself was quantified with a power meter for the femtosecond laser and with an energy meter for the nanosecond laser, placed just in front of the sample position. In each measurement series, to ensure that samples were unaffected by the strong excitation intensity, we verified that luminescence spectra and decay lifetimes of the Qrods, obtained *via* 2PA at 800 nm, were comparable to the luminescence spectra obtained by one-photon-induced PL employing a 400 nm light source.

At all wavelengths, we verified the quadratic dependence of the 2PA by measuring the PL signal as function of input power. To determine the absolute 2PA cross section of the Qrods, the 2PA cross section of rhodamine B in methanol was used as a reference.[42] Luminescence signals were normalized over the respective concentrations of the samples and over the emission quantum efficiency of samples and reference dye.

Numerical simulations of 1PA and 2PA transition rates were obtained from first- and second-order Fermi golden rules:

$$W_{1PA} = \frac{2\pi}{\hbar}\sum_{c,v}|\langle c|\mathbf{e}\cdot\mathbf{p}|v\rangle|^2\delta(E_c - E_v) \quad (1)$$

and

$$W_{2PA} = \frac{2\pi}{\hbar}\sum_{c,v}\left|\sum_i \frac{\langle c|\mathbf{e}\cdot\mathbf{p}|i\rangle\langle i|\mathbf{e}\cdot\mathbf{p}|v\rangle}{E_i - E_v - h\nu}\right|^2 \delta(E_c - E_v - 2h\nu) \quad (2)$$

where $h\nu$ is the photon energy, e is the polarization vector of the light, c and v are the final (conduction band) and initial (valence band) states, and i labels the intermediate states of the two-photon transition, which are the one-photon accessible states in the valence or conduction bands.

Electron and hole states in eqs 1 and 2 were calculated within the $k\cdot p$ formalism in the single-band, single-particle approximation. This simple model captures the effect of the confinement strength and symmetry, which suffices to explain the experimentally observed blue shifts.[43] In cylindrical coordinates and atomic units, the corresponding three-dimensional effective mass Hamiltonians read[44]

$$H_j = -\frac{1}{2\rho}\frac{\partial}{\partial\rho}\left(\frac{\rho}{m^*_{j,\rho}(\rho,z)}\frac{\partial}{\partial\rho}\right) - \frac{1}{2}\frac{\partial}{\partial z}\frac{1}{m^*_{j\parallel}(\rho,z)}\frac{\partial}{\partial z} + \frac{m_j^2}{\rho^2 m^*_{j\perp}(\rho,z)} + V_j(\rho,z) \quad (3)$$

In eq 3, j = e, h denotes the electron and hole, respectively, m_j is the azimuthal angular momentum, and $V_j(\rho,z)$ is the spatial confinement potential. At the CdSe/CdS interface, $V_j(\rho,z)$ presents a step-like profile determined by the corresponding band offset. $m^*_{j\perp}(\rho,z)$ and $m^*_{j\parallel}(\rho,z)$ are the position-dependent transversal and longitudinal effective masses, respectively. The valence band anisotropy of both CdSe and CdS leads to anisotropic hole masses, which are heavier along the longitudinal (growth) direction. We used $m^*_{h\parallel} = 1.19m_0$ and $m^*_{h\perp} = 0.48m_0$.[45] In contrast, the electron effective mass can be considered isotropic in the conduction band, though different for core ($m^*_{e,CdSe} = 0.13m_0$) and shell ($m^*_{e,CdS} = 0.17m_0$) materials.[45,46] The CdSe core was modeled as a sphere embedded in a cylindrical CdS shell, 2 nm away from its base (see insets in Figure 4). The valence band offset at the heterojunction is 0.44 eV, and the conduction band offset is 0.3 eV.[6,45,46] The whole structure is surrounded by a 4 eV potential barrier. By means of a finite differences scheme, the Hamiltonians in eq 3 were integrated numerically to obtain electron and hole energies and wave functions. Finally, the energy gap was taken so as to fit the fundamental $1S_h \rightarrow 1S_e$ transition with the energy of the first experimental 1PA peak.

Conflict of Interest: The authors declare no competing financial interest.

Supporting Information Available: Structural parameters of the CdSe/CdS Qrods used for the measurement of the 2PA cross section, CdSe photoluminescence lifetime of the trap emission, and estimated effect of long-lived trap states on the fluorescence autocorrelation, additional 2PPLE spectra for CdSe core Qdots and CdSe/CdS core/shell Qrods, plots of the relevant electron and hole wave functions, and assessment of the effect of Coulomb interactions and a reduced conduction band offset in the $k\cdot p$ calculations. This material is available free of charge *via* the Internet at http://pubs.acs.org.

Acknowledgment. F. De Donato is acknowledged for providing CdSe and CdSe/CdS nanocrystal samples. The research leading to these results has received funding from the European Union's Seventh Framework Program (FP7/2007-2013) under REA grant agreement no. PIEF-GA-2011-298022 (NIRPLANA). Support from MICINN project CTQ-2011-27324, UJI-Bancaixa projects P1-1A2009-03 and P1-1B2011-01, and the Spanish FPI (MICINN) program (A.B.) is also acknowledged.

REFERENCES AND NOTES

1. Efros, A. L.; Rosen, M.; Kuno, M.; Nirmal, M.; Norris, D. J.; Bawendi, M. Band-Edge Exciton in Quantum Dots of Semiconductors with a Degenerate Valence Band: Dark and Bright Exciton States. *Phys. Rev. B* **1996**, *54*, 4843–4856.
2. Efros, A. L.; Rosen, M. The Electronic Structure of Semiconductor Nanocrystals. *Annu. Rev. Mater. Sci.* **2000**, *30*, 475–521.
3. Allan, G.; Delerue, C. Confinement Effects in PbSe Quantum Wells and Nanocrystals. *Phys. Rev. B* **2004**, *70*, 245321.
4. An, J. M.; Franceschetti, A.; Dudiy, S. V.; Zunger, A. The Peculiar Electronic Structure of PbSe Quantum Dots. *Nano Lett.* **2006**, *6*, 2728–2735.
5. Tischler, J. G.; Kennedy, T. A.; Glaser, E. R.; Efros, A. L.; Foos, E. E.; Boercker, J. E.; Zega, T. J.; Stroud, R. M.; Erwin, S. C. Band-Edge Excitons in PbSe Nanocrystals and Nanorods. *Phys. Rev. B* **2010**, *82*, 245303.
6. Steiner, D.; Dorfs, D.; Banin, U.; Della Sala, F.; Manna, L.; Millo, O. Determination of Band Offsets in Heterostructured Colloidal Nanorods Using Scanning Tunneling Spectroscopy. *Nano Lett.* **2008**, *8*, 2954–2958.
7. Brovelli, S.; Schaller, R. D.; Crooker, S. A.; García-Santamaría, F.; Chen, Y.; Viswanatha, R.; Hollingsworth, J. A.; Htoon, H.; Klimov, V. I. Nano-Engineered Electron–Hole Exchange Interaction Controls Exciton Dynamics in Core–Shell Semiconductor Nanocrystals. *Nat. Commun.* **2011**, *2*, 280.
8. Ithurria, S.; Tessier, M. D.; Mahler, B.; Lobo, R. P. S. M.; Dubertret, B.; Efros, A. L. Colloidal Nanoplatelets with Two-Dimensional Electronic Structure. *Nat. Mater.* **2011**, *10*, 936–941.
9. Rainò, G.; Stöferle, T.; Moreels, I.; Gomes, R.; Hens, Z.; Mahrt, R. F. Controlling the Exciton Fine Structure Splitting in CdSe/CdS Dot-in-Rod Nanojunctions. *ACS Nano* **2012**, *6*, 1979–1987.
10. Dang, C.; Lee, J.; Breen, C.; Steckel, J. S.; Coe-Sullivan, S.; Nurmikko, A. Red, Green and Blue Lasing Enabled by Single-Exciton Gain in Colloidal Quantum Dot Films. *Nat. Nanotechnol.* **2012**, *7*, 335–339.
11. Carbone, L.; Nobile, C.; Giorgi, M. De; Della Sala, F.; Morello, G.; Pompa, P.; Hytch, M.; Snoeck, E.; Fiore, A.; Franchini, I. R.; *et al*. Synthesis and Micrometer-Scale Assembly of Colloidal CdSe/CdS Nanorods Prepared by a Seeded Growth Approach. *Nano Lett.* **2007**, *7*, 2942–2950.
12. Li, X.; Embden, J.; van; Chon, J. W. M.; Gu, M. Enhanced Two-Photon Absorption of CdS Nanocrystal Rods. *Appl. Phys. Lett.* **2009**, *94*, 103117.
13. Xing, G.; Chakrabortty, S.; Chou, K. L.; Mishra, N.; Huan, C. H. A.; Chan, Y.; Sum, T. C. Enhanced Tunability of the Multiphoton Absorption Cross-Section in Seeded CdSe/CdS Nanorod Heterostructures. *Appl. Phys. Lett.* **2010**, *97*, 061112.
14. Larson, D. R.; Zipfel, W. R.; Williams, R. M.; Clark, S. W.; Bruchez, M. P.; Wise, F. W.; Webb, W. W. Water-Soluble Quantum Dots for Multiphoton Fluorescence Imaging in Vivo. *Science* **2003**, *300*, 1434–1436.

15. Jasieniak, J. J.; Fortunati, I.; Gardin, S.; Signorini, R.; Bozio, R.; Martucci, A.; Mulvaney, P. Highly Efficient Amplified Stimulated Emission from CdSe-CdS-ZnS Quantum Dot Doped Waveguides with Two-Photon Infrared Optical Pumping. *Adv. Mater.* **2008**, *20*, 69–73.
16. Todescato, F.; Fortunati, I.; Gardin, S.; Garbin, E.; Collini, E.; Bozio, R.; Jasieniak, J. J.; Della Giustina, G.; Brusatin, G.; Toffanin, S.; *et al*. Distributed Feedback Laser: Soft-Lithographed Up-Converted Distributed Feedback Visible Lasers Based on CdS-CdZnS-ZnS Quantum Dots. *Adv. Funct. Mater.* **2012**, *22*, 337–344.
17. Xing, G.; Liao, Y.; Wu, X.; Chakrabortty, S.; Liu, X.; Yeow, E. K. L.; Chan, Y.; Sum, T. C. Ultralow-Threshold Two-Photon Pumped Amplified Spontaneous Emission and Lasing from Seeded CdSe/CdS Nanorod Heterostructures. *ACS Nano* **2012**, *6*, 10835–10844.
18. Li, X.; Bullen, C.; Chon, J. W. M.; Evans, R. A.; Gu, M. Two-Photon-Induced Three-Dimensional Optical Data Storage in CdS Quantum-Dot Doped Photopolymer. *Appl. Phys. Lett.* **2007**, *90*, 161116.
19. Dallari, W.; Scotto d'Abbusco, M.; Zanella, M.; Marras, S.; Manna, L.; Diaspro, A.; Allione, M. Light-Induced Inhibition of Photoluminescence Emission of Core/Shell Semiconductor Nanorods and Its Application for Optical Data Storage. *J. Phys. Chem. C* **2012**, *116*, 25576–25580.
20. Peterson, J. J.; Huang, L.; Delerue, C.; Allan, G.; Krauss, T. D. Uncovering Forbidden Optical Transitions in PbSe Nanocrystals. *Nano Lett.* **2007**, *7*, 3827–3831.
21. Nootz, G.; Padilha, L. A.; Olszak, P. D.; Webster, S.; Hagan, D. J.; Stryland, E. W. V.; Levina, L.; Sukhovatkin, V.; Brzozowski, L.; Sargent, E. H. Role of Symmetry Breaking on the Optical Transitions in Lead-Salt Quantum Dots. *Nano Lett.* **2010**, *10*, 3577–3582.
22. Blanton, S. A.; Hines, M. A.; Schmidt, M. E.; Guyot-Sionnest, P. Two-Photon Spectroscopy and Microscopy of II-VI Semiconductor Nanocrystals. *J. Lumin.* **1996**, *70*, 253–268.
23. Padilha, L. A.; Fu, J.; Hagan, D.; Stryland, E.; Van; Cesar, C.; Barbosa, L.; Cruz, C. Two-Photon Absorption in CdTe Quantum Dots. *Opt. Express* **2005**, *13*, 6460–6467.
24. Qu, Y. L.; Ji, W. Two-Photon Absorption of Quantum Dots in the Regime of Very Strong Confinement: Size and Wavelength Dependence. *J. Opt. Soc. Am. B* **2009**, *26*, 1897–1904.
25. Xing, G.; Ji, W.; Zheng, Y.; Ying, J. Y. Two- and Three-Photon Absorption of Semiconductor Quantum Dots in the Vicinity of Half of Lowest Exciton Energy. *Appl. Phys. Lett.* **2008**, *93*, 241114.
26. Xing, G.; Chakrabortty, S.; Ngiam, S. W.; Chan, Y.; Sum, T. C. Three-Photon Absorption in Seeded CdSe/CdS Nanorod Heterostructures. *J. Phys. Chem. C* **2011**, *115*, 17711–17716.
27. Hu, J.; Li, L.; Yang, W.; Manna, L.; Wang, L.; Alivisatos, A. P. Linearly Polarized Emission from Colloidal Semiconductor Quantum Rods. *Science* **2001**, *292*, 2060–2063.
28. Kan, S.; Mokari, T.; Rothenberg, E.; Banin, U. Synthesis and Size-Dependent Properties of Zinc-Blende Semiconductor Quantum Rods. *Nat. Mater.* **2003**, *2*, 155–158.
29. Rainò, G.; Stöferle, T.; Moreels, I.; Gomes, R.; Kamal, J. S.; Hens, Z.; Mahrt, R. F. Probing the Wave Function Delocalization in CdSe/CdS Dot-in-Rod Nanocrystals by Time- and Temperature-Resolved Spectroscopy. *ACS Nano* **2011**, *5*, 4031–4036.
30. Pu, S.-C.; Yang, M.-J.; Hsu, C.-C.; Lai, C.-W.; Hsieh, C.-C.; Lin, S. H.; Cheng, Y.-M.; Chou, P.-T. The Empirical Correlation Between Size and Two-Photon Absorption Cross Section of CdSe and CdTe Quantum Dots. *Small* **2006**, *2*, 1308–1313.
31. Padilha, L. A.; Nootz, G.; Olszak, P. D.; Webster, S.; Hagan, D. J.; Stryland, E. W. V.; Levina, L.; Sukhovatkin, V.; Brzozowski, L.; Sargent, E. H. Optimization of Band Structure and Quantum-Size-Effect Tuning for Two-Photon Absorption Enhancement in Quantum Dots. *Nano Lett.* **2011**, *11*, 1227–1231.
32. Schmidt, M. E.; Blanton, S. A.; Hines, M. A.; Guyot-Sionnest, P. Size-Dependent Two-Photon Excitation Spectroscopy of CdSe Nanocrystals. *Phys. Rev. B* **1996**, *53*, 12629–12632.
33. Franceschetti, A.; Luo, J. W.; An, J. M.; Zunger, A. Origin of One-Photon and Two-Photon Optical Transitions in PbSe Nanocrystals. *Phys. Rev. B* **2009**, *79*, 241311.
34. Goupalov, S. V. Selection Rules for Optical Transitions in PbSe Nanocrystal Quantum Dots: Drastic Effect of Structure Inversion Asymmetry. *Phys. Rev. B* **2009**, *79*, 233305.
35. Tudury, G. E.; Marquezini, M. V.; Ferreira, L. G.; Barbosa, L. C.; Cesar, C. L. Effect of Band Anisotropy on Electronic Structure of PbS, PbSe, and PbTe Quantum Dots. *Phys. Rev. B* **2000**, *62*, 7357–7364.
36. Norris, D. J.; Bawendi, M. G. Measurement and Assignment of the Size-Dependent Optical Spectrum in CdSe Quantum Dots. *Phys. Rev. B* **1996**, *53*, 16338–16346.
37. Chen, O.; Yang, Y.; Wang, T.; Wu, H.; Niu, C.; Yang, J.; Cao, Y. C. Surface-Functionalization-Dependent Optical Properties of II-VI Semiconductor Nanocrystals. *J. Am. Chem. Soc.* **2011**, *133*, 17504–17512.
38. To probe the robustness of this result we also performed simulations reducing artificially the conduction band offset at the CdSe/CdS heterojunction to 0.1 eV (see Supporting Information). The calculated spectra did not reveal qualitative differences despite the enhanced asymmetry of the electron wave functions.
39. Hens, Z.; Moreels, I. Light Absorption by Colloidal Semiconductor Quantum Dots. *J. Mater. Chem.* **2012**, *22*, 10406.
40. Ninomiya, S.; Adachi, S. Optical Properties of Cubic and Hexagonal CdSe. *J. Appl. Phys.* **1995**, *78*, 4681–4689.
41. Ninomiya, S.; Adachi, S. Optical Properties of Wurtzite CdS. *J. Appl. Phys.* **1995**, *78*, 1183–1190.
42. Xu, C.; Webb, W. W. Measurement of Two-Photon Excitation Cross Sections of Molecular Fluorophores with Data from 690 to 1050 nm. *J. Opt. Soc. Am. B* **1996**, *13*, 481–491.
43. Configuration-interaction calculations of the lowest lying excitonic states were also conducted to probe the influence of the Coulomb energy and electron−hole correlations on the predicted blue shifts (see Supporting Information). No noticeable changes arose with respect to the single particle model.
44. Rajadell, F.; Climente, J. I.; Planelles, J.; Bertoni, A. Excitons, Biexcitons, and Trions in CdSe Nanorods. *J. Phys. Chem. C* **2009**, *113*, 11268–11272.
45. Laheld, U. E. H.; Einevoll, G. T. Excitons in CdSe Quantum Dots. *Phys. Rev. B* **1997**, *55*, 5184–5204.
46. Button, K. J.; Lax, B.; Cohn, D. R. Piezoelectric Polaron-Cyclotron Resonance in the Quantum Limit in n-CdS. *Phys. Rev. Lett.* **1970**, *24*, 375–378.
47. Sitt, A.; Della Sala, F.; Menagen, G.; Banin, U. Multiexciton Engineering in Seeded Core/Shell Nanorods: Transfer from Type-I to Quasi-Type-II Regimes. *Nano Lett.* **2009**, *9*, 3470–3476.

Two-Photon Induced Blue Shift of Core and Shell Optical Transitions in Colloidal CdSe/CdS Quasi-Type II Quantum Rods – Supporting information

Marco Allione,[1] Ana Ballester,[2] Hongbo Li,[1] Alberto Comin,[1] José L. Movilla,[2] Juan I. Climente,[2] Liberato Manna[1] and Iwan Moreels[1]

1 Istituto Italiano di Tecnologia, Via Morego 30, IT-16163 Genova, Italy
2 Departament de Quimica Fisica i Analitica, Universitat Jaume I, E-12080 Castellón, Spain

1. CdSe PL spectrum and temporal decay

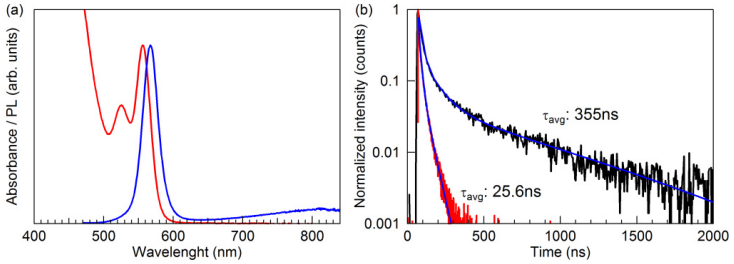

Figure S1: (a) CdSe core-only absorbance (red) and PL (blue) spectrum. (b) PL decay traces are collected at the band edge (570nm, red) and at the trap emission band (800nm, black). The decay is multi-exponential in both cases, with an average decay time of 355 ns for the trap emission. This value is far larger than the femtosecond and even nanosecond pulse duration.

2. Calculated auto-correlation trace in presence of trap states

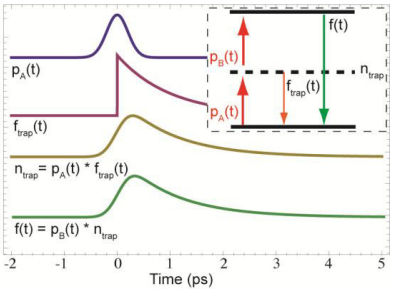

Figure S2: Asymmetric broadening of the two-photon fluorescence autocorrelation, due to finite lifetime of a possible trap state. A fist laser pulse (blue curve, p_A) populates a mid-gap state, with a density of states given by n_{trap} and a finite lifetime, symbolized by the purple curve $f_{trap}(t)$. After the absorption of the first laser pulse, the density of occupied trap states is therefore given by the convolution of the temporal

profile of the laser pulse, with $f_{trap}(t)$. A second laser pulse (p_B) promotes the carriers from the trap state to the final excited state, from which the two-photon fluorescence f(t) is then detected. The two-photon fluorescence autocorrelation is then determined by the convolution of the second laser pulse (p_B) with the time-dependent density of trap-states n_{trap}, hence shows a tail clearly extending beyond the laser autocorrelation time.

3. CdSe/CdS Qrod structural parameters, samples used for the absolute 2PA cross section.

type	Core diameter	Rod diameter	Length
	nm	nm	nm
CdSe Qdots	2.8	--	--
CdSe/CdS Qrods	2.8	4.3	57
CdSe/CdS Qrods	3.5	4.1	36
CdSe/CdS Qrods	3.5	7.1	29
CdSe/CdS Qrods	4.9	4.9	31
CdSe/CdS Qrods	4.9	5.0	37
CdSe/CdS Qrods	5.2	5.5	17

Table S1: Structural parameters of the CdSe/CdS Qrods used for the measurement of the 2PA cross section, as determined by TEM.

4. CdSe Qdot and CdSe/CdS core/shell Qrod 2PA spectra.

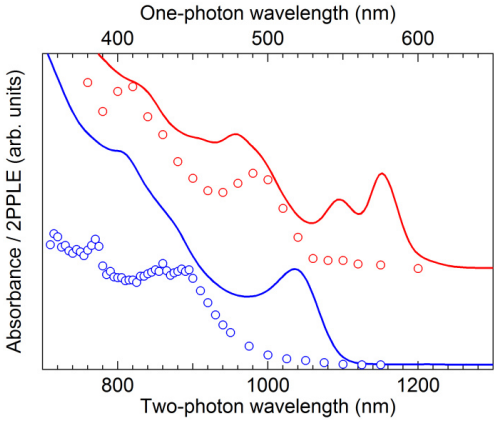

Figure S3: One-photon absorbance (full lines) and 2PPLE (open symbols) spectra for 2.7 nm (bottom, blue) and 3.9 nm (top, red) CdSe Qdots. An 85 nm blue shift of the first 2PPLE transition is observed in both cases. Top spectra are offset for clarity.

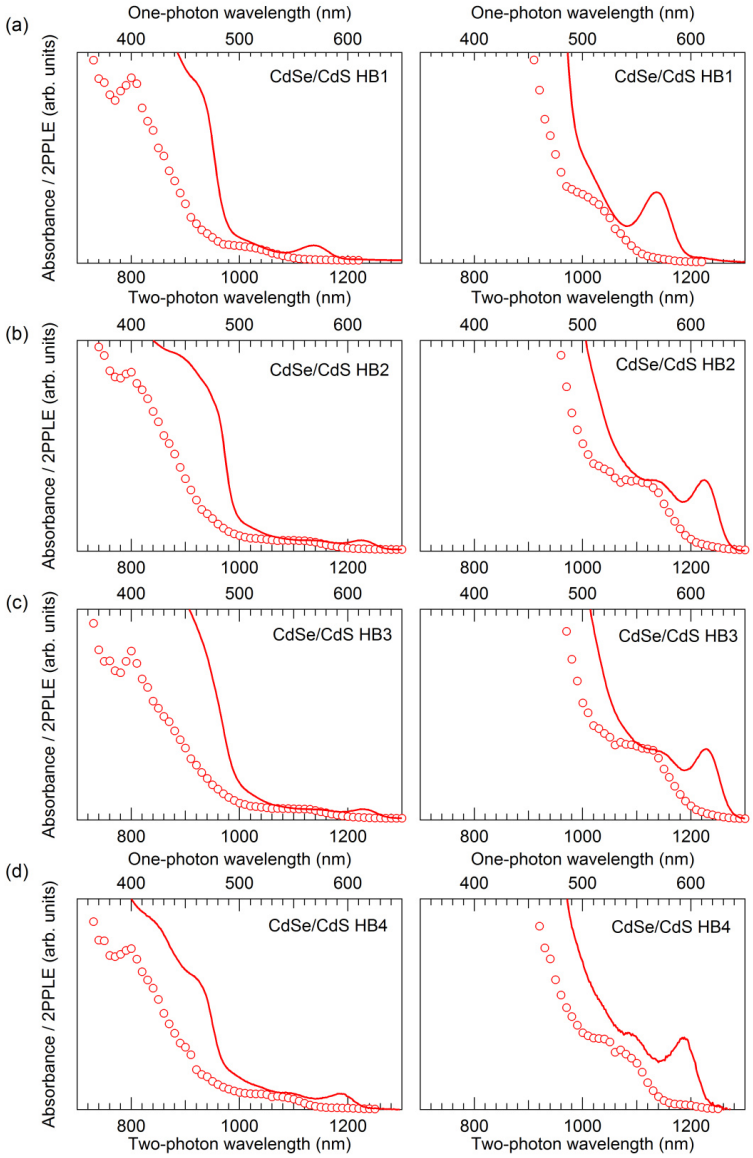

Figure S4: CdSe/CdS Qrod absorbance (full lines) and 2PPLE (open symbols) spectra of sample HB1 (a), HB2 (b), HB3 (c), and HB4 (d). Both in the region of core and shell absorption, strong blue shifts are observed for the 2PPLE spectra.

5. Longitudinal profile of the electron and hole wave functions involved in the transitions assigned in figure 5.

Dashed lines indicate the Qdot core spatial limits.

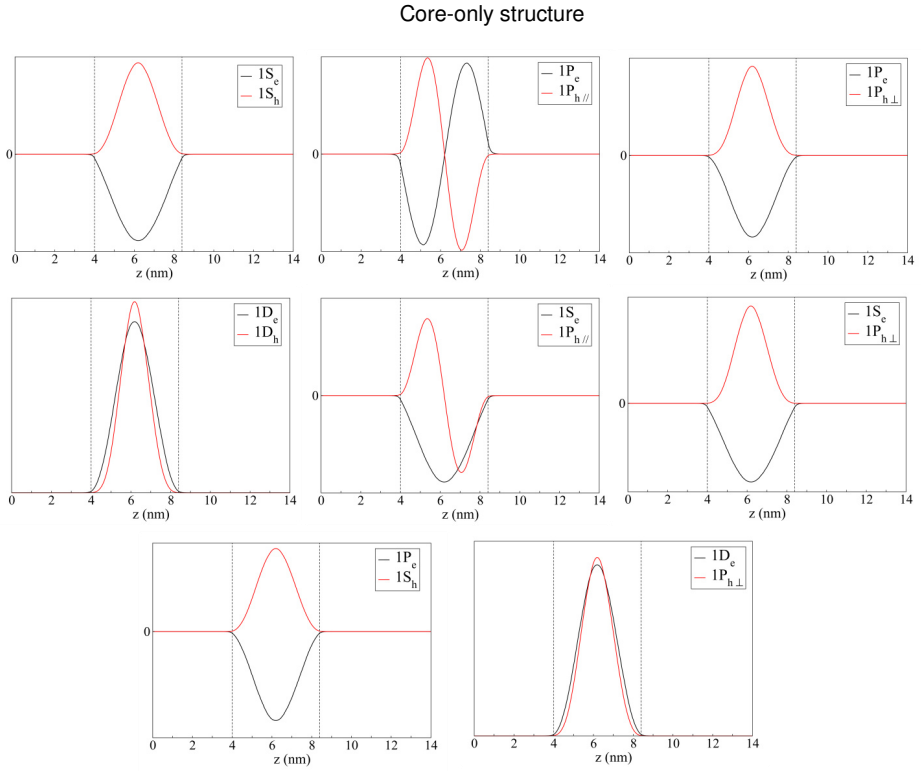

Figure S5: Wavefunctions for a 4.4 nm core CdSe Qdot.

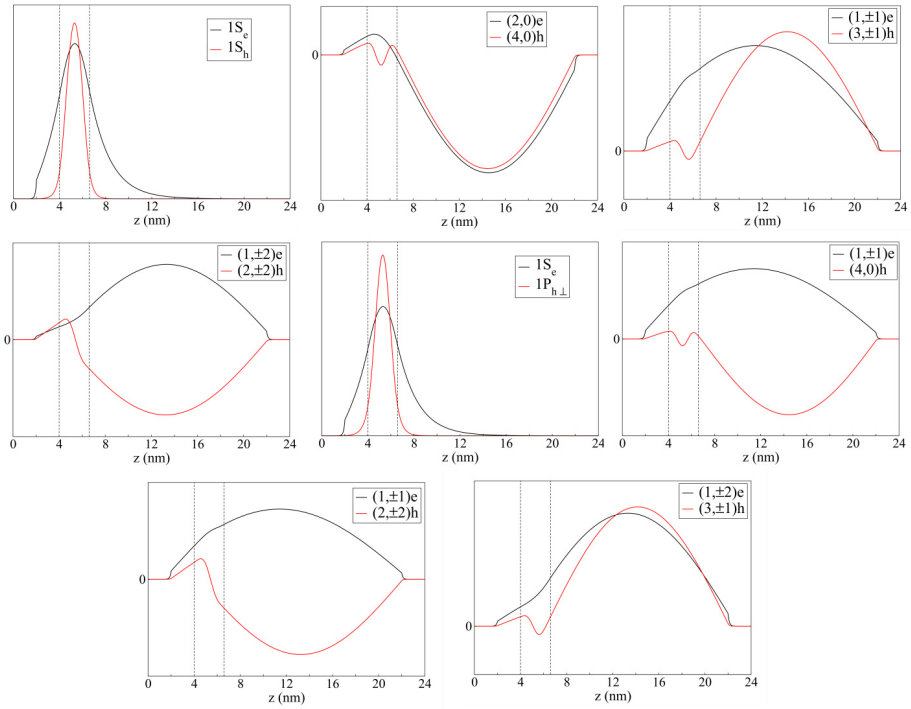

Figure S6: Wavefunctions for core/shell Qrod HB1.

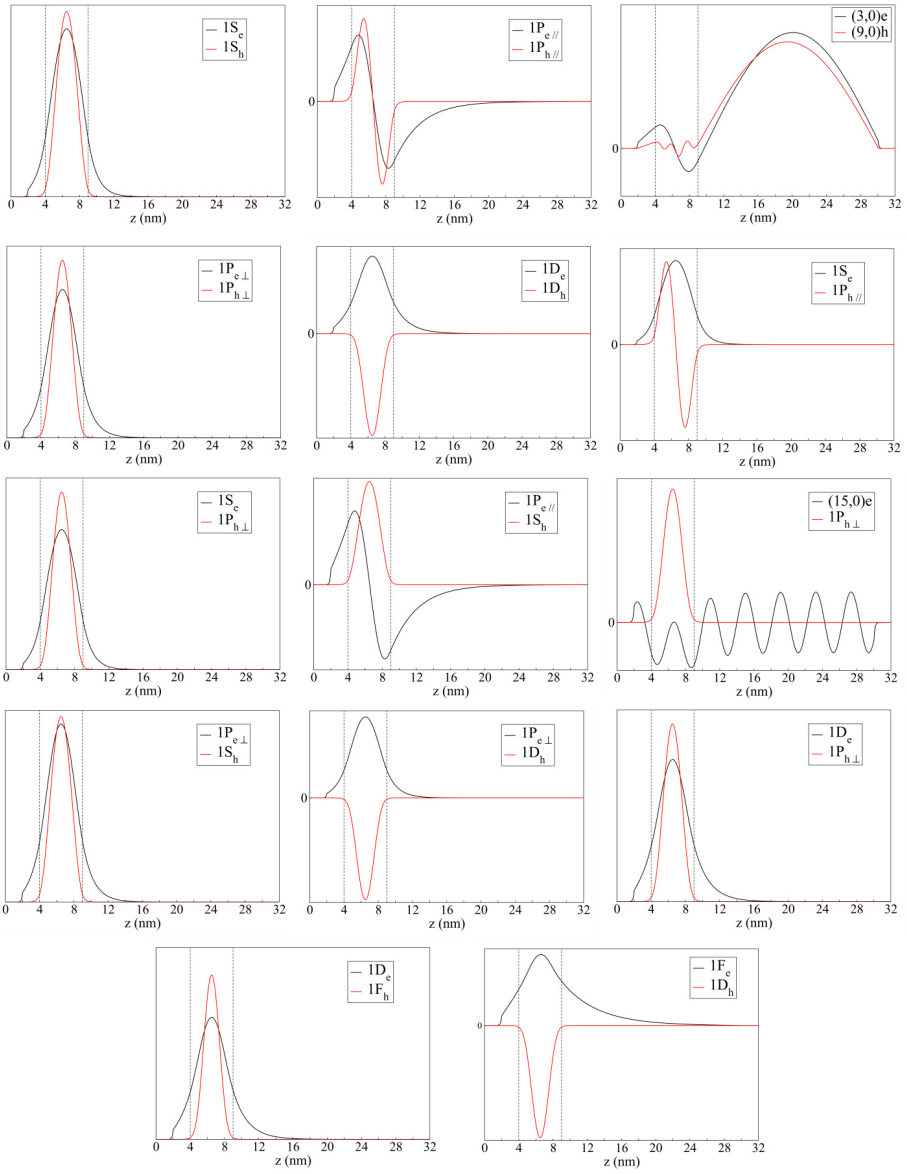

Figure S7: Wavefunctions for core/shell Qrod HB5.

6. Effect of Coulomb energy and electron-hole correlation on the simulated spectra.

Full configuration-interaction (CI) calculations of the lowest excitonic states in both HB1 and HB5 samples were conducted in order to determine the influence of Coulomb effects on the predicted blue shifts. The excitonic states were built as linear combinations of a large number of Hartree products of the single-particle electron and hole states. The results revealed negligible electron-hole correlations in the core states, owing to the small dot sizes. Indeed, the contribution of the $1S_h1S_e$ configuration to the HB5 ground excitonic state was above a 99%, and similar contributions were obtained for the $1P_{h\perp}1S_e$ or $1S_h1P_{e\perp}$ configurations in their respective states. Likewise, the Coulomb matrix elements corresponding to $1X_h1Y_e$ configurations with X and Y = S, P turned out to differ by less than 15 meV, which, in particular, translates into an increase of the predicted shift between the $1S_h \rightarrow 1S_e$ and $1P_{h\perp} \rightarrow 1S_e$ transitions of barely 10 nm. Since the above configurations determine the lowest energy range of the 1PA and 2PA spectra we conclude that Coulomb effects do not affect significantly the reported blue shifts.

Regarding the high-energy range of the spectra, non-negligible electron-hole correlations are expected as a result of the relaxed confinement in the rod direction, which could eventually mould the intensity of rod-to-rod and dot-to-rod absorptions. Further, Coulomb energies are expected to be somewhat weaker than in core states, which would translate into a slight blue shift of dot-to-rod and rod-to-rod absorptions with respect to the single-particle ones. At any rate, compared with the large kinetic energy yielded by the strong lateral confinement these effects are presumably so small as not to affect qualitatively the agreement between the experimental and the simulated spectra.

7. Effect of the conduction band offset

Recent studies on the band alignment in wurtzite CdSe/CdS core/shell nanocrystal heterorods reported experimental measurements consistent with a conduction band offset of 0.3 eV at the heterojunction.[1-3] Such a value implies the localization of the ground electron wave function mainly in the CdSe seed (type I band alignment), though quasi-type II behavior, linked to the degree of the electron delocalization in the shell, could be obtained by increasing temperature and/or decreasing the core size.

In the present case, the conduction band offset is crucial to determine the asymmetry of the electron wave function, and thus the breakdown of the parity selection rules. Thus, to probe the robustness of our conclusions we performed additional calculations employing a lower band offset of 0.1 eV. Results are shown in figure S8 for both HB1 and HB5 samples. As can be seen, the fitting with the experimental data is less accurate than using 0.3 eV, although the qualitative interpretation of the spectra is essentially the same. Only in the sample with smaller core (HB1) minor differences stand out, as e.g. in the assignment of the fundamental 2PA transition. Now, the $1P_{h\perp} \rightarrow 1S_e$ transition rate is lower because of the large leakage of the $1S_e$ electron in the rod (see figure S9), and the main peak corresponds to the $1S_h \rightarrow (3,\pm1)_e$ dot-to-rod absorption. As can be observed in figure S9, the asymmetry of the electron wave function in these

transitions is clearly enhanced compared to the case with 0.3 eV, yet without appreciable consequences for the profile of the spectra.

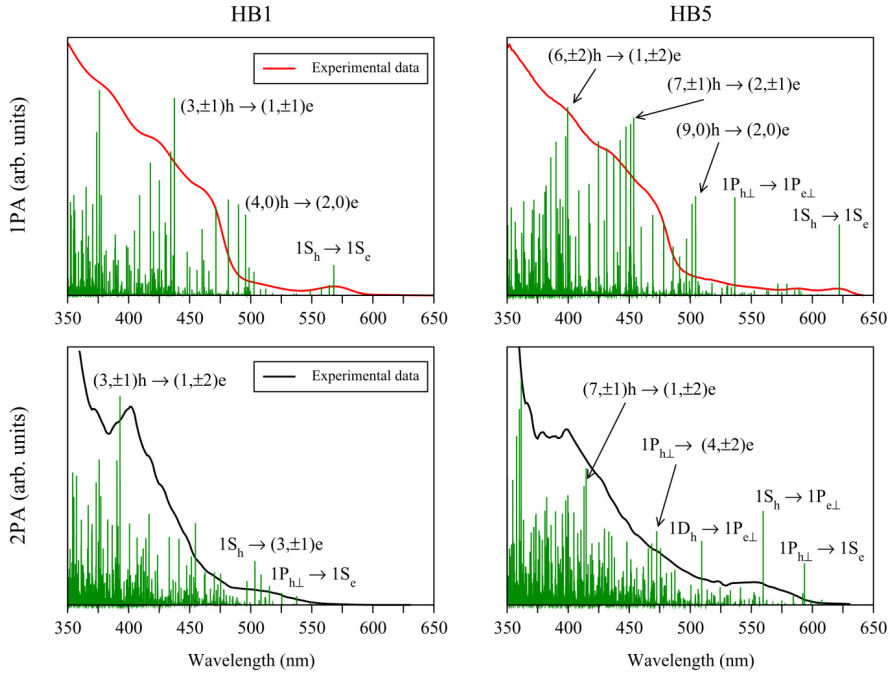

Figure S8: 1PA (top) and 2PA (bottom) experimental and calculated spectra for the HB1 (left) and HB5 (right) core/shell Qrods, using a conduction band offset of 0.1 eV at the heterojunction. To facilitate the comparison between linear and non-linear resonances, the wavelength in the horizontal axis has been set equal to the photon wavelength for the 1PA spectra and to half the photon wavelength for the 2PA spectra.

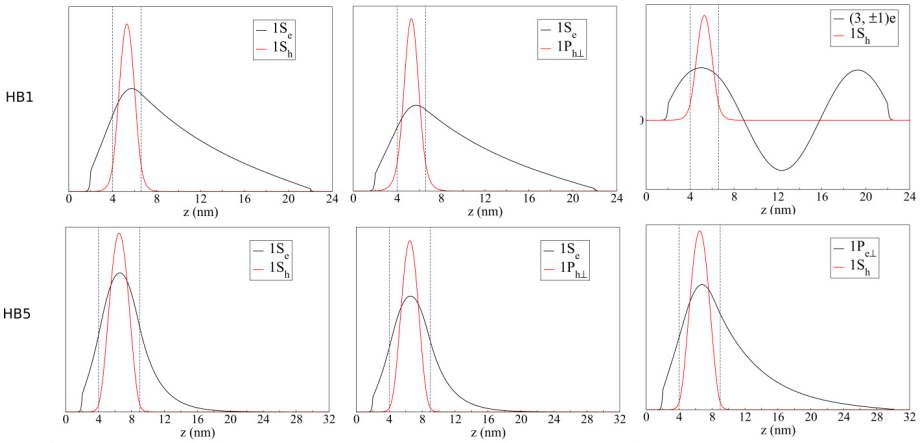

Figure S9: Longitudinal profiles of the initial and final states involved in some of the 1PA and 2PA transitions assigned in figure S8. Vertical dashed lines indicate the limits of the CdSe core.

8. Limitations of the *k·p* model

In this work we have used single-band effective mass Hamiltonians. This model provides a simple, yet accurate description of the electronic structure of quantum dots in the low energy region, as determined by the bulk effective masses of the charge carriers, and the quantum confinement of the nanostructure.[4] As we have shown, the model captures the main features of the 1PA and 2PA spectra of the heterostructures under study, including the blue shift between the two absorption peaks, the symmetry selection rules ensuing from the nanocrystal shape and the physical origin of the low oscillator strength of some dipole-allowed transitions.

However, as mentioned in the manuscript, a few experimental transitions lack an assignment (e.g. the second peak of the 1PA spectrum in figure 5) and a few theoretical transitions lack an experimental counterpart (e.g. the $1P_h \rightarrow 1P_e$ transition in the 1PA of HB5 in figure 5). Also, the agreement between theory and experiment is gradually reduced as we explore the high energy (shell) region. These disagreements reflect the inability of the k·p model to properly account for band mixing and valley mixing effects in the high energy region,[5] as well as the absence of possible interface and surface irregularities which would lower the symmetry of the system.[6] Further atomistic tight-binding and pseudopotential calculations could contribute to understand these details.

References

1. Steiner, D.; Dorfs, D.; Banin, U.; Della Sala, F.; Manna, L.; Millo, O. Determination of Band Offsets in Heterostructured Colloidal Nanorods Using Scanning Tunneling Spectroscopy. *Nano Lett.* **2008**, *8*, 2954–2958.
2. Sitt, A.; Sala, F. D.; Menagen, G.; Banin, U. Multiexciton Engineering in Seeded Core/Shell Nanorods: Transfer from Type-I to Quasi-Type-II Regimes. *Nano Lett.* **2009**, *9*, 3470–3476.
3. Rainò, G.; Stöferle, T.; Moreels, I.; Gomes, R.; Kamal, J. S.; Hens, Z.; Mahrt, R. F. Probing the Wave Function Delocalization in CdSe/CdS Dot-in-Rod Nanocrystals by Time- and Temperature-Resolved Spectroscopy. *ACS Nano* **2011**, *5*, 4031–4036.
4. Efros, Al. L.; Rosen, M. Comment on “Comparison of the k.p and the Direct Diagonalization Approaches for Describing the Electron Structure of Quantum Dots”. *Appl. Phys. Lett.* **1998**, *73*, 1155.
5. Fu, H.; Wang, L. W.; Zunger, A. Comparison of the k.p and the Direct Diagonalization Approaches for Describing the Electron Structure of Quantum dots. *Appl. Phys. Lett.* **1997**, *71*, 3433.
6. An, J.M.; Franceschetti, A.; Zunger, A. Pauli Blocking Versus Electrostatic Attenuation of Optical Transition Intensities in Charged PbSe Quantum Dots. *Phys. Rev. B* **2007**, *76,* 161310(R).

Suppression of the Aharonov-Bohm effect in six-electron hexagonal quantum rings

A. Ballester, C. Segarra, and J. Planelles*
Departament de Química Física i Analítica, Universitat Jaume I, Castelló de la Plana, Spain

A. Bertoni
Centro S3, CNR - Istituto Nanoscienze, Via Campi 213/A, 41125 Modena, Italy
(Dated: July 30, 2013)

Few-electron states of AlAs-GaAs-AlAs hexagonal quantum rings pierced by an axial magnetic field are computed through full configuration interaction calculations. The quantum ring is in the low-density regime, populated with $N = 1$ up to $N = 7$ electrons. $N = 2$ and $N = 3$ display a perfect fractional Aharonov-Bohm effect. $N = 4$ and especially $N = 5$ have not regular oscillation amplitude patterns, and $N = 7$ shows a period like that of $N = 1$. A complete suppression of the Aharonov-Bohm effect and a completely flat magnetization profile holds for $N = 6$. This is a peculiar symmetry-related response of the $N = 6$ system that only can emerge in the low-density regime.

PACS numbers: 75.75.-c,73.21.Hb,73.21.La,03.65.-w,73.63.Nm
Keywords: Fractional Aharonov-Bohm effect, Quantum ring, Magnetization, Artificial Benzene

Core-multishell nanowires with an unconstrained longitudinal direction and different material composition along the orthogonal plane (radial direction), may become an effective 2D system when a proper material modulation along the growth axis generates a strong confinement of carriers in that direction.[1–4] Most III-V nanowires with a diameter less than about 400 nm have a very neat hexagonal section even after a few overcoating processes.[5–10] They can eventually be cut to form an hexagonal flat quantum ring that can confine the free carriers on a square-well type potential in the radial direction.[11] In a recent paper[12] we presented a theoretical study of correlated multi-electron states of hexagonal semiconductor rings populated with $N = 1$ up to $N = 7$ electrons and found that charges get more localized in the corners as the number of electrons increases up to $N = 6$, where we found a maximum of localization. The result evidences the deficiency of a picture based on orbitals delocalized on the whole ring, i.e., that electron correlation becomes crucial. In this Letter we investigate the response of this system to an externally applied axial magnetic field. Specifically, we focus on the different response in comparison to circular quantum rings (QRs).[13–19] By increasing the strength of an externally applied axial magnetic field, oscillations of the QR ground state energy occur. The period and amplitude of the oscillations depends on the electron population and it is referred to as fractional Aharanov-Bohm (AB) effect.[20] The first unambiguous experimental evidence of this effect may be traced back to the work by Keyser.[21] Soon after, Emperador et al.[22] related this fractional response to a low kinetic energy and a phenomenon of electronic localization. Full configuration interaction (FCI) calculations by Niemelä et al.[23] of QRs populated up to four electrons revealed the crucial role of electron-electron interaction on the decrease of the period and amplitude of the ground state energy and its fractional character. Liu et al.[24] extended the FCI calculation to QRs populated with $N = 5$ and $N = 6$ electrons as a function of the magnetic field and the QR radius, thus yielding a phase diagram with a rich variety of ground states. The fractional character of the AB effect was though fully explored earlier using the empirical Hubbard model,[25] where it was concluded that fractional AB oscillations arise for small values of the factor $\alpha = N\,t/(U\,L)$, where N is the number of electrons in the QR, t is the tunneling integral, U the repulsion one and L the number of sites along the QR where the single-particle functions are located. For α to be small the ratio two-electron/one-electron integrals, U/t, must be large, i.e., a low kinetic energy and a strong electron-electron interaction is required. Also, since α is proportional to N, a low-density regime is needed. Additionally, L introduces the possible role of symmetry lowering: the larger L the sooner the Hubbard model reaches the fractional AB regime.

In our work, we consider an hexagonal quantum ring since, as pointed out above, most III-V multishell thin nanowires have a neat hexagonal section and they can eventually be cut to form an hexagonal flat quantum ring. In particular, we deal with the same AlAs-GaAs-AlAs hexagonal QR studied in ref. 12, where all physical parameters, namely effective masses, conduction-band offset and dielectric constant can be found. We carry out calculations for $N = 2$ up to $N = 7$ interacting electrons in the low-density regime. This system may be related to the $L = 6$ Hubbard model, and in fact, we recover the main trends predicted by this and more sophisticated models. Additionally, we theoretically demonstrate the complete suppression of the AB effect when the hexagonal ring is in the low-density regime and it is populated with $N = 6$ electrons. This suppression translates into a smooth magnetization profile that should be observed experimentally. We show that this symmetry-related response is specific of the low-density regime.

We perform an exact diagonalization of the multiparticle Schrödinger equation via a FCI procedure. As a

first step, the single-particle orbitals ϕ_i and energies ϵ_i of the conduction band are computed for the AlAs-GaAs-AlAs hexagonal QR, through a real-space numerical solution of the eigenvalue equation of the effective-mass Hamiltonian,

$$h = -\frac{1}{2}(\mathbf{p}+\mathbf{A})\frac{1}{m^*(\mathbf{r})}(\mathbf{p}+\mathbf{A}) + V(\mathbf{r}) \qquad (1)$$

where $\mathbf{r}$ is the 2D coordinate on the hexagonal domain, $m^*(\mathbf{r})$ is the isotropic material-dependent effective mass of electrons, $\mathbf{A}$ is the potential vector and $V(\mathbf{r})$ is the confining potential. This equation is numerically integrated using the finite-elements method on a regular triangular mesh with hexagonal elements. The grid reproduces the symmetry of the system thus avoiding numerical artifacts originated by discretization asymmetries of the six domain boundaries, as would be the case, e.g., using a rectangular grid. Unless otherwise indicated, the employed geometry is the same as in ref. 12, i.e., a regular hexagon domain with edges 66.5 nm long including a GaAs well of 6.8 nm wide with uniform thickness all around the 37.3 nm AlAs core, covered by a 13.5 nm AlAs capping layer (see inset in Figure 1).
Finally we diagonalize the multi-particle Hamiltonian

$$H = \sum_{i\sigma} \epsilon_i e^\dagger_{i\sigma} e_{i\sigma} + \frac{1}{2}\sum_{ijkl}\sum_{\sigma\sigma'} U_{ijkl} e^\dagger_{i\sigma} e^\dagger_{j\sigma'} e_{k\sigma'} e_{j\sigma} \qquad (2)$$

where $e_{i\sigma}$ ($e^\dagger_{i\sigma}$) is the annihilation (creation) operator for an electron in the orbital state i and with spin σ. For all the calculations we use 24 spin-orbital single-particle states, giving $\binom{24}{N}$ Slater determinants, with N being the number of electrons.

We find that in a large range of low-lying N-electron states only the lowest 6 orbitals (spin-independent real space wave functions) have significant population. Taking into account all 12 orbitals, we can identify two different types of shells, namely two groups of orbitals well separated in energy, having the same degeneracy pattern (see figure 1). The behavior, quite different from the one of a circular QR, originates in the symmetry lowering going from circular to hexagonal. In the first case we have an infinite number of irreducible representations which associated orbital can cross, while the hexagonal ring has only six irreducible representations and the anticrossings between orbitals with the same symmetry yield different non-crossing shells where states with different symmetry repeatedly cross as the magnetic field increases (see figure 1).

In figure 2 we summarize the behaviour of the energy of lowest-lying few-electron states vs. the magnetic field. The represented energies are relative to the N-electron ground state energy in the absence of magnetic field (horizontal red line). The few-electron states are labeled according to the C_6 symmetry group and spin multiplicity of states. Figure 3 displays the corresponding magnetization in meV/T. A main feature emerges for the case $N = 6$ in both figures: the complete supression of the

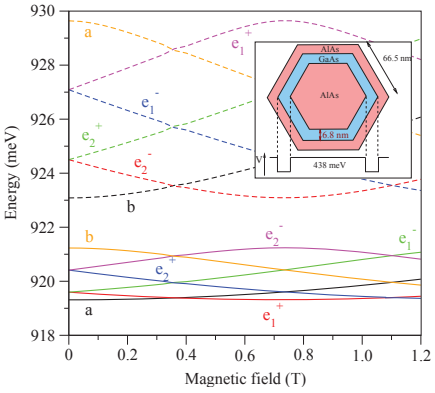

FIG. 1. Orbital energies vs. magnetic field, labeled according to the C_6 symmetry group. Two well-separated shells composed by 6 orbitals can be identified, with an 2 meV energy gap between them. Inset: Schematics of the system. The GaAs ring is wrapped around an hexagonal AlAs core and capped by an additional AlAs shell. The free electrons are confined in the GaAs region.

AB oscillation that turns into a completely flat magnetization profile. Also, we can see that for $N = 2$ and $N = 3$ a perfect fractional AB is observed. For $N = 4$ and especially for $N = 5$ the oscillation amplitude pattern is not regular. When the hexagonal QR is populated with $N = 6$ electrons a complete suppresion of the AB effect occurs, while the system with $N = 7$ shows a period similar to $N = 1$. Except for the case $N = 6$, the observed behavior is consistent with the abovementioned calculations on QRs. In particular, the behavior vs. N is consistent with an increasing α factor that prevents the fractional behavior of the AB oscillations.[25]

In order to understand the peculiar behavior of the $N = 6$ system, we repeated the set of FCI calculations but introducing a scaling factor f that multiplies the electron-electron interaction integrals. For $f = 0$ we obtain the non-interacting particle spectrum (not shown) with a crossing, at about 1/2 of flux, of two configurations namely, $a^2(e_1^+)^2(e_1^-)^2$ and $(e_1^+)^2a^2(e_2^+)^2$. The first one is the lowest-lying configuration at $B = 0$ while the second one represents a highly excited configuration at this magnetic field. When the electron-electron repulsion is included the string of symmetry-labels of the orbitals cannot be used as good quantum numbers, since the configuration interaction takes place. Then, only the total symmetry and total spin are good labels. However we can still identify these configurations as dominant, with a large contribution in the case of small f factors. The full orbital occupancy and the products of orbital symmetries yield the same total symmetry and total spin, ^1A, for both configurations. Then, the corresponding states an-

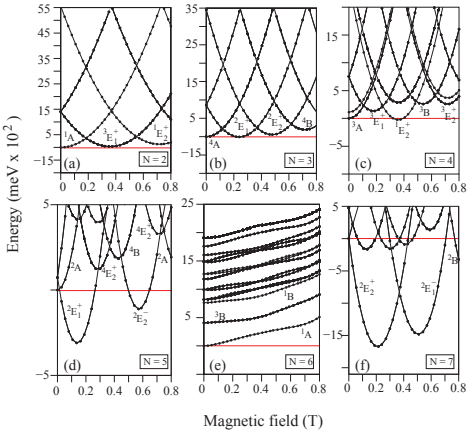

FIG. 2. Energy of low-lying few-electron states, labeled according to the C_6 symmetry group and spin multiplicity, vs. the magnetic field. The six panels show the cases of $N = 2$ to $N = 7$ electrons, as indicated. Zero energy, indicated by the straigth reference line, corresponds to the ground state energy without magnetic field.

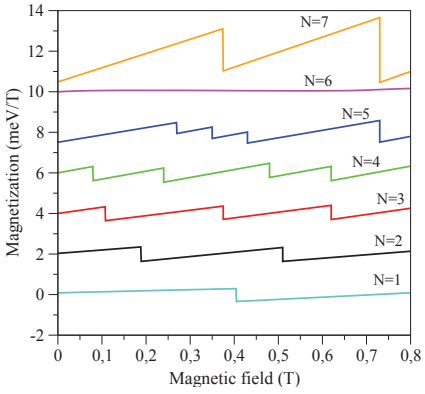

FIG. 3. Magnetization of the N-electron hexagonal QR vs. the applied magnetic field, for $N = 1$ (bottom) up to $N = 7$ (top). For the sake of clarity, the different magnetization profiles have been offset by 2 meV/T.

ticross, the anticrossing being larger as electron-electron interaction increases (see figure 4).

To asses the role of the regime of density, we carried out calculations for an hexagonal QR three times smaller than the above sample. Simulations of magnetizations are reported in Fig 5. In this case, we can observe fractional behavior only for $N = 2$. As expected, by using a factor f larger than unity (not shown) multiplying the electron-electron interaction integrals we can reach fractional behavior for increasing number of electrons. As far as the $N = 6$ case is concerned, figure 5 reveals that in this density regime the magnitude of the anticrossing between ^1A states cannot overcome the relative stabilization of the triplet ^3B state coming from the exchange integrals (see figure 4) so that ^3B emerges as the ground state in a narrow window around one half of flux, yielding an irregular discontinuity in the magnetization profile, as reported in figure 5.

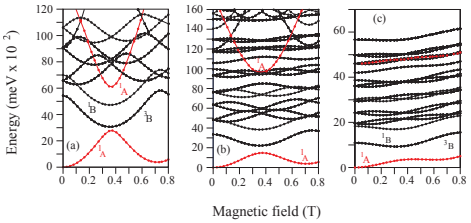

FIG. 4. Lowest-lying magnetic states for $N = 6$ for increasing Coulomb interaction. In the three panels from left to right, Coulomb repulsion is scaled by a factor of 0.1, 0.2 and 0.5. Red lines correspond to the states which anticrossing is responsible of the suppression of the AB effect and of the flat magnetization profile.

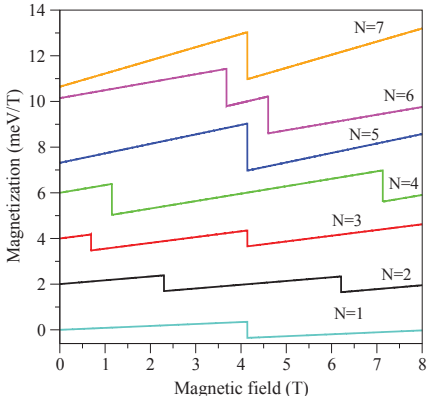

FIG. 5. Magnetization of the small hexagonal QR for $N = 1$ (bottom) up to $N = 7$ (top). For the sake of clarity, the different magnetization profiles have been offset by 2 meV/T.

In summary, the complete suppression of the AB effect in an hexagonal QR populated with $N = 6$ electrons is a symmetry-related response that can only emerge in the

low-density regime. This suppression translates into a flat magnetization profile that should by detectable in experiments.

ACKNOWLEDGMENTS

This work was partially supported by UJI-Bancaixa Project No. P1-1B2011-01, MCINN Project No. CTQ2011-27324, and FPI and FPU Grants (A.Ba. and C.S.). A.Be. acknowledges the CINECA award under the ISCRA initiative for high performance computing resources.

* josep.planelles@uji.es

[1] L. J. Lauhon, M. S. Gudiksen, D. Wang, and C. M. Lieber *Nature* **420**, 57 (2002).

[2] G. Shen, D. Chen, Y. Bando, and D. Golberg *J. Mater. Sci. Technol.* **24**, 541 (2008).

[3] G. Shen and D. Chen *Sci. Adv. Mater.* **1**, 353 (2009).

[4] M. Heigoldt, J. Arbiol, D. Spirkoska, J. M. Rebled, S. Conesa-Boj, G. Abstreiter, F. Peir, J. R. Morante, and A. Fontcuberta i Morral *J. Mater. Chem.* **19**, 840 (2009).

[5] J. Noborisaka, J. Motohisa, S. Hara, and T. Fuku *Appl. Phys. Lett.* **87**, 093109 (2005).

[6] A. Fontcuberta i Morral, D. Spirkoska, J. Arbiol, M. Heigoldt, J. R. Morante, and G. Abstreiter *Small* **4**, 899 (2008).

[7] R. E. Algra, M. Hocevar, M. A. Verheijen, I. Zardo, G. G. W. Immink, W. J. P. van Enckevort, G. Abstreiter, L. P. Kouwenhoven, E. Vlieg, and E. P. A. M. Bakkers *Nano Letters* **11**, 1690 (2011).

[8] T. M. M. Keplinger, J. Stangl, E. Wintersberger, B. Mandl, D. Kriegner, V. Hol, G. Bauer, K. Deppert, and L. Samuelson *Nano Letters* **9**, 1877 (2009).

[9] D. Rudolph, S. Funk, M. Döblinger, S. Morkötter, S. Hertenberger, L. Schweickert, J. Becker, S. Matich, M. Bichler, D. Spirkoska, I. Zardo, J.J. Finley, G. Abstreite and G. Koblmüller *Nano Letters* **13**, 1522 (2013).

[10] M. Royo, A. Bertoni, G. Goldoni, *Phys. Rev. B* **87**, 115316 (2013).

[11] J. Hasen, L.N. Pfeiffer, A. Pinczuk1, S. He, K.W. West and B.S. Dennis, *Nature* **390**, 54 (1997); C. Fasth, A. Fuhrer, M.T. Björk, and L. Samuelson, *NanoLett.* **5**, 1487 (2005); J. Tatebayashi, Y. Ota, S. Ishida, M. Nishioka, S. Iwamoto, and Y. Arakawa, *Appl. Phys. Lett.* **100**, 263101 (2012)

[12] A. Ballester, J. Planelles, and A. Bertoni *J. Appl. Phys.* **112**, 104317 (2012).

[13] A. Fuhrer, S. Lscher, T. Ihn, T. Heinzel, K. Ensslin, W.Wegscheider, and M. Bichler *Nature* **413**, 822 (2001).

[14] A. Lorke, R. J. Luyken, A. O. Govorov, J. Kotthaus, J. M. Garca, and P. M. Petroff *Phys. Rev. Lett.* **84**, 2223 (2000).

[15] S. Viefers, P. Koskinen, P. S. Deo, and M. Manninen *Physica E* **21**, 1 (2004).

[16] I. Filikhin, V. M. Suslov, and B. Vlahovic *Physica E* **33**, 349 (2006).

[17] T. Chakraborty and P. Pietilainen *Phys. Rev. B* **50**, 8460 (1994).

[18] Z. Barticevic, M. Pacheco, and A. Latg *Phys. Rev. B* **62**, 6963 (2000).

[19] J.I. Climente, J. Planelles and W. Jaskolski *Phys. Rev. B* **68**, 075307 (2003); J.I. Climente, J. Planelles and J.L. Movilla, *Phys. Rev. B* **70**, 081301 (2004).

[20] L. E. Lipparini *Modern Many-Particle Physics*, World Scientific, (Singapore, 2008).

[21] U.F. Keyser, C. Fühner, S. Borck, R.J. Haug, M. Bichler, G. Abstreiter and W. Wegscheider *Phys. Rev. Lett.* **90**, 196601 (2003).

[22] A. Emperador, F. Pederiva and E. Lipparini *Phys. Rev. B* **68**, 115312 (2003).

[23] K. Niemelä, P. Pietiläinen, P. Hyvönen, and T. Chakraborty *Europhys. Lett.* **36**, 533 (1996).

[24] Y. M. Liu, G. M. Huang, and T. Y. Shi *Phys. Rev. B* **77**, 115311 (2008)

[25] F. V. Kusmartsev, J. F. Weisz, R. Kishore, and M. Takahashi *Phys. Rev. B* **49**, 16234 (1994).

Bibliography

[1] A. Biswas, I. S. Bayer, A. S. Biris, T. Wang, E. Dervishi, F. Faupel, Advances in Colloid and Interface Science **170**, 2 (2012).

[2] S. M. Reimann and M. Manninen, Rev. Mod. Phys. **74**, 1283 (2002).

[3] S. D. Sarma, R. de Sousa, X. Hu, and B. Koiller, Solid State Communications **133**, 737 (2005).

[4] N. Tessler, V. Medvedev, M. Kazes, S. Kan, and U. Banin, Science **295**, 1506 (2002).

[5] A. P. Alivisatos, Science **271**, 933 (1996).

[6] A. P. Alivisatos, Nature Biotechnology **22**, 47 (2004).

[7] W. C. W. Chan and S. Nie, Science **281**, 2016 (1998).

[8] M. B. Jr., M. Moronne, P. Gin, S. Weiss, and A. P. Alivisatos, Science **281**, 2013 (1998).

[9] C. B. Murray, C. R. Kagan, and M. G. Bawendi, Annu. Rev. Mater. Sci. **30**, 545 (2000).

[10] R. C. Ashoori, H. L. Stormer, J. S. Weiner, L. N. Pfeiffer, S. J. Pearton, K. W. Baldwin, and K. W. West, Phys. Rev. Lett. **68**, 3088 (1992).

[11] M. Braun, C. Burda, and M. A. El-Sayed, J. Phys. Chem. A **105**, 5548 (2001).

[12] X. Wang, X. Ren, K. Kahen, M. A. Hahn, M. Rajeswaran, S. Maccagnano-Zacher, J. Silcox, G. E. Cragg, A. L. Efros, and T. D. Krauss, Nature **459**, 686 (2009).

[13] D. Oron, M. Kazes, and U. Banin, Phys. Rev. B **75**, 035330 (2007).

[14] F. García-Santamaría, S. Brovelli, R. Viswanatha, J. A. Hollingsworth, H. Htoon, S. A. Crooker, and V. I. Klimov, Nano Lett. **11**, 687 (2011).

[15] J. J. Li, Y. A. Wang, W. Guo, J. C. Keay, T. D. Mishima, M. B. Johnson, and X. Peng, J. Am. Chem. Soc. **125**, 12567 (2003).

[16] R. Xie, U. Kolb, J. Li, T. Basché, and A. Mews, J. Am. Chem. Soc. **127**, 7480 (2005).

[17] S. Brovelli, R. D. Schaller, S. A. Crooker, F. Garcí-Santamaría, Y. Chen, R. Viswanatha, J. A. Hollingsworth, H. Htoon, and V. I. Klimov, Nature Communications **2**, 280 (2011).

[18] P. Yang, Y. Wu, and R. Fan, International Journal of Nanoscience **1**, 1 (2002).

[19] S. Kan, T. Mokari, E. Rothenberg, and U. Banin, Nature Materials **2**, 155 (2003).

[20] J. E. Halpert, V. J. Porter, J. P. Zimmer, and M. G. Bawendi, J. Am. Chem. Soc. **128**, 12590 (2006).

[21] L. C. L. Y. Voon and M. Willatzen, *The k.p method. Electronic Properties of Semiconductors* (Springer, 2009).

[22] P. Harrison, *Quantum Wells, Wires and Dots* (John Wiley and Sons, Guilford, 2000).

[23] G. Bastard, *Wave mechanics applied to semiconductor structures* (Halsted Press, New York, 1988).

[24] A. G. Petukhov, V. V. Osipov, and V. N. Smelyanskiy, Appl. Phys. Lett. **89**, 153127 (2006).

[25] D. J. Norris and M. G. Bawendi, Phys. Rev. B **53**, 16338 (1996).

[26] P. C. Sercel and K. J. Vahala, Phys. Rev. B **42**, 3690 (1990).

[27] M. G. Burt, J. Phys.: Condens. Matt. **11**, 53 (1999).

[28] E. O. Kane, Journal of Physics and Chemistry of Solids **1**, 249 (1957).

[29] E. O. Kane, *Narrow Gap Semiconductors. Physics and Applications,* (edited by W. Zawadzki Lect. Notes Phys., Volume 133, Springer Verlag, (Berlin), 1980).

[30] D. J. BenDaniel and C. B. Duke, Phys. Rev. **152**, 683 (1966).

[31] I. Galbraith and G. Duggan, Phys. Rev. B **38**, 10057 (1988).

[32] R. L. Burden and J. D. Faires, *Análisis numérico* (International Thomson Editores, México, 2002).

[33] W. E. Arnoldi, Quart. J. Applied Mathematics **9**, 17 (1951).

[34] R. B. Morgan, Math. Comp. **65**, 1213 (1996).

[35] R. B. Lehoucq, K. Maschhoff, D. C. Sorensen, and C. Yang, *See http:// www.caam.rice.edu/software/ARPACK/ for more information about arpack computer code.*

[36] M. Pi, F. Ancilotto, E. Lipparini, and R. Mayol, Physica E **24**, 297 (2004).

[37] A. Szabo and N. S. Ostlund, *Modern Quantum Chemistry* (Dover Publications, INC., 1996).

[38] J. K. L. MacDonald, Phys. Rev. **43**, 830 (1933).

[39] J. Planelles, J. I. Climente, and J. G. Díaz, *Espectroscòpia* (Publicacions de la Universitat Jaume I, 2002).

[40] W. Kohn, Rev. Mod. Phys. **71**, 1253 (1998).

[41] R. G. Parr and W. Yang, *Density Functional Theory of atoms and molecules* (Oxford Science Publications, New York, 1989).

[42] E. Lipparini, *Modern many-particle physics* (World Scientific, Singapore, 2008).

[43] P. Hohenberg and W. Kohn, Phys. Rev. **136**, B864 (1964).

[44] M. Levy, Phys. Rev. A **26**, 1200 (1982).

[45] W. Kohn and L. J. Sham, Phys. Rev. **140**, A1133 (1965).

[46] M. Pi, A. Emperador, M. Barranco, and F. Garcias, Phys. Rev. B **63**, 115316 (2001).

[47] M. Pi, A. Emperador, M. Barranco, F. Garcias, K. Muraki, S. Tarucha, and D. G. Austing, Phys. Rev. Lett. **87**, 066801 (2001).

[48] E. Räsänen, H. Saarikoski, V. N. Stavrou, A. Harju, M. J. Puska, and R. M. Nieminen, Phys. Rev. B **67**, 235307 (2003).

[49] A. Wensauer, O. Steffens, M. Suhrke, and U. Rössler, Phys. Rev. B **62**, 2605 (2000).

[50] J. P. Perdew and A. Zunger, Phys. Rev. B **23**, 5048 (1981).

[51] L. E. Brus, J. Chem. Phys. **80**, 4403 (1984).

[52] G. Goldoni, F. Rossi, and E. Molinari, Phys. Rev. Lett. **80**, 4995 (1998).

[53] G. Goldoni, F. Rossi, A. Orlandi, M. Rontani, F. Manghi, and E. Molinari, Physica E **6**, 482 (2000).

[54] A. Orlandi, M. Rontani, G. Goldoni, F. Manghi, and E. Molinari, Phys. Rev. B **63**, 045310 (2001).

[55] C. Delerue, M. Lannoo, and G. Allan, Phys. Rev. B **68**, 115411 (2003).

[56] X. Cartoixà and L. W. Wang, Phys. Rev. Lett. **94**, 236804 (2005).

[57] P. G. Bolcatto and C. R. Proetto, J. Phys.: Condens. Matter **13**, 319 (2001).

[58] A. Nozik, Physica E: Low-dimensional Systems and Nanostructures **14**, 115 (2002).

[59] E. Stinaff, M. Scheibner, A. Bracker, I. Ponomarev, V. L. Korenev, M. E. Ware, M. F. Doty, T. L. Reinecke, and D. Gammon, Science **311**, 636 (2006).

[60] S. A. Wolf, D. D. Awschalom, R. A. Buhrman, J. M. Daughton, S. von Molnár, M. L. Roukes, A. Y. Chtchelkanova, and D. M. Treger, Science **294**, 1488 (2001).

[61] B. Partoens, V. A. Schweigert, and F. M. Peeters, Phys. Rev. Lett. **79**, 3990 (1997).

[62] K. A. Matveev, L. I. Glazman, and H. U. Baranger, Phys. Rev. B **53**, 1034 (1996).

[63] J. M. Golden and B. I. Halperin, Phys. Rev. B **53**, 3893 (1996).

[64] T. Schmidt, R. Haug, K. V. Klitzing, A. Förster, and H. Lüth, Phys. Rev. Lett. **78**, 1544 (1997).

[65] D. Austing, T. Honda, K. Muraki, Y. Tokura, and S. Tarucha, Physica B **249-251**, 206 (1998).

[66] J. R. Petta, A. Johnson, C. M. Marcus, M. P. Hanson, and A. C. Gossard, Phys. Rev. Lett. **93**, 186802 (2004).

[67] D. Loss and D. P. DiVincenzo, Phys. Rev. A **57**, 120 (1998).

[68] M. Bayer, P. Hawrylak, K. Hinzer, S. Fafard, M. Korkusinski, Z. R. Wasilewski, O. Stern, and A. Forchel, Science **291**, 451 (2001).

[69] A. Barenco, D. Deutsch, A. Ekert, and R. Jozsa, Phys. Rev. Lett. **74**, 4083 (1995).

[70] H. J. Queisser and E. E. Haller, Science **281**, 945 (1998).

[71] R. Tsu and D. Babić, Appl. Phys. Lett. **64**, 1806 (1994).

[72] S. Kang, Y.-M. Liu, and T. Y. Shi, Eur. Phys. J. B **63**, 37 (2008).

[73] G. Allan and C. Delerue and M. Lannoo and E. Martin, Phys. Rev. B **52**, 11982 (1995).

[74] J. M. Ferreyra, P. Bosshard, and C. R. Proetto, Phys. Rev. B **55**, 13682 (1997).

[75] B. Li, A. F. Slachmuylders, B. Partoens, W. Magnus, and F. M. Peeters, Phys. Rev. B **77**, 115335 (2008).

[76] F. J. Ribeiro and A. Latgé, Phys. Rev. B **50**, 4913 (1994).

[77] P. G. Bolcatto and C. R. Proetto, Phys. Rev. B **59**, 12487 (1999).

[78] G. Bastard, Phys. Rev. B **24**, 4714 (1981).

[79] J. L. Zhu and X. Chen, Phys. Rev. B **50**, 4497 (1994).

[80] N. Porras-Montenegro, S. T. PérezMerchancano, and A. Latgé, J. Appl. Phys. **74**, 7624 (1993).

[81] J. L. Movilla and J. Planelles, Phys. Rev. B **71**, 075319 (2005).

[82] L. Bin, B. Partoens, F. M. Peeters, and W. Magnus, Phys. Rev. B **79**, 085306 (2009).

[83] J. L. Movilla and J. Planelles, Computer Physics Communications **170**, 144 (2005).

[84] A. Thränhardt, C. Ell, G. Khitrova, and H. M. Gibbs, Phys. Rev. B **65**, 035327 (2002).

[85] R. J. Glauber and M. Lewenstein, Phys. Rev. A **43**, 467 (1991).

[86] B. Alperson, I. Rubinstein, G. Hodes, D. Porath, and O. Millo, Appl. Phys. Lett. **75**, 1751 (1999).

[87] U. Banin and O. Millo, Annu. Rev. Phys. Chem. **54**, 465 (2003).

[88] S. Kan, T. Mokari, E. Rothenberg, and U. Banin, Nature materials **2**, 155 (2003).

[89] X. Peng, L. Manna, W. Yang, J. Wickham, E. Scher, A. Kadavanich, and A. P. Alivisatos, Nature **404**, 59 (2000).

[90] U. Woggon, J. Appl. Phys. **101**, 081727 (2007).

[91] J. Hu, L. S. Li, W. Yang, L. Manna, L.-W. Wang, and A. P. Alivisatos, Science **292**, 2060 (2001).

[92] L.-S. Li, J. Hu, W. Yang, and A. P. Alivisatos, Nano Letters **1**, 349 (2001).

[93] D. Katz, T. Wizansky, and O. Millo, Phys. Rev. Lett. **89**, 086801 (2002).

[94] F. Shieh, A. E. Saunders, and B. A. Korgel, J. Phys. Chem. B **109**, 8538 (2005).

[95] E. J. Mueller, Phys. Rev. B **72**, 075322 (2005).

[96] L. Carbone, C. Nobile, M. D. Giorgi, F. D. Sala, G. Morello, P. Pompa, M. Hytch, E. Snoeck, A. Fiore, I. R. Franchini, M. Nadasan, A. F. Silvestre, L. Chiodo, S. Kudera, R. Cingolani, R. Krahne, and L. Manna, Nano Letters **7**, 2942 (2007).

[97] A. L. Efros, M. Rosen, M. Kuno, M. Nirmal, D. J. Norris, and M. Bawendi, Phys. Rev. B **54**, 4843 (1996).

[98] G. Allan and C. Delerue, Phys. Rev. B **70**, 245321 (2004).

[99] J. M. An, A. Franceschetti, S. V. Dudiy, and A. Zunger, Nano Letters **6**, 2728 (2006).

[100] S. Brovelli, R. D. Schaller, S. A. Crooker, F. García-Santamaría, Y. Chen, R. Viswanatha, J. A. Hollingsworth, H. Htoon, and V. I. Klimov, Nature Communications **2**, 280 (2011).

[101] G. Xing, S. Chakrabortty, K. L. Chou, N. Mishra, C. H. A. Huan, Y. Chan, and T. C. Sum, Appl. Phys. Lett. **97**, 061112 (2010).

[102] G. Xing, W. Ji, Y. Zheng, and J. Y. Ying, Appl. Phys. Lett. **93**, 241114 (2008).

[103] G. Xing, S. Chakrabortty, S. W. Ngiam, Y. Chan, and T. C. Sum, J. Phys. Chem. C **115**, 17711 (2011).

[104] J. J. Peterson, L. Huang, C. Delerue, G. Allan, and T. D. Krauss, Nano Letters **7**, 3827 (2007).

[105] G. Nootz, L. A. Padilha, P. D. Olszak, S. Webster, D. J. Hagan, E. W. V. Stryland, L. Levina, V. Sukhovatkin, L. Brzozowski, and E. H. Sargent, Nano Letters **10**, 3577 (2010).

[106] J. L. Movilla, M. Pi, and J. Planelles, J. Appl. Phys. **108**, 064311 (2010).

[107] B. Szafran, F. M. Peeters, S. Bednarek, T. Chwiej, and J. Adamowski, Phys. Rev. B **70**, 035401 (2004).

[108] D. Steiner, T. Mokari, U. Banin, and U. Millo, Phys. Rev. Lett. **95**, 056805 (2005).

[109] T. Mokari, E. Rothenberg, I. Popov, R. Costi, and U. Banin, Science **304**, 1787 (2004).

[110] L. Carbone, S. Kudera, C. Giannini, G. Ciccarella, R. Cingolani, P. D. Cozzoli, and L. Manna, J. Mater. Chem. **16**, 3952 (2006).

[111] J. E. Halpert, V. J. Porter, J. P. Zimmer, and M. G. Bawendi, J. Am. Chem. Soc. **128**, 12590 (2006).

[112] C. H. Wang, T. T. Chen, Y. F. Chen, M. L. Ho, C. W. Lai, and P. T. Chou, Nanotechnology **19**, 115702 (2008).

[113] U. E. H. Laheld and G. T. Einevoll, Phys. Rev. B **55**, 5184 (1997).

[114] O. Mayrock, S. A. Mikhailov, O. Steffens, and U. Rössler, Physica E **1**, 232 (1997).

[115] O. Mayrock, S. A. Mikhailov, T. Darnhofer, and U. Rössler, Phys. Rev. B **56**, 15760 (1997).

[116] X. Li, J. van Embden, J. W. M. Chon, and M. Gu, Appl. Phys. Lett. **94**, 103117 (2009).

[117] D. Steiner, D. Dorfs, U. Banin, F. della Sala, L. Manna, and O. Millo, Nano Letters **8**, 2954 (2008).

[118] K. J. Button, B. Lax, and D. R. Cohn, Phys. Rev. Lett. **24**, 375 (1970).

[119] M. E. Schmidt, S. A. Blanton, M. A. Hines, and P. Guyot-Sionnest, Phys. Rev. B **53**, 12629 (1996).

[120] S. A. Blanton, M. A. Hines, and P. GuyotSionnest, Appl. Phys. Lett. **69**, 3905 (1996).

[121] L. J. Lauhon, M. S. Gudiksen, D. Wang, and C. M. Lieber, Nature **420**, 57 (2002).

[122] G. Shen and D. Chen, Sci. Adv. Mater. **1**, 353 (2009).

[123] G. Shen, D. Chen, Y. Bando, and D. Golberg, J. Mater. Sci. Technol. **24**, 541 (2008).

[124] M. Heigoldt, J. Arbiol, D. Spirkoska, J. M. Rebled, S. Conesa-Boj, G. Abstreiter, F. Peiró, J. R. Morante, and A. Fontcuberta i Morral, J. Mater. Chem. **19**, 840 (2009).

[125] J. Noborisaka, J. Motohisa, S. Hara, and T. Fukui, Appl. Phys. Lett. **87**, 093109 (2005).

[126] A. Fontcuberta i Morral, D. Spirkoska, J. Arbiol, M. Heigoldt, J. R. Morante, and G. Abstreiter, Small **4**, 899 (2008).

[127] R. E. Algra, M. Hocevar, M. A. Verheijen, I. Zardo, G. G. W. Immink, W. J. P. van Enckevort, G. Abstreiter, L. P. Kouwenhoven, E. Vlieg, and E. P. A. M. Bakkers, Nano Letters **11**, 1690 (2011).

[128] T. M. M. Keplinger, J. Stangl, E. Wintersberger, B. Mandl, D. Kriegner, V. Holý, G. Bauer, K. Deppert, and L. Samuelson, Nano Letters **9**, 1877 (2009).

[129] J. Hasen, L. N. Pfeiffer, A. Pinczuk, S. He, K. W. West, and B. S. Dennis, Nature **390**, 54 (1997).

[130] C. Fasth, A. Fuhrer, M. T. Björk, and L. Samuelson, Nano Letters **5**, 1487 (2005).

[131] J. Tatebayashi, Y. Ota, S. Ishida, M. Nishioka, S. Iwamoto, and Y. Arakawa, Appl. Phys. Lett. **100**, 263101 (2012).

[132] C. Colombo, M. Heib, M. Grätzel, and A. Fontcuberta i Morral, Appl. Phys. Lett. **94**, 173108 (2009).

[133] A. Fuhrer, S. Lüscher, T. Ihn, T. Heinzel, K. Ensslin, W. Wegscheider, and M. Bichler, Nature **413**, 822 (2001).

[134] A. Lorke, R. J. Luyken, A. O. Govorov, J. Kotthaus, J. M. García, and P. M. Petroff, Phys. Rev. Lett. **84**, 2223 (2000).

[135] S. Viefers, P. Koskinen, P. S. Deo, and M. Manninen, Physica E **21**, 1 (2004).

[136] I. Filikhin, V. M. Suslov, and B. Vlahovic, Physica E **33**, 349 (2006).

[137] T. Chakraborty and P. Pietilainen, Phys. Rev. B **50**, 8460 (1994).

[138] Z. Barticevic, M. Pacheco, and A. Latgé, Phys. Rev. B **62**, 6963 (2000).

[139] L. E. Lipparini, *Modern Many-Particle Physics* (World Scientific, (Singapore), 2003).

[140] U. F. Keyser, C. Fühner, S. Borck, R. J. Haug, M. Bichler, G. Abstreiter, and W. Wegscheider, Phys. Rev. Lett. **90**, 196601 (2003).

[141] A. Emperador, F. Pederiva, and E. Lipparini, Phys. Rev. B **68**, 115312 (2003).

[142] K. Niemelä, P. Pietiläinen, P. Hyvönen, and T. Chakraborty, Europhys. Lett. **36**, 533 (1996).

[143] F. V. Kusmartsev, J. F. Weisz, R. Kishore, and M. Takahashi, Phys. Rev. B **49**, 16234 (1994).

[144] M. M. Fogler, Phys. Rev. Lett. **94**, 056405 (2005).

[145] W. Häusler and B. Kramer, Phys. Rev. B **47**, 16353 (1993).

[146] J. Planelles, J. I. Climente, and F. Rajadell, Physica E: Low-dimensional Systems and Nanostructures **33**, 370 (2006).